Modal Dispersal of Information and Wave Mixing in Photorefractive Crystals for Information Retrieval, Processing and Sensing

Thesis by

Yasuo Tomita

In Partial Fulfillment of the Requirements

for the Degree of

Doctor of Philosophy

California Institute of Technology

Pasadena, California

1989

(Submitted April 11, 1989)

To My Parents

ACKNOWLEDGEMENTS

First of all I am deeply indebted to my parents, Minoru and Emiko Tomita, and my sister, Keiko, for their constant encouragement and love. Because of their warmth and understanding I could accomplish all these achievements.

I would like to especially express my deep appreciation for the superb guidance, support and constant encouragement of my advisor, Prof. Amnon Yariv, who provided me the keen physical insight and how to "smell" good flavor among many physical problems. He also provided me a laboratory where I had freedom to explore. It truly has been both a privilege and a rewarding experience to work in the creative and dynamic environment of his Quantum Electronics group.

Special thanks go to my colleague Dr. Ram Yahalom whose infectious enthusiasm, criticism, suggestion and encouragement were a source of great inspiration to me.

Thanks are also due to Dr. Kazuo Kyuma for his advice and constant encouragement. I learned a lot from his ingenious physical intuition and warm personality.

I would like to thank Dr. Norman S.-K. Kwong for his helpful discussions and enjoyable company.

I would also like to express my appreciation to Dr. Hajime Mitarai and Dr. Kazuya Matsumoto of Canon Inc. for their constant encouragement and understanding during my leave of absence from the Canon Research Center, Japan.

Finally, I am grateful to Mrs. Jana Mercado for her constant encouragement and help on day-to-day matters, to Mr. Desmond Armstrong for his technical expertise, and the friends I have made during my four-year stay in Southern

California.

ABSTRACT

This thesis describes an experimental and theoretical study on modal dispersal of information and wave mixing in photorefractive crystals for vector phase conjugation and real-time information processing. Photorefractive crystals with short drift lengths ($BaTiO_3$ and $Ba_{1-x}Sr_xNb_2O_6$) and long drift ones ($Bi_{12}SiO_{20}$ and semi-insulating GaAs) are particularly used in this thesis.

In the first part, the photorefractive effect in electrooptic crystals is described in terms of Kukhtarev's band transport model. The explicit solution of the space-charge electric field for the case of one photorefractive species and one type of charge carrier is extended to the case of two photorefractive species and two types of charge carriers. The enhancement of the space-charge electric field is also described. In particular an approximate solution to Stepanov and Petrov's enhancement method of using AC external electric field is extended to a general case that describes the transient behavior for AC external electric field of arbitrary waveform. The anisotropic refractive index change due to the space-charge field formation is then described in terms of tensorial forms of the nonlinear susceptibility.

In the second part, anisotropic beam coupling in photorefractive crystals is presented and a general set of coupled-wave equations that describes beam coupling in amplitude, phase, and polarization is derived by using the nonlinear and tensorial susceptibility. The polarization properties of the interacting waves are particularly stressed. Two limiting cases, i.e., one for scalar beam coupling and the other for cross-polarization beam coupling, are obtained from the general expression and solved. Experimental results of beam coupling in semi-insulating GaAs are presented, and the signs of dominant charge carriers and the density of photorefractive species are estimated from beam-coupling gain. The enhancement

of beam-coupling gain and its temperature dependence are also discussed.

In the third part, four-wave mixing for scalar and vector phase conjugation is described. Self-pumped phase-conjugate mirrors using photorefractive crystals are presented and one of the most interesting properties of these mirrors, i.e., the response to phase changes of inputs, is emphasized both theoretically and experimentally.

In the fourth part, two-wave and four-wave mixing in photorefractive crystals are applied to moving object detection, mathematical operation on images, and one-way image transmission through phase-distorting media. In these applications, polarization properties of interacting waves are particularly utilized.

In the fifth part, a novel method of vector phase conjugation by modal dispersal and scalar phase conjugation is discussed. The propagation characteristics of conjugate waves in strongly scattering media (e.g., mode-scrambling multimode fibers) are described theoretically, followed by the experimental demonstration of vector phase conjugation. In the theory the unitarity and time-reversal symmetry of the scattering matrix are incorporated into the analysis of the coherency matrix of the conjugate field. This theory which describes the physical process of the generation of vector phase conjugation can successfully explain the experimental results of its fidelity.

In the last part, we describe experiments in which the new concept of modal dispersal of information and scalar phase conjugation is used for several novel applications that include nonreciprocal polarization-distortion correction, amplitude-distortion correction, and phase-conjugate multimode fiber-optic sensors. Experiments as well as proposals for these applications are presented.

Part of the material presented in this thesis is based on the following published and unpublished papers:

Chapters 2 and 3:

1. Y. Tomita and A. Yariv, "Photorefractive beam coupling in semi-insulating undoped and Cr-doped GaAs: identification of the signs of dominant photocarriers and deep level densities, and temperature dependence of two-beam coupling gain," unpublished.

Chapter 4:

1. Y. Tomita, R. Yahalom, and A. Yariv, "On the phase shift of a self-pumped phase-conjugate mirror," in *Technical Digest of Annual Meeting of Optical Society of America* (Optical Society of America, Washington D.C., 1988), paper FB8, p.161.

Chapter 5:

1. Y. Tomita, R. Yahalom, and A. Yariv, "Real-time image subtraction with the use of wave polarization and phase conjugation," Appl. Phys. Lett. **52**, 425-427 (1988).
2. N. S.-K. Kwong, Y. Tomita, and A. Yariv, "Optical tracking filter using transient two-beam coupling," J. Opt. Soc. Am. B**5**, 1788-1791 (1988).
3. K. Sayano, Y. Tomita, and A. Yariv, "One-way image transmission through distorting media using orthogonally polarized beams and phase conjugation," unpublished.

Chapters 6 and 7:

1. Y. Tomita, R. Yahalom, K. Kyuma, A. Yariv, and N. S.-K. Kwong, "Polarization and spatial information recovery by modal dispersal and phase conjugation:properties and applications," IEEE J. Quantum Electron. **QE-25**, 315-338 (1989).
2. Y. Tomita, R. Yahalom, and A. Yariv, "Theory of polarization and spatial information recovery by modal dispersal and phase conjugation,"

J. Opt. Soc. Am. B**5**, 690-700 (1988).

3. Y. Tomita, R. Yahalom, and A. Yariv, "Fidelity of polarization and spatial information recovery using a fiber-coupled phase-conjugate mirror," Opt. Lett. **12**, 1017-1019 (1987).

4. Y. Tomita, K. Kyuma, R. Yahalom, and A. Yariv, "Demonstration of amplitude-distortion correction by modal dispersal and phase conjugation," Opt. Lett. **12**, 1020-1022 (1987).

5. R. Yahalom, Y. Tomita, and A. Yariv, "Effect of modal dispersal on the polarization and spatial recovery in a fiber-coupled phase-conjugate mirror," in *Postdeadline Papers of Conference on Lasers and Electro-Optics* (Optical Society of America, Washington, D.C., 1987), paper THT6, p.237.

6. A. Yariv, Y. Tomita, and K. Kyuma, "Theoretical model for modal dispersal of polarization information and its recovery by phase conjugation," Opt. Lett. **11**, 809-811 (1986).

CONTENTS

CHAPTER ONE

Introduction

1.1 Optical phase conjugation and beam coupling via photorefractive nonlinear optics

Optical phase conjugation is a method to reverse wavefronts and (usually) the direction of propagation by which an incoming optical wave is time reversed [1.1,2]. Let us consider a forward-travelling monochromatic electric field in the positive z direction

$$\mathbf{E}(\mathbf{r},t) = \frac{1}{2}\mathbf{e}\mathrm{A}(\mathbf{r})e^{i(\mathbf{k}\cdot\mathbf{r}-\omega t)} + c.c., \tag{1.1}$$

where $\mathbf{e}$ is a unit (complex) vector representing a polarization state, $\mathrm{A}(\mathbf{r})$ is a complex amplitude and the abbreviation *c.c.* denotes the complex conjugate. Its phase-conjugate field is expressed, in terms of the complex-conjugate operation of the spatial part and the polarization vector, that is,

$$\begin{aligned}\mathbf{E}_{\mathrm{pc}}(\mathbf{r},t) &= \frac{1}{2}\mathbf{e}^*\mathbf{A}^*(\mathbf{r})e^{i(-\mathbf{k}\cdot\mathbf{r}-\omega t)} + c.c. \\ &= \mathbf{E}(\mathbf{r},-t),\end{aligned} \tag{1.2}$$

showing the *time reversal* of the forward-travelling wave. Because of the time-reversal symmetry property of Maxwell's equations in lossless nonmagnetic media, such a phase-conjugate wave can propagate as an electromagnetic wave.

Generation of phase-conjugate waves can be performed by a device called a phase-conjugate mirror (PCM). Figure 1.1 illustrates its property in comparison with an ordinary mirror. For the case of the ordinary mirror (with 100% reflectivity) an incoming plane wave with a left-handed circular polarization (i.e., the ellipse is

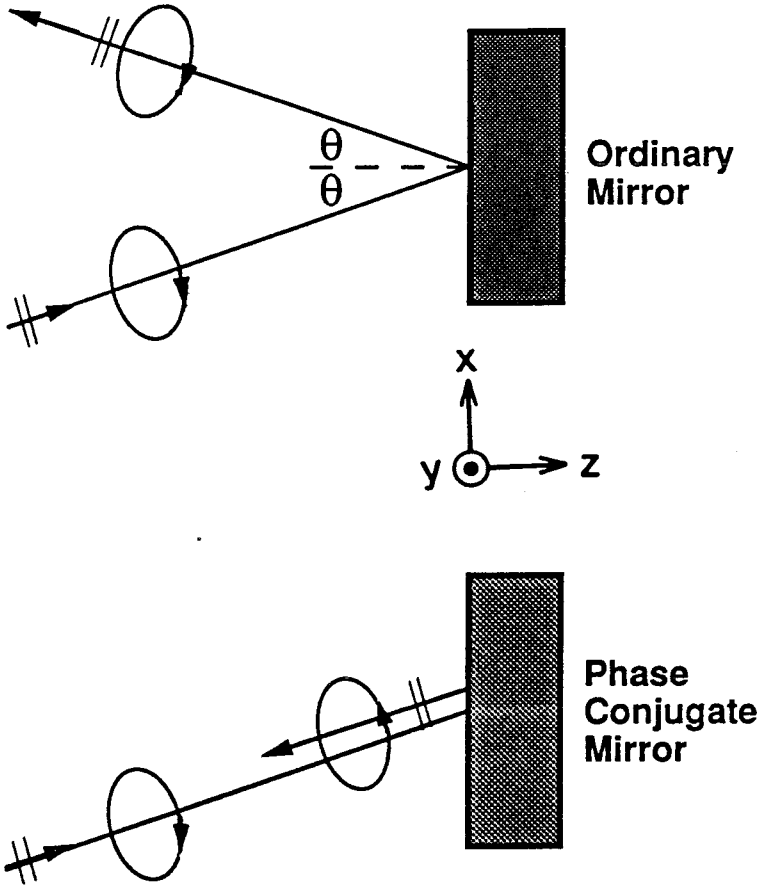

Figure 1.1 Comparison of an ordinary mirror to a phase-conjugate mirror.

traversed in a counter-clockwise sense when looking against the direction of light propagation) is reflected off the mirror with a right-handed circular polarization. The angle of reflection, of course, obeys the law of reflection [1.3]. On the other hand, a PCM reflects the incoming wave back on itself with the same left-handed circular polarization. This is because the reflected wave is a time-reversed replica whose polarization state is represented by the term $\mathbf{e}^*$ in Eq. (1.2) with the direction of propagation reversed.

From a viewpoint of a photon picture, the incoming wave shown in Fig. 1.1 has the linear momentum $\mathbf{p}_{in} = +\hbar\mathbf{k}$, the angular momentum $\mathbf{J}_{in} = +\hbar\mathbf{k}/|\mathbf{k}|$ and the helicity $\lambda_{in}(\equiv \mathbf{p}_{in} \cdot \mathbf{J}_{in}/|\mathbf{p}_{in}||\mathbf{J}_{in}|) = +1$, respectively. Since the reflected wave from the ordinary mirror possesses $\mathbf{p}_{ref} = +\hbar\mathbf{k}'(\mathbf{k}'_z = -\mathbf{k}_z), \mathbf{J}_{ref} = -\hbar\mathbf{k}'/|\mathbf{k}'|$ and thus $\lambda_{ref} = -1$, radiation pressure and torque are imparted to the ordinary mirror [1.3,4]. On the other hand, the reflected phase-conjugate wave from the PCM has $\mathbf{p}_{pc} = \hbar\mathbf{k}''(\mathbf{k}'' = -\mathbf{k}), \mathbf{J}_{pc} = \hbar\mathbf{k}''/|\mathbf{k}''|$ and thus $\lambda_{pc} = +1$. This means that no radiation pressure and torque are imparted to the PCM because linear momentum is conserved upon reflection among all the waves involved in the generation of the phase-conjugate wave in the PCM (i.e., the phase-matching condition is satisfied) and $\lambda_{pc} = \lambda_{in}$ [1.4,5].

Phase conjugation allows for the distortion correction, which is depicted in Fig. 1.2. The wavefront phase and polarization distortions due to a medium having spatially nonuniform phase distribution and anisotropy can be corrected by a double pass via a PCM. In this case, the distorting medium could represent modal dispersal and scattering in multimode fibers, nonuniformities of refractive indices in laser gain media (amplifiers), imperfect optics including birefringent optical components etc. Another aspect of phase conjugation is real-time holography applications for spatial, temporal and spatio-temporal information processing [1.1]. Phase conjugation also

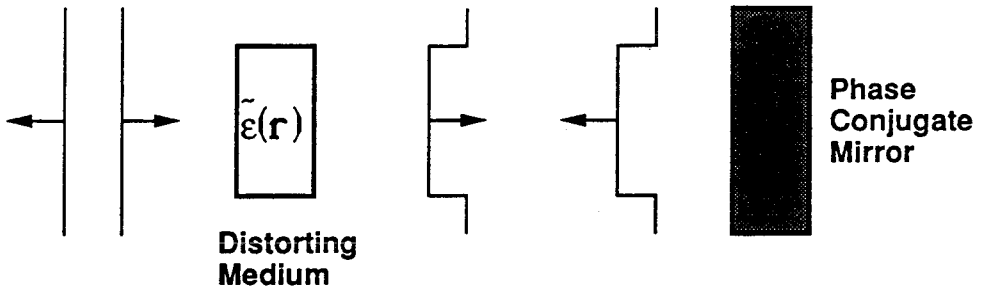

Figure 1.2 Compensation of phase and polarization distortions arising from a medium with a nonuniform tensorial dielectric constant $\tilde{\epsilon}(\mathbf{r})$ by a PCM. By double passing through the medium the distortions can be corrected, provided that $\tilde{\epsilon}(\mathbf{r})$ of the medium is Hermitian, i.e., the distortions are reciprocal.

allows for constructing a phase-conjugate interferometer and/or sensor in which PCM's are used for enhancing sensitivities and robustness against unwanted environmental noise. Figure 1.3 illustrates a comparison of a conventional Michelson interferometer to a phase-conjugate interferometer. In the conventional one two waves interfere each other with (ideally) the same wavefront curvature unless any test object or tilt is introduced in one arm. In the phase-conjugate version two waves interfere each other with the opposite wavefront curvature. Because of this property of the phase-conjugate interferometer even a very small wavefront curvature of an incoming wave can be measured easily (see Fig. 4.7).

Historically, the ideas to use conjugate waves were suggested and demonstrated in conventional holography in the late 1960s. These include imaging through distorting media [1.6,7] and fibers [1.8], and interferometric methods called "conjugate-wavefront interference" [1.9] and "phase-difference amplification" [1.10]. In the 1970s the generation of conjugate waves using wave interactions in nonlinear media was realized [1.11-14] and the richer physical phenomena (e.g., amplification and oscillation) were also found [1.15,16]. A short time later the above applications using holograms were implemented and extended by using nonlinear media which act as PCM's [1.4, 1.17-20].

The physical realization of PCM's via nonlinear optics includes stimulated Brillouin [1.11], Raman [1.21] and Rayleigh line-wing [1.22] backscattering, three-wave mixing [1.12,13] and four-wave mixing [1.14]. Among them four-wave mixing takes advantage of automatic phase-matching geometry between probe and pump beams (see Fig. 1.4) and thus has become the most important technique for the generation of phase-conjugate waves.

The nonlinear media for four-wave mixing include atomic vapors, dyes, liquid crystals, bulk and lower dimensional semiconductors and photorefractive crystals.

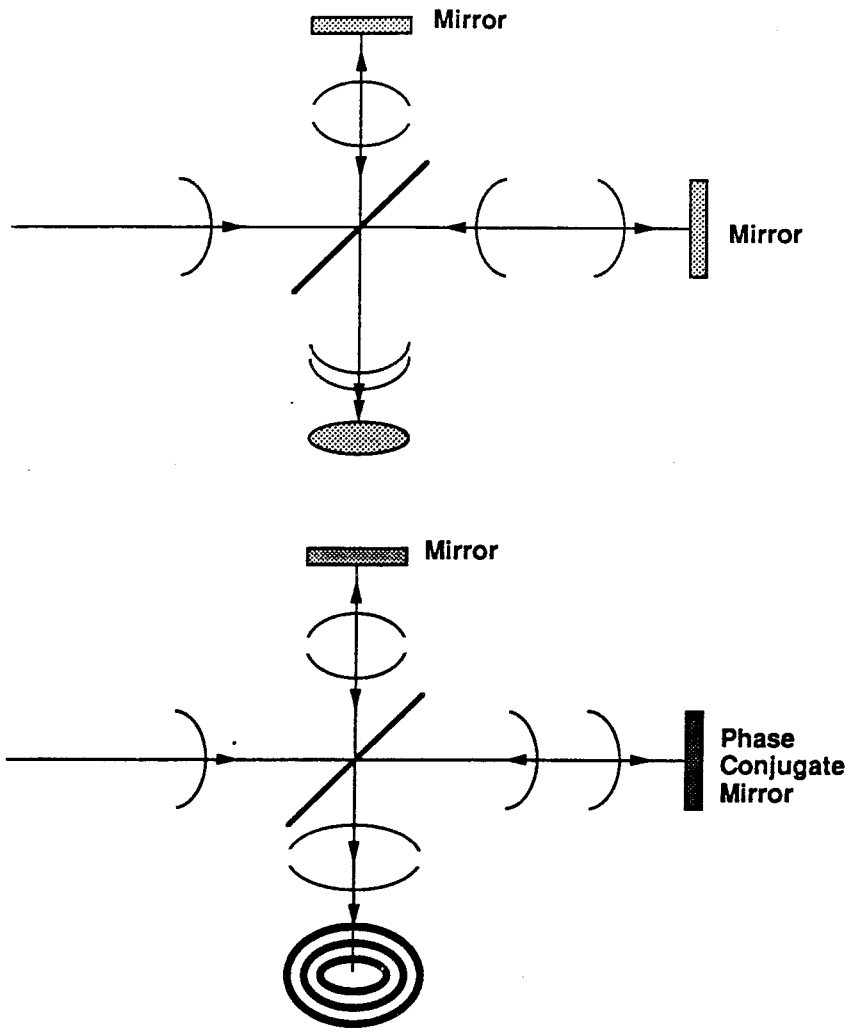

Figure 1.3 Comparison of a conventional Michelson interferometer (upper) to a phase-conjugate version (lower).

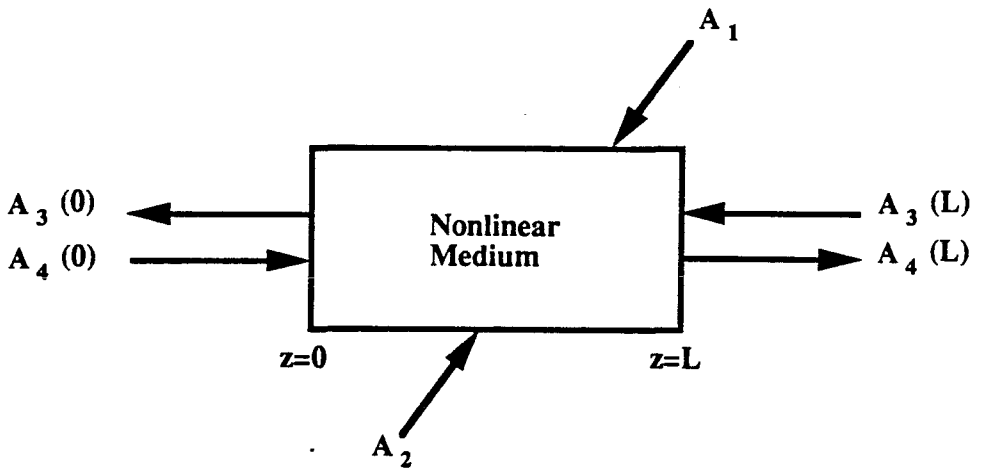

Figure 1.4 Four-wave mixing configuration. A_1 and A_2 are the pump beams, while A_3 and A_4 are the conjugate and probe beams, respectively.

In particular photorefractive crystals are of considerable interest because of the nonlinear effect with milliwatt laser beams and nonresonant sensitivities over the visible and infrared spectra. Furthermore, the photorefractive effect allows the induced index grating written by two beams to be $\pi/2$ out of phase with respect to the intensity-interference pattern. Because of this phase shift one of the beams experiences gain at the expense of the other in their intensities and no phase cross talk between the beams occurs. This phenomenon, called two-beam coupling, also occurs as polarization coupling between two interacting beams because of the tensorial nature of linear (and also quadratic) electrooptic effects. Two-beam coupling and four-wave mixing in photorefractive crystals have been used to realize many novel applications such as image amplifiers [1.23], unidirectional ring oscillators [1.24], and self-pumped PCM's [1.25].

Beam coupling and four-wave mixing phase conjugation in photorefractive crystals have also been used for beam combining. The purpose is to coherently couple together two or more lasers and/or laser gain media to obtain a single diffraction-limited beam whose total power is a coherent superposition of their individual outputs. Figure 1.5(a) shows a schematic of phase-conjugate coupling and locking of individual lasers. In this example, one of the two lasers acts as a "master" laser and the other as a "slave" laser. The slave laser locks to the master laser in frequency as well as phase. This configuration has been successfully demonstrated by using two cw argon ion lasers [1.26,27], two single GaAlAs diode lasers [1.28] and two ten-element laser diode arrays [1.29]. Figure 1.5(b) illustrates another technique for coupling multiple laser amplifiers by phase conjugation. The possible wavefront distortion caused by the amplifiers can be corrected by a double pass. The demonstration of this scheme has been made by using four pulsed dye gain media [1.30] and a single GaAlAs semiconductor laser amplifier [1.31]. In all the above experimental demonstrations [1.26-31] photorefractive $BaTiO_3$ crystals

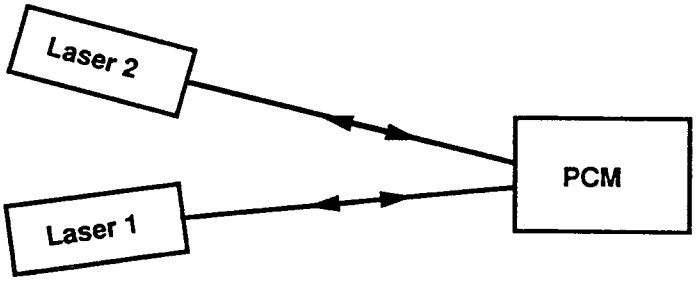

(a)

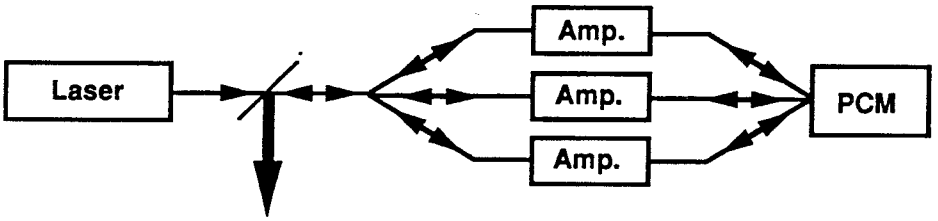

(b)

Figure 1.5 Beam combining techniques using phase conjugation. (a) Phase-conjugate coupling and locking of individual lasers. (b) Coherent coupling of multiple laser amplifiers.

were employed as self-pumped PCM's because of large phase-conjugate reflectivities. (The pioneering works of beam combining with phase conjugation used nine independent regions of a Nd:YAG laser amplifier and a four-wave hypersonic PCM [1.32] and two Nd:YAG laser amplifiers with stimulated Brillouin scattering phase conjugation [1.33].)

PCM's using photorefractive crystals usually respond only to an input with linear polarization. However this limitation can be obviated by either simply phase conjugating each polarization component separately [1.34], a method originally used by Basov et al. [1.35] or more interestingly introducing an information-scrambling medium (e.g., a mode-scrambling multimode fiber) prior to a photorefractive PCM [1.36-40]. The latter method for vector phase conjugation works because initial modes are fully scrambled among all the other modes during the propagation in such an information-scrambling medium and any one of spatial modes (or frequencies) of the output from the information-scrambling medium contains all the input information. This permits the full recovery of the original information via phase conjugating a portion of the scrambled fields and modal averaging during backpropagation through the information-scrambling medium. This new concept, called *modal dispersal of information and phase conjugation*, may be regarded as a real-time version of holography with a diffused signal [1.41]. In addition, the fact that a tandem combination of multimode fibers and a photorefractive PCM allows for vector phase conjugation gives another possible application in optical interconnection and/or communication [1.42,43] (see Fig. 1.6). The theoretical and experimental study on the new concept and its applications will be described in great detail in this thesis.

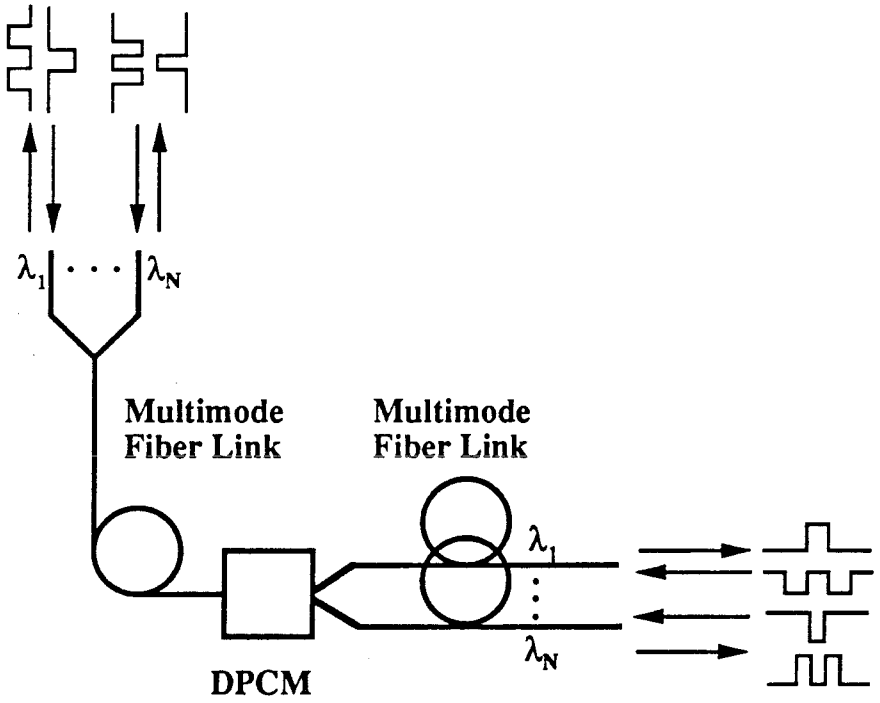

Figure 1.6 Potential application to optical interconnection and/or communication using multimode fibers and a double phase-conjugate mirror (DPCM). In this example DPCM conjugates wavefronts of mutually incoherent inputs from both fiber links but allows for transmitting temporal information of inputs possessing the same wavelength from one fiber link to the other. (The properties and applications of DPCM are described in Chapters 4 and 5.) Modal noise and depolarization (caused by modal dispersion and scattering) during propagation in multimode fibers can be corrected even by scalar phase conjugation (i.e., by conjugating only one polarization component of depolarized waves), which is described in detail in Chapter 6.

1.2 Outline of thesis

This thesis describes theory and applications of modal dispersal of information and wave mixing in photorefractive crystals for vector phase conjugation and real-time information processing. In particular, properties of wave polarizations in wave mixing processes are stressed.

Chapter 2 describes the photorefractive effect in electrooptic crystals. The space-charge field formation is considered for two cases that describe the photorefractive mechanism with one photorefractive species and one type of charge carrier and with two photorefractive species and two types of charge carriers. The transient- and steady-state solutions are obtained by using Kukhtarev's band transport model. Symmetry properties of anisotropic photorefractive index gratings arising from the space-charge field are also discussed.

Chapter 3 details the beam coupling phemonena in photorefractive anisotropic crystals. A set of coupled-wave equations that describe polarization coupling as well as energy coupling is derived in the most general form. Solutions are given particularly for scalar and cross-polarization beam coupling. Beam coupling in semi-insulating GaAs is then described. In the experimental part the sign of the dominant charge carriers and the density of photorefractive species are identified from a comparison between the theoretical beam coupling gain and the experimental one. In the theoretical part the enhancement of the beam coupling gain and its temperature dependence are discussed.

Chapter 4 treats four-wave mixing in photorefractive crystals. Scalar and vector phase conjugation using four-wave mixing processes are described briefly. Self-pumped PCM's using photorefractive crystals are then introduced. Because these mirrors can generate scalar phase-conjugate waves without additional pump waves, they possess several unique properties. The response to phase changes of inputs, one of the most important properties in self-pumped PCM's, is investigated

both theoretically and experimentally. This property is used for the construction of phase-conjugate multimode fiber-optic interferometers described in Chapter 7.

In Chapter 5 three applications of two- and four-wave mixing in photorefractive crystals are presented. These include an optical tracking filter for transient image detection, mathematical operations on images, and one-way image transmission through wavefront phase-distorting media. The principles of these methods are explained by the theories presented in the earlier chapters.

Chapter 6 discusses a novel method for vector phase conjugation, which uses modal dispersal of information (by mode-scrambling multimode fibers) and scalar phase conjugation. The theory is given to describe propagation characteristics of conjugate waves in strongly scattering media. The fidelity of this phase conjugation process is given as a function of input-beam spatial frequencies. The experimental demonstration of this method is given, and the experimental results of the fidelity of phase conjugation are also compared with the theory.

In Chapter 7 several applications of modal dispersal and phase conjugation are presented. These include nonreciprocal polarization-distortion correction, amplitude-distortion correction and phase-conjugate multimode fiber-optic sensors. In the first two applications it is shown that, despite a breakdown of the time-reversal symmetry of the system (due to nonreciprocal and lossy distortions), the original information can be recovered (under certain conditions) by virtue of phase conjugation followed by modal dispersal of the initial information. In the third application it is shown that sensitive sensors with robustness, self-alignment, and inexpensive cost can be constructed.

References for Chapter 1

1.1. R.A. Fisher, ed., *Optical Phase Conjugation* (Academic Press, New York, 1983).

1.2. B.Ya Zel'dovich, N.F. Pilipetsky, and V.V. Shkunov, *Principles of Phase Conjugation* (Springer-Verlag, New York, 1985).

1.3. E. Hecht and A. Zajac, *Optics* (Addison-Wesley, Reading, 1979).

1.4. D.M. Pepper, Opt. Eng. **21**, 156 (1982); Ph.D. Dissertation (California Institute of Technology, Pasadena, California, 1980, unpublished).

1.5. M. Schubert and B. Wilhelmi, *Nonlinear Optics and Quantum Electronics* (Wiley, New York, 1986).

1.6. H. Kogelnik, Bell Sys. Tech. J. **44**, 2451 (1965); H. Kogelnik and K.S. Pennington, J. Opt. Soc. Am. **58**, 273 (1968).

1.7. W. Lukosz, J. Opt. Soc. Am. **58**, 1084 (1968).

1.8. M.M. Ponte, C.R. Acad. Soc. Paris t.**264**, 1015 (1967).

1.9. K. Matsumoto and T. Ose, Seisan-Kenkyu (Mon. J. Inst. Industrial Sci., Univ. of Tokyo) **19**, 18 (1967).

1.10. K. Matsumoto and M. Takashima, J. Opt. Soc. Am. **60**, 30 (1970).

1.11. B.Ya Zel'dovich, V.I. Popovichev, V.V. Ragul'skii, and F.S. Fasisullov, Sov. Phys. JETP Lett. **15**, 109 (1972).

1.12. A. Yariv, Appl. Phys. Lett. **28**, 88 (1976); J. Opt. Soc. Am. **66**, 301 (1976).

1.13. A. Yariv, Opt. Commum. **21**, 49 (1977).

1.14. R.W. Hellworth, J. Opt. Soc. Am. **67**, 1 (1977).

1.15. A. Yariv and D.M. Pepper, Opt. Lett. **1**, 16 (1977).

1.16. D.M. Bloom and G.C. Bjorklund, Appl. Phys. Lett. **31**, 592 (1977).

1.17. G.J. Dunning and R.C. Lind, Opt. Lett. **7**, 558 (1982).

1.18. F.A. Hopf, A. Tomita, and G. Al-Jumaily, Opt. Lett. **5**, 386 (1980).

1.19. F.A. Hopf and M. Cervantes, Appl. Opt. **21**, 668 (1982).

1.20. J. Feinberg, Opt. Lett. **8**, 569 (1983).

1.21. V. Wang and C.R. Giuliano, Opt. Lett. **2**, 4 (1978).

1.22. B.Ya Zel'dovich, N.F. Pilipelskii, V.V. Ragul'skii, and V.V. Shkunov, Sov. J. Quantum Electron. **8**, 1021 (1978).

1.23. T. Tschudi, A. Herden, J. Goltz, H. Klumb, F. Laeri, and F. Albers, IEEE J. Quantum Electron. **QE-19**, 1493 (1986).

1.24. J.O. White, M. Cronin-Golomb, B. Fischer, and A. Yariv, Appl. Phys. Lett. **40**, 450 (1982).

1.25. M. Cronin-Golomb, B. Fischer, J.O. White, and A. Yariv, IEEE J. Quantum Electron. **QE-20**, 12 (1984).

1.26. J. Feinberg and G.D. Bacher, Appl. Phys. Lett. **48**, 570 (1986).

1.27. S. Sternklar, S. Weiss, M. Segev, and B. Fischer, Opt. Lett. **11**, 528 (1986).

1.28. M. Cronin-Golomb, A. Yariv, and I. Ury, Appl. Phys. Lett. **48**, 1240 (1986).

1.29. M. Segev, S. Weiss, and B. Fischer, Appl. Phys. Lett. **50**, 1397 (1987).

1.30. J.O. White, G.C. Valley, and R.A. McFarlane, Appl. Phys. Lett. **50**, 880 (1987).

1.31. R.R. Stephens, R.C. Lind, and C.R. Giuliano, Appl. Phys. Lett. **50**, 647 (1987).

1.32. N.G. Basov, V.F. Efimkov, I.G. Zubarev, A.V. Kotov, and S.I. Mikhailov, Sov. J. Quantum Electron. **11**, 1335 (1981).

1.33. D.A. Rockwell and C.R. Giuliano, Opt. Lett. **11**, 147 (1986).

1.34. I. McMichael, M. Khoshnevisan, and P. Yeh, Opt. Lett. **11**, 525 (1986).

1.35. N.G. Basov, V.F. Efimkov, I.G. Zubarev, A.V. Kotov,S.I. Mikhailov, and M.G. Smirnov, Sov. Phys. JETP Lett. **28**, 197 (1978).

1.36. K. Kyuma, A. Yariv, and S.-K. Kwong, Appl. Phys. Lett. **49**, 617 (1986).

1.37. A. Yariv, Y. Tomita, and K. Kyuma, Opt. Lett. **11**, 809 (1986).

1.38. Y. Tomita, R. Yahalom, and A. Yariv, Opt. Lett. **12**, 1017 (1987).

1.39. Y. Tomita, R. Yahalom, and A. Yariv, J. Opt. Soc. Am. B**5**, 690 (1988).

1.40. Y. Tomita, R. Yahalom, K. Kyuma, A. Yariv, and N. S.-K. Kwong, IEEE J. Quantum Electron. **QE-25**, 315 (1989).

1.41. R.J. Collier, C.B. Burckhardt, and L.H. Lin, *Optical Holography* (Academic Press, New York, 1971).

1.42. H.J. Caulfield, J. Shamir, and Q. He, Appl. Opt. **26**, 2291 (1987).

1.43. S. Weiss, M. Segev, S. Sternklar, and B. Fischer, Appl. Opt. **27**, 3422 (1988).

CHAPTER TWO

The Photorefractive Effect in Electrooptic Crystals

2.1 Introduction

The light-induced changes of refractive index in electrooptic crystals, called the photorefractive effect, has been studied extensively in the field of nonlinear optics. This is because its strong nonlinearity (via the electrooptic effect) with milliwatt laser beams of visible and infrared wavelengths and with existing bulk materials is well suited for an ever increasing number of optical information processing applications.

The history of its study began with the discovery of unwanted "optical damage" in electrooptic crystals such as $LiNbO_3$ and $LiTaO_3$ in 1966 [2.1]. It was observed that the light-induced changes of refractive indices caused defocusing and scattering of laser beams in such crystals used as frequency doublers and modulators. It was also found that the changes persisted in the dark but were erasable by uniform illumination of the crystals.

Soon afterward applications of such an optical damage in $LiNbO_3$ to "3-dimensional" mass-storage (supposedly with a maximum storage density of 10^{12} bits/cm^3) and erasable holographic optical memories were recognized [2.2-4]. Although the interest in the realization of the holographic optical memory system drove enormous studies until the mid-1970s [2.5-9], the problems of degradation of the stored information both during readout and in the dark attenuated the interest. Instead the "2-dimensional" erasable optical disk memories using magnetooptic media are now put into practice [2.10].

With a viewpoint of eliminating optical damage in electrooptic devices, numerous studies on the mechanism of the photorefractive effect were done in the 1970s [2.11-29]. The basic mechanism of the photorefractive effect results from the spatial modulation of photocurrents by spatially nonuniform illumination and is summarized as follows: the photoexcited electrons (or holes) from some impurity centers migrate due to diffusion or drift and are trapped at other sites in the crystal, leaving behind positive (or negative) charges of ionized impurity centers. These photoexcited carriers, once trapped, are reexcited and retrapped until they are finally trapped at the darker illuminated region. Because of the resulting asymmetric charge distributions between the photoexcited carriers and the ionized impurity centers, a space-charge field is established in the crystal and modulates the refractive index via the electrooptic effect. In this case the induced refractive index grating is in general shifted from the light-intensity distribution. The space-charge field can be negated by uniform illumination of a suitable wavelength (see Fig. 2.1 for the whole process of the effect).

The most general set of material equations describing the photorefractive effect was introduced by Kukhtarev *et al.* [2.20,25,28] and also by Moharam *et al.* [2.29]. Their analyses treat the deterministic transport of carriers and are called the "band transport model." Later the "hopping model" was proposed by Feinberg *et al.* [2.30]. Instead of describing diffusion and drift of carriers, this model assumes that carriers hop from filled sites to vacant ones under illumination, and its hopping rate is treated statistically. In spite of the physical difference between these two models, one particular form of the hopping probability distribution (i.e., the Yukawa potential form) gives the same results as those of the band transport model. This coincidence, however, has not been physically clarified yet. Although we have not reached a complete understanding of the effect so far, the band transport model

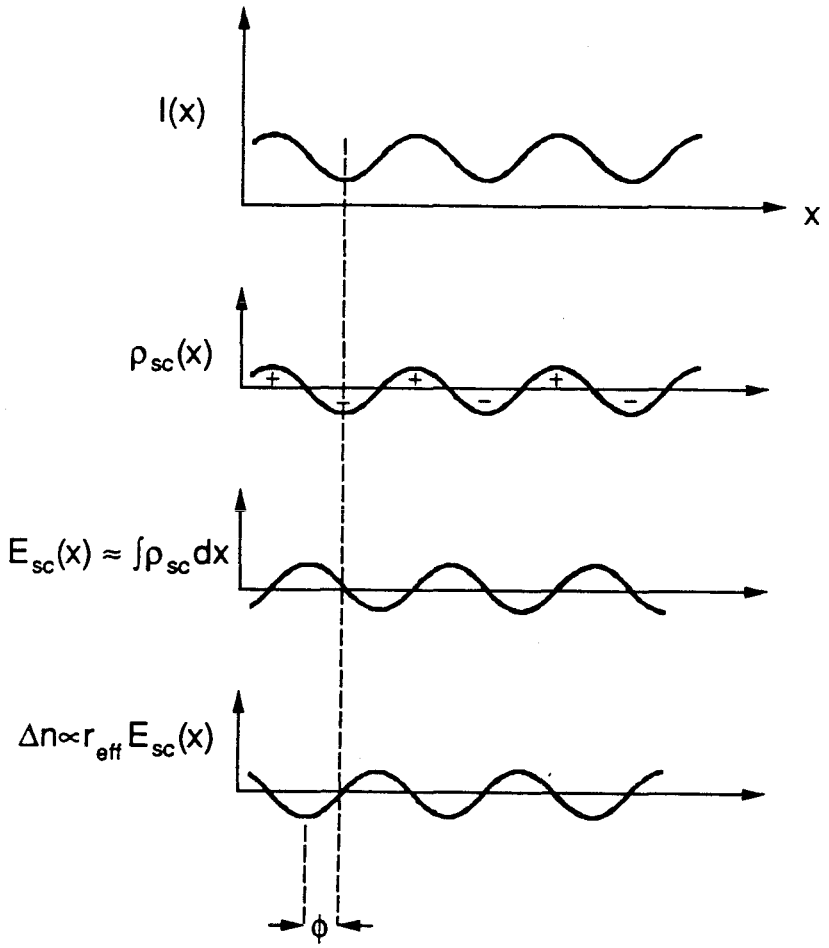

Figure 2.1 The photorefractive mechanism. The photoexcited carriers from some impurity centers migrate to the darker regions of the nonuniform illumination $I(x)$, leaving behind opposite charges of ionized impurity centers. The resulting asymmetric charge distribution $\rho_{sc}(x)$ between the carriers and the ionized impurity centers causes the space-charge field $E_{sc}(x)$ which induces the refractive index grating $\Delta n(x)$ via the electrooptic effect.

seems well supported by many experimental observations and is also employed in this thesis.

As the theoretical and experimental investigations of the photorefractive origins were progressing, several theories describing nonlinear wave interactions in photorefractive crystals were also reported in the mid-1970s[2.31-34]. Since then new and more precise theories have been advanced [2.28,35-41] and new optical phenomena based on these theories have also been demonstrated [2.42]. With the help of these theories the real-time write and readout property of the photorefractive effect has opened numerous applications of real-time optical information processing, dynamic holography, and phase conjugation [2.42].

So far the photorefractive effect has been observed in many electrooptic crystals. These include $LiNbO_3$ and $LiTaO_3$ [2.1], $BaTiO_3$ [2.43], $KNbO_3$ [2.44], $K(TaNb)O_3$(KTN) [2.44,45], $Ba_2NaNb_5O_{15}$ [2.46], $Ba_{1-x}Sr_xNb_2O_6$(SBN) [2.47] and other tungsten bronze ferroelectrics [2.48], $Bi_4Ti_3O_{12}$(BTO) [2.49], $Bi_{12}SiO_{20}$(BSO) and $Bi_{12}GeO_{20}$(BGO) [2.50,51], KH_2PO_4 [2.52], Rb_2ZnBr_4 [2.53], $(Pb,La)(Zr,Ti)O_3$ [2.54], CdS [2.55], and compound semiconductors such as undoped GaAs [2.56], GaAs:Cr [2.57], InP:Fe [2.57], and CdTe:In [2.58].

In this chapter the space-charge field formation using the band transport model is described. One photorefractive species (i.e., one impurity center) and one type of carrier solution, and two photorefractive species and two types of carriers solution to the band transport equations are given. Two possible methods for the enhancement of the space-charge field are also described. Tensorial refractive index changes due to the space-charge field via the electrooptic effect are discussed particularly for several crystal symmetry classes which include important photorefractive materials cited above. These refractive index changes cause the isotropic and anisotropic beam coupling phenomena in photorefractive crystals, which will be discussed in the next chapter.

2.2 Space-charge field formation by photoexcited carriers

2.2.1 The band transport model

In Kukhtarev's original band transport model [2.25,28], the transport of one type of carrier with one species responsible for the carrier emission and trap is treated. In recent years multiple species and/or simultaneous electron and hole transport models have been suggested to properly explain either the transient-state or the steady-state behavior of photorefractive materials (e.g., $LiNbO_3$ [2.59-61], BSO and BGO [2.62-66], and $BaTiO_3$ [2.67-69]). In this section we consider the case where there are two independent sets of photoactive species, one in which the dominant carriers are electrons and the other in which they are holes. This would occur if the photoionization cross sections and the recombination rate coefficients of one species are significant for electrons and those of the other species for holes. In the analysis the "quasi-steady approximation" [2.25] (i.e., the response time of the space-charge field formation is slower than the carrier recombination time so that the mean carrier densities are constant during the space-charge formation) is used.

Figure 2.2 shows the two species and two types of carriers model. Electrons photoexcited from the neutral donor level D_n of the species D to the conduction band are trapped by the ionized donor level D_i after diffusion or drift, and thereby the space-charge field is formed. Likewise, holes photoexcited from the neutral acceptor level A_n of the species A to the valence band are trapped by the ionized acceptor level A_i, and thereby a space-charge field in opposite direction to that of electrons is formed. The total space-charge field in turn exercises a force on transporting electrons and holes. This interaction process continues until the steady state is reached. The refractive index variation is finally created by the space-charge field via the electrooptic effect. This nonlinear transport process is described by the following set of equations:

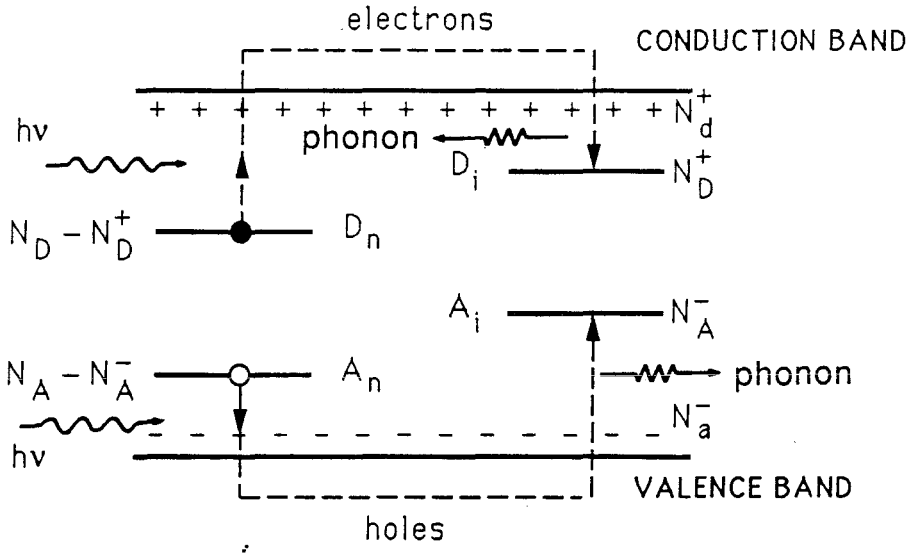

Figure 2.2 Band transport model for the case of two photorefractive species (the donor impurity center D and the acceptor impurity center A) and two types of carriers (electrons and holes). The shallow ionized donors and acceptors that compensate the ionized donor and acceptor impurity centers in the dark (D_i and A_i, respectively) are shown by the signs + and −.

Continuity equation

$$\frac{\partial}{\partial t}(n + \mathrm{N_A^-} - \mathrm{N_D^+} + p) - \frac{1}{e}\nabla \cdot \mathbf{J} = 0, \tag{2.1}$$

Rate equations

$$\frac{\partial \mathrm{N_D^+}}{\partial t} = (\beta_\mathrm{e} + s_\mathrm{e}\mathrm{I}/\hbar\omega)(\mathrm{N_D} - \mathrm{N_D^+}) - \gamma_\mathrm{e} n \mathrm{N_D^+}, \tag{2.2a}$$

$$\frac{\partial \mathrm{N_A^-}}{\partial t} = (\beta_\mathrm{h} + s_\mathrm{h}\mathrm{I}/\hbar\omega)(\mathrm{N_A} - \mathrm{N_A^-}) - \gamma_\mathrm{h} p \mathrm{N_A^-}, \tag{2.2b}$$

Current equation

$$\mathbf{J} = e(\mu_\mathrm{e} n + \mu_\mathrm{h} p)\mathbf{E} - k_\mathrm{B}\mathrm{T}(\mu_\mathrm{h}\nabla p - \mu_\mathrm{e}\nabla n), \tag{2.3}$$

Poisson equation

$$\nabla \cdot \mathbf{E} = -\frac{4\pi}{\epsilon_s} e(n + \mathrm{N_a^-} + \mathrm{N_A^-} - p - \mathrm{N_d^+} - \mathrm{N_D^+}), \tag{2.4}$$

Charge – neutrality condition

$$p_0 + \mathrm{N_d^+} + \mathrm{N_{D0}^+} = n_0 + \mathrm{N_a^-} + \mathrm{N_{A0}^-}, \tag{2.5}$$

where we neglect the photovoltaic contribution [2.18], and the parameters are defined as follows:

J: current density

E: space-charge electric field

n: electron number density

p: hole number density

$\mathrm{N_D}$: total number density of the species D

$\mathrm{N_D^+}$: number density of $\mathrm{D_i}$ that acts as acceptors for electron transport

$\mathrm{N_{D0}^+}$: number density of $\mathrm{D_i}$ under uniform illumination

N_A: total number density of the species A

N_A^-: number density of A_i that acts as donors for hole transport

N_{A0}^-: number density of A_i under uniform illumination

N_d^+: number density of ionized non-photoactive shallow donors that compensate for the charge of N_A^- in the dark

N_a^-: number density of ionized non-photoactive shallow acceptors that compensate for the charge of N_D^+ in the dark

ϵ_s: static dielectric constant

$\mu_e(\mu_h)$: electron (hole) mobility

$\beta_e(\beta_h)$: thermal ionization rate of the donor (acceptor)

$s_e(s_h)$: photoionization cross section of the donor (acceptor)

$\gamma_e(\gamma_h)$: two-body recombination rate coefficient for electrons (holes)

T: temperature

ω: circular frequency of the optical field ($=2\pi\nu$)

e: magnitude of the charge on the electron

$\hbar$: Planck's constant ($=h/2\pi$)

k_B: Boltzmann's constant

and the nonuniform light intensity I is assumed to be sinusoidally modulated along the x direction such that

$$I(x) = I_0 + \frac{1}{2} I_0 m e^{iKx} + c.c., \tag{2.6}$$

where K is the wavenumber of the light interference pattern and m is the light modulation index. We note that μ_e, μ_h, and e, defined above, are all positive.

In the following two subsections the two solutions for the lowest Fourier component K of the space-charge field are given: one for one species and one

type of carrier, the other for two species and two types of carriers. This is done by using the small modulation index approximation, i.e., $|m| \ll 1$, and taking only the lowest Fourier components of $n, p, \mathrm{N_D^+}, \mathrm{N_A^-}$, and E into account, that is,

$$n = n_0 + \frac{1}{2} n_1 e^{iKx} + c.c.,$$

$$p = p_0 + \frac{1}{2} p_1 e^{iKx} + c.c.,$$

$$\mathrm{N_D^+} = \mathrm{N_{D0}^+} + \frac{1}{2} \mathrm{N_{D1}^+} e^{iKx} + c.c.,$$

$$\mathrm{N_A^-} = \mathrm{N_{A0}^-} + \frac{1}{2} \mathrm{N_{A1}^-} e^{iKx} + c.c.,$$

$$\mathrm{E} = \mathrm{E_0} + \frac{1}{2} \mathrm{E_1} e^{iKx} + c.c.,$$

where $\mathrm{E_0}$ is an externally applied electric field. We note that, though not treated in this thesis, the higher-order Fourier components of the space-charge field become important as the modulation index approaches unity [2.28,70-72].

2.2.2 The one species and one type of carrier solution

We first consider the simplest case where one species, e.g., the species D in Fig. 2.2, and one type of carriers (electrons) only participate the photorefractive effect. In this case we set $\mathrm{N_A} = \mathrm{N_A^-} = \mathrm{N_{A0}^-} = \mathrm{N_d^+} = p = 0$ in Eqs. (2.1)–(2.5) and obtain the following inhomogeneous ordinary differential equation for the lowest Fourier component of the space-charge field:

$$\frac{\partial^2 \mathrm{E_1}}{\partial t^2} + a_1 \frac{\partial \mathrm{E_1}}{\partial t} + a_2 \mathrm{E_1} = F, \tag{2.7}$$

where

$$a_1 = \frac{1}{\tau_{\mathrm{de}}} + \frac{1}{\tau_{0\mathrm{e}}} + \frac{1}{\tau_{\mathrm{De}}} - \frac{i}{\tau_{\mathrm{Ee}}}, \tag{2.8a}$$

$$a_2 = \frac{1}{\tau_{\mathrm{de}} \tau_{0\mathrm{e}}} - \frac{1}{\tau_{\mathrm{Ie}}} \left(\frac{i}{\tau_{\mathrm{Ee}}} - \frac{1}{\tau_{\mathrm{De}}} \right), \tag{2.8b}$$

$$F = \frac{im}{1+\beta_e\hbar\omega/s_e I_0}\frac{i/\tau_{Ee}-1/\tau_{De}}{\mu_e\tau_{Re}\tau_{de}K}, \tag{2.8c}$$

in which

$$\tau_{de} = \frac{\epsilon_s}{4\pi e\mu_e n_0} \quad \text{(dielectric relaxation time)}, \tag{2.9a}$$

$$\tau_{De} = \frac{e}{\mu_e k_B T K^2} \quad \text{(diffusion time)}, \tag{2.9b}$$

$$\tau_{Ee} = \frac{1}{K\mu_e E_0} \quad \text{(drift time)}, \tag{2.9c}$$

$$\tau_{Re} = \frac{1}{\gamma_e N_{D0}^+} \quad \text{(two-body recombination time)}, \tag{2.9d}$$

$$\tau_{0e} = \frac{1}{\beta_e + s_e I_0/\hbar\omega + \gamma_e(2n_0 + N_{D0}^+)}$$
$$\tau_{Ie} = \frac{1}{\beta_e + s_e I_0/\hbar\omega + \gamma_e n_0} \quad \text{(other characteristic time)}, \tag{2.9e}$$

$$n_0 = \frac{(\beta_e + s_e I_0/\hbar\omega)(N_D - N_{D0}^+)}{\gamma_e N_{D0}^+} \quad \text{(mean number density of electrons)}. \tag{2.9f}$$

Equations (2.5) and (2.9*f*) constitute the zeroth-order equations for the mean number density of electrons. But for typical cw laser intensities($I_0 \leq 1 W/cm^2$) in photorefractive experiments the number density of electrons is of the order of $10^7 - 10^{12}$ cm^{-3} while N_{D0}^+ and N_a^- are of the order of $10^{15} - 10^{17}$ cm^{-3} [2.73]. Thus we can reasonably assume that $N_{D0}^+ \approx N_a^-$ (and also $N_{A0}^- \approx N_d^+$ for holes)

in Eqs. (2.9). Together with the parameters defined in Eqs. (2.9) the following relevant transport lengths will be also employed hereafter:

$$l_{se} = \left(\frac{\epsilon_s k_B T}{4\pi e^2 N_{Te}}\right)^{\frac{1}{2}} \quad \text{(Debye screening length)}, \tag{2.10a}$$

$$l_{Ee} = \frac{\epsilon_s E_0}{4\pi e N_{Te}} \quad \text{(length of electron tightening by } E_0\text{)}, \tag{2.10b}$$

$$r_{De} = \left(\frac{\mu_e \tau_{Re} k_B T}{e}\right)^{\frac{1}{2}} \quad \text{(electron diffusion length)}, \tag{2.10c}$$

$$r_{Ee} = \mu_e \tau_{Re} E_0 \quad \text{(electron drift length)}, \tag{2.10d}$$

where

$$N_{Te} = \frac{N_{D0}^{+}(N_D - N_{D0}^{+})}{N_D} \quad \text{(number density of mobile carriers)}, \tag{2.11}$$

in which we note again $N_{D0}^{+} \approx N_a^{-}$.

In most of the photorefractive materials it is appropriate to assume that $\tau_{0e} \approx \tau_{Re} \ll \tau_{De}, \tau_{Ee}, \tau_{de}\tau_{Ie} < \tau_e$ (= response time of the space-charge field formation). Equation (2.7) is then reduced to

$$\frac{\partial E_1}{\partial t} + \frac{1}{T_e} E_1 = \frac{1}{T_e} E_{sc}^0, \tag{2.12}$$

where T_e is the complex time constant of E_1 given by

$$\begin{aligned} T_e &= \frac{a_1}{a_2} \\ &= \frac{1/\tau_{de} + 1/\tau_{0e} + 1/\tau_{De} - i/\tau_{Ee}}{1/\tau_{de}\tau_{0e} - 1/\tau_{Ie}(i/\tau_{Ee} - 1/\tau_{De})}, \end{aligned} \tag{2.13}$$

and E_{sc}^0 is the steady-state lowest Fourier component of the space-charge field given by

$$E_{sc}^0 = \frac{-im}{1 + \beta_e \hbar\omega / s_e I_0} \frac{E_{qe}(E_D - iE_0)}{E_{qe} + E_D - iE_0}, \tag{2.14}$$

in which

$$E_{qe} = \frac{4\pi e N_{Te}}{\epsilon_s K} \quad \text{(maximum space} - \text{charge field)}, \tag{2.15a}$$

$$E_D = \frac{K k_B T}{e} \quad \text{(diffusion field)}. \tag{2.15b}$$

The solution to Eq. (2.12) has the following exponential form for the time response:

Writing phase

$$E_1(t) = E_{sc}^0 \left[1 - e^{-t/\tau_e - i\omega_e t}\right], \tag{2.16a}$$

Erasing phase

$$E_1(t) = E_{sc}^0 e^{-t/\tau_e - i\omega_e t}, \tag{2.16b}$$

where

$$\tau_e = \tau_{de} \frac{\left(1 + \tau_{0e}/\tau_{De}\right)^2 + \left(\tau_{0e}/\tau_{Ee}\right)^2}{\left(1 + \tau_{0e}\tau_{de}/\tau_{Ie}\tau_{De}\right)\left(1 + \tau_{0e}/\tau_{De}\right) + \left(\tau_{0e}/\tau_{Ee}\right)^2\left(\tau_{de}/\tau_{Ie}\right)}, \tag{2.17a}$$

$$\omega_e = \frac{1}{\tau_{de}\tau_{Ee}} \frac{\tau_{0e}\left(\tau_{de}/\tau_{Ie} - 1\right)}{\left(1 + \tau_{0e}/\tau_{De}\right)^2 + \left(\tau_{0e}/\tau_{Ee}\right)^2}. \tag{2.17b}$$

It is seen from Eqs. (2.14)-(2.17) that E_1 has the following properties:

1) there exists only one time constant for the formation of the space-charge field,
2) when $E_0 = 0$ (i.e., the diffusion mechanism is dominant), there is no oscillation (i.e., $\omega_e = 0$) in the transient state, and E_1 is $\pi/2$ out of phase with respect to the light-interference pattern in the steady state [which is an optimum phase shift for two-beam coupling gain (see Chapter 3)],
3) when $E_0 \neq 0$ (i.e., the drift mechanism is dominant), there is oscillation in the transient state and E_1 is not, in general, $\pi/2$ out of phase in the steady state.

In order to see the dependence of the steady-state space-charge field E_{sc}^0 on the wavenumber K, which is a measure of spatial resolution of photorefractive materials, we consider the simplest case of E_0=0 and rewrite Eq. (2.14) as

$$E_{sc}^0 = \frac{-im E_{qe}^{(0)}}{1 + \beta_e \hbar\omega / s_e I_0} \frac{K l_{se}}{1 + (K l_{se})^2}, \tag{2.18}$$

where $E_{qe}^{(0)}=E_{qe}|_{Kl_{se}=1}$ and $Kl_{se} = \sqrt{E_D/E_{qe}}$. Figure 2.3 shows the plot of Eq. (2.18) as a function of $(Kl_{se})^{-1}$. It is seen that E_{sc}^0 reaches the maximum value when $Kl_{se} = 1$ (i.e., $E_D = E_{qe}$) while it is dominated by $E_D(E_{qe})$ when $Kl_{se} < 1(> 1)$. The value of l_{se} is more or less the same (of the order of 0.1μm) in most of the photorefractive materials which include short drift length ($r_{Ee} < l_{se}$) materials such as $BaTiO_3$ to long drift length ($r_{Ee} > l_{se}$) ones such as BSO and GaAs. This is because N_{Te} in all these materials varies between $10^{15}cm^{-3}$ and $10^{16}cm^{-3}$ as long as no intentional treatment such as reduction and oxdation is made. Therefore the dependence of E_{sc}^0 on the interference fringe period is almost the same in most of the photorefractive materials in the diffusion regime.

2.2.3 The two species and two types of carriers solution

Using the quasi-steady approximation, we obtain the following inhomogenenous differential equation for the lowest Fourier component of the space-charge field [2.74]:

$$\frac{\partial^2 E_1}{\partial t^2} + \left(\frac{1}{T_e} + \frac{1}{T_h}\right)\frac{\partial E_1}{\partial t} + \frac{Q}{T_e T_h}E_1 = \frac{Q}{T_e T_h}E_{sc}^0, \tag{2.19}$$

where the time constant T_e due to electrons is given by Eq. (2.13) while the time constant T_h due to holes is also obtained by Eq. (2.13) with the interchange of the subscript e→h,

$$Q = 1 - \left\{\left[1 - \frac{\tau_{de}\tau_{0e}}{\tau_{Ie}}\left(\frac{i}{\tau_{Ee}} - \frac{1}{\tau_{De}}\right)\right]\left[1 + \frac{\tau_{dh}\tau_{0h}}{\tau_{Ih}}\left(\frac{i}{\tau_{Eh}} + \frac{1}{\tau_{Dh}}\right)\right]\right\}^{-1},$$

and the steady-state space-charge field E_{sc}^0 is given by

$$E_{sc}^0 = im\frac{E_{qh}/(1+\beta_h\hbar\omega/s_h I_0) - E_{qe}/(1+\beta_e\hbar\omega/s_e I_0)}{1 + E_{qe}/(E_D - iE_0) + E_{qh}/(E_D + iE_0)}. \tag{2.20}$$

It is seen from Eq. (2.20) that there exists a competition between two space-charge fields with opposite directions: one due to electrons and the other due to holes. This result is reduced to the one species and one type of carrier result given by Eq.

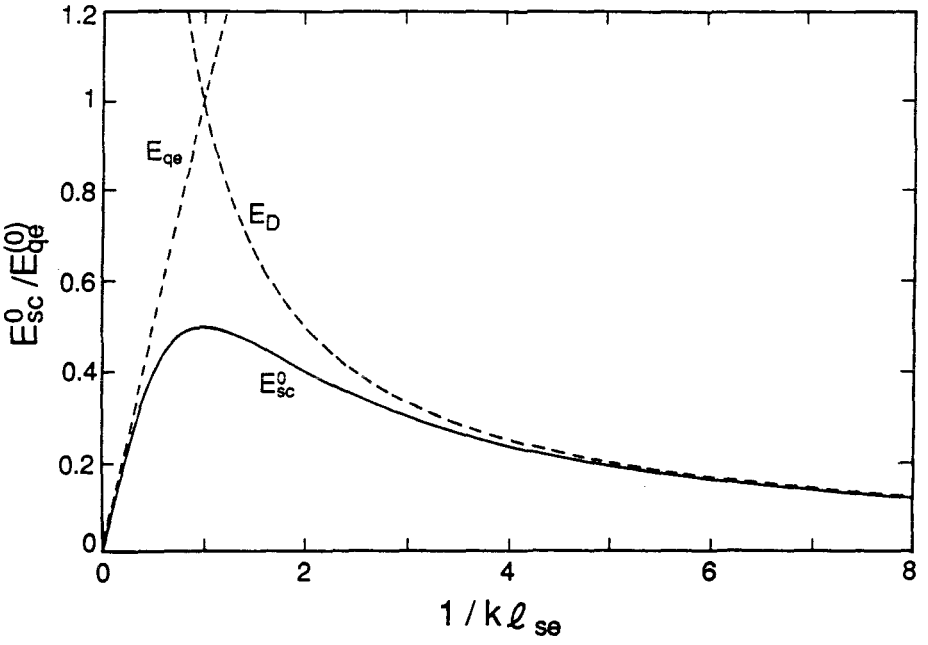

Figure 2.3 Dependence of E^0_{sc}, E_{qe} and E_D on Kl_{se} when E_0=0.

(2.14) when hole transport is absent (i.e., $E_{qh} = 0$). We also note that, unlike the case of one species and one type of carrier [see Eq. (2.19)], the second derivative in Eq. (2.19) cannot be neglected with respect to the other two terms. This is so because T_e and T_h are the response times of the space-charge field formation for electron and hole transport, respectively, and the first term in the left-hand side of Eq. (2.19) is in this case the same order of magnitude as the second term. Consequently we see that there exist two characteristic time constants in the two species and two types of carriers model. These two characteristic time constants are given by

$$\tau_+ = 2\left[\left(\frac{1}{T_e} + \frac{1}{T_h}\right) + \sqrt{\left(\frac{1}{T_e} - \frac{1}{T_h}\right)^2 + \frac{4Q}{T_e T_h}}\right]^{-1}, \tag{2.21a}$$

$$\tau_- = 2\left[\left(\frac{1}{T_e} + \frac{1}{T_h}\right) - \sqrt{\left(\frac{1}{T_e} - \frac{1}{T_h}\right)^2 + \frac{4Q}{T_e T_h}}\right]^{-1}. \tag{2.21b}$$

With these time constants the general solutions to Eq. (2.19) can be written for the following two cases:

Writing phase

$$E_1(t) = E_{sc}^0\left\{1 - [A_+ e^{-t/\tau_+} - A_- e^{-t/\tau_-}]\right\}, \tag{2.22}$$

where $A_+ = \tau_+/(\tau_+ - \tau_-)$ and $A_- = \tau_-/(\tau_+ - \tau_-)$.

Erasing phase

$$E_1(t) = E_{sc}^0\left[B_+ e^{-t/\tau_+} - B_- e^{-t/\tau_-}\right], \tag{2.23}$$

where $B_+ = (1 - \tau_-/\tau_0)A_+$ and $B_- = (1 - \tau_+/\tau_0)A_-$ with $\tau_0^{-1} \equiv \tau_{de}^{-1} + \tau_{dh}^{-1}$. In Chapter 3 the results given here will be used for the estimation of deep levels in semi-insulating GaAs.

2.2.4 Enhancement of the space-charge field

It is interesting to note that, since T_e is complex when $E_0 \neq 0$, the expression Eq. (2.12) for the space-charge field E_1 is formally similar to that of lossy harmonic oscillators and LCR circuits with driving forces [2.75,76]. It follows immediately from this equivalence that the oscillatory response of E_1 at an appropriate frequency will exhibit resonance and E_1 will be enhanced. This can be done by modulating either m or E_0 in E_{sc}^0 [see Eq. (2.14)]. In fact with the moving light-interference pattern[2.71, 77-80] or the AC external electric field [2.81-84] the amplitude of E_{sc}^0 can be enhanced, while E_{sc}^0 is still $\pi/2$ out of phase. This enhancement with the $\pi/2$-phase shift occurs particularly in long drift length materials where the carriers move over many fringe periods under the application of the DC external field before they are captured by the traps. In the moving fringe method the created space-charge field (which is enhanced by the DC external field but is not $\pi/2$ out of phase as in the usual drift mechanism) can synchronize with the fringe movement with some time delay (due to the finite response of the space-charge field formation). This results in a $\pi/2$-phase shift at the optimized fringe velocity. In the AC external field method the time period of the AC external field is taken to be much shorter than the response time of the space-charge field formation. The movement of photoexcited carriers due to the AC external field is symmetric with respect to the maxima of the light-interference pattern, and the drift force is zero on average during the period of the space-charge field formation. Thus the maxima of the carrier number density coincide with those of the light-interference pattern. For this reason this method creates the space-charge field with a $\pi/2$-phase shift much more efficiently than that in the usual thermal diffusion mechanism. We shall show below the theoretical results of the enhanced space-charge fields by means of these two methods. These will be used for evaluating the enhancement of the space-charge field (and thereby the two-beam coupling gain) in semi-insulating GaAs in Chapter 3.

In the moving fringe method the steady-state space-charge field with the optimized fringe velocity [2.71] is given by

$$\mathrm{E}_{\mathrm{sc}}^{0} = \frac{-im}{1+\beta_{\mathrm{e}}\hbar\omega/s_{\mathrm{e}}\mathrm{I}_0}\,\frac{\mathrm{E}_{\mathrm{qe}}\mathrm{E}_0^2}{\mathrm{E}_{\mathrm{qe}}\mathrm{E}_{\mathrm{Me}}+\mathrm{E}_0^2}, \tag{2.24}$$

where

$$\mathrm{E}_{\mathrm{Me}} = \frac{\gamma_{\mathrm{Re}}\mathrm{N}_{\mathrm{Te}}}{\mu_{\mathrm{e}}K}, \tag{2.25}$$

and $\mathrm{E}_0 \gg \mathrm{E}_{\mathrm{Me}}$ and $Kl_{\mathrm{se}} \ll 1$ are assumed. For a given E_0, Eq. (2.24) has a maximum value of

$$\mathrm{E}_{\mathrm{sc}}^{0}|_{\max} = \frac{-im}{1+\beta_{\mathrm{e}}\hbar\omega/s_{\mathrm{e}}\mathrm{I}_0}\,\frac{\mathrm{E}_{\mathrm{qe}}}{2}, \tag{2.26}$$

at the optimum grating vector of $K_{\mathrm{opt}} = 1/\sqrt{r_{\mathrm{Ee}}l_{\mathrm{Ee}}}$.

In the AC external field method a general solution [2.74] for an arbitrary waveform of $\mathrm{E}_0(t)$ is given by

$$\mathrm{E}_1(t) = \left\{\mathrm{E}_1(0) - \frac{im}{1+\beta_{\mathrm{e}}\hbar\omega/s_{\mathrm{e}}\mathrm{I}_0}\int_0^t g(\tau)e^{h(\tau)}\,d\tau\right\}e^{-h(t)}, \tag{2.27}$$

where

$$h(t) = \int_0^t \left[\left(1-\frac{\mathrm{E}_0(\tau)}{\mathrm{E}_{\mathrm{qe}}}\right)\left(1+\frac{\mathrm{E}_{\mathrm{D}}}{\mathrm{E}_{\mathrm{Me}}}\right)+\frac{\mathrm{E}_0^2(\tau)}{\mathrm{E}_{\mathrm{Me}}\mathrm{E}_{\mathrm{qe}}} + i\mathrm{E}_0(\tau)\left(\frac{1}{\mathrm{E}_{\mathrm{Me}}}-\frac{1}{\mathrm{E}_{\mathrm{qe}}}\right)\right]\left\{\tau_{\mathrm{de}}\left[\left(1+\frac{\mathrm{E}_{\mathrm{D}}}{\mathrm{E}_{\mathrm{Me}}}\right)^2+\left(\frac{\mathrm{E}_0(\tau)}{\mathrm{E}_{\mathrm{Me}}}\right)^2\right]\right\}^{-1}d\tau,$$

$$g(t) = \left[\mathrm{E}_{\mathrm{D}}\left(1+\frac{\mathrm{E}_{\mathrm{D}}}{\mathrm{E}_{\mathrm{Me}}}\right)+\frac{\mathrm{E}_0^2(t)}{\mathrm{E}_{\mathrm{Me}}}+i\mathrm{E}_0(t)\right]\left\{\tau_{\mathrm{de}}\left[\left(1+\frac{\mathrm{E}_{\mathrm{D}}}{\mathrm{E}_{\mathrm{Me}}}\right)^2+\left(\frac{\mathrm{E}_0(t)}{\mathrm{E}_{\mathrm{Me}}}\right)^2\right]\right\}^{-1}.$$

If we apply a bipolar rectangular electric field whose duty cycle is 50/50, and a period much shorter than τ_{e} as given by Eq. (2.17a), the steady-state result [2.83] can be obtained straightforwardly from Eq. (2.27) as

$$\mathrm{E}_{\mathrm{sc}}^{0} = \frac{-im}{1+\beta_{\mathrm{e}}\hbar\omega/s_{\mathrm{e}}\mathrm{I}_0}\,\frac{\mathrm{E}_{\mathrm{D}}(1+\mathrm{E}_{\mathrm{D}}/\mathrm{E}_{\mathrm{Me}}+\mathrm{E}_0^2/\mathrm{E}_{\mathrm{D}}\mathrm{E}_{\mathrm{Me}})}{(1+\mathrm{E}_{\mathrm{D}}/\mathrm{E}_{\mathrm{qe}})(1+\mathrm{E}_{\mathrm{D}}/\mathrm{E}_{\mathrm{Me}})+\mathrm{E}_0^2/\mathrm{E}_{\mathrm{qe}}\mathrm{E}_{\mathrm{Me}}}. \tag{2.28}$$

This also gives values similar to Eq. (2.24) at $K < 1/\sqrt{r_{\mathrm{Ee}}l_{\mathrm{Ee}}-r_{\mathrm{De}}^2}$ and Eq. (2.26) at $K > 1/\sqrt{r_{\mathrm{Ee}}l_{\mathrm{Ee}}-r_{\mathrm{De}}^2}$, respectively, with the assumption of $Kl_{\mathrm{se}} \ll 1$

and $Kr_{Ee} > (E_D/E_0)(1 + K^2 r_{De}^2)$ for both cases [2.83]. We note that since E_{qe} is inversely proportional to K the enhanced $E_{sc}^0|_{max}$ ($Kl_{se} \ll 1$) given by Eq. (2.26) is much larger than the maximum space-charge field E_{qe} at $Kl_{se} = 1$ (i.e., $E_{qe}^{(0)}$) in the diffusion mechanism [see Eq. (2.18)].

It is seen from the above results that, using the moving fringe or the AC external field, the space-charge field with a $\pi/2$-phase shift can be obtained in the long drift length mechanism (i.e., $Kr_{Ee} = E_0/E_{Me} > 1$). These methods are well suited particularly to the photorefractive BSO and GaAs crystals because they are long drift length materials with fast response time but have small electrooptic coefficients (therefore small photorefractive nonlinearities). Experiments of using such enhancement methods have been reported in BSO and BGO [2.71, 77-80, 82], BTO [2.83-87] and GaAs [2.88-90].

2.3 Symmetry properties of photoinduced refractive index changes

So far we have described the photoinduced space-charge field formation by means of the band transport model. We complete the discussion by describing the refractive index changes caused by the space-charge electric field via the electrooptic effect.

The electrooptic effect is formally defined as a change in the second-rank optical impermeability tensor $\tilde{\eta}$ ($\equiv \tilde{\epsilon}_{tot}^{-1}$, where $\tilde{\epsilon}_{tot}$ is the second-rank optical dielectric tensor). This change occurs when an electric field $\mathbf{E}$ [$= \mathbf{E}^0 + \frac{1}{2}\mathbf{E}^\omega e^{-i\omega t} + c.c.$] causes a redistribution of the bond charges and possibly a slight deformation of the ion lattice in the crystal [2.91]. This is expressed by

$$\begin{aligned} \tilde{\eta}_{ij}(\mathbf{E}) - \tilde{\eta}_{ij}(0) &\equiv \Delta\tilde{\eta}_{ij} \\ &= \tilde{\tilde{r}}_{ijk}E_k + \tilde{\tilde{\tilde{s}}}_{ijkl}E_kE_l, \end{aligned} \tag{2.29}$$

where i, j, k and l are defined as the principal coordinate subscripts and $\tilde{\tilde{r}}$ and $\tilde{\tilde{\tilde{s}}}$ are

the third-rank linear (or Pockels) electrooptic tensor and the fourth-rank quadratic (or Kerr) electrooptic tensor, respectively. Most applications using photorefractive materials rely upon the linear electrooptic effect which is also considered in this section. The quadratic electrooptic effect has also been employed in cubic KTN crystals [2.92] and the following argument can be easily extended to the quadratic electrooptic effect.

We can also formally describe the electrooptic effect in terms of a second-order nonlinear polarization $\mathbf{P}_{\rm NL}$ $[= \frac{1}{2}\mathbf{P}^{\omega}_{\rm NL}e^{-i\omega t} + c.c.]$ arising from the space-charge field $\mathbf{E}_{\rm sc}$ ($\equiv \mathrm{E}_{\rm sc}\mathbf{e}_{\rm sc}$, where $\mathrm{E}_{\rm sc} = \mathrm{E}_0 + \frac{1}{2}\mathrm{E}^0_{\rm sc}e^{i\mathbf{K}\cdot\mathbf{r}} + c.c.$ and $\mathbf{e}_{\rm sc}$ is a unit vector). In this case the complex amplitude vector of the second-order nonlinear polarization $\mathbf{P}^{\omega}_{\rm NL}$ is given by

$$\mathbf{P}^{\omega}_{\rm NL} = \Delta\tilde{\chi} : \mathbf{E}^{\omega}. \tag{2.30}$$

In Eq. (2.30) $\mathbf{E}^{\omega}$ is again the complex amplitude vector of the electric field at the optical frequency ω and $\Delta\tilde{\chi}$ is the second-rank nonlinear susceptibility tensor due to $\mathbf{E}_{\rm sc}$. Since we can rewrite Eq. (2.29) for a DC electric field $\mathbf{E} = \mathbf{E}^0$ as

$$\begin{aligned}\Delta\tilde{\eta}_{ij} &= [\tilde{\epsilon}_{\rm tot}(\mathbf{E})^{-1}]_{ij} - [\tilde{\epsilon}_{\rm tot}(0)^{-1}]_{ij} \\ &\simeq -[\tilde{\epsilon}^{-1} : \Delta\tilde{\epsilon} : \tilde{\epsilon}^{-1}]_{ij},\end{aligned} \tag{2.31}$$

where $\Delta\tilde{\epsilon} \equiv \tilde{\epsilon}_{\rm tot} - \tilde{\epsilon}$ ($\tilde{\epsilon}$ is the second-rank linear optical dielectric tensor at the optical frequency ω) and $|\Delta\tilde{\epsilon}| \ll |\tilde{\epsilon}|$ is assumed, $\Delta\tilde{\chi}$ in Eq. (2.30) can be expressed from Eqs. (2.29) and (2.31) as

$$\begin{aligned}\Delta\tilde{\chi} &= \frac{1}{4\pi}\Delta\tilde{\epsilon} \\ &= -\frac{\mathrm{E}_{\rm sc}}{4\pi}[\tilde{\epsilon} : (\tilde{\tilde{r}} : \mathbf{e}_{\rm sc}) : \tilde{\epsilon}],\end{aligned} \tag{2.32}$$

where $\mathbf{E}^0 = \mathbf{E}_{\rm sc}$ is used. The form of $\tilde{\epsilon}$ as well as that of $\tilde{\tilde{r}}$ can be found in the literature [2.91]. The symmetry properties of $\Delta\tilde{\chi}$ for several crystal symmetry classes which include most of the important photorefractive materials are given

in Table 2.1, where the angles θ and φ are defined in Fig. 2.4, the directions x, y, and z are the principal axes, and n_o and n_e denote the ordinary refractive index ($=n_x = n_y$) and the extraordinary refractive index ($=n_z$), respectively. As is shown below and detailed in Chapter 3, this nonlinear polarization causes scalar and/or polarization beam coupling phenomena in photorefractive crystals. The use of photorefractive crystals possessing a $\Delta\tilde{\chi}$ for vector phase conjugation will be discussed in Chapters 4 and 6.

As an example we shall consider a common configuration, where the space-charge field is parallel to the c-axis (i.e., $\theta = 0$ and $\varphi = \pi/2$ in Fig. 2.4). From Table 2.1 we find the following forms of $\Delta\tilde{\chi}$:

$$\Delta\tilde{\chi} = -\frac{E_{sc}}{4\pi}\begin{pmatrix} a & 0 & 0 \\ 0 & b & 0 \\ 0 & 0 & c \end{pmatrix} \quad \text{for 2mm, 4mm and 3m symmetry classes,} \qquad (2.33a)$$

and

$$\Delta\tilde{\chi} = -\frac{E_{sc}}{4\pi} n_0^4 r_{41}\begin{pmatrix} 0 & 1 & 0 \\ 1 & 0 & 0 \\ 0 & 0 & 0 \end{pmatrix} \quad \text{for } \bar{4}3m \text{ and 23 symmetry classes.} \qquad (2.33b)$$

We see from Eqs. (2.32) that

a) for 2mm, 4mm and 3m crystal symmetry classes $\Delta\tilde{\chi}$ is diagonal so that the photorefractive effect can cause scalar (isotropic) beam coupling only between two beams of the same polarization and there is no coupling between orthogonally polarized beams, and

b) for $\bar{4}3m$ and 23 crystal symmetry classes there is scalar beam coupling between two beams of the same polarization (e.g., a linear polarization along $< 110 >$ crystal direction) and there is also cross-polarization coupling between the x- and y-polarized beams.

For the scalar beam coupling we can write $\Delta\tilde{\chi} = \Delta\chi I$ (I is a unit matrix) in some appropriate coordinate system. In this case $\Delta\chi$ is expressed by the following

Table 2.1 Symmetry properties of the second-rank nonlinear susceptibility tensor $\Delta\tilde{\chi}$ arising from the photorefractive effect for several crystal symmetry classes.

Orthorhombic: 2mm symmetry class (e.g., $KNbO_3$ and $BaNaNb_5O_{15}$)

$$-\frac{E_{sc}}{4\pi}\begin{pmatrix} n_x^4 r_{13}\cos\theta & 0 & n_x^2 n_z^2 r_{51}\sin\theta\cos\varphi \\ 0 & n_y^4 r_{23}\cos\theta & n_y^2 n_z^2 r_{42}\sin\theta\sin\varphi \\ n_x^2 n_z^2 r_{51}\sin\theta\cos\varphi & n_y^2 n_z^2 r_{42}\sin\theta\sin\varphi & n_z^4 r_{33}\cos\theta \end{pmatrix}$$

Tetragonal: 4mm symmetry class (e.g., $BaTiO_3$, SBN, and BSKNN)

$$-\frac{E_{sc}}{4\pi}\begin{pmatrix} n_o^4 r_{13}\cos\theta & 0 & n_o^2 n_e^2 r_{42}\sin\theta\cos\varphi \\ 0 & n_o^4 r_{13}\cos\theta & n_o^2 n_e^2 r_{42}\sin\theta\sin\varphi \\ n_o^2 n_e^2 r_{42}\sin\theta\cos\varphi & n_o^2 n_e^2 r_{42}\sin\theta\sin\varphi & n_e^4 r_{33}\cos\theta \end{pmatrix}$$

Trigonal: 3m (m$\perp$x) symmetry class (e.g., $LiNbO_3$)

$$-\frac{E_{sc}}{4\pi}\times$$
$$\begin{pmatrix} n_o^4(-r_{22}\sin\theta\cos\varphi + r_{13}\cos\theta) & -n_o^4 r_{22}\sin\theta\cos\varphi & n_o^2 n_e^2 r_{42}\sin\theta\cos\varphi \\ -n_o^4 r_{22}\sin\theta\cos\varphi & n_o^4(r_{22}\sin\theta\sin\varphi + r_{13}\cos\theta) & n_o^2 n_e^2 r_{42}\sin\theta\sin\varphi \\ n_o^2 n_e^2 r_{42}\sin\theta\cos\varphi & n_o^2 n_e^2 r_{42}\sin\theta\sin\varphi & n_e^4 r_{33}\cos\theta \end{pmatrix}$$

Cubic: $\bar{4}$3m and 23 symmetry classes (e.g., GaAs, BSO, BGO, and BTO)

$$-\frac{E_{sc}}{4\pi}n_o^4 r_{41}\begin{pmatrix} 0 & \cos\theta & \sin\theta\sin\varphi \\ \cos\theta & 0 & \sin\theta\cos\varphi \\ \sin\theta\sin\varphi & \sin\theta\cos\varphi & 0 \end{pmatrix}$$

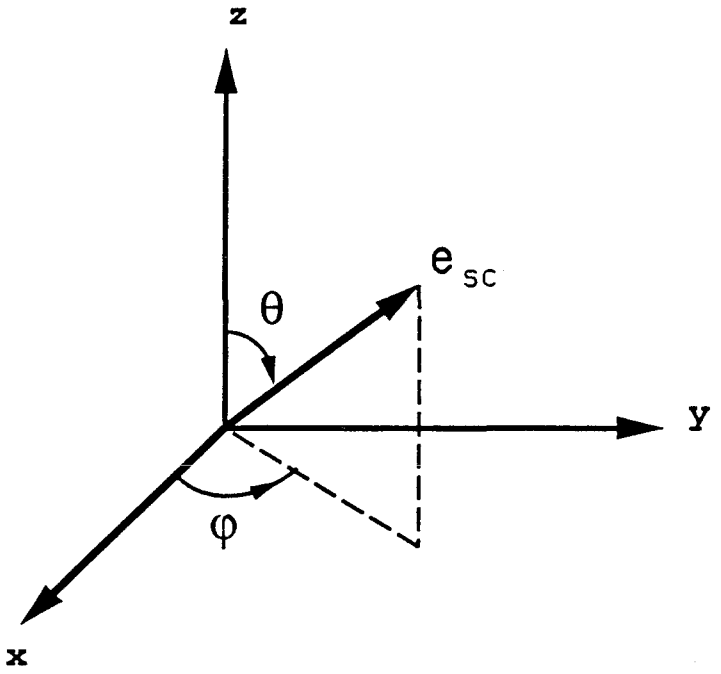

Figure 2.4 Diagram showing the direction of the space-charge field, where e_{sc} is a unit vector of the space-charge field and the x, y, and z axes are the principle axes of the crystallographic coordinate system.

refractive index change Δn:

$$\Delta n = \frac{2\pi}{n_0}\Delta\chi, \tag{2.34}$$

where $\Delta\chi$ is measured in esu.

References for Chapter 2

2.1. A. Ashkin, G.D. Boyd, J.M. Dziedzic, R.G. Smith, A.A. Ballman, H.J. Levinstein, and K. Nassau, Appl. Phys. Lett. **9**, 72 (1966).

2.2. F.S. Chen, J.T. Macchia, and D.B. Fraser, Appl. Phys. Lett. **13**, 223 (1968).

2.3. F.S. Chen, J. Appl. Phys. **40**, 3389 (1969).

2.4. D.L. Staebler and J.J. Amodei, Ferroelectrics **3**, 107 (1972).

2.5. O.N. Tufe and D. Chen, IEEE Spectrum **10**, 26 (1973).

2.6. J.D. Zook, Appl. Opt. **13**, 875 (1974).

2.7. D. von der Linde and A.M. Glass, Appl. Opt. **8**, 88 (1975).

2.8. H. Kurz, Philips Tech. Rev. **37**, 109 (1977).

2.9. H. Kurz, Optica Acta **24**, 463 (1977).

2.10. R.P. Freese, IEEE Spectrum **25**, 41 (1988).

2.11. F.S. Chen, J. Appl. Phys. **38**, 3418 (1967).

2.12. J.J. Amodei, Appl. Phys. Lett. **18**, 22 (1971).

2.13. J.J. Amodei, RCA Rev. **32**, 185 (1971).

2.14. G.E. Peterson, A.M. Glass, and T.J. Negran, Appl. Phys. Lett. **19**, 130 (1971).

2.15. D.L. Staebler and J.J. Amodei, J. Appl. Phys. **43**, 1042 (1972).

2.16. V.E. Wood, J. Appl. Phys. **44**, 1391 (1973).

2.17. L. Young, W.K.Y. Wong, M.L.W. Thewalt, and W.D. Cornish, Appl. Phys. Lett. **24**, 264 (1974).

2.18. A.M. Glass, D. von der Linde, and T.J. Negran, Appl. Phys. Lett. **25**, 233 (1974).

2.19. M.F. Deigen, S.G. Odulov, M.S. Soskin, and B.D. Shanina, Sov. Phys. Solid

State Phys. **16**, 1695 (1974).

2.20. V.L. Vinetskii and N.V. Kukhtarev, Sov. Phys. Solid State Phys. **16**, 2414 (1975).

2.21. S.F. Su and T.K. Gaylord, J. Appl. Phys. **46**, 5208 (1975).

2.22. G.A. Alphonse, R.C. Alig, D.L. Staebler, and W. Phillips, RCA Rev. **36**, 213 (1975).

2.23. D.M. Kim, R.R. Shah, T.A. Rabson, and F.K. Tittel, Appl. Phys. Lett. **28**, 338 (1976).

2.24. M.G. Moharam and L. Young, J. Appl. Phys. **47**, 4048 (1976).

2.25. N.V. Kukhtarev, Sov. Tech. Phys. Lett. **2**, 438 (1976).

2.26. M.G. Moharam and L. Young, J. Appl. Phys. **48**, 3230 (1977).

2.27. B.I. Sturman, Sov. Phys. Tech. Phys. **23**, 589 (1978).

2.28. N.V. Kukhtarev, V.B. Markov, S.G. Odulov, M.S. Soskin, and V.L. Vietskii, Ferroelectrics **22**, 949, 961 (1979).

2.29. M.G. Moharam, T.K. Gaylord, and R. Magnusson, J. Appl. Phys. **50**, 5642 (1979).

2.30. J. Feinberg, D. Heiman, A.R. Tanguay, Jr., and R.W. Hellwarth, J. Appl. Phys. **51**, 1297 (1980).

2.31. Y. Ninomiya, J. Opt. Soc. Am. **63**, 1124 (1973).

2.32. V.G. Sidorovitch and D.I. Stasiel'ko, Sov. Phys. Tech. Phys. **44**, 580 (1974).

2.33. D.W. Vahey, J. Appl. Phys. **46**, 3510 (1975).

2.34. R. Magnusson and T.K. Gaylord, J. Appl. Phys. **47**, 190 (1976).

2.35. N.V. Kukhtarev, V.B. Markov, and S.G. Odulov, Opt. Commun. **23**, 338 (1977).

2.36. V.L. Vinetskii and N.V. Kukhtarev, Sov. J. Quantum Electron. **8**, 231 (1978).

2.37. N.V. Kukhtarev and S.G. Odulov, JETP Lett. **30**, 4 (1979).

2.38. M. Croning-Golomb, B. Fischer, J.O. White, and A. Yariv, IEEE J. Quantum Eletron. **QE-20**, 12 (1984).

2.39. Y.H. Ja, Opt. Quantum Electron. **14**, 547 (1982); *ibid* **15**, 529, 539 (1983); Appl. Phys. B**33**, 51 (1984); *ibid* B**33**, 161 (1984).

2.40. M.R. Belić, Phys. Rev. A**31**, 3169 (1985); Opt. Quantum Electron. **16**, 551 (1984); Opt. Lett. **12**, 105 (1987); M.R. Belić and M. Lax, Opt. Commun. **56**, 197 (1985).

2.41. P. Yeh, Opt. Commun. **45**, 323 (1983).

2.42. See, for example, *Photorefractive Materials and Their Applications I, II*, ed. by P. Günter and J.P. Huignard, (Springer-Verlag, Berlin, Heidelberg, 1988).

2.43. R.L. Townsend and J.T. LaMacchia, J. Appl. Phys. **41**, 5188 (1970).

2.44. P. Günter, U. Flückinger, J.P. Huignard, and F. Micheron, Ferroelectrics **13**, 297 (1976).

2.45. R. Orlowski, L.A. Boatner, and E. Krätzig, Opt. Commun. **35**, 45 (1980).

2.46. J.J. Amodei, D.L. Staebler, and A.W. Stephens, Appl. Phys. Lett. **18**, 507 (1971).

2.47. J.B. Thaxter, Appl. Phys. Lett. **15**, 210 (1969).

2.48. R.R. Neurgaonkar and W.K. Cory, J. Opt. Soc. Am. B**3**, 274 (1986).

2.49. L.H. Lin, Proc. IEEE **57**, 252 (1969).

2.50. J.P. Huignard and F. Micheron, Appl. Phys. Lett. **29**, 591 (1976).

2.51. M. Peltier and F. Micheron, J. Appl. Phys. **48**, 3683 (1977).

2.52. V.M. Fridkin, B.N. Popov, K.A. Verkhovskaya, Appl. Phys. **16**, 313 (1978).

2.53. T. Nakamura, V. Fridkin, R. Magomadov, M. Takashige, and K. Verkhovskaya, J. Phys. Soc. Jpn. **48**, 1588 (1980).

2.54. F. Micheron, A. Hermosin, G.B. Simith, and J. Nicolas, C.R. Acad. Sci. 8 (Dec. 1971).

2.55. A. Ashkin, B. Tell, and J.M. Dziedzic, IEEE J. Quantum Electron. **QE-3**, 400 (1967).

2.56. M.B. Klein, Opt. Lett. **9**, 350 (1984).

2.57. A.M. Glass, A.M. Johnson, D.H. Olson, W. Simpson, and A.A. Ballmann, Appl. Phys. Lett. **44**, 948 (1984).

2.58. J. Strait and A.M. Glass, J. Opt. Soc. Am. B**3**, 342 (1986).

2.59. E. Krätzig, Ferroelectrics **21**, 635 (1978).

2.60. R. Orlowski and E. Krätizig, Solid State Commun. **27**, 1351 (1978).

2.61. E. Krätzig and R. Orlowski, Ferroelectrics **27**, 241 (1980); Opt. Quantum Electron. **12**, 495 (1980).

2.62. G.C. Valley, Appl. Opt. **22**, 3160 (1983); *ibid* **23**, 1131 (1984).

2.63. N.V. Kukharev, G.E. Dovgalenko, and V.N. Starkov, Appl. Phys. A**33**, 227 (1984).

2.64. S.I. Stepanov and G.S. Trofimov, Sov. Phys. Tech. Phys. **30**, 331 (1985).

2.65. F.P. Strohkende, J.M.C. Jonathan, and R.W. Hellwarth, Opt. Lett. **11**, 312 (1986).

2.66. F.P. Strohkendl and R.W. Hellwarth, J. Appl. Phys. **62**, 2450 (1987).

2.67. M.B. Klein and G.C. Valley, J. Appl. Phys. **57**, 4901 (1985).

2.68. S. Ducharme and J. Feinberg, J. Opt. Soc. Am. B**3**, 283 (1986).

2.69. G.C. Valley, J. Appl. Phys. **59**, 3363 (1986).

2.70. M.P. Petrov, S.V. Miridonov, S.I. Stepanov, and V.V. Kulikov, Opt. Commun. **31**, 301 (1979).

2.71. P. Refregier, L. Solymar, H. Rajbenbach, and J.P. Huignard, J. Appl. Phys.

58, 45 (1985).

2.72. E. Ocha, F. Vachss, and L. Hesselink, J. Opt. Soc. Am. **A3**, 181 (1986).

2.73. G.C. Valley, IEEE J. Quantum Electron. **QE-19**, 1637 (1983).

2.74. Y. Tomita and A. Yariv, unpublished.

2.75. A.B. Pippard, *Response and Stability* (Cambridge University Press, New York, 1985).

2.76. L. Solymar, Opt. Commun. **63**, 413 (1987).

2.77. J.P. Huignard and A. Marrakchi, Opt. Commun. **38**, 249 (1981).

2.78. P. Günter, Opt. Commun. **41**, 83 (1981).

2.79. S.I. Stepanov, V.V. Kulikov, and M.P. Petrov, Sov. Tech. Phys. Lett. **8**, 229 (1982); Opt. Commun. **44**, 19 (1982).

2.80. H. Rajbenbach, J.P. Huignard, and B. Loiseaux, Opt. Commun. **48**, 247 (1983).

2.81. G.C. Valley, J. Opt. Soc. Am. **B1**, 868 (1984).

2.82. P. Refregier, L. Solymar, H. Rajbenbach, and J.P. Huignard, Electron. Lett. **20**, 656 (1984).

2.83. S.I. Stepanov and M.P. Petrov, Sov. Tech. Phys. Lett. **10**, 572 (1984); Opt. Commun. **53**, 292 (1985).

2.84. S.I. Stepanov, M.P. Petrov, and M.V. Krasin'kova, Sov. Phys. Tech. Phys. **29**, 703 (1984).

2.85. S.I. Stepanov and M.P. Petrov, Opt. Acta **31**, 1335 (1984); Opt. Commun. **53**, 64 (1985).

2.86. M.P. Petrov and S.I. Stepanov, Proc. ICO-13 Conf., Sapporo, Japan, August 20-24, 1984, p. 430.

2.87. S.I. Stepanov and S.L. Sochava, Sov. Phys. Tech. Phys. **32**, 1054 (1987).

2.88. J. Kumar, G. Albanese, W.H. Steier, and M. Ziari, Opt. Lett. **12**, 120 (1987).

2.89. J. Kumar, G. Albanese, and W.H. Steier, J. Opt. Soc. Am. B4, 1079 (1987); Opt. Commun. **63**, 191 (1987).

2.90. W. Walsh and T.J. Hall, Electron. Lett. **24**, 477 (1988).

2.91. A. Yariv and P. Yeh, *Optical Waves in Crystals* (Wiley, New York, 1984); J.F. Nye, *Physical Properties of Crystals* (Oxford University Press, New York, 1985).

2.92. A. Agranat, K. Sayano, and A. Yariv, *Technical Digest, Topical Meeting on Photorefractive Materials, Effects, and Devices*, Los Angeles, August 1987 (OSA, Washington DC, 1987), postdeadline paper PD1.

CHAPTER THREE

Beam Coupling in Photorefractive Crystals

3.1 Introduction

We have shown in the previous chapter that the maxima and minima of the photoinduced refractive index grating are, in general, shifted spatially from those of the light-interference pattern, i.e., the photorefractive grating is "nonlocal". As one of the limiting cases, this nonlocal phase shift becomes $\pm\pi/2$ in the pure diffusion regime. Such nonlocal (and also tensorial) photorefractive gratings written by two beams cause energy transfer between these beams during propagation in the crystal. This is because one of the two beams diffracted by the nonlocal gratings interferes constructively (or destructively) with the other beam, depending on the sign of the phase shift [3.1,2].

The simplest geometry of such beam coupling is that of isotropic beam coupling shown in Fig. 3.1(a). The two input beams create the "isotropic" photorefractive grating. This grating, in turn, diffracts the two beams into each other while satisfying the Bragg condition so that the power exchange is spatially cumulative. In this case the diffracted beams possess the same polarization state as that of the input beams. This effect also gives rise to isotropic light scattering into a fanned shape, which is called "beam fanning" [3.3]: a single input beam is scattered by the crystal's inhomogenities, etc., and forms a continuum of "noisy" photorefractive gratings with these scattered beams, by which asymmetric energy transfer from the input to the scattered beams occurs. These phenomena are the basis of various novel optical devices such as image amplifiers [3.2,4], unidirectional ring oscillators

[3.5], optical limiters [3.6], and beam cleanup devices [3.7].

Since photorefractive gratings arise from electrooptic effects and are in general optically anisotropic [3.8,9] (see Table 2.1), anisotropic beam coupling via the nonlinear susceptibility tensor $\Delta\tilde{\chi}$ also occurs. Figure 3.1(b) shows cross-polarization beam coupling in cubic crystals, where the two input beams are diffracted into the beams that are orthogonal to the input polarization by the anisotropic photorefractive gratings. In this case the Bragg condition is automatically satisfied because the wavenumbers of the diffracted beams are the same as those of the input beams in cubic crystals. Figure 3.1(c) shows anisotropic self-diffraction in uniaxial and biaxial crystals. The anisotropic photorefractive grating written by the two input beams of well-defined incident angles and polarization states [i.e., the extraordinary polarization in Fig. 3.1(c)] scatters such input beams into the beams that are orthogonal to the input polarization. In this case the orthogonally polarized beams of specific propagation directions are allowed because of the anisotropic Bragg condition [3.8]. This results in the output beams of four different propagation directions. Figure 3.1(d) shows anisotropic light scattering in uniaxial and biaxial crystals. In this situation, as is the case in isotropic light scattering, a single input beam of a well-defined polarization [i.e., the extraordinary polarization in Fig. 3.1(d)] creates noisy photorefractive gratings. If these gratings are anisotropic, they create the diffracted beams of an orthogonal polarization [i.e., the ordinary polarization in Fig. 3.1(d)] with a specific propagation direction that satisfies the anisotropic Bragg condition. This creates a conical ring pattern of the Bragg-matched scattered beams of ordinary polarization.

The above anisotropic beam-coupling phenomena have been studied in photorefractive crystals such as $LiNbO_3$ and $LiTaO_3$ [3.10-19], $BaTiO_3$ [3.15,20,21], SBN [3.22], $KNbO_3$ [3.23-25], and GaAs [3.26-31]. In the cubic sillenite crystals such

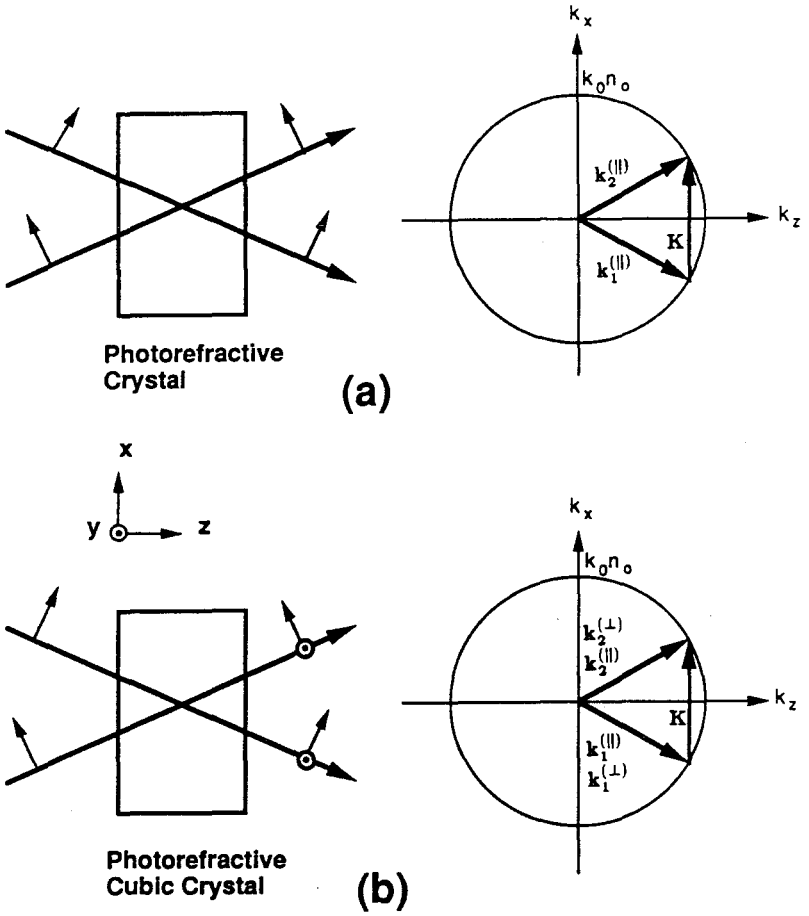

Figure 3.1 Beam coupling configurations, where n_o and n_e denote the ordinary and extraordinary refractive indices, respectively, and k_0 is the wavenumber in vacuum. (a) Isotropic beam coupling, where $|\mathbf{k}_1^{(\|)}| = |\mathbf{k}_2^{(\|)}|$ and $\mathbf{k}_2^{(\|)} = \mathbf{k}_1^{(\|)} + \mathbf{K}$. (b) Cross-polarization beam coupling in cubic crystals, where $|\mathbf{k}_1^{(\|)}| = |\mathbf{k}_2^{(\|)}| = |\mathbf{k}_1^{(\perp)}| = |\mathbf{k}_2^{(\perp)}|$ and $\mathbf{k}_2^{(\|)} = \mathbf{k}_2^{(\perp)} = \mathbf{k}_1^{(\|)} + \mathbf{K} = \mathbf{k}_1^{(\perp)} + \mathbf{K}$.

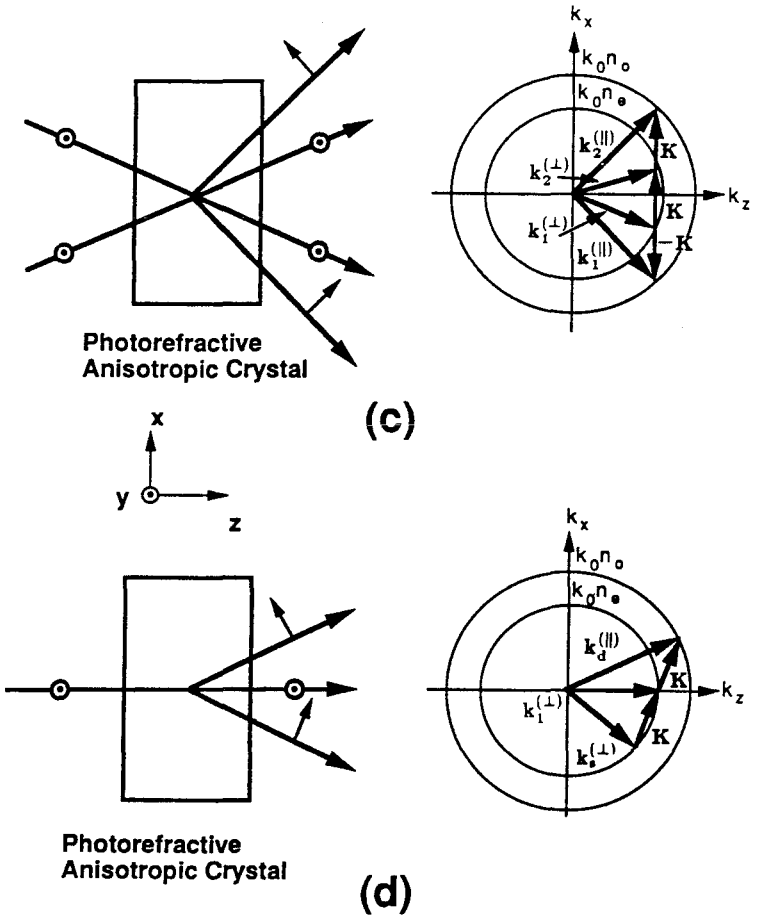

Figure 3.1 (Continued). (c) Anisotropic self-diffraction in anisotropic crystals (negative uniaxial crystals in this figure), where $|\mathbf{k}_1^{(\perp)}| = |\mathbf{k}_2^{(\perp)}| < |\mathbf{k}_1^{(\parallel)}| = |\mathbf{k}_2^{(\parallel)}|$, $\mathbf{k}_1^{(\parallel)} = \mathbf{k}_1^{(\perp)} + \mathbf{K}$, $\mathbf{k}_2^{(\parallel)} = \mathbf{k}_2^{(\perp)} + \mathbf{K}$ and $\mathbf{k}_2^{(\perp)} = \mathbf{k}_1^{(\perp)} + \mathbf{K}$. (d) Anisotropic light scattering in anisotropic crystals (negative uniaxial crystals in this figure), where $|\mathbf{k}_1^{(\perp)}| = |\mathbf{k}_s^{(\perp)}| < |\mathbf{k}_d^{(\parallel)}|$, $\mathbf{k}_s^{(\perp)} = \mathbf{k}_1^{(\perp)} - \mathbf{K}$ and $\mathbf{k}_d^{(\parallel)} = \mathbf{k}_1^{(\perp)} + \mathbf{K}$.

as BSO, BGO, and BTO the effect of the optical activity causes further complication on the polarization properties in photorefractive beam coupling and/or diffraction, which has also led to further studies [3.32-47]. Applications of the anisotropic beam coupling and/or self-diffraction phenomena include light deflection [3.23,25,48], spatial light modulation [3.49], and image processing [3.50-52].

In this chapter we describe beam coupling phenomena in photorefractive anisotropic cystals. A general set of coupled-wave equations that describes isotropic and anisotropic beam coupling phenomena is derived. The explicit solutions are shown particularly for two specific cases: isotropic beam coupling and anisotropic cross-polarization beam coupling in cubic crystals. Beam coupling in semi-insulating GaAs is then described. The densities of the deep levels and the sign of dominant carriers in semi-insulating undoped and Cr-doped GaAs are estimated from the two-beam coupling gain measurement. The enhancement of the two-beam coupling gain in semi-insulating GaAs and its temperature dependence are also discussed.

3.2 Coupled-wave equations in photorefractive anisotropic crystals

Let us consider the wave mixing of plane waves 1 and 2 in a photorefractive anisotropic crystal (see Fig. 3.2). We take the x, y, and z axes as the beam propagation coordinate system which is related to the crystallographic coordinate system by means of a simple linear transformation [3.8]. Any wave propagation in an anisotropic (and optically active) medium can be decomposed into a linear combination of "unperturbed" normal (eigen) modes which have spatially invariant and well-defined polarization states and phase velocities [3.8,9]. In the analysis that follows we use these normal modes as bases, and beam coupling is described in terms of the evolution of the complex amplitudes of the normal modes as a function

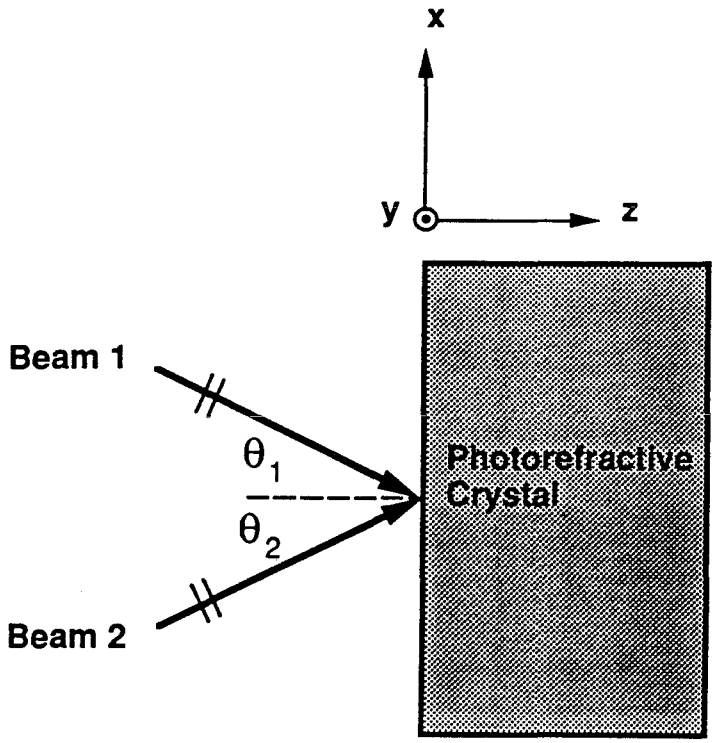

Figure 3.2 Beam coupling configuration. Two plane waves of arbitrary polarizations are incident on the photorefractive crystal. The beam propagation coordinate system is shown as the x, y, and z axes.

of the propagation direction.

The propagation of the two interacting waves can be written, in terms of the normal modes, as

$$\mathbf{E}_1(z,t) = \frac{1}{2}[\mathrm{A}_1^{(1)}(z)\mathbf{e}_1^{(1)}e^{i(\mathbf{k}_1^{(1)}\cdot\mathbf{r}-\omega t)} + \mathrm{A}_1^{(2)}(z)\mathbf{e}_1^{(2)}e^{i(\mathbf{k}_1^{(2)}\cdot\mathbf{r}-\omega t)}] + c.c., \qquad (3.1a)$$

$$\mathbf{E}_2(z,t) = \frac{1}{2}[\mathrm{A}_2^{(1)}(z)\mathbf{e}_2^{(1)}e^{i(\mathbf{k}_2^{(1)}\cdot\mathbf{r}-\omega t)} + \mathrm{A}_2^{(2)}(z)\mathbf{e}_2^{(2)}e^{i(\mathbf{k}_2^{(2)}\cdot\mathbf{r}-\omega t)}] + c.c., \qquad (3.1b)$$

where $\mathbf{e}_n^{(m)}$ (m, n = 1, 2) denotes a unit complex vector representing a state of polarization at the m^{th} normal mode of the beam n in the beam propagation coordinate system, $\mathbf{k}_n^{(m)}$ the corresponding wave vector, and $\mathrm{A}_n^{(m)}$ the complex amplitude of the beam n at the m^{th} normal mode. $\mathrm{A}_n^{(m)}$ is allowed to depend only on z. This corresponds to the paraxial approximation in photorefractive beam coupling. The effect of optical activity can be incorporated into the normal mode representation. We note that the orthonormality of the normal modes, i.e., $\mathbf{e}_l^{(m)} \cdot \mathbf{e}_{l'}^{(n)*} = \delta_{mn}$ (l, l', m, n = 1, 2) can still hold in the beam propagation coordinate system. The wave equation for the complex amplitude of the total field vector $\mathbf{E}^\omega$ $(= \mathbf{E}_1^\omega + \mathbf{E}_2^\omega)$ of angular optical frequency ω is given by

$$\nabla \times \nabla \times \mathbf{E}^\omega = (\frac{\omega}{c})^2(\tilde{\epsilon} : \mathbf{E}^\omega + 4\pi\mathbf{P}_{\mathrm{NL}}^\omega + i4\pi\omega c\tilde{\sigma} : \mathbf{E}^\omega), \qquad (3.2)$$

where c is the speed of light in vacuum, $\tilde{\epsilon}$ the second-rank linear dielectric tensor, $\tilde{\sigma}$ the second-rank conductivity tensor, and $\mathbf{P}_{\mathrm{NL}}^\omega$ the nonlinear polarization given by Eq. (2.30), all measured in the beam propagation coordinate system.

The arbitrary polarized two waves given by Eqs. (3.1) form an intensity-interference pattern in the crystal

$$\mathrm{I} = \mathrm{I}_0[1 + \frac{1}{2}(m_1 e^{i\mathbf{K}^{(1)}\cdot\mathbf{r}} + m_2 e^{i\mathbf{K}^{(2)}\cdot\mathbf{r}}) + c.c.], \qquad (3.3)$$

where $\mathrm{I}_0 = |\mathrm{A}_1^{(1)}|^2 + |\mathrm{A}_1^{(2)}|^2 + |\mathrm{A}_2^{(1)}|^2 + |\mathrm{A}_2^{(2)}|^2$, $\mathbf{K}^{(1)} = \mathbf{k}_1^{(1)} - \mathbf{k}_2^{(1)}$, $\mathbf{K}^{(2)} = \mathbf{k}_1^{(2)} - \mathbf{k}_2^{(2)}$, and

$$m_1 = \frac{2}{\mathrm{I}_0}[\mathrm{A}_1^{(1)}\mathrm{A}_2^{(1)*}(\mathbf{e}_1^{(1)} \cdot \mathbf{e}_2^{(1)*})], \qquad (3.4a)$$

$$m_2 = \frac{2}{I_0}[A_1^{(2)} A_2^{(2)*}(\mathbf{e}_1^{(2)} \cdot \mathbf{e}_2^{(2)*})]. \tag{3.4b}$$

This interference pattern creates the space-charge electric field in the photorefractive crystal [3.53], thereby causing $\mathbf{P}_{NL}^{\omega}$ in Eq. (3.2) via the electrooptic effect. The wave vector and grating configuration in k space is depicted in Fig. 3.3.

In what follows we shall consider the case where the two input waves possess the same eigen polarizations which we denote $\mathbf{e}_1^{(1)}$ and $\mathbf{e}_2^{(1)}$. In this case one photorefractive grating with grating vector $\mathbf{K}^{(1)}$ is created initially inside the crystal. Because of the possible anisotropic Bragg condition $\mathbf{k}_1^{(2)} = \mathbf{k}_1^{(1)} + \mathbf{K}^{(1)}$ and $\mathbf{k}_2^{(2)} = \mathbf{k}_2^{(1)} - \mathbf{K}^{(1)}$ [see Fig. 3.1(c)], two new waves having k vectors of $\mathbf{k}_1^{(2)}$ and $\mathbf{k}_2^{(2)}$ are then created by the initial grating and write a new photorefractive grating with the grating vector $\mathbf{K}^{(2)}$. We note that, for the most general case where the two input waves are arbitrarily polarized, at least six waves and three photorefractive gratings are involoved in the beam coupling process. These coupled-wave equations can be straightforwardly obtained by the symmetry consideration of the following result.

Substituting Eqs. (2.30), (2.32), and (3.1) into Eq. (3.2) and using the orthonormality of the normal modes and the slowly varying field approximation [3.8], i.e., $|d^2 A_n^{(m)}/dz^2| \ll |k_n^{(m)} dA_n^{(m)}/dz|$, we obtain the following set of coupled-wave equations for the four interacting waves [3.54]:

$$\frac{d}{dz}\begin{pmatrix} A_1^{(1)} \\ A_1^{(2)} \\ A_2^{(1)} \\ A_2^{(2)} \end{pmatrix} = \begin{pmatrix} [P_1] & [Q_1] \\ [Q_2] & [P_2] \end{pmatrix} \begin{pmatrix} A_1^{(1)} \\ A_1^{(2)} \\ A_2^{(1)} \\ A_2^{(2)} \end{pmatrix}, \tag{3.5}$$

where

$$[P_1] = [P_1'] + [P_1'']$$

$$= \begin{pmatrix} \dfrac{-\alpha/2 - i(\omega/c)\Delta n_1^{(11)}}{\cos\theta_1^{(1)}} & \dfrac{-i(\omega/c)\Delta n_1^{(12)} e^{i\Delta k z}}{\cos\theta_1^{(1)}} \\ \dfrac{-i(\omega/c)\Delta n_1^{(21)} e^{-i\Delta k z}}{\cos\theta_1^{(2)}} & \dfrac{-\alpha/2 - i(\omega/c)\Delta n_1^{(22)}}{\cos\theta_1^{(2)}} \end{pmatrix}$$

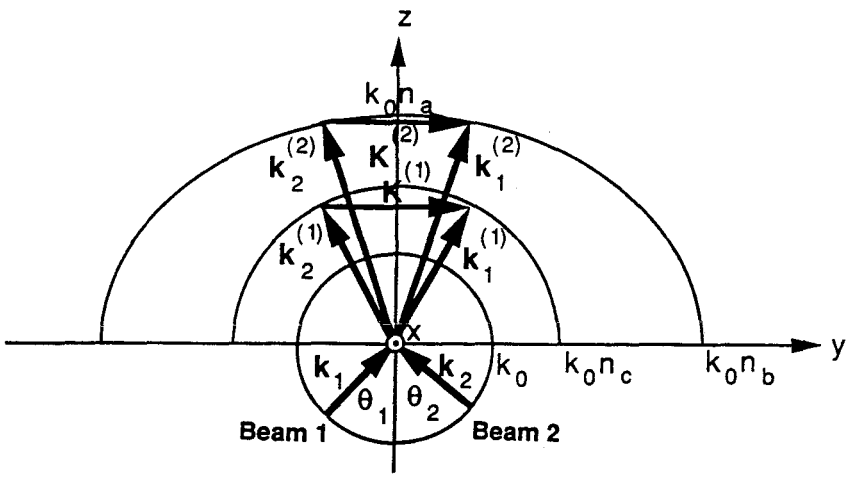

Figure 3.3 Wave vector and grating configuration in k space. The case of a biaxial crystal such as $KNbO_3$ is depicted. In this example the x, y, and z axes correspond to the crystallographic c, a, and b axes, respectively. The k vectors $\mathbf{k}_1^{(1)}$ and $\mathbf{k}_1^{(2)}$ correspond to the two normal modes of beam 1 inside the crystal, while $\mathbf{k}_2^{(1)}$ and $\mathbf{k}_2^{(2)}$ correspond to those of beam 2. The grating vectors $\mathbf{K}^{(1)}(\equiv \mathbf{k}_1^{(1)} - \mathbf{k}_2^{(1)})$ and $\mathbf{K}^{(2)}(\equiv \mathbf{k}_1^{(2)} - \mathbf{k}_2^{(2)})$ correspond to the two different photorefractive gratings.

$$+\begin{pmatrix} 0 & \dfrac{(d_1^{(12)}m_1^*+d_2^{(12)}m_2^*e^{-i\Delta Kz})e^{i(\Delta k-K_z^{(1)})z}}{\cos\theta_1^{(1)}} \\ \dfrac{(d_1^{(21)}m_1+d_2^{(21)}m_2e^{i\Delta Kz})e^{-i(\Delta k-K_z^{(1)})z}}{\cos\theta_1^{(2)}} & 0 \end{pmatrix}, \tag{3.6a}$$

$$[P_2] = [P_2'] + [P_2'']$$

$$= \begin{pmatrix} \dfrac{-\alpha/2-i(\omega/c)\Delta n_2^{(11)}}{\cos\theta_2^{(1)}} & \dfrac{-i(\omega/c)\Delta n_2^{(12)}e^{i(\Delta k-\Delta K)z}}{\cos\theta_2^{(1)}} \\ \dfrac{-i(\omega/c)\Delta n_2^{(21)}e^{-i(\Delta k-\Delta K)z}}{\cos\theta_2^{(2)}} & \dfrac{-\alpha/2-i(\omega/c)\Delta n_2^{(22)}}{\cos\theta_2^{(2)}} \end{pmatrix}$$

$$+\begin{pmatrix} 0 & \dfrac{(f_1^{(12)}m_1+f_2^{(12)}m_2e^{i\Delta Kz})e^{i(\Delta k-\Delta K+K_z^{(1)})z}}{\cos\theta_2^{(1)}} \\ \dfrac{(f_1^{(21)}m_1^*+f_2^{(21)}m_2^*e^{-i\Delta Kz})e^{-i(\Delta k-\Delta K+K_z^{(1)})z}}{\cos\theta_2^{(2)}} & 0 \end{pmatrix}, \tag{3.6b}$$

$$[Q_1] = -\frac{1}{2}\begin{pmatrix} \dfrac{(\gamma_1^{(11)}m_1+\gamma_2^{(11)}m_2e^{i\Delta Kz})}{\cos\theta_1^{(1)}} & \dfrac{(\gamma_1^{(12)}m_1+\gamma_2^{(12)}m_2e^{i\Delta Kz})e^{i(\Delta k-\Delta K)z}}{\cos\theta_1^{(1)}} \\ \dfrac{(\gamma_1^{(21)}m_1+\gamma_2^{(21)}m_2e^{i\Delta Kz})e^{-i\Delta kz}}{\cos\theta_1^{(2)}} & \dfrac{(\gamma_1^{(22)}m_1+\gamma_2^{(22)}m_2e^{i\Delta Kz})e^{-i\Delta Kz}}{\cos\theta_1^{(2)}} \end{pmatrix}, \tag{3.6c}$$

$$[Q_2] = \frac{1}{2}\begin{pmatrix} \dfrac{(g_1^{(11)}m_1^*+g_2^{(11)}m_2^*e^{-i\Delta Kz})}{\cos\theta_2^{(1)}} & \dfrac{(g_1^{(12)}m_1^*+g_2^{(12)}m_2^*e^{-i\Delta Kz})e^{i\Delta kz}}{\cos\theta_2^{(1)}} \\ \dfrac{(g_1^{(21)}m_1^*+g_2^{(21)}m_2^*e^{-i\Delta Kz})e^{-i(\Delta k-\Delta K)z}}{\cos\theta_2^{(2)}} & \dfrac{(g_1^{(22)}m_1^*+g_2^{(22)}m_2^*e^{-i\Delta Kz})e^{i\Delta Kz}}{\cos\theta_2^{(2)}} \end{pmatrix}, \tag{3.6d}$$

and $\alpha_n^m = 4\pi\omega\sigma/c^2k_n^{(m)} \approx \alpha(m, n = 1, 2)$, where we assumed an isotropic conductivity of the crystal $\tilde{\sigma} = \sigma I$ (I is a unit matrix). Also in Eqs. (3.6) m_1 and m_2 are given by Eqs. (3.4), and $\Delta k = (\mathbf{k}_1^{(2)} - \mathbf{k}_1^{(1)}) \cdot \mathbf{e}_z, \Delta K = (\mathbf{K}^{(2)} - \mathbf{K}^{(1)}) \cdot \mathbf{e}_z$, $K_z^{(1)} = \mathbf{K}^{(1)} \cdot \mathbf{e}_z$, $\theta_l^{(m)} = \cos^{-1}(\mathbf{k}_l^{(m)} \cdot \mathbf{e}_z/|\mathbf{k}_l^{(m)}|)$ (l, m = 1, 2). The parameters Δn, d, f, γ, and g in Eqs. (3.6) are given in Table 3.1. We see from Eq. (3.5) that the submatrices $[P_1']$ and $[P_2']$ denote the absorption and linear birefringence due to the application of the external DC electric field and the submatrices $[P_1'']$ and $[P_2'']$ denote the photorefractive anisotropic self-diffraction [see Fig. 3.1(c)], while the submatrices $[Q_1]$ and $[Q_2]$ denote the photorefractive isotropic and cross-polarization beam coupling [see Figs. 3.1(a) and (b)]. We note that the coupling

Table 3.1 Parameters used in Eqs. (3.6).

$$d_l^{(12)} = \frac{\omega}{2n_1^{(1)}c}\Xi_{sc}^{(l)*}\xi_l^{(12)}(\mathbf{e}_1^{(1)*}\cdot\Delta\tilde{q}\cdot\mathbf{e}_1^{(2)})^*,\ d_l^{(21)} = \frac{n_1^{(1)}}{n_1^{(2)}}d_l^{(12)*}$$

$$f_l^{(12)} = \frac{\omega}{2n_2^{(1)}c}\Xi_{sc}^{(l)}\varsigma_l^{(12)}(\mathbf{e}_2^{(1)*}\cdot\Delta\tilde{q}\cdot\mathbf{e}_2^{(2)}),\ f_l^{(21)} = \frac{n_1^{(1)}}{n_2^{(2)}}f_l^{(12)*}$$

$$\gamma_l^{(ij)} = \frac{\omega}{2n_1^{(i)}c}\Xi_{sc}^{(l)}a_l^{(ij)}(\mathbf{e}_1^{(i)*}\cdot\Delta\tilde{q}\cdot\mathbf{e}_2^{(j)})$$

$$g_l^{(ij)} = \frac{\omega}{2n_2^{(i)}c}\Xi_{sc}^{(l)*}a_l^{(ji)*}(\mathbf{e}_2^{(i)*}\cdot\Delta\tilde{q}\cdot\mathbf{e}_1^{(j)}) = \frac{n_1^{(i)}}{n_2^{(i)}}\gamma_l^{(ji)*}$$

$$\Delta n_l^{(ij)} = \frac{E_0}{2n_l^{(i)}}(a_j^{(ij)}\delta_{1l} + a_i^{(ij)}\delta_{2l})(\mathbf{e}_l^{(i)*}\cdot\Delta\tilde{q}\cdot\mathbf{e}_l^{(j)}),\quad (i,j,l = 1,2)$$

$$\Delta\tilde{q} = \tilde{\epsilon} : (\tilde{\tilde{r}} : \mathbf{e}_{sc}) : \tilde{\epsilon}$$

$$\xi_l^{(12)} = \frac{1}{V}\iint_S e^{i[(\Delta\mathbf{k}-\mathbf{K}^{(l)})\cdot(x\mathbf{e}_x+y\mathbf{e}_y)]}dx\,dy$$

$$\varsigma_l^{(12)} = \frac{1}{V}\iint_S e^{i[(\Delta\mathbf{k}-\Delta\mathbf{K}+\mathbf{K}^{(l)})\cdot(x\mathbf{e}_x+y\mathbf{e}_y)]}dx\,dy$$

$$a_1^{(11)} = a_2^{(22)} = 1$$

$$a_1^{(12)} = [a_1^{(21)}]^* = \frac{1}{V}\iint_S e^{i[(\Delta\mathbf{k}-\Delta\mathbf{K})\cdot(x\mathbf{e}_x+y\mathbf{e}_y)]}dx\,dy$$

$$a_2^{(12)} = [a_1^{(21)}]^* = \frac{1}{V}\iint_S e^{i[\Delta\mathbf{k}\cdot(x\mathbf{e}_x+y\mathbf{e}_y)]}dx\,dy$$

$$a_2^{(11)} = [a_1^{(22)}]^* = \frac{1}{V}\iint_S e^{i[\Delta\mathbf{K}\cdot(x\mathbf{e}_x+y\mathbf{e}_y)]}dx\,dy$$

$$V = \iint_{(\text{grating area})S} dx\,dy$$

In the above formulae E_0 and $\Xi_{sc}^{(l)}$ are related to the space-charge electric field as follows:

$$\mathbf{E}_{sc} = \mathbf{e}_{sc}[E_0 + \frac{1}{2}(E_{sc}^{(1)}e^{i\mathbf{K}^{(1)}\cdot\mathbf{r}} + E_{sc}^{(2)}e^{i\mathbf{K}^{(2)}\cdot\mathbf{r}}) + c.c.]$$
$$= \mathbf{e}_{sc}[E_0 - \frac{i}{2}(m_1\Xi_{sc}^{(1)}e^{i\mathbf{K}^{(1)}\cdot\mathbf{r}} + m_2\Xi_{sc}^{(2)}e^{i\mathbf{K}^{(2)}\cdot\mathbf{r}}) + c.c.]$$

into other possible waves due to the linear birefringence is neglected for simplicity. The inclusion of these waves also requires the inclusion of other possible photorefractive gratings. The present treatment is, however, complete for the case of anisotropic crystals without DC electric field and the two special cases described in the following section.

Some of the elements in the above matrices involve the modulation indices m_1 and m_2. The set of coupled-wave equations is thus nonlinear and general solutions to Eq. (3.5) are difficult to solve exactly. We therefore look for the exact and/or approximate analytic solutions for two special cases which are described in the following two sections.

3.3 Scalar two-beam coupling

3.3.1 Coupled-wave equations

Scalar two-beam coupling is the simplest case since $\Delta\tilde{q}$ [$= \Delta\tilde{\chi}/(-\mathrm{E_{sc}}/4\pi)$, see Table 2.1] and therefore the submatrices $[P_1], [P_2], [Q_1]$, and $[Q_2]$ are all diagonal. This occurs, for example, when the space-charge field is parallel to the crystallographic $< 001 >$ axis and

a) for 2mm, 4mm and 3m crystal symmetry classes the input beams are linearly polarized along one of the principal axes, or

b) for cubic $\bar{4}3$m crystal symmetry class the input beams are linearly polarized along the crystallographic $< 110 >$ axis or $< \bar{1}10 >$ axis [see Eqs. (2.33)].

In these cases Eq. (3.5) can be reduced to the following simple form:

$$\cos\theta_1' \frac{d\mathrm{A}_1}{dz} = -\frac{\alpha}{2}\mathrm{A}_1 - \frac{\gamma}{\mathrm{I}_0}\mathrm{A}_1|\mathrm{A}_2|^2 - i(\frac{\omega}{c})\Delta n_1^{(11)}\mathrm{A}_1, \tag{3.7a}$$

$$\cos\theta_2' \frac{d\mathrm{A}_2}{dz} = -\frac{\alpha}{2}\mathrm{A}_2 + \frac{\gamma^*}{\mathrm{I}_0}\mathrm{A}_2|\mathrm{A}_1|^2 - i(\frac{\omega}{c})\Delta n_2^{(11)}\mathrm{A}_2, \tag{3.7b}$$

where we set $\mathrm{A}_1 = \mathrm{A}_1^{(1)}$, $\mathrm{A}_2 = \mathrm{A}_2^{(1)}$ and $\mathrm{A}_1^{(2)} = \mathrm{A}_2^{(2)} = 0$ for the two input waves of the same eigen polarizations ($\mathbf{e}_1 = \mathbf{e}_1^{(1)}$ and $\mathbf{e}_2 = \mathbf{e}_2^{(1)}$), $\theta_{1,2}'$ is measured in a

crystal, and

$$\gamma = \frac{\omega}{2n_\lambda c}\Xi_{sc}(\mathbf{e}_1^* \cdot \Delta\tilde{q} \cdot \mathbf{e}_2)(\mathbf{e}_1 \cdot \mathbf{e}_2^*), \tag{3.8}$$

in which n_λ is n_e or n_o depending on whether the mixing beams are of extraordinary or ordinary polarization, and $\Xi_{sc}(=\Xi_{sc}^{(1)})$ is given, for example, by

$$\Xi_{sc} = \frac{1}{1+\beta_e\hbar\omega/s_e I_0}\frac{E_{qe}(E_D - iE_0)}{E_{qe}+E_D-iE_0}. \tag{3.9}$$

for one species and one type of carrier transport [see Eq. (2.14)].

Equations (3.7*a*) and (3.7*b*) can be rewritten, in terms of the intensity and the phase of each beam $A_j = \sqrt{I_j}e^{i\psi_j}(j=1,2)$, as

$$\cos\theta_1'\frac{dI_1}{dz} = -\Gamma\frac{I_1 I_2}{I_0} - \alpha I_1, \tag{3.10a}$$

$$\cos\theta_2'\frac{dI_2}{dz} = \Gamma\frac{I_1 I_2}{I_0} - \alpha I_2, \tag{3.10b}$$

$$\cos\theta_1'\frac{d\psi_1}{dz} = -\Gamma'\frac{I_2}{I_0} - \Delta\psi_1, \tag{3.10c}$$

$$\cos\theta_2'\frac{d\psi_2}{dz} = -\Gamma'\frac{I_1}{I_0} - \Delta\psi_2, \tag{3.10d}$$

where $I_0 = I_1 + I_2$, $\Gamma = 2Re(\gamma)$, and $\Gamma' = Im(\gamma)$ are the real and imaginary parts of the beam coupling gain coefficient, respectively, and $\Delta\psi_m = (\omega/c)\Delta n_m^{(11)}(m=1,2)$ is a phase retardation (per unit length) caused by the linear birefringence under application of the DC electric field E_0. It is seen that the real part of γ is responsible for the intensity coupling, while the imaginary part of γ is responsible for the phase coupling. Since γ is a function of Ξ_{sc} which is related to the space-charge electric field by $E_{sc}^0 = -im\Xi_{sc}$ [see Eq. (2.14)], the intensity coupling is due to the shifted grating formed through the pure diffusion mechanism ($E_0 = 0$) or the special case of the drift mechanism ($E_0 \gg E_D, E_{qe}$). On the other hand, phase coupling is due to the unshifted grating formed through the usual drift mechanism ($E_0 \neq 0$). The maximum intensity coupling, of course, occurs when the displacement of the photorefractive grating with respect to the intensity interference pattern is $\pm\pi/2$.

3.3.2 Steady-state solution

Equations(3.10a) – (3.10d) can be solved exactly in the symmetric codirectional beam coupling configuration (i.e., $\theta_1' = \theta_2' = \theta'$) [3.2]:

$$I_1(s) = \frac{I_0(0)e^{-\alpha s}}{1 + [I_2(0)/I_1(0)]e^{\Gamma s}}, \tag{3.11a}$$

$$I_2(s) = \frac{I_0(0)e^{-\alpha s}}{1 + [I_1(0)/I_2(0)]e^{-\Gamma s}}, \tag{3.11b}$$

$$\psi_1(s) = \psi_1(0) - \Delta\psi_1 s - \Gamma' s + \frac{\Gamma'}{\Gamma} ln\left\{\frac{1 + I_1(0)/I_2(0)}{1 + [I_1(0)/I_2(0)]e^{-\Gamma s}}\right\}, \tag{3.11c}$$

$$\psi_2(s) = \psi_2(0) - \Delta\psi_2 s - \Gamma' s - \frac{\Gamma'}{\Gamma} ln\left\{\frac{1 + I_2(0)/I_1(0)}{1 + [I_2(0)/I_1(0)]e^{\Gamma s}}\right\}, \tag{3.11d}$$

where $s = z/\cos\theta'$. We see from Eqs.(3.11a) – (3.11d) that one of the two beams is amplified while the other is deamplified, depending on the sign of Γ. This optical beam amplification allows us to construct the unidirectional ring oscillator with photorefractive gain [3.5] in which the nonlinear phase shift due to the non-zero value of Γ' is the origin of the frequency shift of the oscillating field inside the ring cavity [3.55]. The solutions for the case of contradirectional two-beam coupling have also been solved [3.56,57]. It has been shown that this contradirectional two-beam coupling causes nonreciprocal transmittance through a photorefractive crystal and can be used to realize an optical diode [3.58,59].

3.3.3 Transient-state solution

The transient-state solution can be obtained by solving Eqs. (2.12) and (3.7) simultaneously. Some approximate analytic solutions have been obtained by means of either the undepleted pump approximation [3.60,61] or the perturbation expansion [3.62]. Here we show the latter result.

For a lumped input case the approximate analytic solution is given by

$$I_{\binom{1}{2}}(s,t) = I^{(0)}_{\binom{1}{2}} \mp 2\delta sa\tau I_1^{(0)} I_2^{(0)}[\sin\phi - e^{-t/\tau_e}\sin(\phi - \omega_e t)] \mp (\delta sa\tau)^2 I_1^{(0)} I_2^{(0)}(I_1^{(0)} - I_2^{(0)})\times$$
$$[\cos 2\phi - e^{-t/\tau_e}\cos(2\phi - \omega_e t) - 1 - \frac{t}{\tau}e^{-t/\tau_e}\cos(\phi_1 - \omega_e t)$$
$$+ 2e^{-t/\tau_e}\cos\omega_e t - e^{-2t/\tau_e}], \tag{3.12}$$

where we set $\alpha = 0$, $I^{(0)}_{\binom{1}{2}} = I_{\binom{1}{2}}(0,0)$,

$$\delta = \frac{\omega}{2n_\lambda c}(\mathbf{e}_1^* \cdot \Delta\tilde{q} \cdot \mathbf{e}_2)(\mathbf{e}_1 \cdot \mathbf{e}_2^*), \tag{3.13a}$$

$$\tau = |T_e|, \tag{3.13b}$$

$$a = \left|\frac{\Xi_{sc}}{2I_0 T_e}\right|, \tag{3.13c}$$

$$\phi = \phi_a + \phi_\tau, \tag{3.13d}$$

$$\phi_1 = 2\phi_a + \phi_\tau, \tag{3.13e}$$

$$\phi_a = Arg\left(\frac{\Xi_{sc}}{2I_0 T_e}\right) - \frac{\pi}{2}, \tag{3.13f}$$

$$\phi_\tau = Arg(T_e), \tag{3.13g}$$

in which T_e, τ_e, ω_e and Ξ_{sc} are given by Eqs.(2.13), (2.17), and (3.9). This perturbative solution (for $\delta s < 1$) can be reduced to the following two asymptotic cases:

1)in the diffusion dominant mechanism ($|\phi| \approx \pi/2$),

$$I_{\binom{1}{2}}(s,t) = I^{(0)}_{\binom{1}{2}} \mp 2\delta as\tau I_1^{(0)} I_2^{(0)}(1 - e^{-t/\tau_e}) \mp (\delta as\tau)^2 I_1^{(0)} I_2^{(0)}(I_1^{(0)} - I_2^{(0)})\times$$
$$[e^{-t/\tau_e}(3 + \frac{t}{\tau_e} - e^{-t/\tau_e}) - 2]; \tag{3.14}$$

2)in the drift dominant mechanism ($|\phi| \approx 0$ or π),

$$I_{\binom{1}{2}}(s,t) = I^{(0)}_{\binom{1}{2}} \mp (\delta a_E s\tau)^2 I_1^{(0)} I_2^{(0)}(I_1^{(0)} - I_2^{(0)})e^{-t/\tau_e}(1 - \frac{t}{\tau_e} - e^{-t/\tau_e}). \tag{3.15}$$

Equation (3.15) is valid for small angles θ and an intermediate DC electric field E_0, and

$$a_E = -\frac{E_0}{\tau_{de} I_0 (1 + E_D/E_{Me})}, \tag{3.16}$$

where τ_{de}, E_D, and E_{Me} are given by Eqs. (2.9*a*), (2.15*b*), and (2.25), respectively.

We see from Eq. (3.14) that for either $I_1^{(0)} \approx I_2^{(0)}$ or $\delta s \ll 1$ a single exponential form of the linear term in δ determines the temporal behavior of the beam coupling, and its time constant τ_e is the same as that of the space-charge electric field formation [see Eqs. (2.16)]. This time dependence has been used for the characterization of photorefractive materials [3.63]. It is seen from Eq. (3.15) that for the unshifted grating with small angles θ there is transient energy coupling between the two beams only when $I_1^{(0)} \neq I_2^{(0)}$ and the energy transfer is always from the higher intensity beam to the weaker one, independently of the sign of E_0. This beam coupling gain becomes maximum when $t \approx 1.59\tau_e$ and approaches zero in the steady state. This transient beam coupling property can be applied to the optical tracking filter device which will be described in Chapter 5.

3.4 Cross-polarization beam coupling in cubic crystals

3.4.1 Coupled-wave equations

In this section we consider cross-polarization beam coupling resulting from the anisotropic nature of $\Delta\tilde{\chi}$ in cubic crystals [see Table 2.1]. Since cubic crystals are isotropic when there is no E_0 and E_{sc}, we can to some extent simplify the coupled-wave equations in terms of the following correspondences:

$$d_l^{(ij)},\ f_l^{(ij)} \approx 0, \tag{3.17a}$$

$$\gamma_l^{(ij)} = \frac{\omega}{2n_0 c}\Xi_{sc}(\mathbf{e}_1^{(i)*} \cdot \Delta\tilde{q} \cdot \mathbf{e}_2^{(j)}) \equiv \gamma^{(ij)}, \tag{3.17b}$$

$$g_l^{(ij)} = \gamma_l^{(ji)*}, \tag{3.17c}$$

$$\Delta n_l^{(ij)} = \frac{E_0}{2n_0}(\mathbf{e}_l^{(i)*} \cdot \Delta\tilde{q} \cdot \mathbf{e}_l^{(j)}), \tag{3.17d}$$

$$\theta_1^{(1)} = \theta_2^{(2)} \equiv \theta_1', \ \theta_2^{(1)} = \theta_2^{(2)} \equiv \theta_2', \tag{3.17e}$$

$$m_1 = \frac{2}{I_0} A_1^{(1)} A_2^{(1)*}, \tag{3.17f}$$

$$m_2 = \frac{2}{I_0} A_1^{(2)} A_2^{(2)*} \cos(\theta_1' + \theta_2'), \tag{3.17g}$$

$$\mathbf{k}_1^{(1)} = \mathbf{k}_1^{(2)}, \ \mathbf{k}_2^{(1)} = \mathbf{k}_2^{(2)}, \ |\mathbf{k}_1^{(1)}| = |\mathbf{k}_2^{(1)}|, \tag{3.17h}$$

$$\Delta\mathbf{k}, \Delta\mathbf{K} = 0, \tag{3.17i}$$

where we identify $\mathbf{e}_1^{(1)} = \mathbf{e}_2^{(1)} = \mathbf{e}_y$ (i.e., the normal mode 1 is polarized linearly along the y axis), n_0 is the background refractive index and Ξ_{sc} is, for example, given by Eq. (3.9). We then obtain the following set of coupled-wave equations:

$$\frac{dA_1^{(1)}}{dz} = -\frac{\alpha}{2\cos\theta_1'} A_1^{(1)} - i\frac{\omega}{c\cos\theta_1'}(\Delta n_1^{(11)} A_1^{(1)} + \Delta n_1^{(12)} A_1^{(2)}) - (\gamma^{(11)} A_2^{(1)} + \gamma^{(12)} A_2^{(2)})(A_1^{(1)} A_2^{(1)*} + A_1^{(2)} A_2^{(2)*} \cos\vartheta)/(I_0 \cos\theta_1'), \tag{3.18a}$$

$$\frac{dA_1^{(2)}}{dz} = -\frac{\alpha}{2\cos\theta_1'} A_1^{(2)} - i\frac{\omega}{c\cos\theta_1'}(\Delta n_1^{(21)} A_1^{(1)} + \Delta n_1^{(22)} A_1^{(2)}) - (\gamma^{(21)} A_2^{(1)} + \gamma^{(22)} A_2^{(2)})(A_1^{(1)} A_2^{(1)*} + A_1^{(2)} A_2^{(2)*} \cos\vartheta)/(I_0 \cos\theta_1'), \tag{3.18b}$$

$$\frac{dA_2^{(1)}}{dz} = -\frac{\alpha}{2\cos\theta_2'} A_2^{(1)} - i\frac{\omega}{c\cos\theta_2'}(\Delta n_2^{(11)} A_2^{(1)} + \Delta n_2^{(12)} A_2^{(2)}) + (\gamma^{(11)*} A_1^{(1)} + \gamma^{(21)*} A_1^{(2)})(A_1^{(1)*} A_2^{(1)} + A_1^{(2)*} A_2^{(2)} \cos\vartheta)/(I_0 \cos\theta_2'), \tag{3.18c}$$

$$\frac{dA_2^{(2)}}{dz} = -\frac{\alpha}{2\cos\theta_2'} A_2^{(2)} - i\frac{\omega}{c\cos\theta_2'}(\Delta n_2^{(21)} A_2^{(1)} + \Delta n_2^{(22)} A_2^{(2)}) + (\gamma^{(12)*} A_1^{(1)} + \gamma^{(22)*} A_1^{(2)})(A_1^{(1)*} A_2^{(1)} + A_1^{(2)*} A_2^{(2)} \cos\vartheta)/(I_0 \cos\theta_2'), \tag{3.18d}$$

where $\vartheta = \theta_1' + \theta_2'$. This set of coupled-wave equations is similar to those derived by Fischer *et al.* [3.64] and Yeh [3.27,30]. (But in their papers the linear birefringence terms $\Delta n_l^{(mn)}$ are not taken into account.) The configurations relevant to Eqs.(3.18*a*) – (3.18*d*) (i.e., codirectional and contradirectional beam coupling) are depicted in Fig. 3.4. The values of $\Delta n_l^{(mn)}$ and $\gamma^{(mn)}$ for various configurations for beam coupling in cubic crystals are given in Table 3.2.

3.4.2 Steady-state solutions

The exact steady-state solutions to Eqs.(3.18*a*) –(3.18*d*) for the special case of codirectional parallel beam coupling (i.e., $\theta_1' = \theta_2'$, $\alpha = 0$, $\Delta n_l^{(mn)} = 0$, $\gamma^{(11)} = \gamma^{(22)} \neq 0$ and $\gamma^{(12)}, \gamma^{(21)} = 0$) were obtained by Fischer *et al.* [3.64] by means of the same method as in the case of scalar four-wave mixing [3.65]. The exact steady-state solutions for the special case of codirectional cross-polarization beam coupling (i.e., $\theta_1' = \theta_2'$, $\alpha = 0$, $\Delta n_l^{(mn)} = 0$, $\gamma^{(11)}$, $\gamma^{(22)} = 0$, and $\gamma^{(12)} = \gamma^{(21)} \neq 0$) were obtained by Yeh [3.27,30]. A general case of the codirectional cross-polarization beam coupling case where $E_0 \neq 0$ (i.e., $\Delta n_l^{(mn)} \neq 0$) has not been solved yet. The exact solutions for the case of contradirectional cross-polarization beam coupling (i.e., $\theta_1' = \pi + \theta_2'$) have not yet been obtained either and only approximate solutions using the undepleted pump approximation (i.e., the beams $A_2^{(1)}$ and $A_2^{(2)}$ remain constant during the interaction in the crystal) have been reported for $E_0 = 0$ [3.28].

To see qualitative behavior of the cross-polarization beam coupling in cubic crystals, we take the example of the third case in Table 3.2 (i.e., the codirectional cross-polarization beam coupling) and use the undepleted pump approximation. Then Eqs.(3.18*a*) – (3.18*d*) are reduced to

$$\frac{dA_1^{(1)}}{dz} = -\frac{\alpha}{2\cos\theta'} A_1^{(1)} + \gamma' a_{11} A_1^{(1)} + \gamma' a_{12} A_1^{(2)}, \tag{3.19a}$$

$$\frac{dA_1^{(2)}}{dz} = -\frac{\alpha}{2\cos\theta'} A_1^{(2)} + \gamma' a_{21} A_1^{(1)} + \gamma' a_{22} A_1^{(2)}, \tag{3.19b}$$

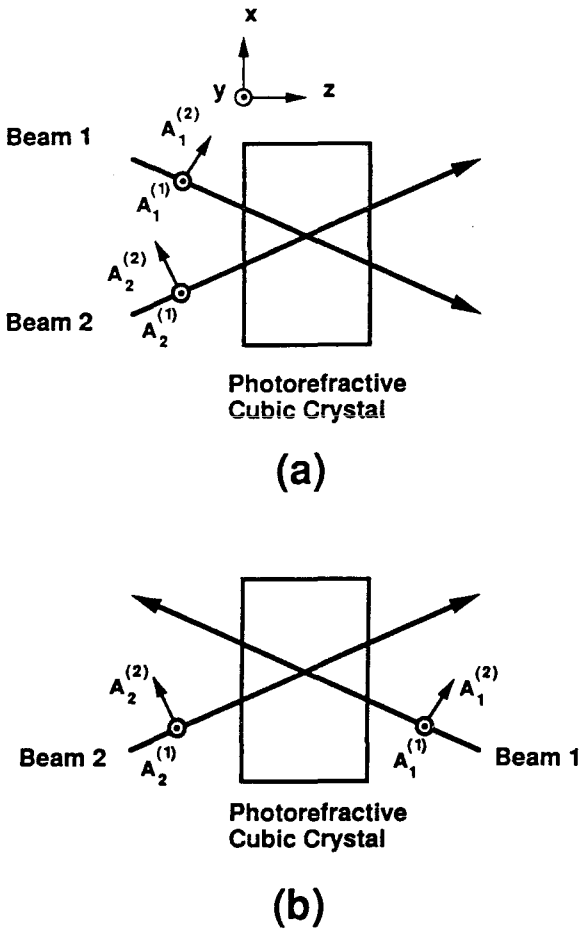

Figure 3.4 Cross-polarization beam coupling in cubic crystals. (a) Codirectional beam coupling. (b) Contradirectional beam coupling.

Table 3.2 Values of $\Delta n_l^{(mn)}$ and $\gamma^{(mn)}$ (l, m, n = 1, 2) for various beam coupling configurations in cubic crystals.

Beam Coupling	$\Delta n_l^{(mn)}$	$\gamma^{(mn)}$
codirectional, parallel		
$\mathbf{e}_x \parallel < 001 >$, $\mathbf{e}_y \parallel < 110 >$	$\Delta n_l^{(11)} = \Delta n$	$\gamma^{(11)} = \gamma_c$
$\mathbf{e}_z \parallel < \bar{1}10 >$, $\mathbf{e}_{sc} \parallel < 001 >$	$\Delta n_l^{(22)} = -2\beta_l^2 \Delta n$	$\gamma^{(22)} = 2\beta_1\beta_2\gamma_c$
	$\Delta n_l^{(12)} = \Delta n_l^{(21)} = 0$	$\gamma^{(12)} = \gamma^{(21)} = 0$
contradirectional, parallel		
$\mathbf{e}_x \parallel < 110 >$, $\mathbf{e}_y \parallel < \bar{1}10 >$	$\Delta n_l^{(11)} = -\Delta n$	$\gamma^{(11)} = -\gamma_c$
$\mathbf{e}_z \parallel < 001 >$, $\mathbf{e}_{sc} \parallel < 001 >$	$\Delta n_l^{(22)} = \vartheta_l \Delta n$	$\gamma^{(22)} = \sqrt{\vartheta_1\vartheta_2}\gamma_c$
	$\Delta n_l^{(12)} = \Delta n_l^{(21)} = 0$	$\gamma^{(12)} = \gamma^{(21)} = 0$
codirectional, cross-polarization		
$\mathbf{e}_x \parallel < \bar{1}10 >$, $\mathbf{e}_y \parallel < 001 >$	$\Delta n_l^{(11)} = \Delta n_l^{(22)} = 0$	$\gamma^{(11)} = \gamma^{(22)} = 0$
$\mathbf{e}_z \parallel < 110 >$, $\mathbf{e}_{sc} \parallel < \bar{1}10 >$	$\Delta n_l^{(12)} = -\sqrt{\vartheta_l}\Delta n$	$\gamma^{(12)} = -\sqrt{\vartheta_2}\gamma_c$
	$\Delta n_l^{(21)} = \Delta n_l^{(12)}$	$\gamma^{(21)} = -\sqrt{\vartheta_1}\gamma_c$
contradirectional, cross-polarization		
$\mathbf{e}_x \parallel < 100 >$, $\mathbf{e}_y \parallel < 010 >$	$\Delta n_l^{(11)} = \Delta n_l^{(22)} = 0$	$\gamma^{(11)} = \gamma^{(22)} = 0$
$\mathbf{e}_z \parallel < 001 >$, $\mathbf{e}_{sc} \parallel < 001 >$	$\Delta n_l^{(12)} = \sqrt{\vartheta_l}\Delta n$	$\gamma^{(12)} = \sqrt{\vartheta_2}\gamma_c$
	$\Delta n_l^{(21)} = \Delta n_l^{(12)}$	$\gamma^{(21)} = \sqrt{\vartheta_1}\gamma_c$

[a] The parameters used in this table are defined as follows:

$$\Delta n \equiv \frac{E_0}{2} n_0^3 r_{41}; \quad \gamma_c \equiv \frac{\omega \Xi_{sc}}{2c} n_0^3 r_{41}; \quad \beta_l \equiv \frac{1}{n_0} \sin\theta_l; \quad \vartheta_l \equiv 1 - \beta_l^2 \quad (l = 1, 2),$$

where θ_l is an incident angle in air.

where we assume $\theta_1' = \theta_2' \equiv \theta'$ and $\beta_l \approx 0$ $(l = 1, 2)$, and

$$a_{11} = A_2^{(1)^*} A_2^{(2)} / I_0, \tag{3.20a}$$

$$a_{12} = |A_2^{(2)}|^2 \cos 2\theta' / I_0 + i \frac{E_0}{\Xi_{sc}}, \tag{3.20b}$$

$$a_{21} = |A_2^{(1)}|^2 / I_0 + i \frac{E_0}{\Xi_{sc}}, \tag{3.20c}$$

$$a_{22} = A_2^{(1)} A_2^{(2)^*} \cos 2\theta' / I_0, \tag{3.20d}$$

$$\gamma' = \frac{\omega n_0^3 r_{41}}{2c \cos \theta'} \Xi_{sc}. \tag{3.20e}$$

The solutions to Eqs. (3.19) are given by

$$\begin{aligned} A_1^{(1)}(z) = \{ & [(a_{11} - \lambda_-) A_1^{(1)}(0) + a_{12} A_1^{(2)}(0)] e^{\lambda + \gamma' z} \\ & - [(a_{11} - \lambda_+) A_1^{(1)}(0) + a_{12} A_1^{(2)}(0)] e^{\lambda - \gamma' z} \} e^{-\alpha z / 2 \cos \theta'} / (\lambda_+ - \lambda_-), \end{aligned} \tag{3.21a}$$

$$\begin{aligned} A_1^{(2)}(z) = \{ & [a_{21} A_1^{(1)}(0) + (a_{22} - \lambda_-) A_1^{(2)}(0)] e^{\lambda + \gamma' z} \\ & - [a_{21} A_1^{(1)}(0) + (a_{22} - \lambda_+) A_1^{(2)}(0)] e^{\lambda - \gamma' z} \} e^{-\alpha z / 2 \cos \theta'} / (\lambda_+ - \lambda_-), \end{aligned} \tag{3.21b}$$

where $\lambda_\pm = [a_{11} + a_{22} \pm \sqrt{(a_{11} - a_{22})^2 + 4 a_{12} a_{21}}]/2$. For the initial condition of $A_1^{(2)}(0) = 0$ these solutions can be written as

$$A_1^{(1)}(z) = A_1^{(1)}(0) [(a_{11} - \lambda_-) e^{\lambda + \gamma' z} - (a_{11} - \lambda_+) e^{\lambda - \gamma' z}] e^{-\alpha z / 2 \cos \theta'} / (\lambda_+ - \lambda_-), \tag{3.21c}$$

$$A_1^{(2)}(z) = A_1^{(1)}(0) a_{21} (e^{\lambda + \gamma' z} - e^{\lambda - \gamma' z}) e^{-\alpha z / 2 \cos \theta'} / (\lambda_+ - \lambda_-). \tag{3.21d}$$

It is seen that the amplitudes and phases of $A_1^{(1)}(z)$ and $A_1^{(2)}(z)$ depend upon the input polarization condition of beam 2, γ' (therefore E_0 as well) and $A_1^{(1)}(0)$. This means that even when beam 1 is linearly polarized initially, it experiences the gain

and changes its polarization state (in general, elliptical polarization) when $E_0 \neq 0$ during propagation in the crystal.

3.5 Beam coupling experiments in semi-insulating GaAs

3.5.1 Elecrooptic semiconductors as photorefractive materials

Semi-insulating (SI) electrooptic semiconductors such as GaAs, InP, and CdTe have recently been considered as important photorefractive materials for the following reasons:

1) high photorefractive sensitivity;
2) infrared (semiconductor laser wavelength) operation;
3) fast response time (mainly due to large mobilities);
4) easy-to-use because of cubic (optically isotropic) crystals without optical activity;
5) availability of large single crystals with high quality;
6) flexible control (tailoring) of optical and electronic properties by doping;
7) compatibility with opto-electronic integrated circuits.

So far Fe-doped InP [3.66], Cr-doped GaAs [3.66], undoped GaAs [3.67], In-doped CdTe [3.68], and V-doped CdTe [3.69] have been experimentally confirmed as being photorefractive, and their photorefractive properties have been reported [3.70-74]. Because of the importance of GaAs for opto-electronic device applications, several detailed studies of photorefractive GaAs have been made. These include the enhancement of the two-beam coupling gain by means of an applied AC electric field [3.75-77] and moving fringes [3.78]. Also studied were the polarization properties of beam coupling [3.26,28,29,31,79] and the picosecond photorefractive effect [3.80-82]. Several applications using photorefractive GaAs have also been reported so far, which include spatial light modulation [3.50], image transfer [3.51], edge

enhancement and autocorrelation [3.52], updatable optical correlator [3.83], and infrared predetection dynamic range compression [3.84].

Moreover, the photorefractive effect in SI GaAs offers a non-destructive method of measuring electronic properties (e.g., deep level densities and signs of dominant photocarriers) of SI GaAs substrates that have been used for important electronic and opto-electronic devices. Recently this idea has been applied successfully to semiconductor wafer imaging [3.85]. In the following two subsections we show our experiment of the photorefractive beam coupling in SI undoped and Cr-doped GaAs [3.54] for the above purpose.

3.5.2 Photorefractive species in semi-insulating GaAs

Deep levels (near the center of the band gap) in SI bulk GaAs have been studied extensively because these levels are responsible for obtaining high resistivity (of the order of 10^7–$10^8\Omega$-cm) GaAs substrates for ultrafast LSI circuits [3.86]. Although the physical origin of these deep levels has not been clarified yet, EL2 (believed to be an antisite native defect involving arsenic on gallium sites) and Cr^{2+}/Cr^{3+} (substitution of gallium sites by chromium) have been well known as the dominant deep levels and studied extensively [3.86,87] (see Fig. 3.5).

EL2 has a dominant one valence electron state $EL2^0$ which acts as a neutral donor in undoped SI GaAs and is responsible for electron transport following the reaction:

$$EL2^0 + h\nu \rightarrow EL2^+ + e^-. \qquad (3.22a)$$

Cr^{3+} acts as a neutral acceptor in Cr-doped SI GaAs and is responsible for hole transport follwing the reaction:

$$Cr^{3+} + h\nu \rightarrow Cr^{2+} + h^+. \qquad (3.22b)$$

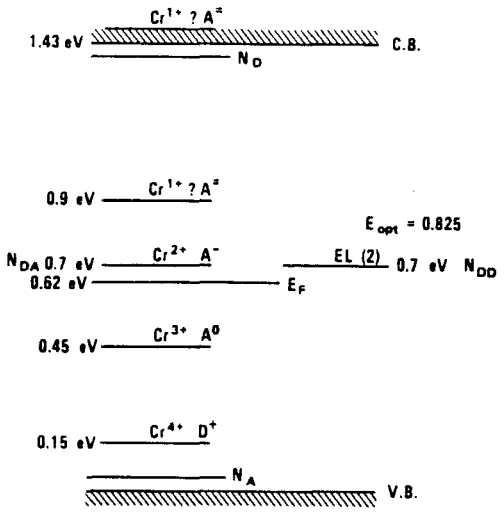

Figure 3.5 Electron energy diagram of semi-insulating GaAs showing the shallow N_D and N_A levels and the deep traps Cr^{2+} and EL2, along with the charge state of Cr in GaAs (after Ref. [3.87]).

In addition to the above two reactions it is also possible to emit holes (electrons) from the $EL2^+$ (Cr^{2+}) level to the valence (conduction) band (see Fig. 3.6). But the photoionization cross-sections of these processes are much smaller than those of the processes given by Eqs. (3.22*a*) and (3.22*b*) at the wavelength of our interest ($\lambda_0 = 1.09\mu$m) [3.86,88].

In Cr-doped SI GaAs the EL2 deep level is still present. In the ground state (T=0) $N_{Cr^{3+}}$ (the number density of the acceptor level Cr^{3+}) of N_{EL2^0} (the number density of the donor level $EL2^0$) electrons in a unit volume drop from the donor level $EL2^0$ to the acceptor level Cr^{3+} when $N_{EL2^0} > N_{Cr^{3+}}$, giving a groud-state configuration in which the $EL2^0$ level is fully ionized into the $EL2^+$ level. Likewise, all of N_{EL2^0} electrons drop from the $EL2^0$ level to the Cr^{3+} level when $N_{EL2^0} < N_{Cr^{3+}}$, giving a ground-state configuration in which the Cr^{3+} level is fully ionized into the Cr^{2+} level. These processes can be expressed by

$$EL2^0 + Cr^{3+} \rightarrow EL2^+ + Cr^{2+}. \tag{3.23}$$

At $T \neq 0$, however, the electrons will be redistributed among all the deep levels. This may cause the simultaneous electron-hole transport (i.e., mixed photoconductivity), which has been observed in Cr-doped SI GaAs by Hall effect measurements [3.86] and photoconductivity spectra [3.88].

Because the above two dominant deep level species are photoactive, it is reasonable to consider these species as photorefractive ones and to apply the band transport model described in Chapter 2 to the photorefractive effect in SI GaAs. In this case the one species and one type of carrier model is used for undoped SI GaAs, while the two species and two types of carriers model is used for Cr-doped SI GaAs. Various photorefractive properties (e.g., the space-charge electric fields and the characteristic time constants) and the beam coupling properties (e.g., the

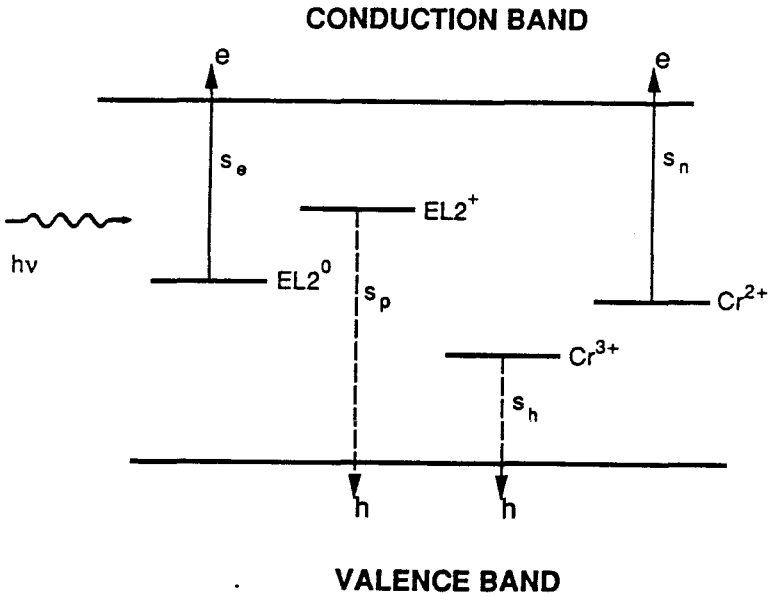

Figure 3.6 Photoionization of carriers form the EL2 and Cr deep levels in SI GaAs. The parameters shown above are photoionization cross-sections at various deep levels.

beam coupling gain including its sign) can be calculated and optimized from these models. In turn, the optical and electronic parameters of SI GaAs (e.g., the deep level densities and sign of dominant photocarriers) can be estimated from the beam coupling experiment described below.

3.5.3 Identification of the signs of dominant photocarriers and deep level densities by scalar two-beam coupling

a) Absorption Spectra

In the experiment we used 5 mm×5 mm×5 mm undoped ($\rho \approx 4 \times 10^7 \Omega$-cm) and Cr-doped ($\rho \approx 1 \times 10^8 \Omega$-cm and Cr doping of 0.2 – 0.5 p.p.m.) GaAs grown by the liquid encapsulated Czochralski (LEC) method [3.89]. The combination of Au(250Å)/AuGe(25Å) was deposited onto both (001) planes for obtaining electrodes with good ohmic contact and both ($\bar{1}10$) planes were polished to have optical flat surfaces. The absorption coefficient $\alpha(\mathrm{cm}^{-1})$ was obtained from the following formula which includes multiple (incoherent) Fresnel reflections:

$$\alpha = \frac{1}{L} \ln \left[[(1-R)^2/2T]\{1 + [1 + 4R^2T^2(1-R)^{-4}]^{\frac{1}{2}}\} \right], \tag{3.24}$$

where T is the measured transmittance and $R[= (1-n_0)^2/(1+n_0)^2]$ is the calculated reflectance in which n_0 is given by the experimental dispersion formula for GaAs [3.90]

$$n_0(h\nu) = \{7.10 + 3.78[1 - 0.180(h\nu)^2]^{-1}\}^{\frac{1}{2}}. \tag{3.25}$$

The absorption spectra of the two SI GaAs samples at room temperature are shown in Fig. 3.7. Because photoionization from the Cr^{3+} level is added to that from the $EL2^0$ level, α of the Cr-doped SI GaAs is larger than that of the undoped SI GaAs.

The deep level densities and α's are related as

$$\alpha = s_e N_{EL2^0} + s_p N_{EL2^+} + \alpha_0$$

$$\approx s_e N_{EL2^0} \qquad \text{for undoped GaAs,}$$

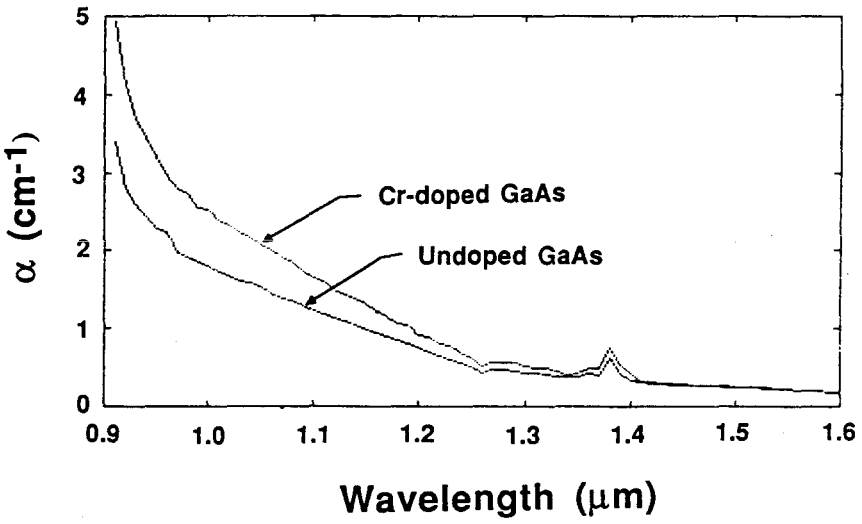

Figure 3.7 Absorption spectra of the undoped and Cr-doped GaAs samples at room temperature.

and

$$\alpha = s_h N_{Cr^{3+}} + s_n N_{Cr^{2+}} + \alpha_{EL2}$$

$$\approx s_h N_{Cr^{3+}} + \alpha_{EL2} \qquad \text{for Cr doped GaAs,}$$

where s_e, s_p, s_h, and s_n are the photoionization cross-sections from various deep levels (see Fig. 3.6), α_0 is due to some residual absorption (e.g., scattering and absorption due to nonphotorefractive species), and the above approximations are made by assuming that $N_{EL2^0} > N_{EL2^+}$, $N_{Cr^{3+}} > N_{Cr^{2+}}$, $s_e > s_p$, and $s_h > s_n$ at $\lambda_0 = 1.09\,\mu$m. We note that N_{EL2^0}, N_{EL2^+}, $N_{Cr^{3+}}$ and $N_{Cr^{2+}}$ correspond to $N_D - N_D^+$, N_D^+, $N_A - N_A^-$ and N_A^- used in Chapter 2, respectively.

Using $s_e = 8.83 \times 10^{-17}\text{cm}^2$ [3.91] and $s_h = 8.4 \times 10^{-17}\text{cm}^2$ [3.92], together with α (undoped GaAs) = 1.286 cm^{-1} and α (Cr-doped GaAs) = 1.734 cm^{-1} at $\lambda_0 = 1.09\,\mu$m taken from Fig. 3.7, we obtain the following number densities in the dark:

$$N_{EL2^0}\,(\text{undoped GaAs}) = 1.46 \times 10^{16}\ \text{cm}^{-3}, \tag{3.26a}$$

and

$$N_{Cr^{3+}}\,(\text{Cr doped GaAs})$$
$$= \begin{cases} 5.30 \times 10^{15}\ \text{cm}^{-3} & \text{if } N_{EL2^0}\,(\text{Cr doped GaAs}) = 1.4 \times 10^{16}\,\text{cm}^{-3}; \\ 2.06 \times 10^{16} - 1.05 N_{EL2^0} & \text{if } N_{EL2^0}\,(\text{Cr doped GaAs}) \neq N_{EL2^0}\,(\text{undoped GaAs}). \end{cases} \tag{3.26b}$$

b) Linear Electrooptic Coefficient

A linear electrooptic coefficient r_{41} of GaAs was measured by an ellipsometric method shown in Fig. 3.8. The value of r_{41} is given in this setup by

$$r_{41} = \frac{2\lambda_0 \phi d}{\pi n_0^3 V L}, \tag{3.27}$$

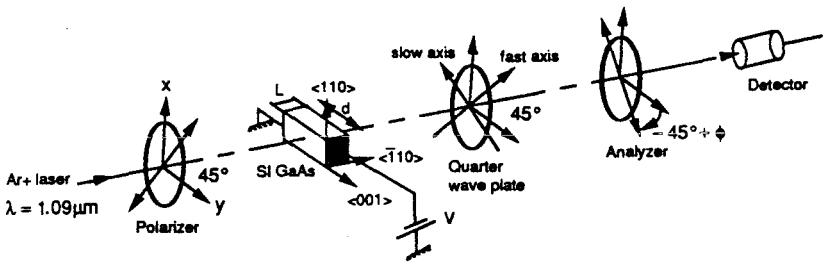

Figure 3.8 Experimental setup for an ellipsometric measurement of a linear electrooptic coefficient r_{41} of SI GaAs. An argon-ion laser of $\lambda = 1.09\,\mu$m was used as a light source.

where ϕ is an analyzer angle from the $-45°$ setting, d is the crystal width between both (001) planes, L is the crystal length between both $(\bar{1}10)$ planes and V is the applied voltage. It was found that at $\lambda_0 = 1.09\,\mu m$

$$r_{41} = r_{41}^{T}(\text{low frequency}) \approx 1.16 \times 10^{-10}\ \text{cm/V},$$

which is consistent with the values measured previously [3.91,93].

c) Measurement of the Two-beam Coupling Gain

The scalar two-beam coupling configuration was used in the experiment (see Fig. 3.9). The exact solutions which describe the scalar two-beam coupling process are given by Eqs. (3.11*a*) - (3.11*d*). If $I_1(0) \gg I_2(0)$, i.e., the undepleted pump approximation is satisfied, the two-beam coupling gain coefficient obtained from Eqs. (3.11*a*) - (3.11*d*) is well approximated by

$$\begin{aligned}\Gamma &= \frac{1}{L}\ln\left[\frac{I_1(0)}{I_1(L)}\frac{I_2(L)}{I_2(0)}\right] \\ &\approx \frac{1}{L}\ln\left[\frac{I_2(L)\text{ with }I_1(0)}{I_2(L)\text{ without }I_1(0)}\right].\end{aligned} \tag{3.28}$$

This relation is particularly useful for the measurement of Γ since possible errors introduced in the measurement of I_1 at both $z = 0$ and L can be avoided. The two-beam coupling gain coefficient can also be expressed by the material parameters [see Eq. (3.8)] and is given in this experimental setup by

$$\Gamma[\equiv 2Re(\gamma)] = -\frac{\omega n_0^3 r_{41}}{c\cos\theta'} Re(\Xi_{sc}), \tag{3.29}$$

where the inclination factor $\cos\theta'(=\sqrt{1-\sin^2\theta/n_0^2})$ is included in this expression so that Eq. (3.29) is identical to Eq. (3.28), and

$$\Xi_{sc} = \frac{E_{qh}/(1+\beta_h\hbar\omega/s_h I_0) - E_{qe}/(1+\beta_e\hbar\omega/s_e I_0)}{1 + E_{qe}/(E_D - iE_0) + E_{qh}/(E_D + iE_0)}$$

for the case of two species and two types of carriers transport [see Eq. (2.20)]. It

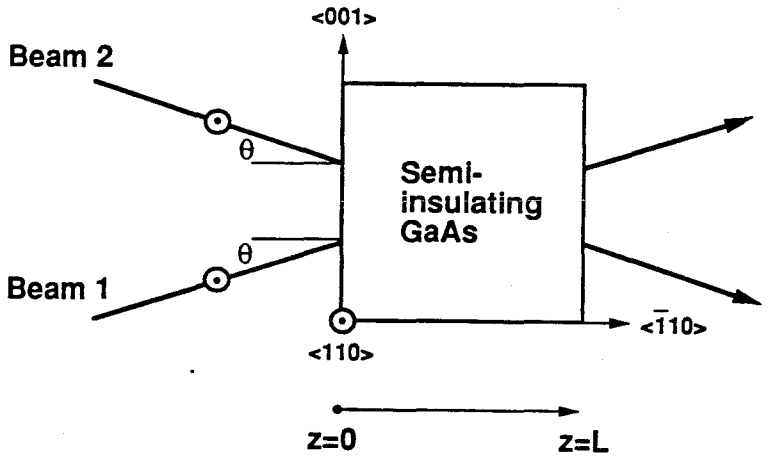

Figure 3.9 Experimental setup for scalar two-beam coupling in SI GaAs. The input beams are linearly polarized along the $< 110 >$ crystallographic axis. The space-charge field is created along the $< 001 >$ crystallographic axis.

is thus possible to estimate both the sign of dominant potocarriers and the deep level densities by measuring the sign and the absolute value of the experimental Γ, respectively, since the other parameters such as r_{41}, N_{EL2^0}, and $N_{Cr^{3+}}$ are measured separately.

In the experiment we chose $I_1(0) = 0.831 W/cm^2$ and $I_2(0) = 0.054 W/cm^2$ so that the undepleted pump approximation $[I_1(0) \gg I_2(0)]$ was valid. As we will see later in this section, the effect of the dark conductivity at room temperature is negligible, i.e., $\beta_e \hbar\omega$, $\beta_h \hbar\omega \ll s_e I_0$, $s_h I_0$ with this total intensity $I_0 (= I_1 + I_2)$. In order to avoid beam walk off inside the crystal, the diameter of beam 1 was chosen to cover the whole crystal while that of beam 2 was chosen to be much smaller than that of beam 1. This procedure was legitimate because the last relation in Eq. (3.28) was used in the experiment.

d) Sign of the Dominant Photocarriers and Deep Level Densities

The sign of Γ can be determined by whether beam 2 at $z = L$ is amplified or deamplified. The sign of Γ is also determined by the signs of r_{41} and $Re(\Xi_{sc})$ [see Eq. (3.29)]. We therefore see that, if $r_{41} > 0$, then $\Gamma > 0$ (< 0) when electrons (holes) are major carriers, leading to the amplification (deamplification) of $I_2(L)$. In the experiment it was found that *electrons* are dominant in both undoped and Cr-doped SI GaAs samples.

Figures 3.10 and 3.11 show the experimental results of the Γ dependence on grating period in the undoped and Cr-doped SI GaAs samples. The dotted lines correspond to the theoretical least square fits with the experimental data. The relevant materials constants used in the theoretical fits are shown in Table 3.3. The estimated deep level densities at room temperature are shown in Table 3.4. In Fig. 3.11 and Table 3.3 two possible cases (i.e., that 1)the number densities of $EL2^0$ are

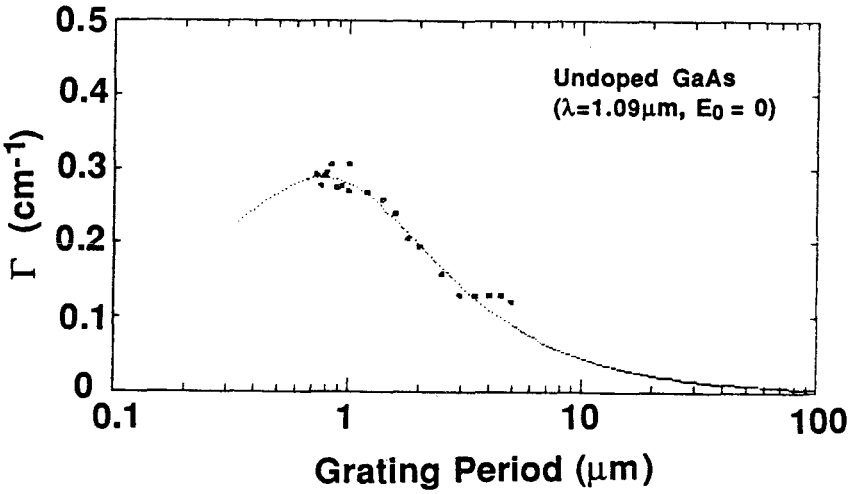

Figure 3.10 Two-beam coupling gain coefficient at room temperature versus grating period in undoped SI GaAs. The experiment was performed at $\lambda = 1.09\,\mu$m and with $E_0 = 0$. The dotted curve corresponds to the least square fit with the experimental data when $N_{EL^0} = 1.46 \times 10^{16}$ cm^{-3}. The standard deviation of the fit is 0.015.

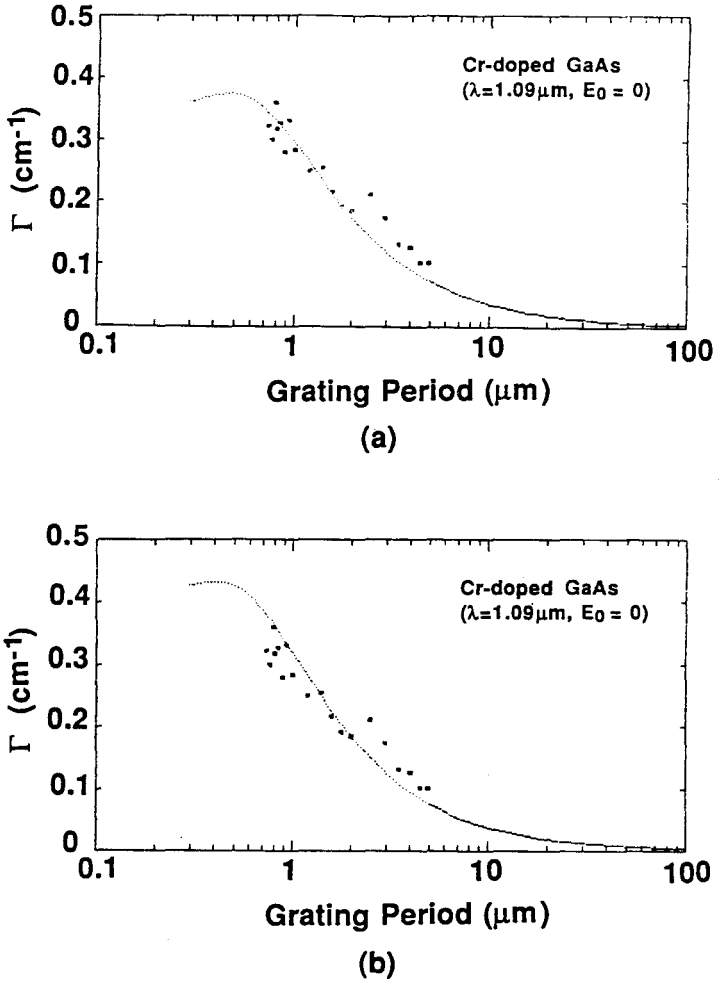

Figure 3.11 Two-beam coupling gain coefficient at room temperature versus grating period in Cr-doped SI GaAs. The experiment was performed at $\lambda = 1.09 \mu m$ and with $E_0 = 0$. The dotted curves correspond to the least square fits with the experimental data when (a) $N_{EL2^0} = 1.46 \times 10^{16}$ cm^{-3} and (b) $N_{EL2} = N_{EL2^0} + N_{EL2^+} = 1.58 \times 10^{16}$ cm^{-3} are assumed. The standard deviations of the fits are (a) 0.027 and (b) 0.03.

Table 3.3 Relevant material constants used for the theoretical curves in Figs. 3.10 and 3.11.

Material Constants	Values	References
ϵ_s	12.9	[3.67]
μ_e	$5800 cm^2/V \cdot s$	[3.67]
μ_h	$400 cm^2/V \cdot s$	[3.86]
s_e	$1.0 \times 10^{-16} cm^2$	[3.91]
s_h	$0.8 \times 10^{-17} cm^2$	[3.92]
γ_e	$2 \times 10^{-8} cm^3/s$	[3.86]
γ_h	$2 \times 10^{-8} cm^3/s$	[3.86]

Table 3.4 Estimated deep level densities in the undoped and Cr-doped SI GaAs samples at room temperature.

The undoped SI GaAs sample

$N_{EL2^0} = 1.46 \times 10^{16} cm^{-3}$

$N_{EL2+} = 1.22 \times 10^{15} cm^{-3}$

The Cr – doped SI GaAs sample

Case 1 [where N_{EL2+} (GaAs:Cr) = N_{EL2+} (undoped GaAS) = $1.46 \times 10^{16} cm^{-3}$]

$N_{Cr^{3+}} = 5.3 \times 10^{15} cm^{-3}$

$N_{Cr^{2+}} < 2.65 \times 10^{14} cm^{-3}$

$N_{EL2+} = 2.92 \times 10^{15} cm^{-3}$

Case 2 [where N_{EL2}(GaAs:Cr) = $N_{EL2^0} + N_{EL2+} = 1.58 \times 10^{16} cm^{-3} = N_{EL2}$ (undoped GaAs)]

$N_{Cr^{3+}} = 8.17 \times 10^{15} cm^{-3}$

$N_{Cr^{2+}} < 4.09 \times 10^{14} cm^{-3}$

$N_{EL2+} = 3.95 \times 10^{15} cm^{-3}$

---

the same and 2)the total number densities of EL2 are the same in both samples) are considered for the estimation of deep level densities in the Cr-doped sample [also see Eq. (3.26*b*)].

It is seen from Fig. 3.10 that the general tendency of Γ as a function of grating period and the optimum grating period at the maximum Γ (i.e., the Debye screening length l_{se} given by Eq. (2.10*a*), also see Fig. 2.3) are consistent with the result reported previously [3.67]. In Fig. 3.11 we also observe the similar dependence of Γ on grating period. But it is seen that l_{se} of the Cr-doped sample is shorter than that of the undoped sample. This may be attributed to the fact that, as is seen in Table 3.4, N_{EL2+} in the Cr-doped sample is larger than that in the undoped sample due to the reaction given by Eq. (3.23). This leads to the shorter l_{se} in the Cr-doped sample. (Note that $l_{se} \propto 1/\sqrt{N_{EL2+}}$ in this case.) From Table 3.4 we see that the estimated values for the undoped sample (i.e., $N_{EL2^0} = 1.46 \times 10^{16}\text{cm}^{-3} \gg N_{EL2+} = 1.22 \times 10^{15}\text{cm}^{-3}$ so that the sample tends to be reduced) are consistent with the previous observations [3.67,86]. We also see from Table 3.4 that the estimated values for the Cr-doped sample $N_{EL2^0} > N_{Cr^{3+}} > N_{EL2+} \gg N_{Cr^{2+}}$ imply the dominant electron transport. This is consistent with the result of the sign of the dominant carriers.

The response time for the rise and decay in two-beam coupling was found to be shorter than 1 msec. in both samples when $I_0 = 0.9\ \text{W/cm}^2$. We note that the measurement of the response time in the two-beam coupling and/or the four-wave mixing configuration offers another method for the estimation of the deep level densities [3.85].

Finally, two comments on this experiment should be stressed. First, it is relatively difficult to find the optimum grating period or l_{se} that gives information on the number densities of photorefractive species. This is because the optimum grating period in this case is less than 1 μm, which is difficult to achieve in usual

experimental situations. This limitation may be obviated by putting a sample in an index-matching liquid so as to obtain shorter grating periods. Second, in our Cr-doped SI GaAs sample we were unable to observe either the significant simultaneous transport or the hole-dominant transport at room temperature. However, it may still be possible to obtain these transport phenomena with this sample by changing temperatures, since the temperature change causes a redistribution of electrons and holes among the EL2 and Cr deep levels at thermal equilibrium.

3.5.4 Enhancement of the two-beam coupling gain

One of the most important applications in photorefractive materials is the generation of self-pumped phase conjugation [3.65]. In particular, photorefractive semiconductors are attractive for this purpose because of fast responses and infrared sensitivities. This self-pumping operation usually requires the two-beam coupling gain Γl larger than unity [3.65]. Table 3.5 shows the two-beam coupling gain coefficients of $BaTiO_3$, SBN, and (undoped and Cr-doped) SI GaAs at several wavelengths. It is seen that the net gain coefficients $|\Gamma| - \alpha$ of SI GaAs are negative because of the small electrooptic coefficient r_{41} and a relatively large absorption at operating wavelengths. This means that the self-pumping operation cannot be realized in SI GaAs, nor in other photorefractive semiconductor materials. In order to overcome this problem, several methods (such as the DC electric field, AC electric field and moving fringe methods) of enhancing the two-beam coupling gain should be employed. (The physical reasons for these enhancement methods have already been described in Chapter 2.)

Figure 3.12 shows the theoretical results of Γ of the undoped SI GaAs as a function of grating period when the enhancement using (a) the DC electric field, (b) the AC electric field and (c) the moving fringe is made. Equations (2.14), (2.24),

Table 3.5 Two-beam coupling gain coefficients of several photorefractive materials[a,b].

Material	λ (nm)	$\lvert\Gamma\rvert$ (cm^{-1})	α (cm^{-1})	$\lvert\Gamma\rvert - \alpha$ (cm^{-1})
$BaTiO_3$	514.5	4.0	3.0	1.0
($I_0 = 100mW/cm^2$)	840	1.8	0.2	1.6
	1090	1.0	~ 0	1.0
SBN : 75	514.5	6.0	0.8	5.2
($I_0 = 100mW/cm^2$)	840	0.5	~ 0	0.5
	1090	~ 0	~ 0	~ 0
undoped SI GaAs	1090	0.3	1.2	−0.9
($I_0 = 900mW/cm^2$)				
Cr-doped SI GaAs	1090	0.37	1.8	−1.43
($I_0 = 900mW/cm^2$)				

[a] The data for $BaTiO_3$ and SNB:75 are taken from Ref.[3.62].

[b] All the data are measured at room temperature.

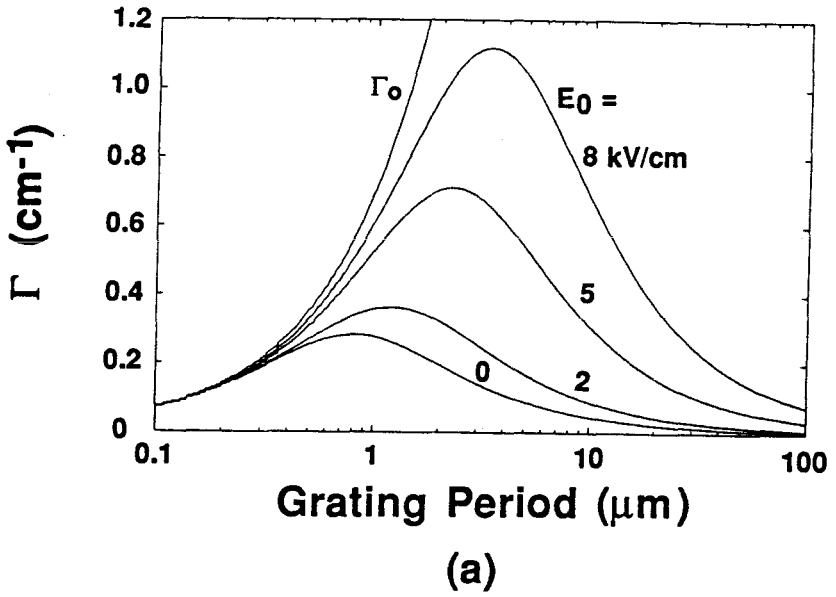

Figure 3.12 Two-beam coupling gain coefficient Γ of undoped SI GaAs versus grating period at T=300K and $\lambda = 1.09\,\mu$m. (a) The DC electric field (E_0) method. Γ_0 denotes the two-beam coupling gain coefficient when $\Xi_{sc} = E_{qe}$.

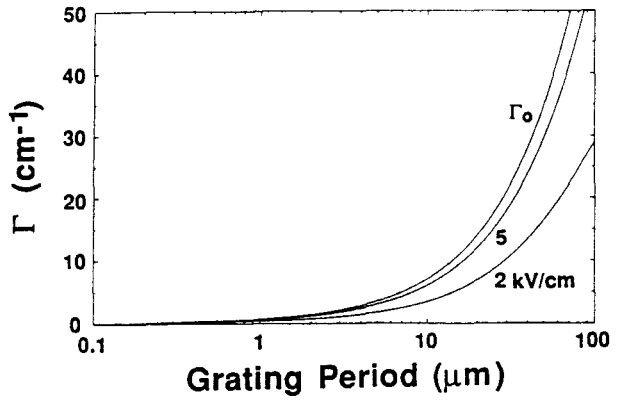

(b)

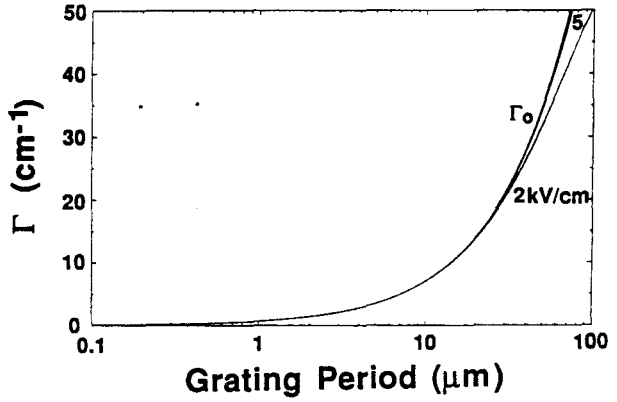

(c)

Figure 3.12 (Continued.) (b) The AC electric field method when the AC rectangular electric field ($\pm E_0$) is applied. (c) The moving fringe method, where the optimum fringe velocity is used for each grating period. Γ_0 denotes the two-beam coupling gain coefficient when $\Xi_{sc} = E_{qe}$.

and (2.28) are used in the calculation together with the relevant material parameters shown in Tables 3.3 and 3.4. In Fig. 3.12(a) it is seen that Γ increases as the DC electric field increases, but its enhancement effect is less efficient than the other two methods. This is so because the application of the DC electric field induces additional phase shifts in the space-charge field so that the phase shift deviates from $\pm\pi/2$. Moreover in long transport length materials such as GaAs and BSO the actual DC electric field inside the crystal tends to be lower than the applied DC electric field due to the migration of charge carriers to the electrodes. (We note that this problem does not occur in the AC electric field method.) In Fig. 3.12(b) the significant enhancement of Γ is seen because the space-charge field approaches E_{qe} by this method. In Fig. 3.12(c) we also see the enhancement of Γ for the same reason as above. With both the AC electric field method and the moving fringe method Γ can exceed 1 cm^{-1}, leading possibly to the generation of self-pumped phase conjugation.

Figure 3.13 shows the response time of the space-charge field as a function of grating period for E_0=0, 2, 5 and 8 kV/cm. We see the strong dependence on grating period when $E_0 = 0$. This is typical in long drift length materials [3.95]. When $E_0 \neq 0$, the response time becomes less sensitive to grating period because the drift transport becomes dominant so that electrons move many grating periods and the effect of the grating period is unimportant. We also note that when $E_0 \neq 0$ the response time is still of the order of 1 msec at $I_0 = 100$ mW/cm^2. This is at least 100 times faster than the response time in ferroelectric oxides such as $BaTiO_3$ and SBN.

3.5.5 Temperature dependence of the two-beam coupling gain

Because of narrow band gaps and large mobilities in semiconductors, it is

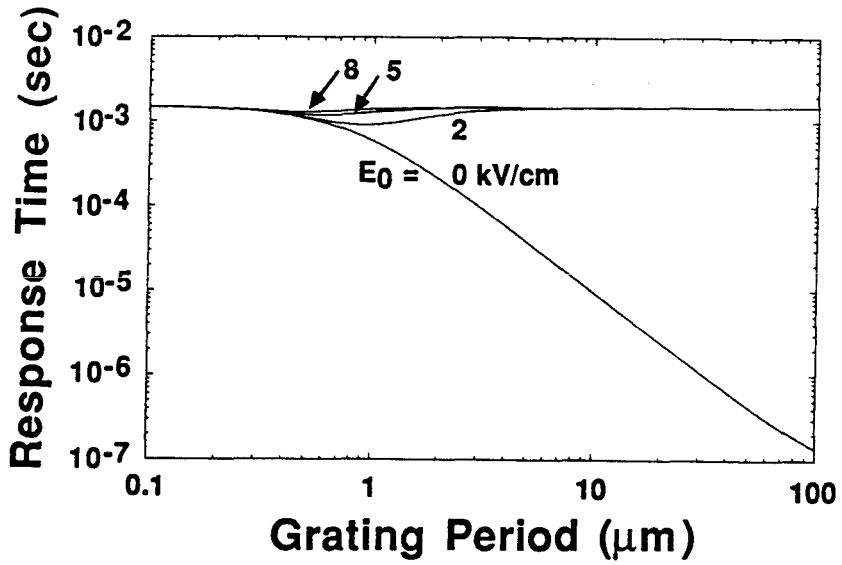

Figure 3.13 Response time of the space-charge field versus grating period in undoped SI GaAs for DC electric fields of E_0=0, 2, 5 and 8 kV/cm at T=300K and $\lambda = 1.09\,\mu$m when the intensity I_0 is 100 mW/cm^2 and $\tau_{de} = 4 \times 10^{-8}$ sec.

expected that the temperature dependence of the space-charge field strength (and therefore the two-beam coupling gain) is significant. An experiment of the temperature and intensity dependence of the two-beam coupling gain in Cr-doped SI GaAs was reported previously by Cheng and Partovi [3.73]. They observed a strong temperature dependence of the gain over a relatively narrow range of temperature (295K–386K) and concluded that this dependence could be attributed to the competing effects of the dark- and photo-conductivities. In order to understand this effect better and to optimize two-beam coupling conditions, in this subsection we discuss the temperature dependence of the relevant photorefractive parameters in SI GaAs, especially the mobility (μ_e), the recombination coefficient (γ_e), the number density of EL2 (N_{EL2+}) and the thermal ionization rate (β_e) [3.54]. The explicit temperature dependence of these relevant photorefractive parameters is discussed in Appendix A.

Numerical evaluations of the temperature dependence of the two-beam coupling gain in undoped SI GaAs are made by using Eqs.(A2), (A4), (A6) and (A12) given in Appendix A. Figure 3.14 shows the temperature dependence of the relevant material parameters. It is seen that β_e/s_e is very sensitive to the temperature change (about 10^{11} changes from T=200K to T=400K), while the other parameters change more or less by a factor of 2. We thus expect that the competing effect of the dark- and photo-conductivities, related to the parameter β_e/s_e, plays a major role in the temperature dependence of the two-beam coupling gain.

Figure 3.15 shows the calculated temperature dependence of the two-beam coupling gain coefficient in undoped SI GaAs (a) without enhancement (E_0=0) and with (b) the DC electric field, (c) the AC electric field and (d) the moving fringe. It is seen that the temperature dependence becomes significant in all the cases as the input intensity decreases and the temperature increases in the range T>300K.

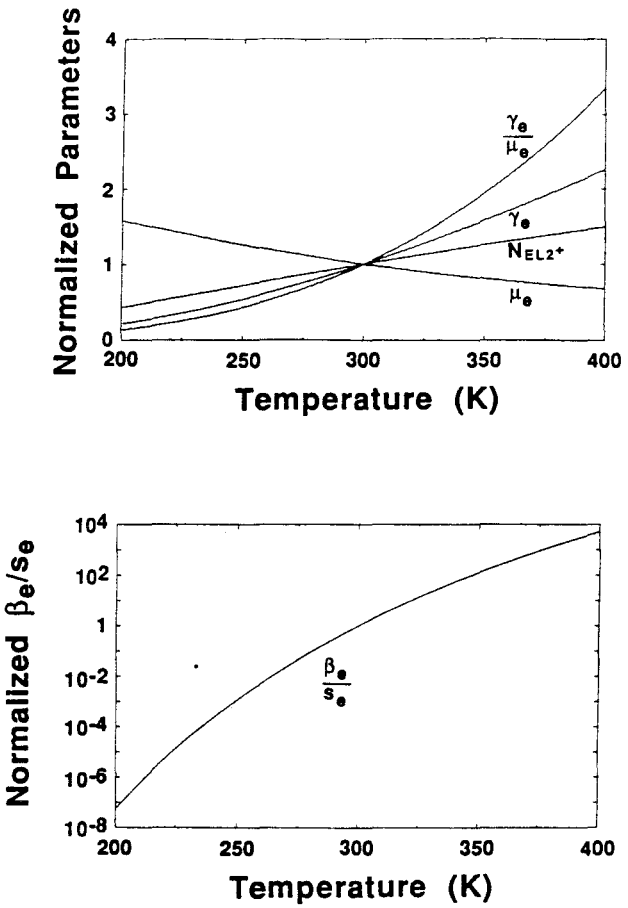

Figure 3.14 Calculated temperature dependence of the relevant material parameters. All the values are normalized by those at T=300K, i.e., N_{EL2+} = 1.22×10^{15} cm^{-3}, $\gamma_e = 2 \times 10^{-8}$ cm^3/sec, $\mu_e = 5800$ $cm^2/V.sec$, β_e/s_e = 3×10^{14} photons/cm^2.sec, see Table 3.3.

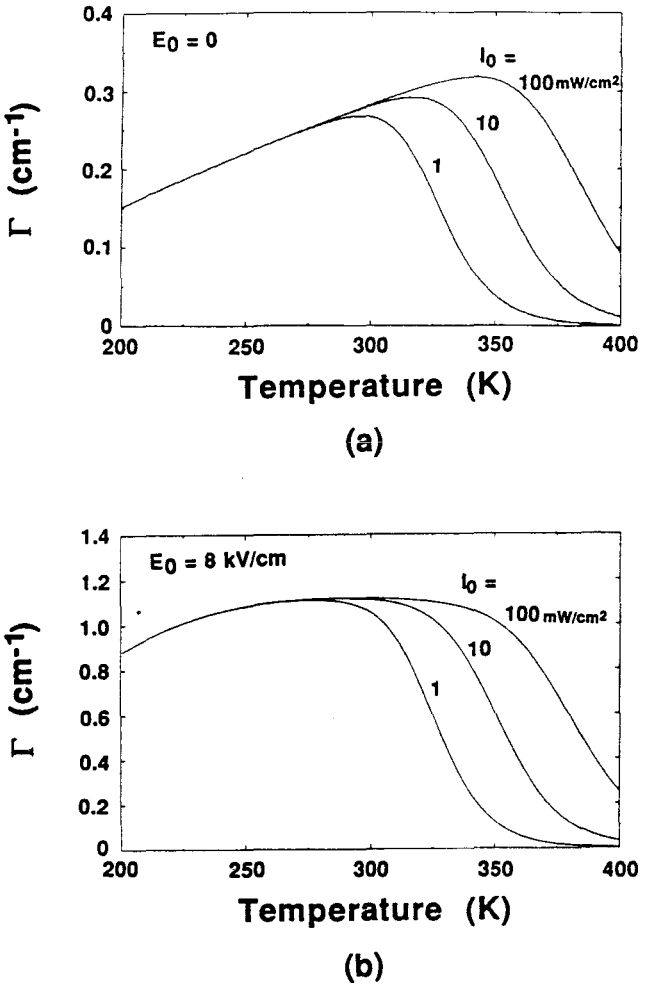

Figure 3.15 Calculated temperature dependence of the two-beam coupling gain coefficient in undoped SI GaAs (a) without enhancement (E_0=0) and (b) with the DC electric field for I_0=1, 10 and 100 mW/cm^2. In (a) and (b) grating periods of 0.8 and 3.5μm are considered, respectively.

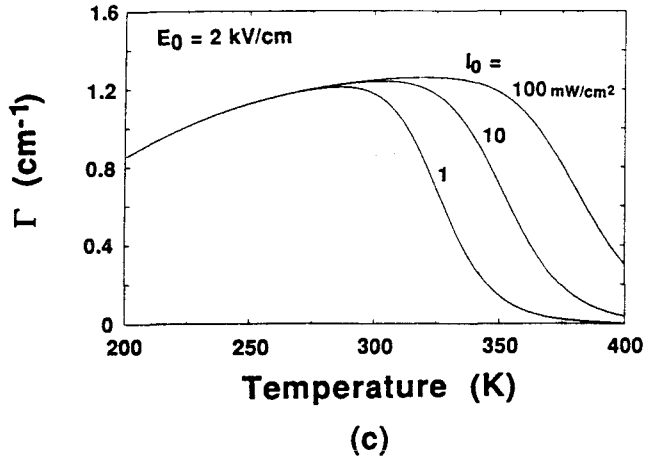

(c)

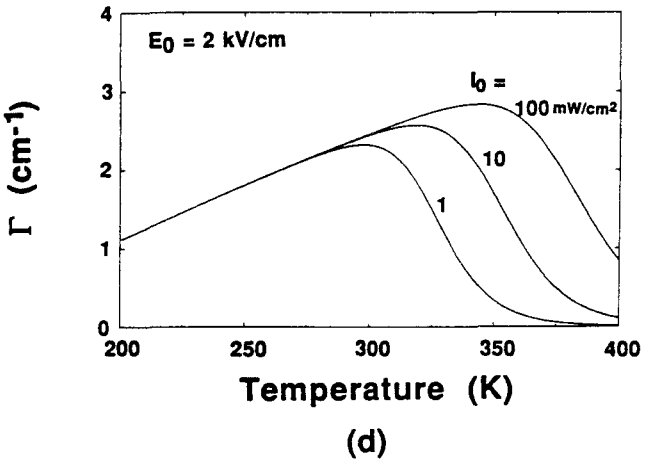

(d)

Figure 3.15 (Continued.) Calculated temperature dependence of the two-beam coupling gain coefficient in undoped SI GaAs with (c) the AC (rectangular) electric field, and (d) the moving fringe for I_0=1, 10 and 100 (mW/cm^2). In (c) and (d) a grating period of 3.5 μm is considered with the optimum fringe velocity for (d).

At higher intensities (I_0 = 100 mW/cm^2) the maximum gain coefficient is obtained at about T = 350K.

The general behavior of the gain coefficient can be explained as follows. In the diffusion dominant case (E_0=0), it is found that

$$\Gamma \propto \frac{E_D}{1+\beta_e\hbar\omega/s_eI_0} \propto \frac{T}{1+aT^2e^{-(E_D+E_\sigma)/k_BT}}, \tag{3.31}$$

where a is constant, and E_D and E_σ are the deep level energy of the neutral deep level (e.g., the EL2^0 level) and the thermal activation energy of the capture cross-section of the ionized deep level (e.g., the EL2$^+$ level), respectively (see Appendix A). From Eq.(3.31) we see that $\Gamma \propto T$ for lower T [$<(E_D+E_\sigma)/k_B$] while $\Gamma \propto 1/T$ for higher T [$>(E_D+E_\sigma)/k_B$]. This explains the behavior seen in Fig. 3.15(a). In the drift dominant case, it is found that

$$\Gamma \propto \frac{E_{qe}}{1+\beta_e\hbar\omega/s_eI_0} \propto \frac{T^\kappa}{1+aT^2e^{-(E_D+E_\sigma)/k_BT}}, \tag{3.32}$$

where κ is between 0 and 2. From Eq. (3.32) we see that $\Gamma \propto T^\kappa$ for lower T [$<(E_D+E_\sigma)/k_B$] and $\Gamma \propto T^{\kappa-2}$ for higher T [$>(E_D+E_\sigma)/k_B$]. This behavior is seen in Figs. 3.15(b) - 3.15(d).

Figure 16 shows a comparison of our model with Cheng and Partovi's experiment [3.75] using Cr-doped SI GaAs. Since no specific value of material parameters is available in their paper, Eq. (3.31) is used to fit their experimental data. An excellent fit is seen in this figure when $E_D + E_\sigma$ = 0.713 eV and $\beta_e\hbar\omega/s_e\{=\hbar\omega\sigma_d[s_e(N_D/N_A-1)\gamma_e e\mu_e]^{-1}\}$=1.25 mW/cm^2 at T=300K. Although a detailed comparison is not appropriate in this case, it seems consistent with our

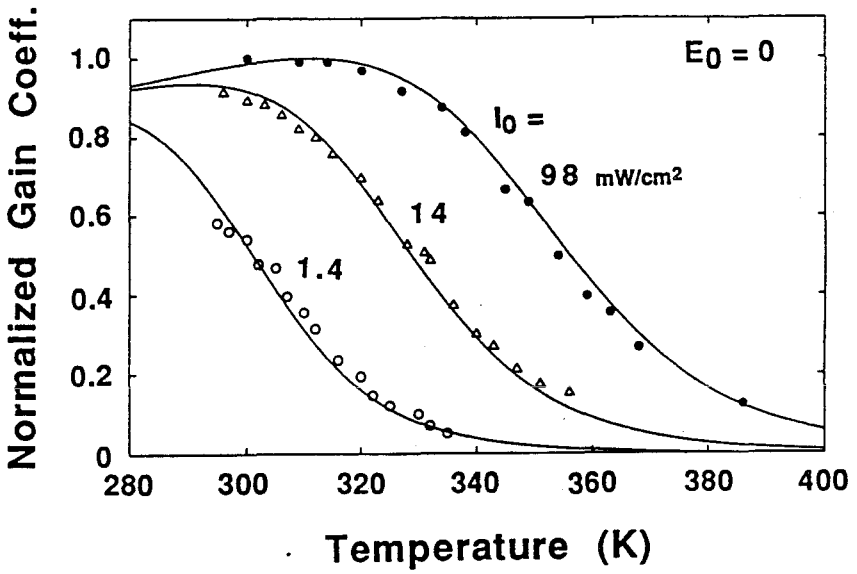

Figure 3.16 Comparison of the present model with the experimental data ($\circ, \triangle, \bullet$) of the two-beam coupling gain coefficient in Cr-doped SI GaAs. In the figure a normalized gain coefficient (normalized by the saturated value of the gain coefficient at T=300K) is used. The solid curves are the theoretical curves, calculated from Eq.(3.31) with $\hbar\omega\beta_e/s_e I_0$=0.9, 0.09 and 0.013 at T=300K which correspond to the experimental conditions of I_0=1.4, 14 and 98 mW/cm^2, respectively. In the experiment SI GaAs doped with a Cr concentration in the high 10^{15} cm^{-3} and $\sigma_d \approx 10^{-8}(\Omega\text{cm})^{-1}$ was used. Also, a grating period of about 1.3μm without an applied electric field (E_0=0) was used at $\lambda = 1.15$ μm. (Experimental data are taken from Ref. [3.37].)

model when $s_e = 3 \times 10^{-15}$ cm^2 given by Bylsma *et al.* [3.98] (instead of the value of s_e given in Table 3.3) is assumed. In this case we obtain $E_D = 0.46$ eV (from the valence band) when the hole transport is assumed and $E_\sigma = 0.25$ eV is used (see Appendix A). This value is consistent with the value reported so far (see Fig. 3.5). Therefore we speculate the possible hole transport in their sample.

In Fig. 3.17 we show the calculated temperature dependence of the time constants given by Eqs. (2.9) for two different intensities I_0=1 and 100 mW/cm^2. Figure 3.18 illustrates the calculated temperature dependence of the response time of the space-charge field in undoped SI GaAs for E_0=0 and 8 kV/cm. It is seen that the response time increases as T increases until T$\approx$ 300K when I_0=100 mW/cm^2 and T$\approx$ 360K when I_0=1 mW/cm^2, and then it decreases rapidly. This is because the response time is expressed as $\tau_{de} f(\tau_{De}, \tau_{Ee}, \tau_{oe}, \tau_{Ie})$ [see Eq. (2.17*a*)] and its behavior is mainly determined by τ_{de}, which is inversely proportional to the dark conductivity σ_d, and thus decreases rapidly as T increases in the range (T> 300K).

In this subsection, we have discussed the temperature dependence of the two-beam coupling gain coefficient and the response time. It is found from the numerical results that it is better to operate undoped SI GaAs at higher temperatures (T$\approx$ 350K) in order to obtain higher gain coefficient and faster response time. This improvement is especially significant when the input intensity is low (I_0 < 100 mW/cm^2). This low intensity input occurs when long wavelength semiconductor lasers are used for this purpose. We have also found that, although semiconductors have narrower bandgaps and shallower deep levels (because of the infrared response) than those of ferroelectric oxides, such as $BaTiO_3$ and SBN, the effect of temperature is less significant than that in the ferroelectric oxides. The main reason is as follows:

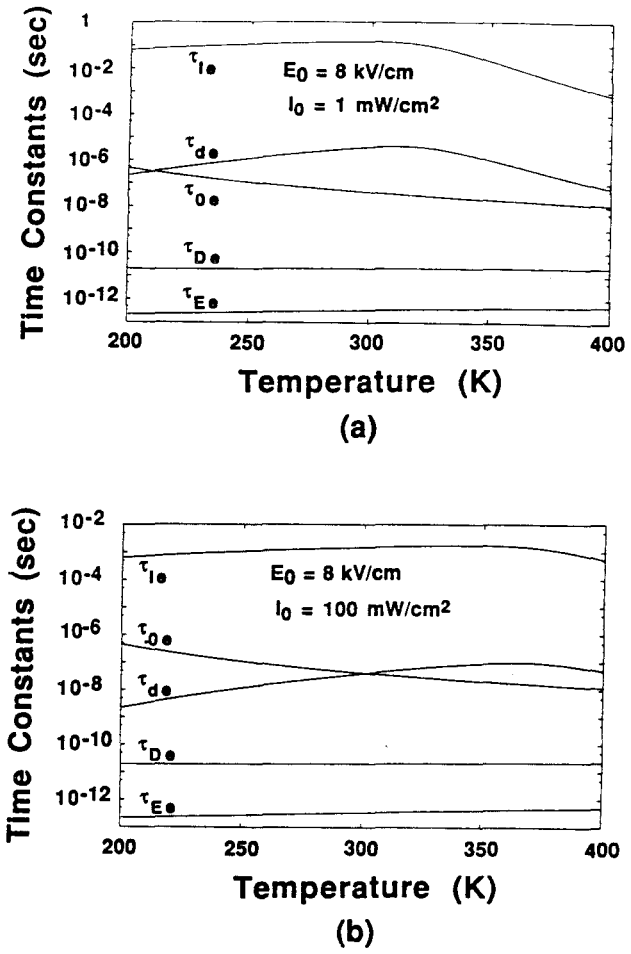

Figure 3.17 Calculated temperature dependence of various time constants defined by Eqs.(2.9) for (a) I_0=1 and (b) 100 mW/cm^2. A DC electric field E_0 of 8 kV/cm and grating period of 3.5 μm are considered for both cases.

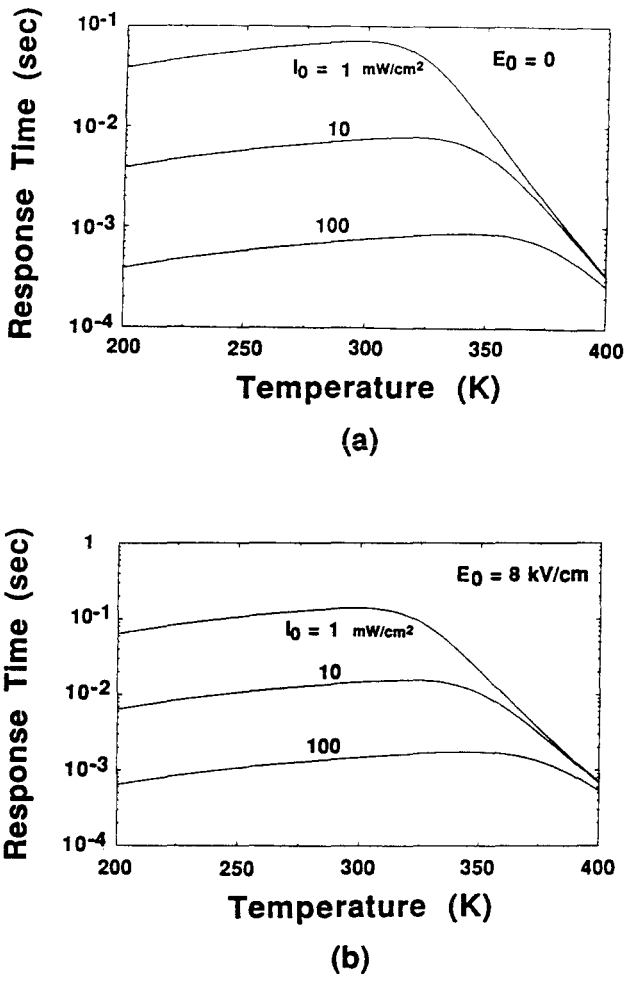

Figure 3.18 Calculated temperature dependence of the response time of the space-charge field in undoped SI GaAs for DC electric fields of (a) 0 and (b) 8 kV/cm. The grating periods are (a) 0.8 μm and (b) 3.5 μm, respectively. Three intensities of I_0=1, 10 and 100 mW/cm^2 are considered.

The parameter β_e/s_e is rewritten as

$$\frac{\beta_e}{s_e} = \frac{1}{e}\sigma_d\left(\frac{\gamma_e}{\mu_e s_e}\right)\left(\frac{N_D^+}{N_D - N_D^+}\right).$$

At room temperature $\sigma_d = 10^{-8}(\Omega\text{cm})^{-1}$ for undoped SI GaAs and $10^{-12}(\Omega\text{cm})^{-1}$ for $BaTiO_3$, $N_D^+/(N_D - N_D^+) \approx 10^{-1}$ for both materials, and $\gamma_e/(\mu_e s_e) = 3 \times 10^4$ V/cm^2 for undoped SI GaAs and $10^{11} - 10^{12}$ V/cm^2 for $BaTiO_3$. Because of a large difference of the values of $\gamma_e/(\mu_e s_e)$ between these two materials, the competing effect of the dark- and photo-conductivities is much more significant in $BaTiO_3$ than in undoped SI GaAs. (Note that since DC dielectric constants ϵ_s of $BaTiO_3$ and SBN are strongly dependent on temperature in the range of our interest, this effect should also be taken into account for these materials.) Finally we speculate that the strong temperature dependence of the two-beam coupling gain (even a change of its sign at some temperature) may be seen in Cr-doped SI GaAs that has the simultaneous electron and hole transport. This effect can be modeled by incorporating the temperature dependence of N_{EL2^0}/N_{EL2^+} and $N_{Cr^{2+}}/N_{Cr^{3+}}$ together with the consideration of the charge neutrality condition between the EL2 and Cr deep levels.

APPENDIX A

Temperature Dependence of Photorefractive Parameters

Look [3.86] discussed the temperature dependence of material constants in SI GaAs in order to understand electrical properties of SI GaAs. In what follows we derive the temperature dependence of photorefractive parameters according to his treatment.

a) Mobility: μ_e

From Matthiessen's approximation [3.86] the temperature dependence of the mobility is expressed by

$$\mu_e^{-1} = AT^{-3/2} + BT^n, \qquad (A1)$$

where A and B are constants. In the right-hand side of Eq. (A1) the dependence of $T^{-3/2}$ comes from the ionized impurity scattering at low temperatures (below 77K), while the dependence of T^n comes from the lattice scattering at high temperatures (above 77K) where $n \approx 3/2$ [3.94]. By using the fact that the peak of μ_e occurs around T=125K in SI GaAs [3.86] and μ_e=5800 cm^2/V.sec at T=300K (see Table 3.3), we obtain the following functional form of μ_e:

$$\mu_e = \frac{3.232 \times 10^7}{T^{3/2} + (125)^3 T^{-3/2}} \quad cm^2/V.sec, \qquad (A2)$$

where T is measured in K.

b) Recombination coefficient: γ_e

The recombination coefficient γ_e can be rewritten as

$$\gamma_e = \sigma_n v_{th}, \qquad (A3)$$

where σ_n is the capture cross-section of the $EL2^+$ level for electrons and $v_{th}(=\sqrt{8k_BT/\pi m^*})$ is the mean thermal velocity of electrons. By allowing σ_n to be "thermally activated", i.e., $\sigma_n(T) = \sigma_n(\infty)e^{-E_\sigma/k_BT}$, where E_σ=0.07 eV for undoped SI GaAs and 0.25 eV for Cr-doped SI GaAs [3.86], we have

$$\gamma_e = 1.7 \times 10^{-8}\sqrt{T}e^{-E_\sigma/k_BT} \quad cm^3/sec, \tag{A4}$$

where we use E_σ=0.07 eV and $\gamma_e = 2 \times 10^{-8}$ cm^3/sec at T=300K (see Table 3.3).

c) Number density of $EL2^+$ in the dark: $N_{EL2+}(I_0=0)$

Since EL2 is considered as an impurity donor, N_{EL2+} is obtained by means of the usual theoretical treatment seen in basic solid-state physics textbooks, i.e., by considering the Fermi-Dirac statistics or "the so-called maximum probability method" [3.86]. The result is given by

$$\begin{aligned} N_{EL2+} &= N_{EL2} - N_{EL2^0} \\ &= N_{EL2} - \frac{N_{EL2}}{1 + (g_0/g_1)e^{(E_F - E_D)/k_BT}} \\ &= \frac{N_{EL2}}{1 + (g_1/g_0)e^{(E_D - E_F)/k_BT}}, \end{aligned} \tag{A5}$$

where g_0 and g_1 are the degeneracy factors for the $EL2^+$ and $EL2^0$ levels, respectively, and E_F and E_D are the Fermi energy and the energy of the $EL2^0$ level, respectively, measured from the conduction band. The value of g_1/g_0 in Eq. (A5) is 2 because of the two spin states at the $EL2^0$ level [3.86]. The temperature dependence of the energy E_D is approximated by $E_D = 0.76 - 2.5 \times 10^{-4}T$ (eV) for SI GaAs [3.96], but this temperature dependence is negligible in the range of our interest (200K<T<400K). So we assume that E_D and E_F are constant in 200k<T<400K. The energy difference $E_F - E_D$ at room temperature is found by using Eq.(A5) together with the data of N_{EL2^0} and N_{EL2+} at T=300K (see Table 3.4). The result is

$$N_{EL2+} = \frac{N_{EL2}}{1 + 2e^{0.0465/k_BT}} \quad cm^{-3}, \tag{A6}$$

where $N_{EL2} = 1.704 \times 10^{16}$ cm^{-3}.

d) Thermal ionization rate: β_e

At thermal equilibrium in the dark, Eq. (2.2a) is written as

$$\frac{\partial N_{EL2+}}{\partial t} = 0 = \beta_e(N_{EL2} - N_{EL2+}) - \gamma_e n N_{EL2+}. \qquad (A7)$$

Thus

$$N_{EL2+} = \frac{N_{EL2}}{1 + n\gamma_e/\beta_e}. \qquad (A8)$$

We neglect the recombination of electrons in the conduction band with holes in the valence band so that n is thermally excited from the $EL2^0$ level to the conduction band. We also assume that the Fermi energy is larger than k_BT, which is appropriate in SI GaAs. Then it is easy to show that

$$n \approx N_c e^{-E_F/k_BT}, \qquad (A9)$$

where $N_c = 2(2\pi m^* k_B T)^{3/2}/h^3$. Substitution of Eq. (A9) into Eq. (A8) yields to

$$N_{EL2+} = \frac{N_{EL2}}{1 + (N_c\gamma_e/\beta_e)e^{-E_F/k_BT}}. \qquad (A10)$$

Comparison of Eq.(A10) with Eq.(A5) immediately gives

$$\begin{aligned} \beta_e &= (g_0/g_1)N_c\gamma_e e^{-E_D/k_BT} \\ &= CT^2 e^{-(E_D+E_\sigma)/k_BT}, \end{aligned} \qquad (A11)$$

where C is constant. Using the fact that the dark conductivity $\sigma_d = 1 \times 10^{-8}(\Omega\text{cm})^{-1}$ at room temperature and $\beta_e/s_e = \sigma_d[s_e(N_{EL2} - N_{EL2+})\tau_{Re}e\mu_e]^{-1}$ at thermal equilibrium in the dark, we obtain

$$\frac{\hbar\omega\beta_e}{s_e} = 5 \times 10^7 T^2 e^{-0.83/k_BT} \ \text{mW/cm}^2 \text{ at } \lambda = 1.09\,\mu\text{m}, \qquad (A12)$$

where s_e is assumed to be constant in the range of our interest (200K < T < 400K) and $\tau_{Re} = 1/(\gamma_e N_{EL2+}) = 3 \times 10^{-8}$ sec. at T=300K is used. When

$\beta_e = s_e I_0/\hbar\omega$, i.e., the number of photoexcited electrons per unit time is the same as that of thermally excited electrons per unit time, it is found to be I_0=3×10^{14} photons/cm^2.sec = 0.06 mW/cm^2 at $\lambda = 1.09\,\mu$m at room temperature. For $BaTiO_3$, using $N_D = 10^{17} - 10^{18}$ cm^{-3}, $N_A = 2 \times 10^{16}$ cm^{-3}, $\gamma_e = 5 \times 10^{-8}$ cm^3/sec, $s_e = 10^{-19} - 10^{-18}$ cm^2 and $\sigma_d = 1.3 \times 10^{-12}$ sec [3.97], we find $I_0 = 2 \times 10^{15} - 2 \times 10^{17}$ photons/cm^2.sec = 0.8–80 mW/cm^2 at $\lambda = 0.5\,\mu$m at room temperature.

References for Chapter 3

3.1. D.W. Vahey, J. Appl. Phys. **46**, 3510 (1975).

3.2. N.V. Kukhtarev, V.B. Markov, S.G. Odulov, M.S. Soskin, and V.L. Vietskii, Ferroelectrics **22**, 961 (1979).

3.3. J. Feinberg, J. Opt. Soc. Am. **72**, 46 (1982).

3.4. T. Tschudi, A. Herden, J. Goltz, H. Klumb, F. Laeri, and F. Albers, IEEE J. Quantum Electron. **QE-19**, 1493 (1986).

3.5. J.O. White, M. Cronin-Golomb, B. Fischer, and A. Yariv, Appl. Phys. Lett. **40**, 450 (1982).

3.6. M. Cronin-Golomb and A. Yariv, J. Appl. Phys. **57**, 4906 (1985).

3.7. A.E. Chiou and P. Yeh, Opt. Lett. **10**, 621 (1985); S.-K. Kwong and A. Yariv, Appl. Phys. Lett. **48**, 564 (1986).

3.8. A. Yariv and P. Yeh, *Optical Waves in Crystals* (Wiley, New York, 1984).

3.9. D. Einerl, IEEE J. Quantum Electron. **QE-23**, 2104 (1987).

3.10. S.I. Stepanov, M.P. Petrov, and A.A. Kamshilin, Sov. Tech. Phys. Lett. **3**, 345 (1978).

3.11. N.V. Kukhtarev and S.G. Odulov, Sov. Tech. Phys. Lett. **6**, 503 (1980).

3.12. N.V. Kukhtarev, Sov. J. Quantum Electron. **11**, 878 (1981).

3.13. S. Odoulov, K. Belabaev, and I. Kiseleva, Opt. Lett. **10**, 31 (1985).

3.14. K. Belabaev, I. Kiseleva, V. Obukhovski, S. Odoulov, and R.A. Taratuta, Sov. Solid State Phys. **28**, 321 (1986).

3.15. D.A. Temple and C. Warde, J. Opt. Soc. Am. B**3**, 337 (1986); *ibid* B**4**, 1335 (1987).

3.16. R.A. Rupp and F.W. Drees, Appl. Phys. B**39**, 223 (1986).

3.17. S.G. Odoulov, J. Opt. Soc. Am. B**4**, 1333 (1987).

3.18. L. Arizmendi and R.C. Powell, J. Appl. Phys. **61**, 2128 (1987).

3.19. V.V. Obukhovskii, A.V. Stoyanov, and V.V. Lemeshko, Sov. J. Quantum Electron. **17**, 64 (1987).

3.20. N.V. Kukhtarev, E. Krätizig, H.C. Külich, and R.A. Rupp, Appl. Phys. B**35**, 17 (1984).

3.21. M.D. Ewbank, P. Yeh, and J. Feinberg, Opt. Commun. **59**, 423 (1986).

3.22. N.V. Bogodaev, Y.S. Kuz'minov, N.V. Kukhtarev, and N.M. Polozkov, Sov. Phys.-Levedev Inst. Rep. No.5, 17 (1987).

3.23. E. Voit, in *Electro-optic and Photorefractive Materials*, P. Günter ed., Proc. Phys. vol.18 (Springer, Berlin, 1987) p. 246.

3.24. H.C. Külich, R.A. Rupp, H. Hesse, and E. Krätizig, Opt. Quantum Electron. **19**, 93 (1987).

3.25. P. Günter and J.P. Huignard, in *Photorefractive Materials and Their Applications* I, P. Günter and J.P. Huignard eds., Topics in Applied Physics vol. 61 (Springer, Berlin, 1988) p. 7.

3.26. A. Partovi, E.M. Garmire, and L.-J. Cheng, Appl. Phys. Lett. **51**, 299 (1987).

3.27. P. Yeh, J. Opt. Soc. Am. B**4**, 1382 (1987)

3.28. L.-J. Cheng and P. Yeh, Opt. Lett. **13**, 50 (1988).

3.29. J.C. Fabre, J.M.C. Jonathan, and G. Rossen, Opt. Commun. **65**, 257 (1988).

3.30. P. Yeh, J. Opt. Soc. Am. B**5**, 1811 (1988).

3.31. T.Y. Chang, A.E. Chiou, and P. Yeh, J. Opt. Soc. Am. B**5**, 1724 (1988).

3.32. S.V. Miridonov, M.P. Petrov, and S.I. Stepanov, Sov. Tech. Phys. Lett. **4**, 393 (1979).

3.33. M.P. Petrov, S.V. Miridonov, S.I. Stepanov, and V.V. Kulikov, Opt. Commun. **31**, 301 (1979).

3.34. T.G. Pencheva and S.I. Stepanov, Sov. Phys. Solid State **24**, 687 (1982).

3.35. N.V. Kukhtarev, G.E. Dovgalenko, and V.N. Starkov, Appl. Phys. **A33**, 227 (1984).

3.36. A.G. Apostolidis, S. Mallick, D. Rouède, J.P. Herriau, and J.P. Huingnard, Opt. Commun. **56**, 73 (1985).

3.37. J.P. Herriau, J.P. Huignard, A.G. Apostolidis, and S. Mallick, Opt. Commun. **56**, 141 (1985).

3.38. A. Marrakchi, R.V. Johnson, and A.R. Tanguay, Jr., J. Opt. Soc. Am. **B3**, 321 (1986).

3.39. R.V. Johnson and A.R. Tanguay, Jr., Opt. Eng. **25**, 235 (1986).

3.40. P.D. Foote and T.J. Hall, Opt. Commun. **57**, 201 (1986).

3.41. N.V. Kukhtarev, B. Pavlik, and T. Semenets, Phys. Stat. Sol. (a)**94**, 623 (1986).

3.42. G.E. Dovgalenko, N.V. Kukhtarev, S.M. Maevskii, and V.V. Murav'ev, Sov. Tech. Phys. Lett. **12**, 399 (1986).

3.43. S. Mallick, D. Rouède, and A.G. Apostolidis, J. Opt. Soc. Am. **B4**, 1247 (1987).

3.44. S. Mallick and D. Rouède, Appl. Phys. **B43**, 239 (1987).

3.45. M.G. Miteva and S.V. Miridonov, Opt. Quantum Electron. **19**, 37 (1987).

3.46. F. Vachss and L. Hesselink, J. Opt. Soc. Am. **A4**, 325 (1987).

3.47. A. Marrakchi, R.V. Johnson, and A.R. Tanguay, IEEE J. Quantum Electron. **QE-23**, 2142 (1987).

3.48. E. Voit, C. Zaldo, and P. Günter, Opt. Lett. **11**, 309 (1986).

3.49. E. Voit and P. Günter, Opt. Lett. **12**, 769 (1987).

3.50. L.-J. Cheng, G. Gheen, T.-H. Chao, H.-K. Liu, A. Partovi, J. Katz, and E. Garmire, Opt. Lett. **12**, 705 (1987).

3.51. L.-J. Cheng and G. Gheen, J. Appl. Phys. **62**, 3991 (1987).

3.52. G. Gheen and L.-J. Cheng, Appl. Phys. Lett. **51**, 1481 (1987).

3.53. We note that when there exist multiple photorefractive gratings in the crystal (e.g., the case shown in Fig. 3.3) the treatment of the space-charge electric field formation should include the effect of multiple interference patterns (i.e., multiple spatial Fourier components of intensity variations).

3.54. Y. Tomita and A. Yariv, unpublished.

3.55. P. Yeh, J. Opt. Soc. Am. B**2**, 1924 (1985).

3.56. Y.H. Ja, Opt. Quantum Electron. **14**, 547 (1982); *ibid* **15**, 529, 539 (1983); Appl. Phys. B**33**, 51 (1984); *ibid* B**33**, 161 (1984).

3.57. P. Yeh, Opt. Commun. **45**, 323 (1983); J. Opt. Soc. Am. **73**, 1268 (1983).

3.58. K.R. MacDonald and J. Feinberg, Opt. Commun. **50**, 146 (1984).

3.59. M.Z. Zha and P. Günter, Opt. Lett. **10**, 187 (1985).

3.60. L. Solymar and J.M. Heaton, Opt. Commun. **51**, 76 (1984).

3.61. J.M. Heaton and L. Solymar, Opt. Acta **32**, 397 (1985).

3.62. N.V. Kukhtarev, V. Markov, and S. Odulov, Opt. Commun. **23**, 338 (1977).

3.63. G.A. Rakuljic, Ph.D. Dissertation (California Institute of Technology, Pasadena, California 1984, unpublished).

3.64. B. Fischer, J.O. White, M. Cronin-Golomb, and A. Yariv, Opt. Lett. **11**, 239 (1986).

3.65. M. Cronin-Golomb, B. Fischer, J.O. White, and A. Yariv, IEEE J. Quantum Electron. **QE-20**, 12 (1984).

3.66. A.M. Glass, A.M. Johnson, D.H. Olson, W. Simpson, and A.A. Ballman,

Appl. Phys. Lett. **44**, 948 (1984).

3.67. M.B. Klein, Opt. Lett. **9**, 350 (1984).

3.68. J. Strait and A.M. Glass, J. Opt. Soc. Am. B**3**, 342 (1986).

3.69. R.B. Bysma, P.M. Bridenbaugh, D.H. Olson, and A.M. Glass, Appl. Phys. Lett. **51**, 889 (1987).

3.70. A.M. Glass, M.B. Klein, and G.C. Valley, Electron. Lett. **21**, 220 (1985).

3.71. J. Strait and A.M. Glass, Appl. Opt. **25**, 338 (1986).

3.72. G. Albanese, J. Kumar, and W.H. Steier, Opt. Lett. **11**, 650 (1986).

3.73. L.-J. Cheng and A. Partovi, Appl. Phys. Lett. **49**, 1456 (1986).

3.74. L.-J. Cheng and A. Partovi, Appl. Opt. **27**, 1760 (1988).

3.75. J. Kumar, G. Albanese, W.H. Steifer, and M. Ziari, Opt. Lett. **12**, 120 (1987).

3.76. J. Kumar, G. Albanese, and W.H. Steifer, J. Opt. Soc. Am. B**4**, 1079 (1987).

3.77. K. Walsh and T.J. Hall, Electron. Lett. **24**, 477 (1988).

3.78. J. Kumar, G. Albanese, and W.H. Steifer, Opt. Commun. **63**, 191 (1987).

3.79. K. Walsh and T.J. Hall, Opt. Lett. **12**, 1026 (1987).

3.80. G.C. Valley, A.L. Smirl, M.B. Klein, K. Bohnert, and T.E. Boggess, Jr., Opt. Lett. **11**, 647 (1986).

3.81. A.L. Smirl, G.C. Valley, K.M. Bohnert, and T.F. Boggess, Jr., IEEE J. Quantum Electron. **QE-24**, 289 (1988).

3.82. G.C. Valley and A.L. Smirl, IEEE J. Quantum Electron. **QE-24**, 304 (1988).

3.83. G. Gheen and L.-J. Cheng, Appl. Opt. **27**, 2756 (1988).

3.84. H.-K. Liu and L.-J. Cheng, Appl. Opt. **27**, 1006 (1988).

3.85. R.B. Bylsma, D.H. Olson, and A.M. Glass, Appl. Phys. Lett. **52**, 1083 (1988).

3.86. D.C. Look, in *Semiconductors and Semimetals* vol. 19 (Academic Press, New

York, 1983), p. 75.

3.87. C.A. Stolte, in *Semiconductors and Semimetals* vol. 20 (Academic Press, New York, 1983), p. 89.

3.88. K. Germanova, V. Donchev, C. Hardalov, and L. Nikolov, J. Phys. D **20**, 1507 (1987).

3.89. INFRARED OPTICS, INC., P. O. Box 216 Farmingdale, New York 11735, USA.

3.90. P. Dobrilla and J.S. Blakemore, J. Appl. Phys. **58**, 208 (1985).

3.91. T.E. Walsh, RCA Review **27**, 323 (1966).

3.92. G.M. Martin, Appl. Phys. Lett. **39**, 747 (1981).

3.93. N. Suzuki and K. Tada, Jpn. J. Appl. Phys. **23**, 1011 (1984).

3.94. S.M. Sze, *Semiconductor Devices: Physics and Technology* (Wiley, New York, 1985).

3.95. R.A. Mullen, in *Photorefractive Materials and Their Applications* I, P. Günter and J.P. Huignard eds., Topics in Applied Physics vol. 61 (Springer, Berlin, 1988) p. 167.

3.96. D. Pons, Appl. Phys. Lett. **37**, 413 (1980).

3.97. G.C. Valley and M.B. Klein, Opt. Eng. **22**, 704 (1983).

3.98. R.B. Bylsma, D.H. Olson, and A.M. Glass, Opt. Lett. **13**, 853 (1988).

CHAPTER
FOUR

Four-wave Mixing in Photorefractive Crystals

4.1 Introduction

Generation of phase-conjugate waves by four-wave mixing in photorefractive crystals has been studied extensively in the past. The main interest is in real-time holographic applications which include distortion correction and real-time optical information processing [4.1]. In photorefractive crystals with large nonlinearities, self-pumped generation of phase-conjugate waves without external pump beams can take place [4.2]. This unique property has led to novel phenomena and applications [4.3]. In this chapter four-wave mixing for scalar and vector wavefront reversal is described briefly in terms of nonlinear polarizations. Next the properties of self-pumped PCM's (SPPCM's) are described. Several SPPCM geometries are shown. The phase shifts of conjugate waves from a SPPCM, one of the most interesting properties of SPPCM's, are also discussed theoretically and experimentally.

4.2 Four-wave mixing for wavefront reversal

4.2.1 Nonlinear polarization

Let us consider the basic four-wave mixing geometry shown in Fig. 4.1. We take the four waves $\mathbf{E}_1, \ldots, \mathbf{E}_4$ as follows:

$$\mathbf{E}_j(\mathbf{r},t) = \frac{1}{2}\sum_{l=1}^{2} \mathbf{e}_j^{(l)} A_j^{(l)}(\mathbf{r}) e^{i[\mathbf{k}_j^{(i)}\cdot\mathbf{r}-\omega t]} + c.c. \quad (j=1,2,3,4), \tag{4.1}$$

where $\mathbf{e}_j^{(l)}$ is the l^{th} eigen polarization vector of the j^{th} wave, $\mathbf{k}_1 = -\mathbf{k}_2$, $\mathbf{k}_3 = -\mathbf{k}_4$,

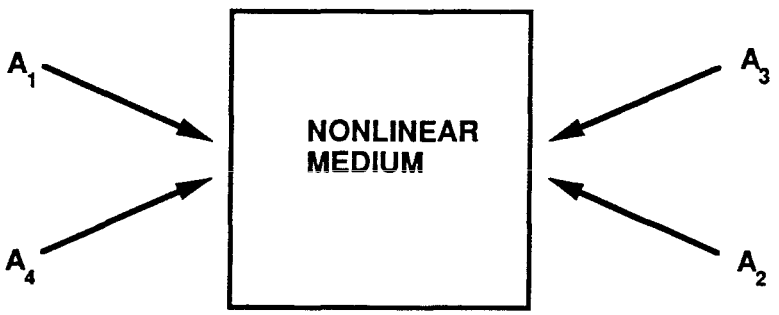

Figure 4.1 Schematic of the four-wave mixing in a nonlinear medium. A_1 and A_2 are pump waves, A_3 is a conjugate wave, and A_4 is an input wave.

and a degenerate case (i.e., $\omega_1 = \omega_2 = \omega_3 = \omega_4 = \omega$) is considered. In isotropic media the third-order nonlinear polarization $\mathbf{P}_{\mathrm{NL}}$ relevant to the generation of the conjugate wave $\mathbf{E}_3$ ($\propto \mathbf{E}_4^*$) can be written as [4.4]

$$\mathbf{P}_{\mathrm{NL}} = \frac{1}{2}[A(\mathbf{E}_1 \cdot \mathbf{E}_4^*)\mathbf{E}_2 + B(\mathbf{E}_2 \cdot \mathbf{E}_4^*)\mathbf{E}_1 + C(\mathbf{E}_1 \cdot \mathbf{E}_2)\mathbf{E}_4^*] + c.c, \qquad (4.2)$$

where A, B, and C are coefficients depending on the type of nonlinear medium and the geometry.

Equation (4.2) consists of a superposition of three gratings. The first two brackets, $(\mathbf{E}_1 \cdot \mathbf{E}_4^*)$ and $(\mathbf{E}_2 \cdot \mathbf{E}_4^*)$, denote static gratings that scatter off $\mathbf{E}_2$ and $\mathbf{E}_1$, respectively, to generate the conjugate wave $\mathbf{E}_3$. In this case the polarization state of $\mathbf{E}_4$ must have a nonzero overlap with those of either $\mathbf{E}_1$ or $\mathbf{E}_2$ to keep these terms meaningful. This requires a special choice of the pump-probe polarization. We note that these two gratings are analogous to those in conventional holography [4.5,6] and give *scalar phase conjugation.* On the other hand, the third bracket, $(\mathbf{E}_1 \cdot \mathbf{E}_2)$, in Eq. (4.2) denotes a moving grating at 2ω and has a nonzero value unless the two pump waves are either orthogonally linearly polarized or co-circularly polarized. Since this condition is independent of the polarization state of $\mathbf{E}_4$, the third bracket gives *vector phase conjugation.* We note that this grating has no holographic analog and is inherent to the third-order nonlinear optical effect.

4.2.2 Scalar wavefront reversal

In photorefractive crystals only the first two terms in Eq. (4.2) are important, since the photorefracitve gratings result from the second-order nonlinear effect (i.e., the Pockels effect). (We note that the quadratic electrooptic effect is not considered in this thesis. See Section 2.3 in Chapter 2). In this case the (photorefractive) nonlinear susceptibility tensor $\Delta\tilde{\chi}$ can be expressed as

$$\Delta\tilde{\chi} = \frac{i}{4\pi}\sum_{l=1}^{2}[\frac{\eta_{14}^{(l)}A_1^{(l)*}A_4^{(l)} + \eta_{23}^{(l)*}A_2^{(l)}A_3^{(l)*}}{\mathrm{I}_0}\Xi_{\mathrm{scI}}^{(l)}\tilde{u}_{\mathrm{I}}e^{i\mathbf{k}_{\mathrm{I}}^{(l)}\cdot\mathbf{r}}$$

$$+\frac{\eta_{13}^{(l)*}A_1^{(l)}A_3^{(l)*}+\eta_{24}^{(l)}A_2^{(l)*}A_4^{(l)}}{I_0}\Xi_{scII}^{(l)}\tilde{u}_{II}e^{i\mathbf{k}_{II}^{(l)}\cdot\mathbf{r}}+\frac{\eta_{12}^{(l)*}A_1^{(l)}A_2^{(l)*}}{I_0}\Xi_{scIII}^{(l)}\tilde{u}_{III}e^{i\mathbf{k}_{III}^{(l)}\cdot\mathbf{r}}$$

$$+\frac{\eta_{34}^{(l)}A_3^{(l)*}A_4^{(l)}}{I_0}\Xi_{scIV}^{(l)}\tilde{u}_{IV}e^{i\mathbf{k}_{IV}^{(l)}\cdot\mathbf{r}}]+c.c., \tag{4.3}$$

where I_0 is the total intensity, $\eta_{ij}^{(l)}=(\mathbf{e}_i^{(l)*}\cdot\mathbf{e}_j^{(l)}),\tilde{u}_I=[\tilde{\epsilon}:(\tilde{\tilde{r}}:\mathbf{e}_{scI}):\tilde{\epsilon}],\Xi_{scI}^{(l)}$ is given, for example, by Eq. (3.9) with $K=|\mathbf{k}_I^{(l)}|$, and $\mathbf{k}_I^{(l)}=\mathbf{k}_4^{(l)}-\mathbf{k}_1^{(l)}=\mathbf{k}_2^{(l)}-\mathbf{k}_3^{(l)},\mathbf{k}_{II}^{(l)}=\mathbf{k}_1^{(l)}-\mathbf{k}_3^{(l)}=\mathbf{k}_4^{(l)}-\mathbf{k}_2^{(l)},\mathbf{k}_{III}^{(l)}=2\mathbf{k}_1^{(l)}$, and $\mathbf{k}_{IV}^{(l)}=2\mathbf{k}_4^{(l)}$. Using the same procedure as that done in Chapter 3, we can obtain a set of (at least) eight coupled-wave equations for $\mathbf{E}_1,\ldots,\mathbf{E}_4$. This set of eight equations can be reduced to four coupled-wave equations for a scalar case and/or special polarization geometries. The approximate and exact solutions to the scalar four coupled-wave equations have been obtained for the cases of copolarized pump waves [4.2,7] and cross-polarized pump waves [4.8–10]. The property of phase of conjugate wave for the case of copolarized pump waves has also been studied [4.11].

4.2.3 Vector wavefront reversal

As discussed in Subsection 4.2.1, vector phase conjugation for an arbitrary polarized input can be obtained by taking advantage of the third term in Eq. (4.2). This vector phase conjugation is required, for example, when a polarization distortion is associated with a spatial distortion. The "wrong" conjugate wave generated from the first two terms in Eq. (4.2) can be eliminated when $\mathbf{k}_1(=-\mathbf{k}_2)$ is chosen to be orthogonal to $\mathbf{k}_4$ so that the first two terms vanish. As an example, for an isotropic third-order nonlinear medium with counterrotating circular polarized pump waves, $\mathbf{P}_{NL}$ relevant to the generation of $\mathbf{E}_4^*$ is given by

$$\mathbf{P}_{NL}=\Delta\tilde{\chi}:\mathbf{E}_4^*, \tag{4.4a}$$

with

$$\Delta\tilde{\chi}=\frac{(\chi_{1111}^{(3)}+\chi_{1221}^{(3)})|\mathbf{E}_1||\mathbf{E}_2|}{2}I, \tag{4.4b}$$

where I is a unit matrix, and the relations $\chi^{(3)}_{1111} = \chi^{(3)}_{1221} + \chi^{(3)}_{1122} + \chi^{(3)}_{1212}$ and $\chi^{(3)}_{1122} = \chi^{(3)}_{1212}$ are used [4.12]. It is seen that $\Delta\tilde{\chi}$ is unit diagonal and thus vector phase conjugation occurs. This method for vector phase conjugation was suggested originally by Zel'dovich *et al.* [4.4], and demonstrated by several workers in liquid CS_2 [4.13,14], the D_2 resonance line of sodium [4.15], and the $3s_{1/2} \rightarrow 6s_{1/2}$ two-photon transition of sodium [4.16].

The more direct method has also been considered by conjugating each orthogonal polarization component using a scalar PCM (in this case, a PCM using stimulated Brillouin scattering [4.17]). This method has been applied to a photorefractive $BaTiO_3$ crystal [4.18]. We note that this method requires the same amplitude phase-conjugate reflectivity for both polarization components in order to obtain perfect vector phase conjugation.

A completely different method has recently been demonstrated [4.19] and analyzed[4.20–23]. This method uses modal dispersal of input polarization, and spatial information and phase conjugation of only one polarization component. In this case a tandem combination of multimode fiber and photorefractive PCM is used. The detailed theoretical and experimental studies of this method will be described in Chapter 6.

4.3 Self-pumped phase-conjugate mirrors (SPPCM's)

4.3.1 Geometry of SPPCM's

The nonlocal nature of photorefractive gratings gives the two-beam coupling phenomena discussed in Chapter 3. This leads to the possibility of self-pumped phase conjugation without additional external pump beams. This happens when scattering of a single input beam creates noisy gratings in a photorefractive crystal. Certain gratings generate the pump beams and are enhanced in turn by the four-wave mixing process [4.2,24,25].

Figures 4.2(a) – 4.2(d) show several geometries of SPPCM's. In particular, the SPPCM's shown in Figs. 4.2(a), 4.2(b), and 4.2(c) require external mirrors, whereas the SPPCM shown in Fig. 4.2(d) uses total internal reflection at one corner inside the crystal [4.26,27]. The properties of these SPPCM's have been analyzed [4.2] and their fidelity of phase conjugation has been studied [4.28]. The self-starting "threshold coupling strength" [denoted by $(\Gamma l)_{\rm th}$] is 0 for the linear SPPCM, 4.98 for the semi-linear SPPCM, 2 for the ring SPPCM, and 9.36 for the SPPCM using total internal reflection, all with negligible loss and when the feedback by the external mirrors is unity [4.2]. For this reason large nonlinear materials such as $BaTiO_3$ and SBN have been the photorefractive materials of choice for constructing these self-starting SPPCM's (see Table 3.5).

The other types of SPPCM's, called "double PCM's", have also been demonstrated. In these SPPCM's two (or more) mutually incoherent beams are incident on the crystal and are phase conjugated simultaneously without any crosstalk with respect to spatial information. This happens because each input beam writes gratings with its scattered beams and the stimulated build-up of these gratings takes place when one set of gratings (written by one of the inputs) matches the other set of gratings (written by the other input). In this case only these matched gratings (which convert one input to a phase-conjugate replica of the other input and vice versa by time-reversal symmetry) are enhanced and survive at the steady state. Figures 4.3(a) – 4.3(d) show several geometries of double PCM's (a) without internal reflection [4.29], (b) with two internal reflections [4.30], (c) with one internal reflection, called a "bird-wing" mirror [4.31], and (d) with three internal reflections, called a "frog-legs" mirror [4.32]. These geometries are different from each other by their paths which are determined by the orientation and dimensions of crystals in an optimum way so that the photorefractive two-beam coupling at each interaction

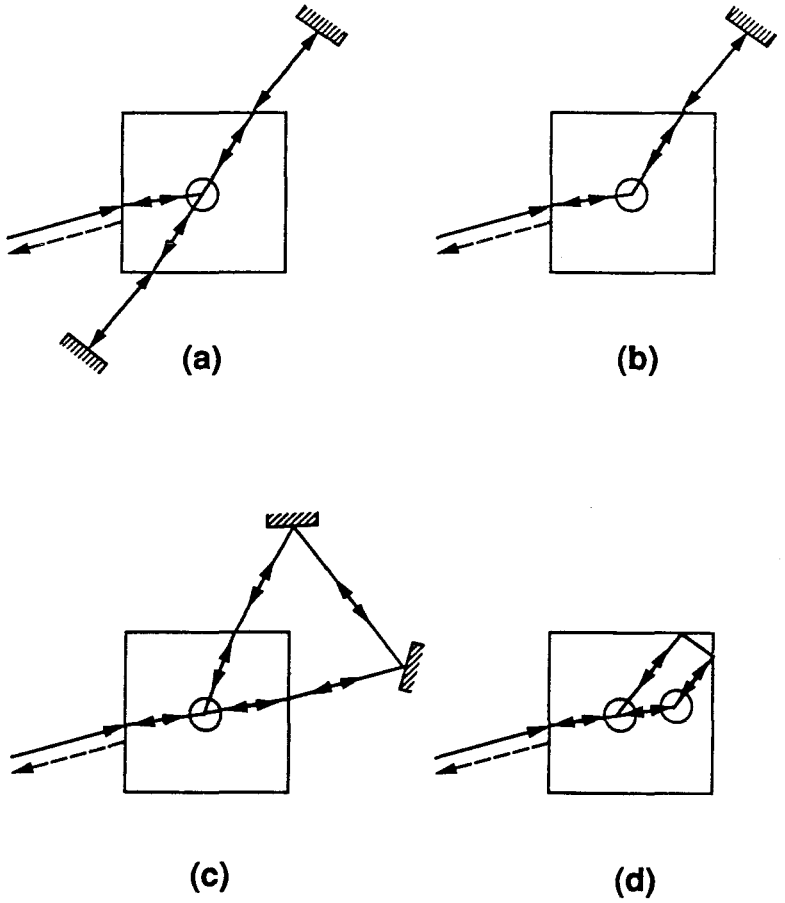

Figure 4.2 Geometry of SPPCM's. (a) Linear SPPCM. (b) Semi-linear SPPCM. (c) Ring SPPCM. (d) SPPCM using total internal reflection. The circles denote the four-wave mixing interaction regions.

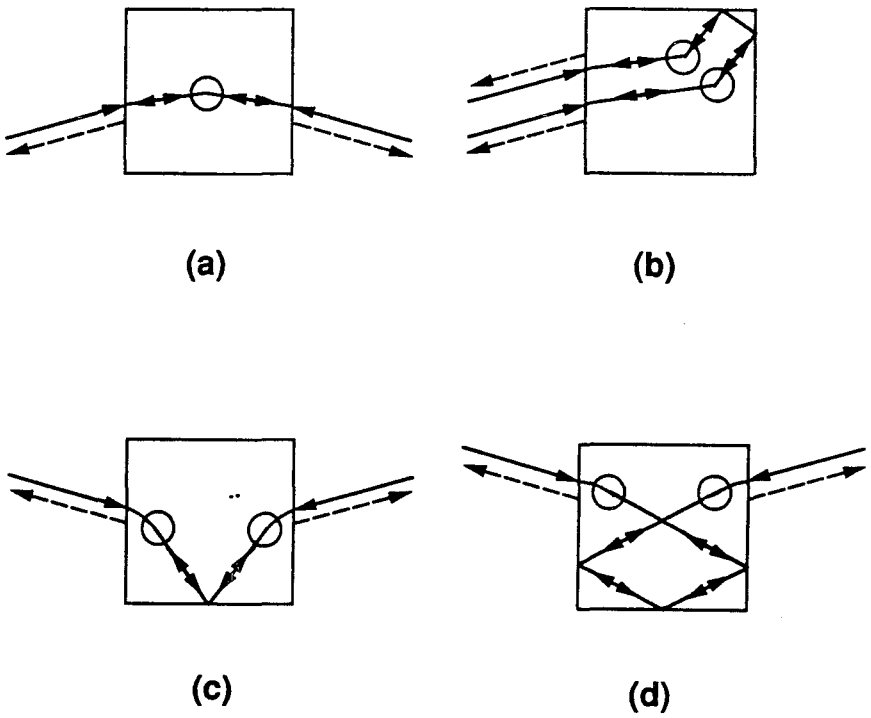

Figure 4.3 Geometry of double PCM's. (a) Zero internal reflection type. (b) Two internal reflection type. (c) "Bird-wing" type. (d) "Frog-legs" type. The circles denote the four-wave mixing interaction regions.

region is maximized.

4.3.2 Phase shift of a SPPCM

Because of compactness, robustness against vibration, and self-alignment, SPPCM's shown in the previous subsection become a key component in an ever increasing number of image processing and interferometric applications [4.23,32]. The key issue in these applications is the relation between the phase (more precisely, the change of phase) of the input beam and that of the output (i.e., the reflected) beam. Feinberg [4.33] reported on an interferometer with a SPPCM in one arm and showed that it compensated for the effects of optical distortions in the beam path. The fact that the device functioned as an interferometer implied, as noted and explained by Feinberg, that spatially uniform phase shifts due to path delays were not reversed in sign by a SPPCM as they would be in an externally-pumped PCM [4.34]. The observation of distortion correction, however, implied that the *relative phases* of the partial (plane) waves making up the distorted input beam were reversed. When Feinberg's explanation for the instantaneous response of the SPPCM to uniform phase shifts is applied to each partial wave, it appears that the SPPCM cannot function as a conjugator for the distorted input beam since a uniform phase carried by each partial wave is not reversed (but preserved) upon reflection and the relative phases (and therefore the distorted wavefront of the input) are not reversed either. A related observation by Ewbank *et al.* [4.35] showed that the relative phase between two input beams was reversed in an interferometer using two coupled SPPCM's. Since a basic understanding of these observations is of great importance for many applications, in this subsection we will clarify the nature of the phase shifts of conjugate waves from a SPPCM theoretically and experimentally [4.36].

Let us first consider the case of a single plane wave input. Figure 4.4 (a) shows the basic four-wave mixing geometry where the incident wave E_4 of frequency ω_4 and wave vector $\mathbf{k}_4$ interacts with two externally-supplied pump waves E_1 and E_2 of the same frequency ω_p and opposite wave vectors $\mathbf{k}_p$ and $-\mathbf{k}_p$ traveling in opposite directions and the conjugate wave E_3 of frequency ω_3 and wave vector $\mathbf{k}_3$ traveling in opposition to E_4. All the waves are assumed to be linearly polarized.

The reflected conjugate wave E_3 at the input to the interaction region is written as

$$\begin{aligned} E_3(\mathbf{r},t) &\equiv \frac{1}{2}A_3 \exp\left[i(\omega_3 t - \mathbf{k}_3 \cdot \mathbf{r})\right] + c.c. \\ &= \frac{1}{2}rA_4^* \exp\left\{i[(2\omega_p - \omega_4)t + \mathbf{k}_4 \cdot \mathbf{r}]\right\} + c.c., \end{aligned} \tag{4.5}$$

where r denotes the complex phase-conjugate reflectivity and is in general a function of A_1, A_2, and A_4 [4.11]. If we take $A_j = |A_j| \exp(i\phi_j)$ $(j = 1, \cdots, 4)$, the phase of the complex amplitude A_3 is then written as

$$\phi_3 = \phi_0 + \phi_1 + \phi_2 - \phi_4, \tag{4.6}$$

where ϕ_0 is the absolute phase shift that can be determined from the solution of the coupled-wave equations describing the "nonlinear" four-wave mixing process, and in general depends on material parameters of a nonlinear medium and the intensities of E_1, E_2 and E_4 (e.g., ϕ_0=0 or π for $\pi/2$-shifted photorefractive gratings). It is seen from Eq. (4.6) that any phase change $\delta\phi_4$ of the input is reversed upon phase conjugation, i.e., $\phi_3 \rightarrow \phi_3 - \delta\phi_4$ as $\phi_4 \rightarrow \phi_4 + \delta\phi_4$. This has been verified recently by quantitative measurements of the phase shifts of reflection from an externally-pumped PCM [4.34].

In SPPCM's where E_1 and E_2 derive directly from the fanning of E_4 and thus possess the same initial phase ϕ_4, we can write ϕ_1 and ϕ_2 as

$$\phi_i = \phi_4 + \varphi_i \qquad (i = 1, 2), \tag{4.7}$$

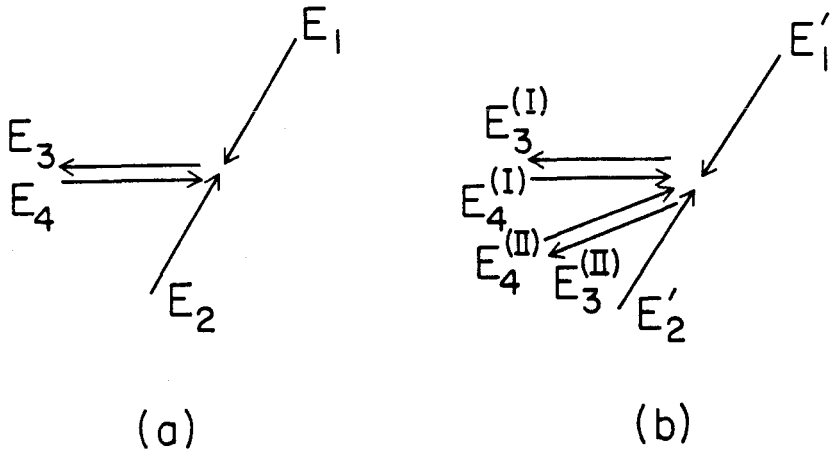

Figure 4.4 Four-wave mixing geometry for (a) a single plane-wave input and (b) two plane-wave inputs.

where φ_i denotes some constant phase determined by the photorefractive beam coupling and oscillation associated, in general, with the frequency detuning $\Delta\omega$ ($= \omega_p - \omega_4$) [4.3]. We note that E_1 and E_2 would spatially be conjugates of each other [4.37] but the uniform phase ϕ_1 is *not* in general equal to $-\phi_2$ in a SPPCM. (Otherwise $\phi_3 \rightarrow \phi_3 - \delta\phi_4$ as $\phi_4 \rightarrow \phi_4 + \delta\phi_4$, which is not the case in SPPCM's.) Then in a manner similar to Eq. (4.6) we obtain

$$\phi_3 = \theta + \phi_4, \tag{4.8}$$

where $\theta(\equiv \phi_0 + \varphi_1 + \varphi_2)$ is *fixed* in a given set up. It is seen from Eq. (4.8) that, in contrast to the externally-pumped PCM result, any phase change $\delta\phi_4$ of the input is *not* reversed but is preserved upon phase conjugation, i.e., $\phi_3 \rightarrow \phi_3 + \delta\phi_4$ as $\phi_4 \rightarrow \phi_4 + \delta\phi_4$. In addition, since all the waves involved in the four-wave mixing process share the common phase ϕ_4, the conjugate wave responds *instantaneously* to any phase change of the input. The above explanation is essentially that given by Feinberg [4.33].

Let us next consider the case where two separate but mutually coherent input plane waves $E_4^{(\mathrm{I})}$ and $E_4^{(\mathrm{II})}$ of frequency ω_4 and wave vectors $\mathbf{k}_4^{(\mathrm{I})}$ and $\mathbf{k}_4^{(\mathrm{II})}$, respectively, are involved in the phase conjugation process, [see Fig. 4.4(b)]. In this case we postulate that in a SPPCM a coherent superposition of $E_4^{(\mathrm{I})}$ and $E_4^{(\mathrm{II})}$ acts as an input to generate by two-beam coupling [4.3] the two counter-propagating oscillating (pump) fields $E_1'\{\equiv 1/2|A_1'|\exp[i(\omega_p' t - \mathbf{k}_p' \cdot \mathbf{r} + \phi_1')] + c.c.\}$ and $E_2'\{\equiv 1/2|A_2'|\exp[i(\omega_p' t + \mathbf{k}_p' \cdot \mathbf{r} + \phi_2')] + c.c.\}$ inside the phase-conjugating crystal. (Again ϕ_1' is not in general equal to $-\phi_2'$.) In this case the phases $\phi_3^{(\mathrm{I})}$ and $\phi_3^{(\mathrm{II})}$ of the reflected waves $E_3^{(\mathrm{I})}$ and $E_3^{(\mathrm{II})}$ are found, by the same procedure used to obtain Eq. (4.6), as

$$\phi_3^{(q)} = \phi_0 + \phi_1' + \phi_2' - \phi_4^{(q)} \qquad (q = \mathrm{I}, \mathrm{II}). \tag{4.9}$$

We thus find that the input waves $E_4^{(\mathrm{I})}$ and $E_4^{(\mathrm{II})}$ are reflected as $E_3^{(\mathrm{I})}$ and $E_3^{(\mathrm{II})}$ with their relative phase $\Delta\phi_4(\equiv \phi_4^{(\mathrm{I})} - \phi_4^{(\mathrm{II})})$ reversed to $-\Delta\phi_4$ as it must be for wavefront

reversal. We note, however, the existence of a common phase $\Psi(E_4^{(\mathrm{I})}, E_4^{(\mathrm{II})})(\equiv \phi_0 + \phi_1' + \phi_2')$ in both the reflected waves $E_3^{(\mathrm{I})}$ and $E_3^{(\mathrm{II})}$. Since we have assumed that the pump waves E_1' and E_2' are generated from a linear combination of $E_4^{(\mathrm{I})}$ and $E_4^{(\mathrm{II})}$, they can be written in the form of $\exp(i\phi_4^{(\mathrm{I})}) + \alpha \exp(i\phi_4^{(\mathrm{II})})$, where α is a contribution of $E_4^{(\mathrm{II})}$ (normalized by $E_4^{(\mathrm{I})}$) to the pump waves and so $\alpha \propto |E_4^{(\mathrm{II})}/E_4^{(\mathrm{I})}|$. We can thus express the common phase Ψ as

$$\Psi = 2\tan^{-1}\left[\frac{\sin\phi_4^{(\mathrm{I})} + \alpha \sin\phi_4^{(\mathrm{II})}}{\cos\phi_4^{(\mathrm{I})} + \alpha\cos\phi_4^{(\mathrm{II})}}\right] + \phi_0 + \beta_1 + \beta_2, \tag{4.10}$$

where β_1 and β_2 are some constant phases of E_1' and E_2', respectively. Then it is seen from Eqs. (4.9) and (4.10) that $\phi_3^{(\mathrm{I})}$ and $\phi_3^{(\mathrm{II})}$ depend upon the phases of the input waves $E_4^{(\mathrm{I})}$ and $E_4^{(\mathrm{II})}$ and the parameter α. This dependence implies "phase cross talk", i.e., a dependence of $\phi_3^{(\mathrm{II})}$ on $\phi_4^{(\mathrm{I})}$ (and of $\phi_3^{(\mathrm{I})}$ on $\phi_4^{(\mathrm{II})}$) for a given α. Also, cross talk between the input amplitudes and the output phases is seen via α.

We are now in a position to apply the above result to a general case where the input wave E_4 suffers a wavefront distortion caused by some random scatterers during propagation (e.g., by air turbulence or modal scrambling in multimode fibers [4.23]). In this case it is possible to express the complex amplitude A_4 as a summation over plane wave components $A_4^{(\mathbf{k})}$, where $\mathbf{k}$ is a wave vector. We then replace $\phi_4^{(\mathrm{II})}$ in Eq. (4.9) by the phase $\bar{\phi}_4$ at the center wave vector $\mathbf{k}_4$ of A_4 [i.e., the uniform (or average) phase of the wavefront] and $\phi_4^{(\mathrm{I})}$ in Eq. (4.9) by the phase $\phi_4^{(\mathbf{k})}$ at wave vector $\mathbf{k}$ of A_4. Then from Eq. (4.9) the phase $\phi_3^{(\mathbf{k})}$ of component $A_3^{(\mathbf{k})}$ is expressed by

$$\phi_3^{(\mathbf{k})} = \Psi' - \bar{\phi}_4 - \Delta\phi_4^{(\mathbf{k})}, \tag{4.11}$$

where Ψ' is a common phase similar to Ψ given by Eq. (4.10) and $\Delta\phi_4^{(\mathbf{k})} \equiv \phi_4^{(\mathbf{k})} - \bar{\phi}_4$. Since the phase factor $\Psi' - \bar{\phi}_4$ is common to all $\phi_3^{(\mathbf{k})}$'s and is in this case a function of all $\phi_4^{(\mathbf{k})}$'s, we see from Eq. (4.11) that a SPPCM can reverse the relative phase $\Delta\phi_4^{(\mathbf{k})}$ but not the uniform phase $\phi_4^{(\mathbf{k}_4)}$, i.e., it can correct phase distortions but *not*

unifrom phase changes in a double pass. This explains Feinberg's observation [4.33] and our experiments described below. This main difference between an externally-pumped PCM and a SPPCM is schematically shown in Fig. 4.5.

To test our model, we performed a series of experiments. In particular we measured the phase shifts of reflected conjugate waves from a SPPCM with two (coherent) input beams as a function of a uniform phase change of one of the inputs. Figure 4.6 shows the experimental arrangement. A collimated beam (~11 mm diameter) derived from a single-longitudinal-mode argon-ion laser at 514.5 nm was divided into two beams $E_4^{(I)}$ and $E_4^{(II)}$ by a beam splitter (BS2). These beams were polarized as extraordinary rays and loosely focused into a $BaTiO_3$ crystal employed as the SPPCM using internal reflection. One of the beams, $E_4^{(I)}$, was reflected off a piezoelectrically-driven (PZT) mirror so that a uniform phase shift of $E_4^{(I)}$ was introduced. The input power of $E_4^{(I)}$ and $E_4^{(II)}$ to the crystal was 3.5 mW and 3.0 mW, and their phase-conjugate reflectivities were about 10 % and 15 %, respectively.

In the first experiment the conjugate beam $E_3^{(I)}$ interfered with a reference beam via BS_3 with $E_4^{(II)}$ blocked. Figures 4.7(a) – 4.7(c) show the photographs of the interference patterns between the reference beam and $E_3^{(I)}$ at D_1 without a glass plate [Fig. 4.7(a)], with a glass plate inserted in a half part of the reference beam [Fig. 4.7(b)], and with a glass plate inserted in a half part of the input beam $E_4^{(I)}$ [Fig. 4.7(c)]. It is seen that the SPPCM can reverse a nonuniform wavefront distortion caused by the glass plate since no fringe shift is seen in Fig. 4.7(c). We also measured the response of the SPPCM to a uniform phase shift. The movement of the interference fringe due to the phase shift of $E_4^{(I)}$ was detected by D_1 with a pinhole of 100 μm diameter (much smaller than the fringe spacing). The sign of the phase shift was determined by the direction of the fringe movement. The

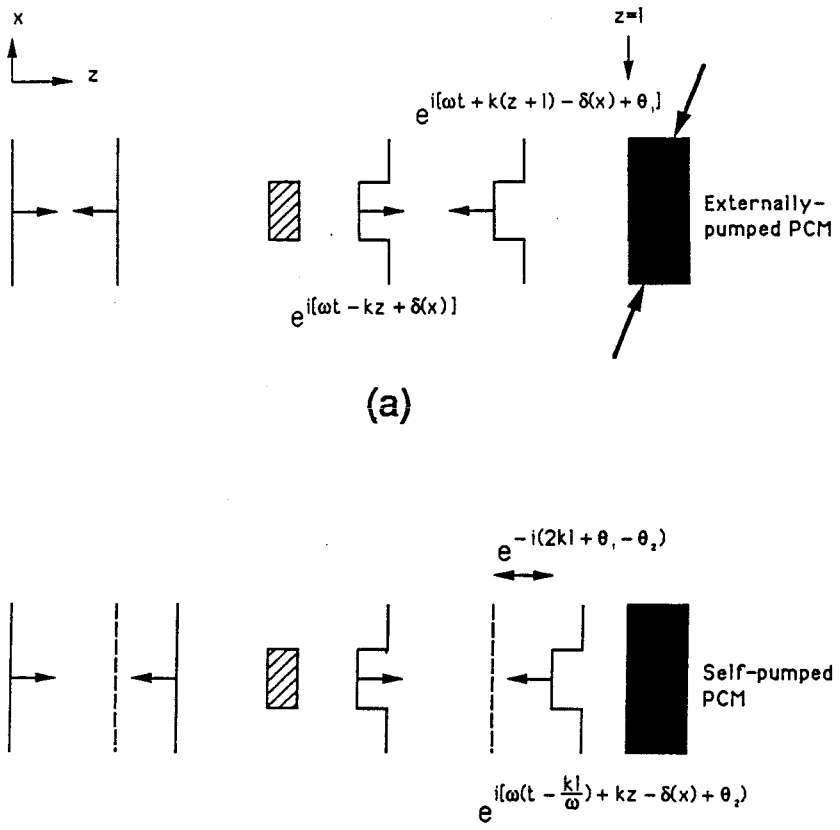

Figure 4.5 Wavefront reversal by an externally-pumped PCM and a SPPCM. In the externally-pumped PCM, the uniform phase factor e^{ikl} at the mirror as well as the nonuniform phase factor $e^{i\delta(x)}$ caused by the phase distorter (shown as a hatched object in the figure) is reversed on reflection. In the SPPCM, $e^{i\delta(x)}$ is reversed but e^{ikl} is preserved on reflection.

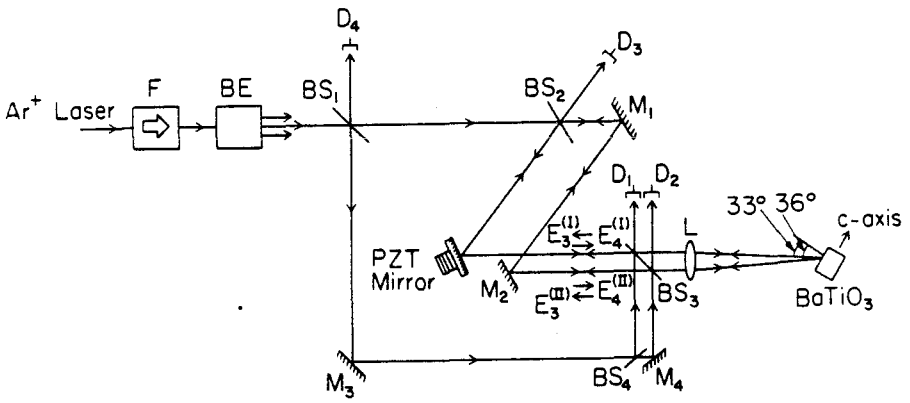

Figure 4.6 Experimental arrangement for the measurement of the phase shifts of conjugate beams from the SPPCM. $E_4^{(I)}$ and $E_4^{(II)}$ are the input beams, and $E_3^{(I)}$ and $E_3^{(II)}$ are their conjugate beams, respectively. The intensity changes of the interference fringes due to the movement of the PZT mirror are detected by D_1 and D_2. The recombined conjugate beams from different ports of BS_2 are detected by D_3 and D_4, respectively. F: Faraday isolator; BE: beam expander; BS: beam splitter; M: mirror; D: detector; L: lens.

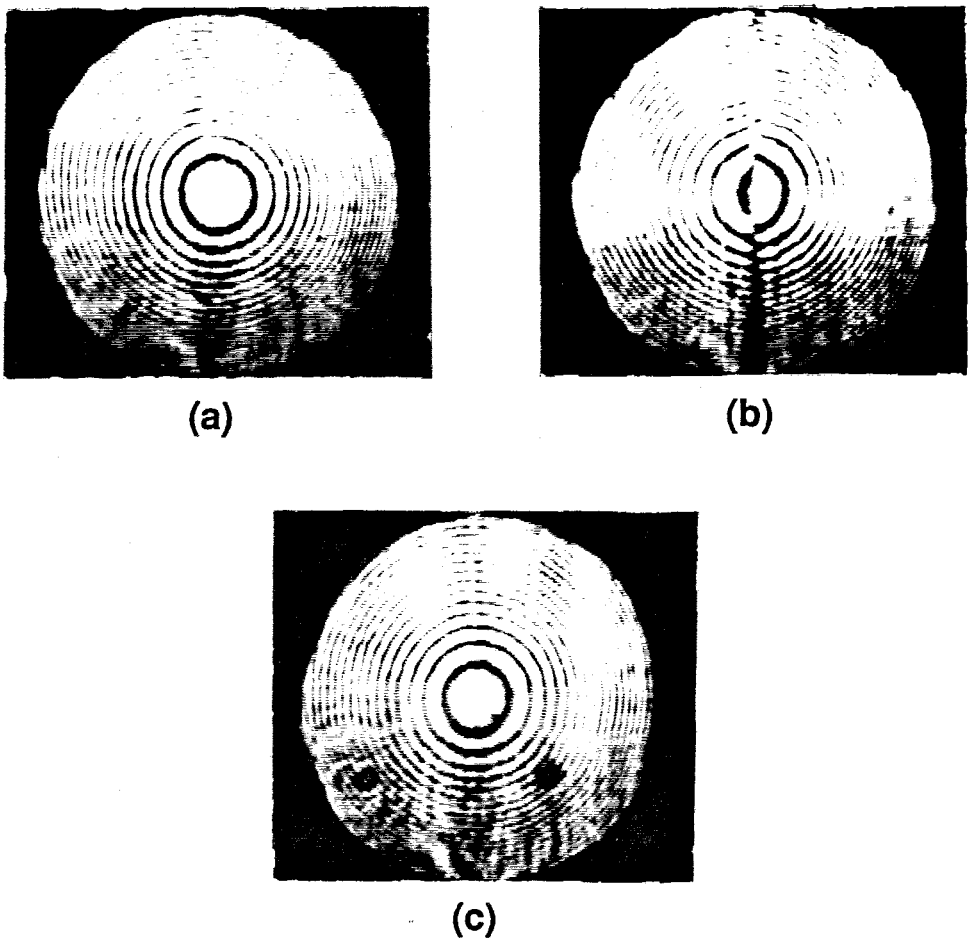

Figure 4.7 Interference fringe patterns between the reference beam and the conjugate beam $E_3^{(I)}$. In (a) no glass plate is inserted between the beams. In (b) and (c) a glass plate is inserted in a half part of (b) the reference beam or (c) the input beam. The radius of curvature of the input beam is estimated to be about 1.6 m.

measurement was completed within a time interval much shorter than the period of the frequency detuning $\Delta\omega$ (~0.014 Hz in the first experiment) of $E_3^{(I)}$. (During the measurement a phase distorter (a sheet of etched glass), not shown in Fig. 4.6, was placed in front of the crystal so that the distortion-correction capability of the SPPCM was also examined at the same time. We observed that the phase distortion of $E_4^{(I)}$ was always corrected in a double pass throughout scanning of the phase of $E_4^{(I)}$.) Figure 4.8 shows the result. It is seen that the phase of $E_3^{(I)}$ increases almost linearly with the increase of the input phase, as expected from Eq. (4.8).

In order to see the response time of the SPPCM on the phase shift, we also phase-modulated the input $E_4^{(I)}$ by $\phi_m \sin \Omega t$ ($\phi_m \leq \pi/2$). Figure 4.9 shows the result of the temporal change of the fringe intensity detected by D_1 due to the sinusoidal phase modulation. It is seen that the phase of $E_3^{(I)}$ follows the phase modulation of the input. In fact it was found that the phase of $E_3^{(I)}$ could follow the phase modulation at any speed (up to ~1 kHz in the experiment), while the phase-conjugate reflectivity remained the same. (Note that the response time of the crystal was about one second.) This instantaneous response of the SPPCM is consistent with Feinberg's observation [4.33] and quite different from the case of phase-modulated conjugate-wave generation from an externally-pumped PCM [4.38].

In the second experiment we allowed two input beams $E_4^{(I)}$ and $E_4^{(II)}$ to be incident on the crystal and measured the phase shifts of the corresponding reflected beams $E_3^{(I)}$ and $E_3^{(II)}$ as a function of the uniform phase change of $E_4^{(I)}$. The speed of the phase change of the input was chosen to be about 0.4 rad/sec, so that the crystal could respond to the input phase change with the stable conjugate-wave reflection and the phase shifts of $E_3^{(I)}$ and $E_3^{(II)}$ could be measured adiabatically. We confirmed this by monitoring D_3, i.e., the intensity at D_3 was constant in time (and close to zero) when the crystal smoothly responded to the input phase change

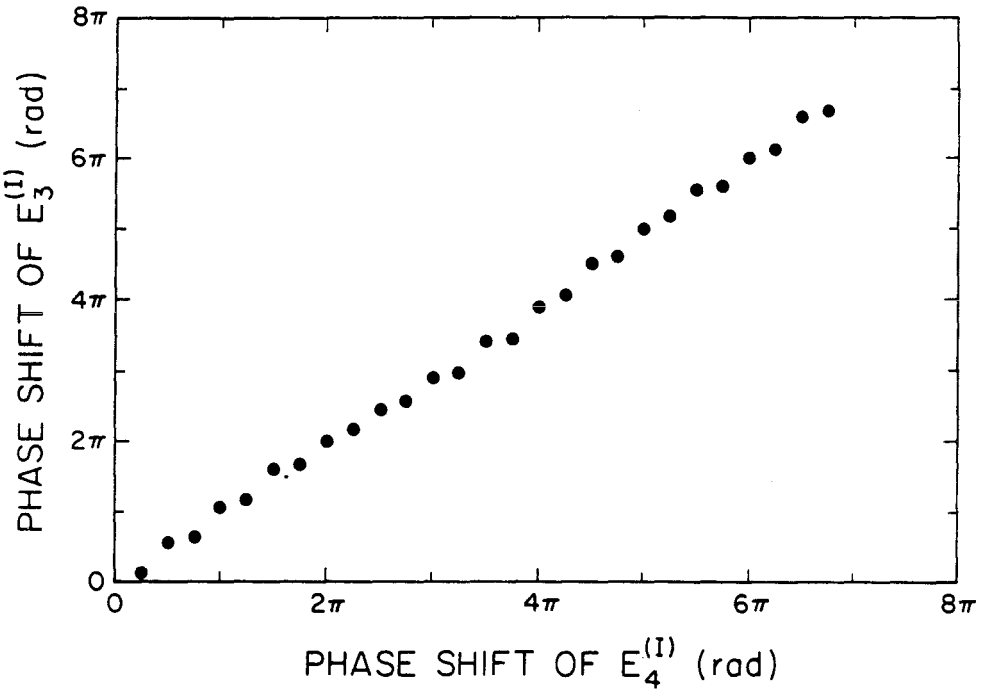

Figure 4.8 Phase shift of the conjugate beam $E_3^{(I)}$ as a function of a uniform phase change of the input $E_4^{(I)}$ introduced by the PZT mirror.

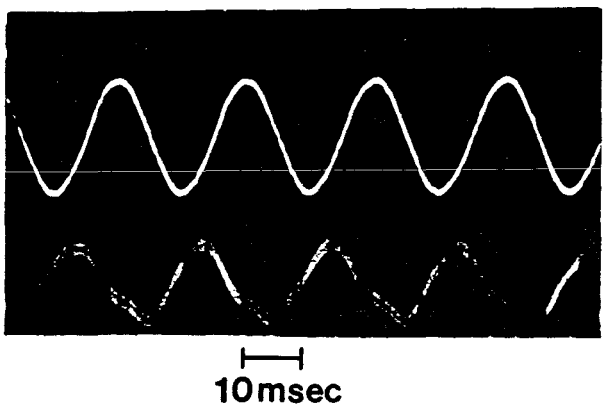

Figure 4.9 The upper trace shows the sinusoidal voltage applied to the PZT mirror, while the lower trace is the signal from the interference fringe intensity between the conjugate and reference beams.

during the continuous linear movement of the PZT mirror. Otherwise it was found that linear movements of the PZT mirror (faster than $\sim$ 1.0 rad/sec) caused the erratic change of the intensity at D_3 and the supression of the phase-conjugate reflection because of the erasure of photorefractive gratings inside the crystal. Figure 4.10 shows the result when the two phase shifts were measured independently. The effect of the frequency detuning ($\sim$0.025 Hz) was taken into account and corrected for the result shown in Fig. 4.10. It is seen that the accumulated phase shifts of $E_3^{(I)}$ and $E_3^{(II)}$ increase almost linearly with the increase of the phase of $E_4^{(I)}$ and their rates of changes (i.e., slopes) are different. But the relative phase shift $\Delta\phi_3(\equiv \phi_3^{(I)} - \phi_3^{(II)})$ is almost equal to $-\Delta\phi_4[= -(\phi_4^{(I)} - \phi_4^{(II)})]$. This means that, despite the phase cross talk, the relative phase $\Delta\phi_4$ between $E_4^{(I)}$ and $E_4^{(II)}$ is reversed to $-\Delta\phi_4$, as predicted by Eq. (4.9). We did not observe a noticeable amplitude dependence of $E_3^{(I)}$ and $E_3^{(II)}$ on the phase shift of $E_4^{(I)}$. Also, no "amplitude cross talk" (more precisely, cross talk of spatial structures) between $E_3^{(I)}$ and $E_3^{(II)}$ was observed [4.37].

The observed linear dependence of the phase shifts of $E_3^{(I)}$ and $E_3^{(II)}$ on the input phase change can be explained by our model. Since a continuous small change of $\phi_4^{(I)}$ was introduced in the second experiment, we may approximate the shift of Ψ given by Eq. (4.10) by $2\delta\phi_4^{(I)}/(1+\alpha)$ for each small increment $\delta\phi_4^{(I)}(\ll 1)$ of $\phi_4^{(I)}$, where we set $\phi_4^{(II)} = 0$ without loss of generality (because $\phi_4^{(II)}$ was constant in the experiment). It then follows from Eq. (4.9) that $\delta\phi_3^{(I)} \simeq \delta\phi_4^{(I)}(1-\alpha)/(1+\alpha)$ and $\delta\phi_3^{(II)} \simeq 2\delta\phi_4^{(I)}/(1+\alpha)$, showing the linear dependence of $\delta\phi_3^{(I)}$ and $\delta\phi_3^{(II)}$ on $\delta\phi_4^{(I)}$. Using these expressions, we also find that the relative difference between two values of $\dot{\alpha}$ (i.e., one from the slope of $\delta\phi_3^{(I)}$ and the other from that of $\delta\phi_3^{(II)}$) estimated from the result in Fig. 4.10 is about 2%. This supports the validity of the above equations. We also made a measurement of the dependence of the phase shifts of $\phi_3^{(I)}$ and $\phi_3^{(II)}$ on $\sqrt{I_4^{(II)}/I_4^{(I)}}(\equiv |E_4^{(II)}/E_4^{(I)}|)$. In this case, the total intensity

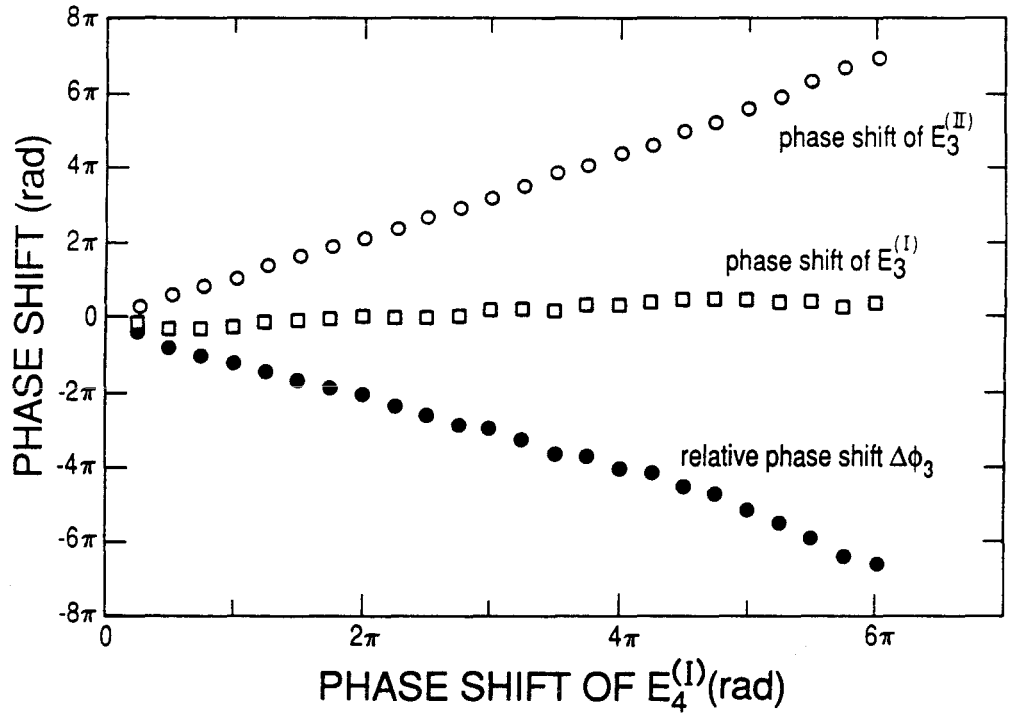

Figure 4.10 Phase shifts of the conjugate beams $E_3^{(\mathrm{I})}$ and $E_3^{(\mathrm{II})}$ and the relative phase shift $\Delta\phi_3$ between the conjugate beams $E_3^{(\mathrm{I})}$ and $E_3^{(\mathrm{II})}$ as a function of a uniform phase change of one of the inputs $E_4^{(\mathrm{I})}$.

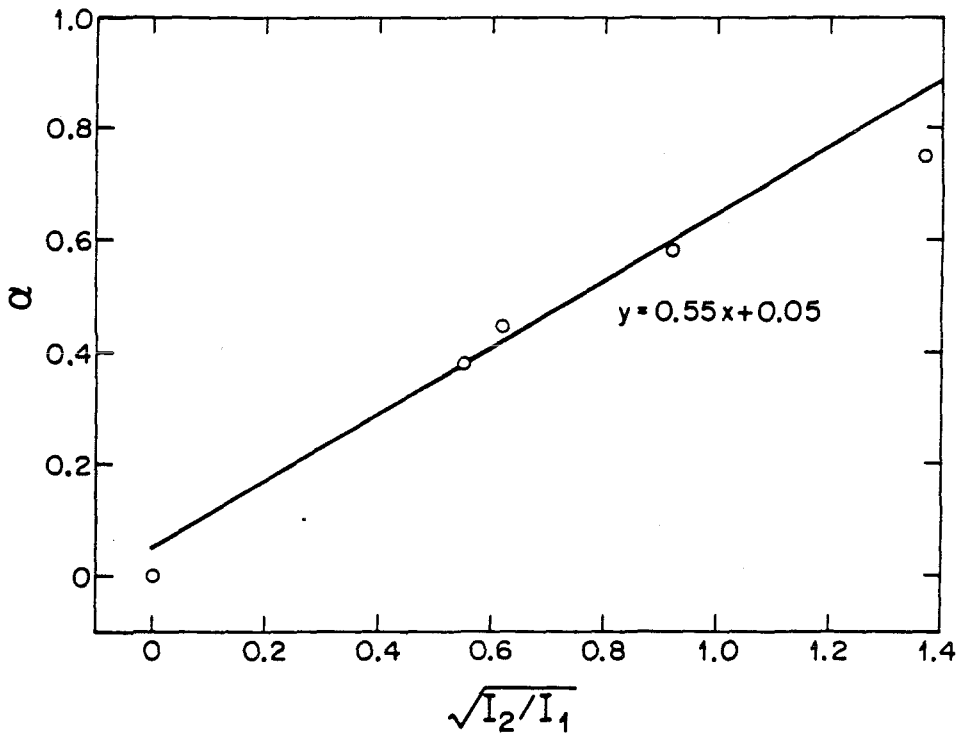

Figure 4.11 Dependence of α on $\sqrt{I_4^{(II)}/I_4^{(I)}}(\equiv |E_4^{(II)}/E_4^{(I)}|)$. The solid line is the best fit to the experimental data.

References for Chapter 4

4.1. R.A. Fisher, ed., *Optical Phase Conjugation* (Academic Press, New York, 1983).

4.2. M. Cronin-Golomb, B. Fischer, J.O. White, and A. Yariv, IEEE J. Quantum Electron. **QE-20**, 12 (1984).

4.3. S.-K. Kwong, M. Cronin-Golomb, and A. Yariv, IEEE J. Quantum Electron. **QE-22**, 1508 (1986).

4.4. B.Ya. Zel'dovich and V.V. Shkunov, Sov. J. Quantum Electron. **9**, 379 (1979).

4.5. A. Yariv, Opt. Commun. **25**, 23 (1978).

4.6. A. Yariv, IEEE J. Quantum Electron. **QE-14**, 650 (1978).

4.7. M.R. Belić, Opt. Lett. **12**, 105 (1987).

4.8. A. Bledowski and W. Krolikowski, IEEE J. Quantum Electron. **QE-24**, 652 (1988).

4.9. H. Kong, C. Lin, A.M. Biernacki, and M. Cronin-Golomb, Opt. Lett. **13**, 324 (1988).

4.10. B. Fischer and S. Weiss, Appl. Phys. Lett. **53**, 257 (1988).

4.11. W. Krolikowski, M.R. Belić, and A. Bledowski, Phys. Rev. **A37**, 2224 (1988).

4.12. R.W. Hellwarth, Prog. Quantum Electron. **5**, 1 (1977).

4.13. V.N. Blashchuk, B.Ya. Zel'dovich, A.V. Mamaev, N.F. Pilipetskii, and V.V. Shkunov, Sov. J. Quantum Electron. **10**, 356 (1980).

4.14. G. Martin, L.K. Lam, and R.W. Hellwarth, Opt. Lett. **5**, 185 (1980).

4.15. S. Saikan and M. Kiguchi, Opt. Lett. **7**, 555 (1982).

4.16. M.S. Malcuit, D.J. Gauthier, and R.W. Boyd, in *Technical Digest of XVI*

International Conference on Quantum Electronics (the Japan Society of Applied Physics, Tokyo, 1988), paper TuF2, p. 266; Opt. Lett. **13**, 663 (1988).

4.17. N.G. Basov, V.F. Efimkov, I.G. Zubarev, A.V. Kotov, S.I. Mikhailov, and M.G. Smirnov, Sov. Phys. JETP Lett. **28**, 197 (1978).

4.18. I. McMichael, M. Khoshnevisan, and P. Yeh, Opt. Lett. **11**, 525 (1986).

4.19. K. Kyuma, A. Yariv, and S.-K. Kwong, Appl. Phys. Lett. **49**, 617 (1986).

4.20. A. Yariv, Y. Tomita, and K. Kyuma, Opt. Lett.**11**, 809 (1986).

4.21. Y. Tomita, R. Yahalom, and A. Yariv, Opt. Lett. **12**, 1017 (1987).

4.22. Y. Tomita, R. Yahalom, and A. Yariv, J. Opt. Soc. Am. B**5**, 690 (1988).

4.23. Y. Tomita, R. Yahalom, K. Kyuma, A. Yariv, and N. S.-K. Kwong, IEEE J. Quantum Electron., **QE-25**, 315 (1989).

4.24. J.O. White, M. Cronin-Golomb, B. Fischer, and A. Yariv, Appl. Phys. Lett. **40**, 450 (1982).

4.25. M. Cronin-Golomb, B. Fischer, J.O. White, and A. Yariv, Appl. Phys. Lett. **41**, 689 (1982).

4.26. J. Feinberg, Opt. Lett. **7**, 486 (1982).

4.27. Recently, the ring SPPCM using internal reflection has been demonstrated by M. Cronin-Golomb and C.D. Brandle, in *Technical Digest of Annual Meeting of Optical Society of America* (Optical Society of America, Washington D.C., 1988), paper FY2, p. 180.

4.28. M.D. Ewbank and P. Yeh, Proc. of SPIE **613**, 11 (1986).

4.29. S. Weiss, S. Sternklar, and B. Fischer, Opt. Lett. **12**, 114 (1987).

4.30. R.W. Eason and A.M.C. Smout, Opt. Lett. **11**, 51 (1987).

4.31. M.D. Ewbank, Opt. Lett. **13**, 47 (1988).

4.32. A.E. Chiou, P. Yeh, and M. Khoshnevisan, Opt. Eng. **27**, 385 (1988), and

references therein.

4.33. J. Feinberg, Opt. Lett. **8**, 569 (1983).

4.34. R.W Boyd, T.M. Habashy, A.A. Jacobs, L. Mandel, M. Nieto-Vesperinas, W. Tompkin, and E. Wolf, Opt. Lett. **12**, 42 (1987); E. Wolf, L. Mandel, R.W. Boyd, T.M. Habashy, and M. Nieto-Vesperinas, J. Opt. Soc. Am. B**4**, 1260 (1987); A.A. Jacobs, W.R. Tompkin, R.W. Boyd, and E. Wolf, J. Opt. Soc. Am. B**4**, 1266 (1987).

4.35. M.D. Ewbank, P. Yeh, M. Khoshnevisan, and J. Feinberg, Opt. Lett. **10**, 282 (1985).

4.36. Y. Tomita, R. Yahalom, and A. Yariv, in *Technical Digiest of Annual Meeting of Optical Society of America* (Optical Society of America, Washington D.C., 1988), paper FB8, p. 161.

4.37. J. Feinberg, Opt. Lett. **8**, 480 (1983).

4.38. H.I. Mandelberg, Opt. Lett. **5**, 258 (1980).

CHAPTER
FIVE

Applications of Photorefractive Wave Mixing to Temporal and Spatial Information Processing

5.1 Introduction

Over the past years, a number of real-time information processing applications based on two-wave and four-wave mixing in photorefractive crystals have been reported. These include (a) temporal information processing (e.g., temporal differentiation and transient image detection), (b) spatial information processing (e.g., mathematical operations on images, distortion correction and interferometry), and (c) spatio-temporal information processing (e.g., optical interconnections and bidirectional communications). In this chapter, three applications to transient image detection, image subtraction, and one-way image transmission through distorting media are described.

5.2 Optical tracking filter using transient two-beam coupling

The two-beam coupling phenomena in photorefractive crystals [5.1] have been used for various novel applications, such as image amplification [5.1,2], unidirectional ring oscillators [5.3], optical limiters [5.4], beam cleanup [5.5], and beam steering [5.6]. Most of the proposed applications use steady-state energy coupling in photorefractive crystals with an induced index grating, which is $\pi/2$ phase shifted from the light-interference pattern. On the other hand, the transient behavior of the energy coupling (e.g., response time) is an important factor in characterizing device performance [5.7]. Transient energy coupling (TEC), including

the interaction between two coherent beams and the induced grating formation, has been studied theoretically, and approximate analytic [5.8 – 12] and numerical [5.13] solutions have been obtained. We have already shown in Chapter 3 that, although there is no steady-state energy exchange between the beams in unshifted dynamic holographic media, TEC occurs in such media with noninstantaneous responses. In particular, it is shown that TEC can be realized in photorefractive crystals by applying an appropriate external electric field and using large grating periods, i.e., by operating in the drift regime.

In this section we demonstrate an optical tracking filter [5.14] based on TEC. First we qualitatively describe the physical origin of TEC by means of scalar steady-state two-beam coupling equations derived in Chapter 3. We then describe the experiment, which uses a photorefractive $Bi_{12}SiO_{20}$ (BSO) crystal with an external electric field.

Let us consider the steady-state two-beam coupling. We rewrite the corresponding equations given by Eqs. (3.10*a*) – (3.10*d*) [see also Fig. 5.1(a)]:

$$\frac{dI_+}{ds} = \Gamma\frac{I_+I_-}{I_0} - \alpha I_+, \tag{5.1a}$$

$$\frac{dI_-}{ds} = -\Gamma\frac{I_+I_-}{I_0} - \alpha I_-, \tag{5.1b}$$

$$\frac{d(\delta\psi)}{ds} = \Gamma'\frac{(I_+ - I_-)}{I_0}, \tag{5.1c}$$

where $s = z/\cos\theta'$, $I_0 = I_+ + I_-$, $\delta\psi = \psi_+ - \psi_-$, I_+ and I_- (ψ_+ and ψ_-) are the intensities (phases) of the interacting beams, respectively, α is the linear absorption coefficient, and $\Gamma[= 2Re(\gamma)]$ and $\Gamma'[= Im(\gamma)]$ are the real and imaginary parts, respectively, of the (complex) two-beam coupling constant γ, which for a degenerate case at a frequency ω, is given by Eq. (3.8) for scalar two-beam coupling and is rewritten as

$$\gamma = \frac{\omega r_{eff} n_0^3}{2c}\Xi_{sc}. \tag{5.2}$$

In Eq. (5.2) r_{eff} is the relevant effective electrooptic coefficient given by

$$r_{\text{eff}} = \frac{1}{n_\lambda n_0^3}(\mathbf{e}_1^* \cdot \Delta\tilde{q} \cdot \mathbf{e}_2)(\mathbf{e}_1 \cdot \mathbf{e}_2^*), \tag{5.3}$$

where $n_\lambda, \mathbf{e}_1, \mathbf{e}_2$, and $\Delta\tilde{q}$ are given in Section 3.3 of Chapter 3, n_0 is the ordinary refractive index of the crystal, and Ξ_{sc} is given, for example, by Eq. (3.9). From Eqs. (3.9) and (5.2), when E_0=0 or $E_0 \gg E_D, E_{qe}$, Γ is finite and Γ'=0 (because Ξ_{sc} is real). This is the case when the index grating is $\pi/2$ phase shifted from the light-interference pattern and steady-state energy coupling occurs. (Remember that a space-charge electric field E_{sc} is given by $-im\Xi_{sc}$, where m is a modulation index of the light-interference pattern.) On the other hand, when the intermediate fields $E_0(\neq 0)$ and large grating periods are used, there exists a region where Ξ_{sc} is nearly pure imaginary so that $|\Gamma'| \gg |\Gamma|$. This corresponds to the unshifted (local) grating case, in which from Eq. (5.1) there is almost no energy transfer but phase transfer between the interacting two beams provided that $I_+ \neq I_-$. Because of the phase transfer, the equiphase contour of the index grating is tilted with respect to the z axis in the crystal in the steady state (t=0) [Fig. 5.1(a)]. If there is any change in the input-beam intensities, the light-interference pattern will modify its position according to Eq. (5.1*c*). In this case, for a medium with noninstantaneous response, a transient phase mismatch between the light-interference pattern and the index grating is created in the time period $0 < t < \tau$ (τ is the medium response time) [Fig. 5.1(b)]. This phase mismatch is responsible for TEC between the interacting beams. When the input-beam intensities become stationary at the time $t \gg \tau$, the index grating catches up with the change of the light-interference pattern. As a result, TEC then ceases [Fig. 5.1(c)]. Therefore the conditions for TEC can be listed as follows:

1. The medium possesses the unshifted index grating with respect to the light-interference pattern and does not respond instantaneously, i.e., $\tau \neq 0$;

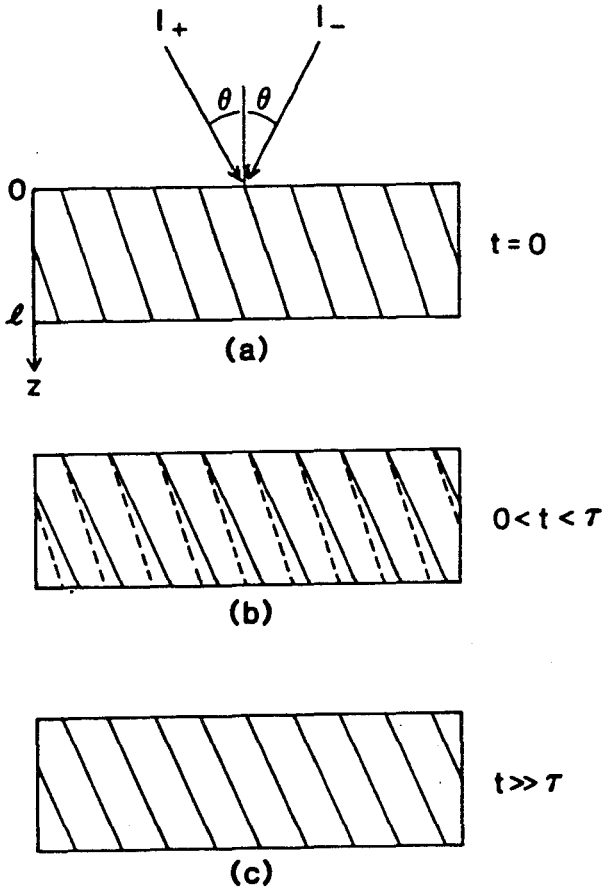

Figure 5.1 Diagram to illustrate the dynamics of the holographic index grating formation. Solid lines indicate light-interference fringes, and dashed lines indicate index gratings. (a) $t = 0$ (both lines overlap), (b) $0 < t < \tau$, and (c) $t \gg \tau$ (both lines overlap).

2. The intensities of the two beams are different at z=0, i.e., $I_+(0) \neq I_-(0)$.

The approximate analytical expression for the amount of TEC under a lumped change of the input beam is given by Eq. (3.12). In the drift regime for the formation of the photorefractive grating it can be written as [see Eq. (3.15)]

$$I_\pm(l) - I_\pm(0) \propto \mp[I_+(0) - I_-(0)]I_+(0)I_-(0)\exp(-\frac{t}{\tau})[\frac{t}{\tau} + \exp(-\frac{t}{\tau}) - 1], \quad (5.4)$$

where τ is given by Eq. (2.17a). Equation (5.4) indicates that the energy transfer always occurs from the stronger beam to the weaker beam. A typical plot of the energy transfer versus the normalized time t/τ is shown in Fig. 5.2. The maximum energy transfer occurs at $t \simeq 1.59\tau$. When τ is small enough to follow a sudden change in the input-beam intensities, TEC can be approximated as the temporal differentiation of input information. In what follows we describe the experimental demonstration of an optical tracking using TEC.

Figure 5.3 shows the experimental setup. The photorefractive BSO crystal (10mm × 10mm × 3mm) was used. An external electric field E_0 (=6 kV/cm) was applied along the crystal < 001 > direction to ensure that the formation of photorefractive gratings was in the drift regime. With this external electric field, the amplitude of the space-charge electric field is high for the grating periods $\Lambda > 5$ μm, and the phase shift between the index grating and the light-interference pattern is less than 0.1 rad [5.15,16]. These features are depicted in Figs. 5.4(a) and 5.4(b). In these figures we used $E_{sc} \equiv |E_{sc}|e^{i\Psi} \approx -i\Xi_{sc}$ (i.e., $m/(1+\beta_e\hbar\omega/s_eI_0) \approx 1$) together with the relevant material constants shown in Table 5.1. The time constant τ in Eq. (5.4) is also shown in Fig. 5.5. We see that the larger the grating period is, the smaller τ is. This is because BSO is a long drift length material like GaAs (see also Fig. 3.13). A single-longitudinal-mode argon-ion laser (λ = 0.5145 μm, 500 mW output power) was expanded and divided by a beam splitter BS. The higher intensity beam I_- passed through a transparency T and was imaged onto

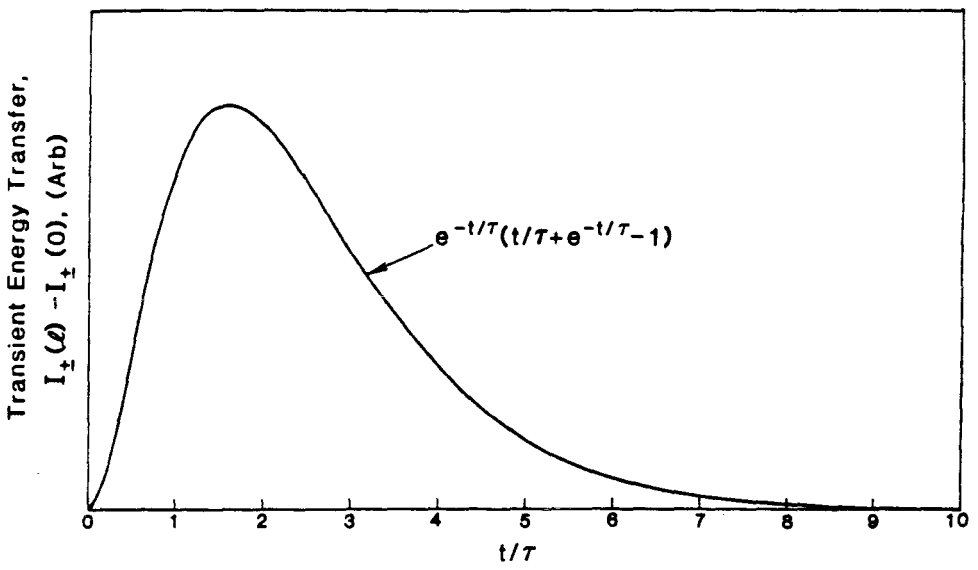

Figure 5.2 Dependence of transient energy transfer on the normalized time t/τ.

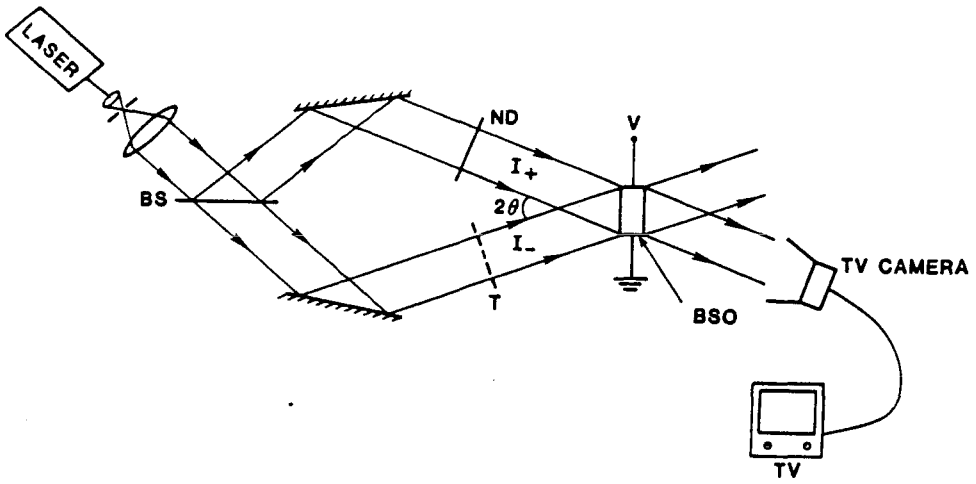

Figure 5.3 Experimental setup to demonstrate the optical tracking filter.

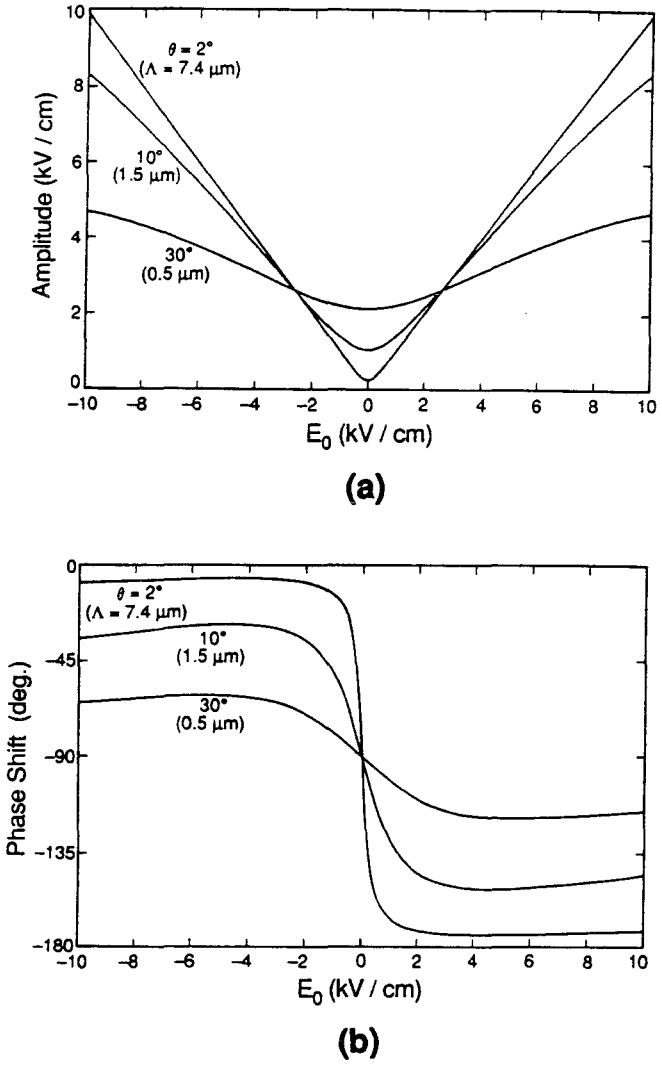

Figure 5.4 Dependence of the space-charge electric field E_{sc} on an external electric field E_0 for grating periods of $\Lambda = 0.5$, 1.5 and 7.4μm. The incident angle between the two input beams is denoted by θ for each grating period. (a) The amplitude $|E_{sc}|$ of E_{sc}. (b) The phase Ψ of E_{sc}.

Table 5.1 Relevant material constants of BSO.

Material Constants	Values
ϵ_s	56
μ_e	$0.03 cm^2/V \cdot sec$
τ_{Re}	$5 \times 10^{-6} sec$
τ_{de}	$5 \times 10^{-5} sec$
$N_{Te}(\approx N_a^-)$	$2 \times 10^{16} cm^{-3}$
T	300°K
λ	$0.5145 \mu m$

[a] See Chapter 2 for the definition of the above parameters.

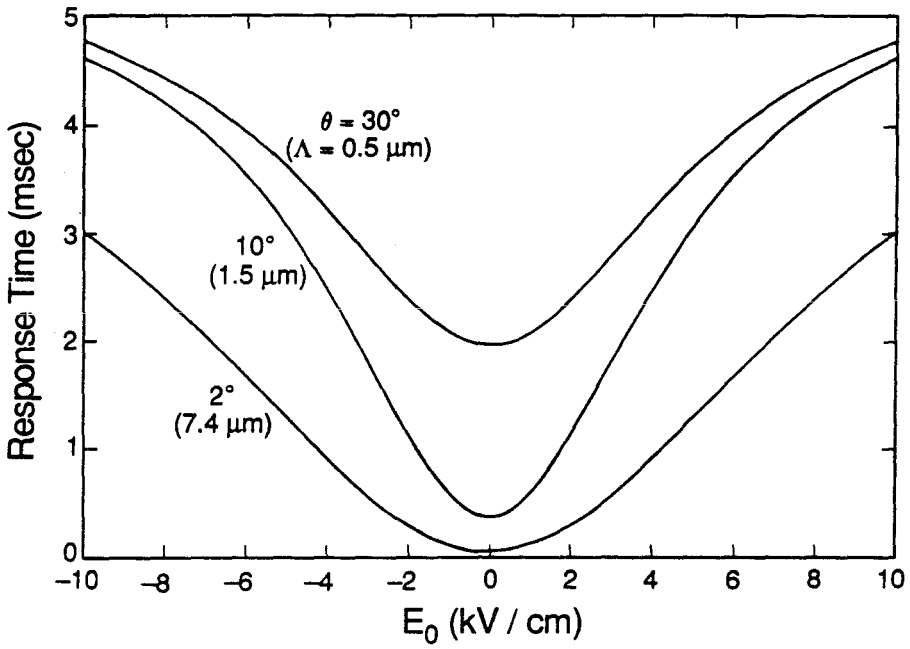

Figure 5.5 Dependence of the time constant τ of the space-charge electric field E_{sc} on an external electric field E_0 for grating periods of $\Lambda = 0.5, 1.5,$ and 7.4 μm. The incident angle between the two input beams is denoted by θ for each grating period.

the crystal $(1\bar{1}0)$ surface. A neutral-density filter ND was inserted into the path of the other uniform beam I_+ and the ratio I_-/I_+ was set to approximately 10. According to Fig. 5.4, the angle between the two beams was chosen to be $2\theta \simeq 1.5°$ so that TEC was enhanced. The measurement of the steady-state two-beam coupling gain versus the input-beam polarization was made beforehand. We found that the gain was nearly maximum when the linear polarization was close to the crystal $< 001 >$ direction (see Fig. 5.6). This is so because BSO has large optical activity by which the polarization direction of the incident beam is rotated by 95° after propagation in the crystal. The beam I_+ transmitted through the crystal was imaged onto a TV camera.

The I_- beam carrying the pictorial information of the letter O from the transparency is shown in Fig. 5.7(a). Some defects on the crystal surface can be seen. When the transparency is moving across the beam I_-, the corresponding letter O appears on the output beam I_+ [Fig. 5.7(b)]. Subsequently, when the transparency returns to rest, only the uniform intensity distribution of the output beam I_+ is seen [Fig. 5.7(c)]. Figure 5.7(d) shows the output beam I_+ when the optical table is shaken with the transparency at rest. In this case the letter O is also seen. The response time in this experiment was found to be faster than 100 msec. From these figures the tracking novelty operation (in other words, the temporal differentiation) of the moving object is apparent.

An optical tracking filter using a phase-conjugate interferometer together with the spatial light phase modulator was reported by Anderson *et al.* [5.17]. The time constant of their device was limited by the time response of the phase conjugator. Cronin-Golomb *et al.* [5.18] and Ford *et al.* [5.19] reported optical tracking filters based on two-beam coupling in photorefractive crystals with nonlocal $\pi/2$ phase shifted gratings. Cudney *et al.* [5.20] also reported a transient detection microscopy

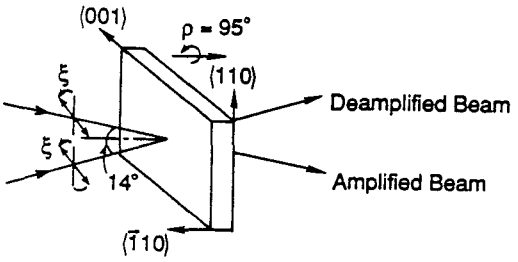

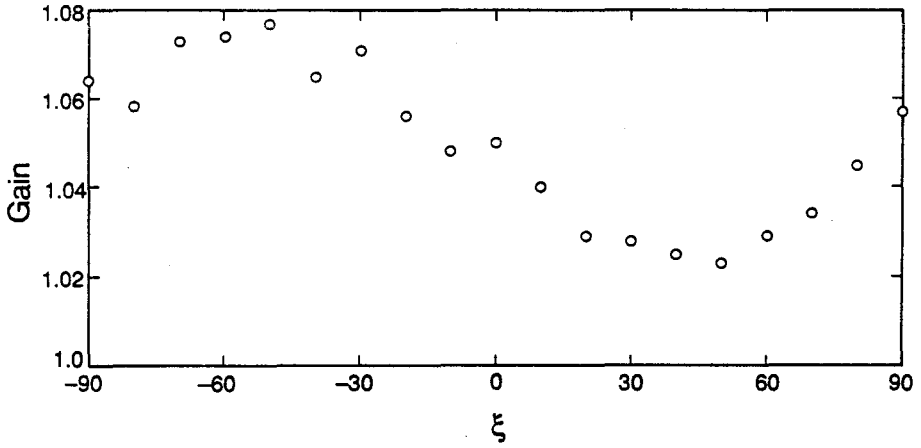

Figure 5.6 Experimental result of dependence of the two-beam coupling gain on the polarization direction of the input beams. The direction of linear polarization with respect to the crystallographic < 110 > axis of BSO is denoted by ξ.

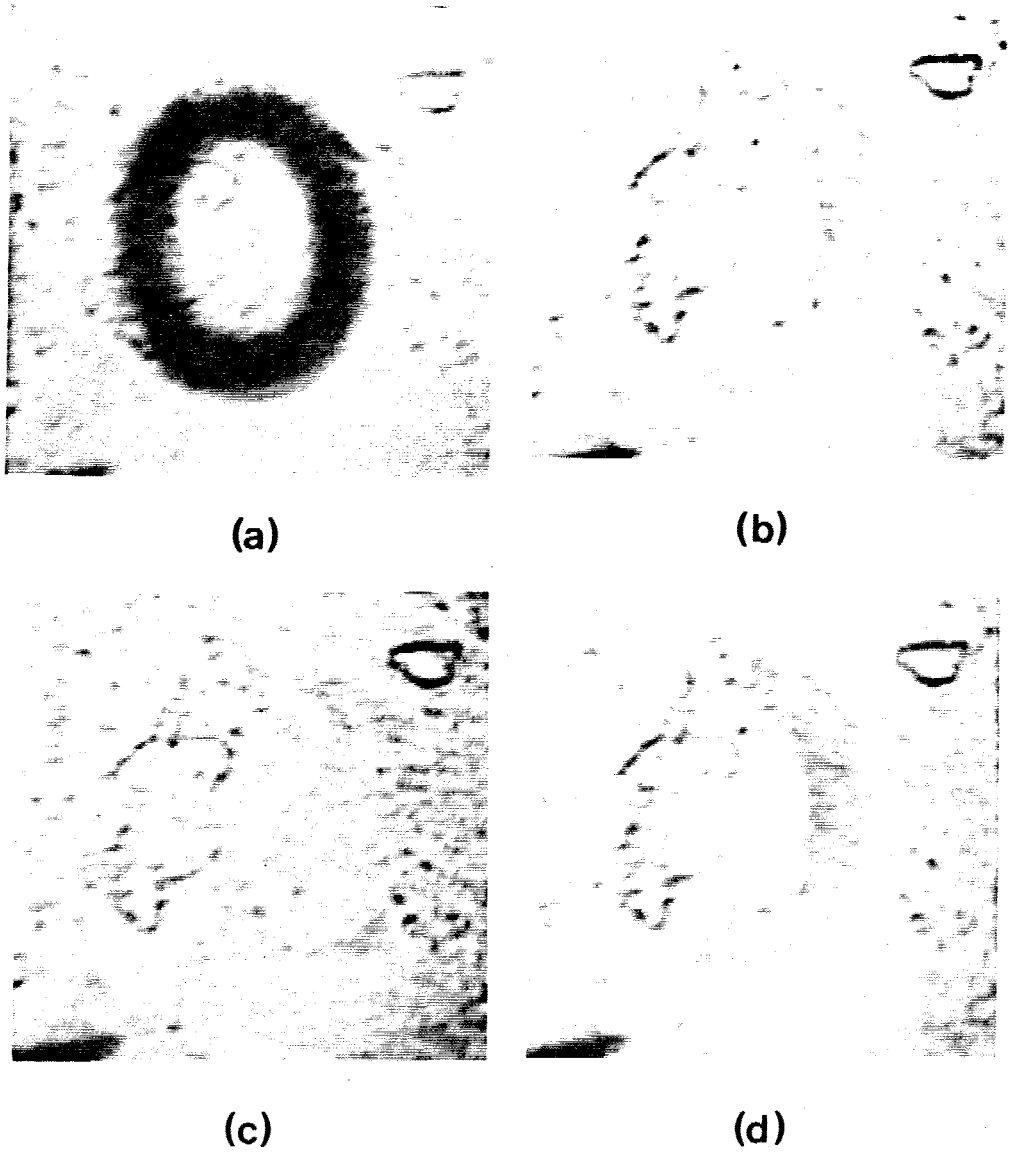

Figure 5.7 (a) The I_- beam transmitted through the crystal. This beam carries the pictorial information of the letter O. (b) The I_+ beam recorded when the transparency was moving across the beam I_-. (c) The I_+ beam recorded subsequently when the transparency returned to rest. (d) The I_+ beam recorded when the optical table was shaken with the transparency at rest.

using the above effect. In these schemes $BaTiO_3$ crystals (whose response time is typically of the order of 0.1 – 1 sec for an input intensity of 100 mW/cm^2 at visible wavelengths) were used to obtain either large phase-conjugate reflectivities or large steady-state two-beam coupling gains for better contrast of the output images. In our scheme, faster response materials, such as a Kerr medium, can be used. The contrast of the output image can be improved by increasing the intensity difference between the two input beams. The uniform background in the signal beam I_+ can be reduced by cross-polarization beam coupling in cubic crystals [5.21] (see Chapter 3). Another possible advantage of our scheme is that, as in Cronin-Golomb's and Ford's schemes, it utilizes a simple spatial light intensity modulator such as a commercially available liquid-crystal television without any modification.

5.3 Real-time image inversion, subtraction and addition using wave polarization and phase conjugation

Over the past years several methods of optical image subtraction have been reported [5.22,23]. Most of them have employed either conventional interferometric techniques or spatial light modulators for real-time operation. Kwong *et al.* [5.24] and Chiou *et al.* [5.25,26] have employed the phase-conjugate interferometric method for real-time image processing. Because of the use of phase conjugation, their method, based on the Stokes principle of the time reversibility of light for any lossless dielectric mirror, has two advantages over conventional interferometric methods: the temporal stability of the operation against fluctuations in the optical path length of the two arms and the insensitivity against phase irregularities of input images. However the method requires *equal* amplitude phase-conjugate reflectivities and/or losses for both inputs for image subtraction, and image subtraction and addition are obtained at two different places.

In this section we describe a method of real-time image subtraction, addition

and intensity inversion using two orthogonally polarized image-bearing phase-conjugate waves [5.27]. This method in fact enables us to obtain any linear combination of the two images at the same plane by simply rotating an analyzer. The need for equal reflectivities and/or losses in the two arms of the phase-conjugate interferometer is obviated in this method. The basic idea is shown in Fig. 5.8. A linearly polarized beam is divided into two orthogonal beams by a polarizing beam splitter PBS. The two linearly polarized beams pass through transparencies T_1, T_2 and are reflected by phase-conjugate mirrors PCM_1 and PCM_2, respectively. After retracing their paths backward, the two phase-conjugate beams are combined into one beam that has two orthogonal polarizations and spatial information: one polarization for T_1 and the other for T_2. This phase-conjugate beam is then picked off by a beam splitter BS and passes through an analyzer A rotated by an angle θ from the y axis. The intensity at a plane S is then given by

$$I(x,y) = |(c_1 r_1 |T_1|^2 \cos\theta + c_2 r_2 |T_2|^2 \sin\theta)|^2, \tag{5.5}$$

where c_1 and c_2 denote complex constants due to the reflection and transmission at the BS and the PBS, and r_1 and r_2 denote amplitude phase-conjugate refrectivities of the PCM_1 and the PCM_2, respectively. Rewriting Eq. (5.5), we have

$$I(x,y) = |c_1|^2 |r_1|^2 \cos^2\theta |(|T_1|^2 + \rho \tan\theta |T_2|^2)|^2, \tag{5.6}$$

where $\rho \equiv c_2 r_2 / c_1 r_1$. Therefore for real ρ we obtain image subtraction

$$I(x,y) \propto ||T_1|^2 - |T_2|^2|^2,$$

when the analyzer is rotated to

$$\theta_{sub} = -\tan^{-1}(\frac{1}{\rho}),$$

and image addition

$$I(x,y) \propto ||T_1|^2 + |T_2|^2|^2,$$

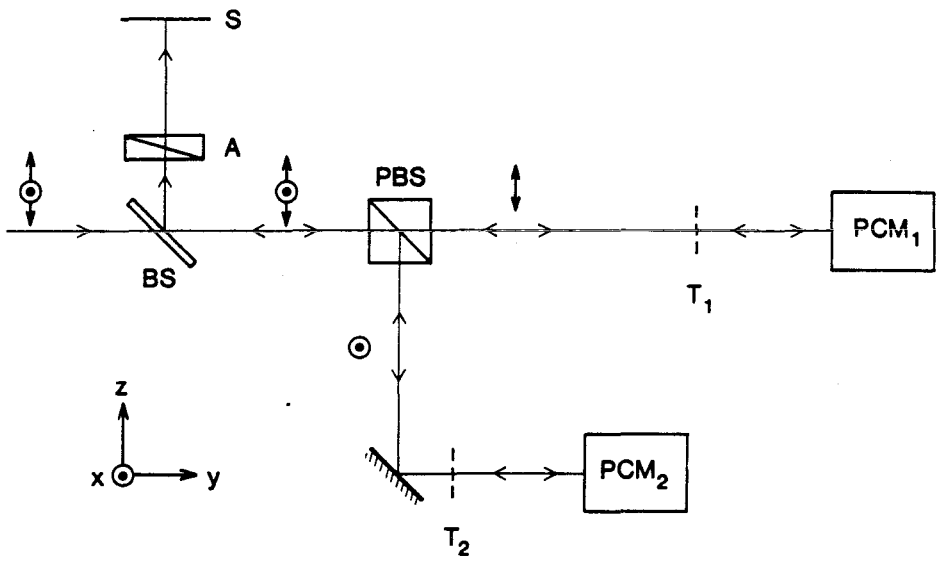

Figure 5.8 Schematic of image subtraction using polarization and phase conjugation.

when

$$\theta_{add} = \tan^{-1}(\frac{1}{\rho}).$$

Note that any other linear combination can also be achieved by simply varying the angle θ. It should also be noted that even when ρ is complex, e.g. $arg(r_1) \neq arg(r_2)$, the above conditions can easily be realized by placing a phase plate in front of the analyzer A. Since the present method is, as mentioned before, valid even when $r_1 \neq r_2$ and/or $c_1 \neq c_2$, low-cost liquid crystal televisions (LCTV's) [5.28] can easily be incorporated as input spatial light modulators without any modification [5.29].

The experimental arrangement is shown in Fig. 5.9. The multilongitudinal-mode argon ion laser beam(λ = 514.5 nm) of linear polarization was collimated by a beam-expanding system BE and divided into two orthogonally polarized beams by the PBS. In our experiment the double phase-conjugate mirror (DPCM) [5.30] configuration was used for phase conjugating two beams. The DPCM of the zero internal reflection type was used (see also Fig. 4.3(a) for this particular geometry). We note that a fiber-coupled phase-conjugate mirror [5.31,32] or a polarization-perserving phase conjugator [5.33] can also be used for this purpose. However, one big advantage of the present DPCM scheme is the large tolerance of the temporal coherence requirement between the two beams [5.30]. In the experiment the path difference between the two beams was chosen to be about 50cm, which is much larger than the coherence length of the laser (a few cm), so that stable phase conjugation can be obtained. After the PBS one beam of horizontal (in the y - z plane) polarization passed through the transparency T_1 and was loosely focused into a 45°-cut $BaTiO_3$ crystal (see Fig. 5.9) by a lens L_1 (f = 500 mm) with the angle of about 11°. Similarly, the other beam of vertical polarization passed through the transparency T_2 after it was converted into the horizontal polarization by a $\lambda/2$ plate. It was loosely focused into the crystal by a lens L_2 (f=120mm) with an angle

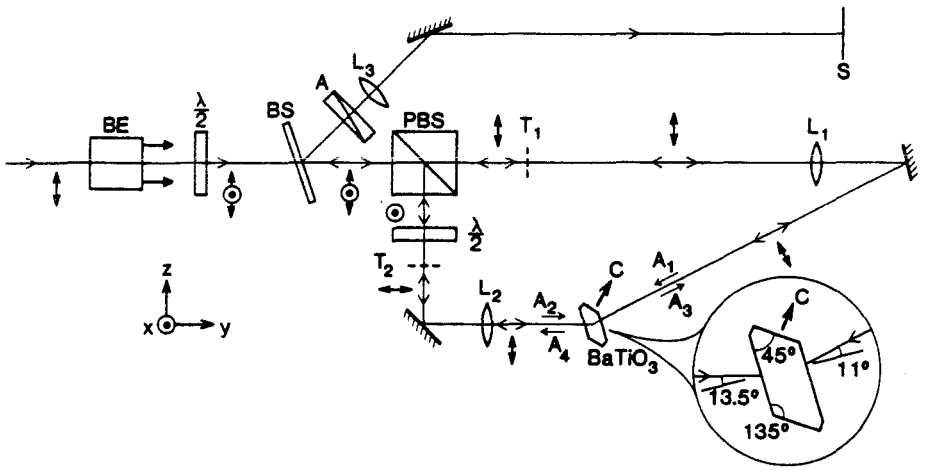

Figure 5.9 Experimental arrangement. The double phase-conjugate mirror (DPCM) configuration is used.

of about 13.5°. The phase-conjugate beams ($A_3 = r_1 A_1^*$ and $A_4 = r_2 A_2^*$) retrace their paths backward to the PBS, where they are combined into a single beam. The phase-conjugate reflectivities of the two beams were $|r_1|^2 = 0.08$ and $|r_2|^2 = 1.07$ for $|A_1|^2 = 1.7$ mW and $|A_2|^2 = 0.4$ mW, respectively, when binary transparencies of "A" and "Λ" were used as T_1 and T_2. It should be noted that although the two input beams A_1 and A_2 are mutually incoherent at the crystal, they can be coherently combined at the PBS after phase conjugation, since the phase-conjugate beams A_3 and A_4 are essentially due to the diffraction of the incident beams A_2 and A_1, respectively [5.30]. Therefore the present system can be regarded as a common-path polarization interferometer with phase conjugation. The beam after the PBS was imaged by a lens L_3 (f = 200 mm) onto the plane S through the analyzer A. We measured beforehand the possible relative phase difference between A_3 and A_4 upon phase conjugation at the crystal by means of the ellipsometric method at the plane S. The effect of the BS was also taken into account. The results are shown in Fig. 5.10, together with the reflectivities of $R_1 \equiv |r_1|^2$ and $R_2 \equiv |r_2|^2$. It is seen that the relative phase difference $\Delta\phi\ (\equiv \phi_3 - \phi_4 + \phi_1 - \phi_2)$ resulting from the photorefractive phase shift is as small as about 10° for the incident beam ratios $q\ (\equiv |A_1/A_2|^2) = 0.1 - 13$. Consequently, the combined phase-conjugate beam is almost linearly polarized as long as the input beam is linearly polarized.

Figure 5.11 shows the experimental results of image subtraction and addition. The phase-conjugate images of the binary transparencies of "A" and "Λ" are shown in Figs. 5.11(a) ($\theta = 0°$) and 5.11(b) ($\theta = 90°$), respectively. Figures 5.11(c) and 5.11(d) show image subtraction ($\theta = -41.5°$) and addition ($\theta = 41.5°$), respectively. Figure 5.12 shows intensity inversion when a U.S. Air Force Resolution Chart is used for the transparency T_2 with the transparency T_1 removed.

The present new method allows reliable and stable results with almost complete flexibility for the system parameters (e.g., reflectivities and losses). It is also

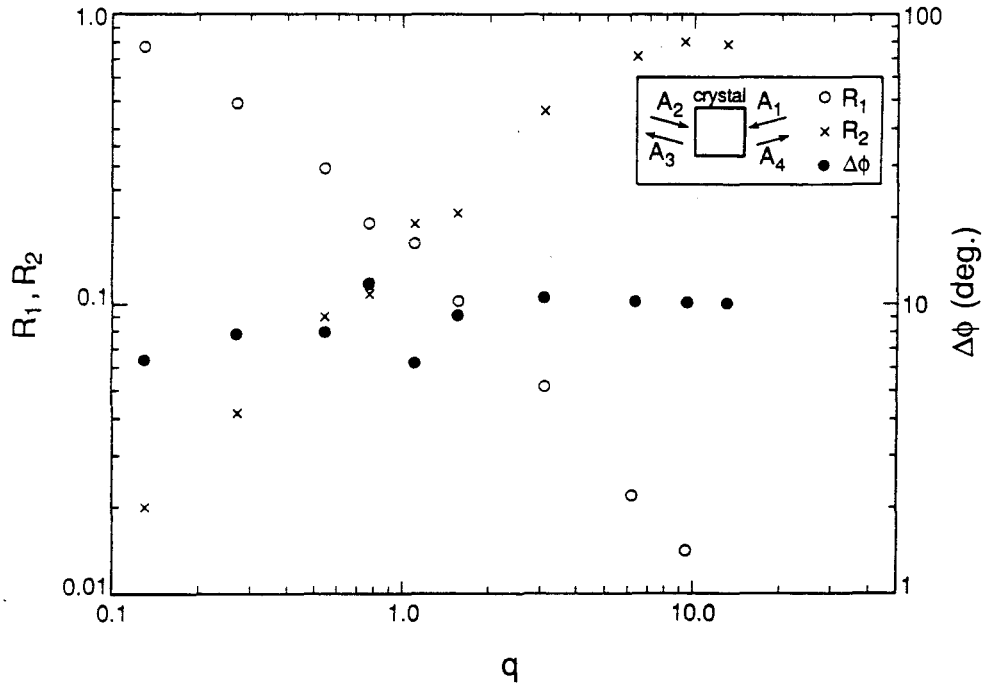

Figure 5.10 Phase-conjugate reflectivities $R_1(\equiv |A_3|^2/|A_1|^2)$ and $R_2(\equiv |A_4|^2/|A_2|^2)$ and relative phase difference $\Delta\phi(\equiv \phi_3 - \phi_4 + \phi_1 - \phi_2)$ as a function of $q(\equiv |A_1|^2/|A_2|^2)$.

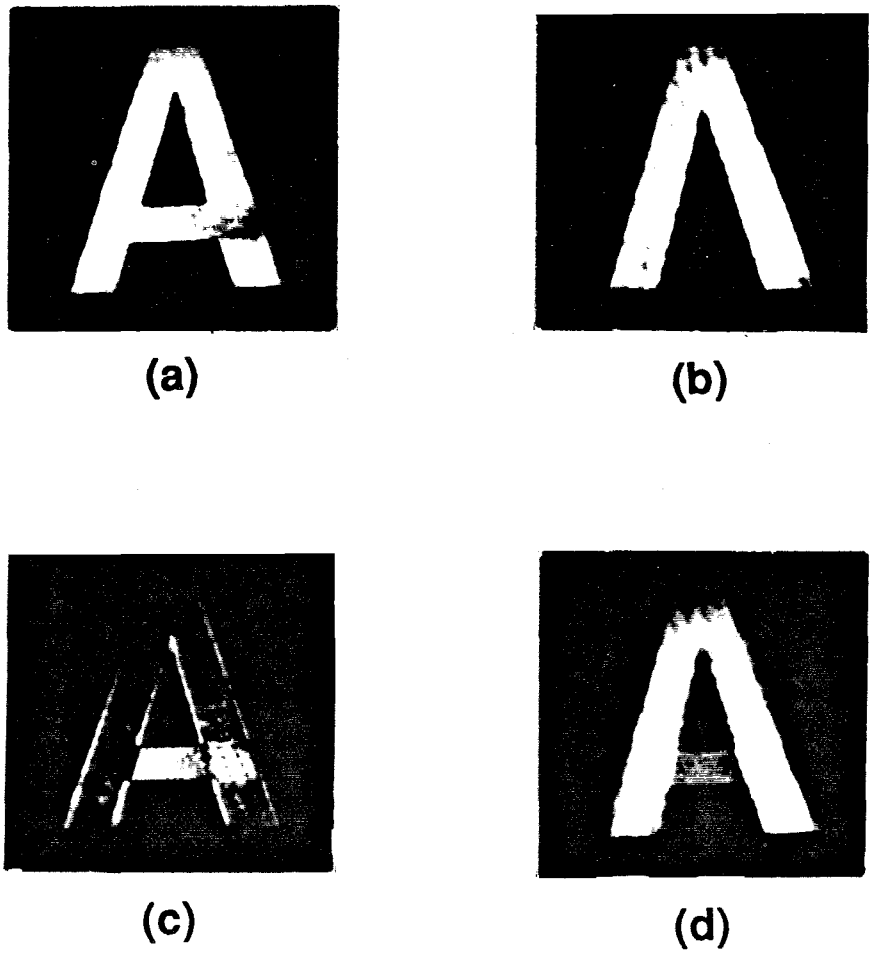

Figure 5.11 (a) Phase-conjugate image "A", (b) phase-conjugate image "Λ", (c) image subtraction, and (d) image addition.

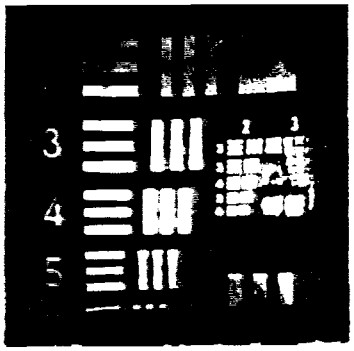

(a)

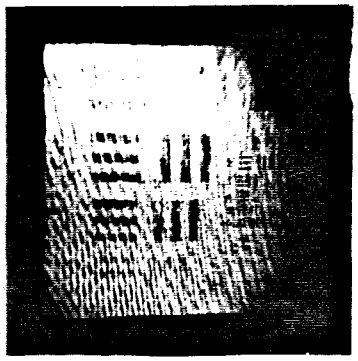

(b)

Figure 5.12 (a) Phase-conjugate image of the resolution chart, and (b) intensity inversion of the resolution chart.

applicable to "exclusive or (XOR)" logic operation and image differentiation [5.24]. In addition, since the present system acts as a phase-conjugate common-path interferometer, a phase-conjugate multimode fiber-optic Sagnac interferometer can be constructed for rotation sensing applications [5.32,33] if multimode fiber coils are incorporated into the beam paths in the system. In this scheme the fast phase modulation for biasing (i.e., for obtaining better signal-to-noise ratio) can be employed since the DPCM prefers mutually incoherent inputs for stable phase-conjugate reflection.

5.4 One-way image transmission through distorting media using orthogonally polarized beams and phase conjugation

Transmission of an image through a phase-distorting medium has been demonstrated using phase conjugation [5.35 – 38]. This has been done by retracing the distorted image-bearing signal back through the distorter using a phase-conjugate mirror in a double-pass configuration. Since this method requires the signal to be received in the same half space as the source, several single-pass schemes, where the signal passes through the distorter only once, have also been suggested [5.39 – 43]. Recently, a further simplification of this method, where the receiver does not need access to the space beyond the distorter, has been demonstrated by impressing nearly the same distortion as that in the signal beam onto a separate beam and combining them in a degenerate four-wave mixing configuration [5.44]. In this method, however, only a slowly (spatially) varying phase distortion can be corrected since the two beams are spatially separated at the distorter. In this section, we describe a method which obviates this problem by using two orthogonally polarized beams traveling exactly the same path through the distorter [5.45,46].

The method relies on the nonlinear polarization in a four-wave mixing setup to eliminate the distorted phase factor $e^{i\phi(x,y)}$ at the nonlinear medium and therefore

reconstruct the original information. Consider photorefractive four-wave mixing in the crystal shown in Fig. 5.13. The index change Δn inside the crystal is given by Eqs. (2.32) and (2.34) and is proportional to the modulation index via the space-charge electric field. Assuming a scalar four-wave mixing, we can write

$$\Delta n \propto \frac{E_1 \cdot E_3^*}{|E_1|^2 + |E_3|^2}, \tag{5.7}$$

where E_1 is the reference beam and E_3 is the signal beam possessing the distorted image information. Then, the nonlinear polarization P_{NL} arising from the four-wave mixing is proportional to [see Eqs. (2.30) and (2.34)]

$$\begin{aligned} P_{NL} &\propto \Delta n E_2 \\ &\propto \frac{E_1 \cdot E_3^*}{|E_1|^2} E_2 \qquad \text{if } |E_1| \gg |E_3|, \end{aligned} \tag{5.8}$$

where E_2 is the uniform readout beam propagating opposite to E_1. Therefore the phase distortion superimposed on the signal can be eliminated at the crystal if the reference beam has the same distorted phase factor $e^{i\phi(x,y)}$ as that of the signal beam impressed at the distorter and that phase factor is preserved at the crystal.

The setup for the system is shown in Fig. 5.14. An argon-ion laser operating at $\lambda = 514.5$ nm was used as a light source. One of the two beams leaving the beam splitter BS_2 was converted to an orthogonal (vertical) polarization by the $\lambda/2$ plate. One became the signal beam and the other served as the reference. The two were recombined at BS_3 and both pass through the phase distorter, which was an acid-etched glass. This way, both beams underwent the same phase distortion, which insured that the distorted phase information carried by the two beams was identical. When two spatially separate beams are used, as is the case in Ref. [5.44], it is more difficult to insure that this occurs.

As previously mentioned, it is necessary to avoid phase mixing due to Fresnel diffraction during propagation, and to preserve the distorted phase factor, $e^{i\phi(x,y)}$

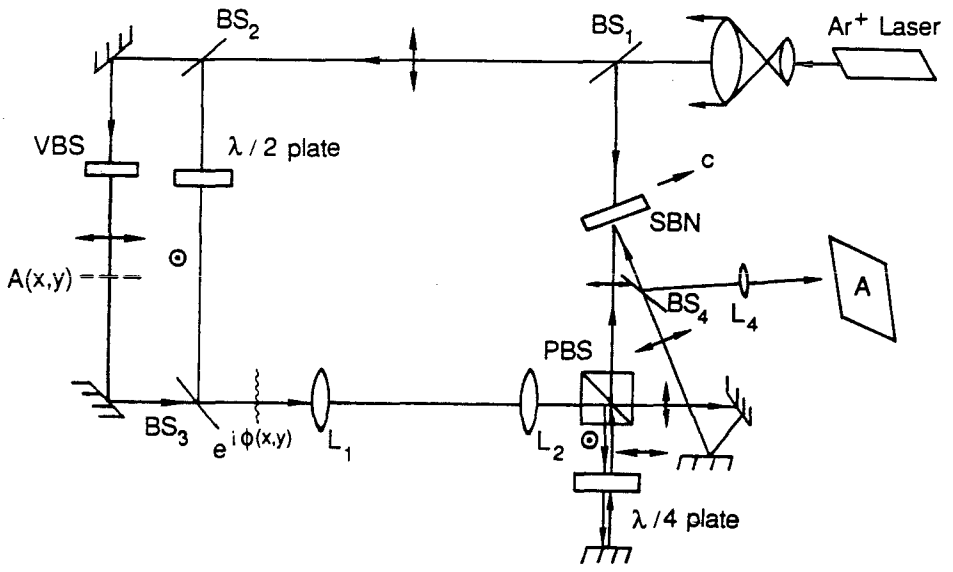

Figure 5.14 Experimental setup for the passive one-way transmission system using orthogonally polarized signal and reference beams. The variable beam splitter (VBS) was used to vary the intensity ratio of the signal and reference. The $\lambda/2$ plate rotates the polarization of the reference to the vertical direction, and the two passes through the $\lambda/4$ plate restores it to horizontal polarization so the two beams can write the grating. The readout beam was picked off from the same argon-ion laser source, but can be from a different laser as well.

at the nonlinear medium, in this case a 10mm × 10mm × 1mm photorefractive strontium barium niobate (SBN) crystal. This necessitates the imaging of the distorter onto the crystal. In addition, the distorter must be thin enough to fall within the depth of focus of the imaging system. In this experiment, the telecentric imaging geometry was used to circumvent unwanted wavefront curvatures at the image plane [5.47]. Two lenses of focal length $f = 40$ cm were used, with the lenses spaced 80 cm apart. The distances from the distorter to lens L_1 and from lens L_2 to the crystal were both 40 cm.

After passing through the lenses, the two beams are separated by the polarizing beam splitter (PBS) and the vertically polarized component is rotated again by 90° in a double-pass through the $\lambda/4$ plate so the two beams can write a *distortion-free* grating in the crystal by perfect calcellation of $e^{i\phi(x,y)}$. The beam intensities were chosen as $I_{ref} = 16$ mW/cm^2 and $I_{sig} = 4$ mW/cm^2, so that the grating Δn, and also the nonlinear polarization P_{NL}, in the crystal are proportional to E_3^* [see Eqs. (5.7) and (5.8)]. The second mirror is necessary in the leg that is transmitted through the PBS so that the image is properly oriented. After the grating is written, a plane wave directed from behind the crystal and Bragg-matched with the grating is used for readout, and the reconstructed signal picked off by BS_4 is imaged onto the screen by lens L_3. We note that in order to create the photorefractive grating, the readout beam need not be coherent with the writing beams.

The results of the distortion correcting capability of this experiment are shown in Figs. 5.15. Figure 5.15(a) is the original image, and Fig. 5.15(b) is the image after the distorter. Figures 5.15(c) and 5.15(d) are the output images without and with the distorter, respectively. It is seen from Fig. 5.15(d) that the system has reconstructed the original image from the given information, and that the image quality with Fig. 5.15(c) is roughly the same.

This new method for passive one-way image transmission through a distorting

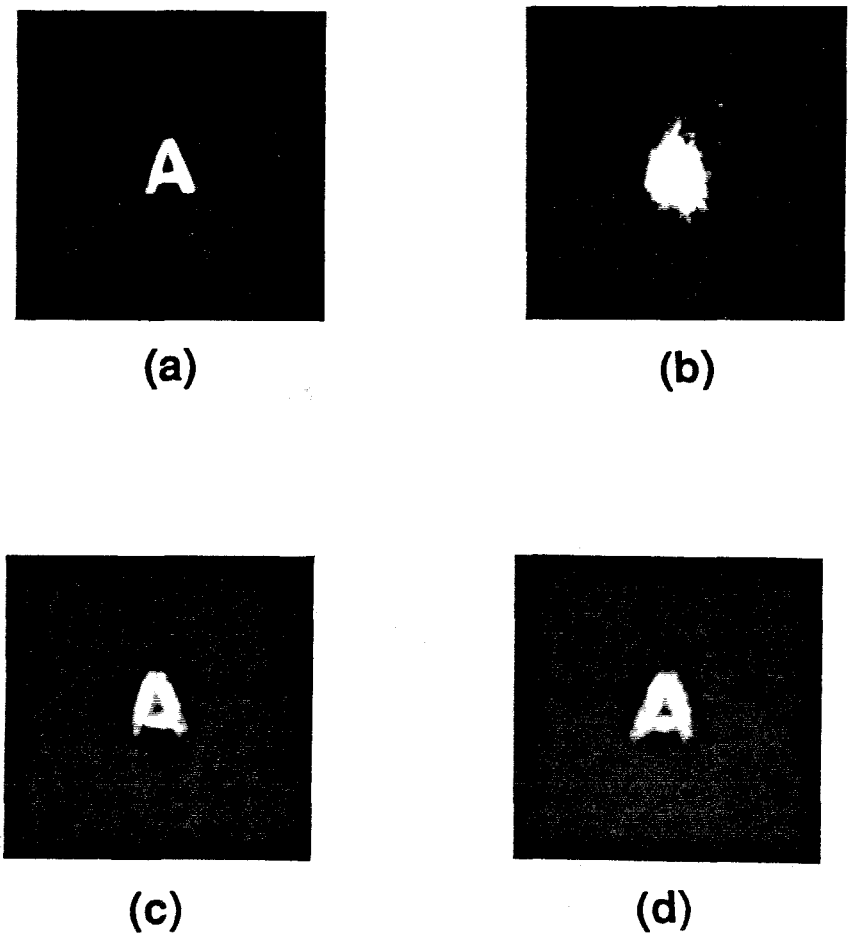

Figure 5.15 Experimental results showing the distortion correction capability of the system, where (a) is the original image, (b) is the image after the distorter, (c) is the phase-conjugate image without the phase distorter, and (d) is the corrected image as viewed on the screen.

medium uses two orthogonally polarized beams — one carrying the signal and the other probing the distortion in order to write the distortion-free grating in the crystal for the reconstruction of the original image by the independent readout beam. This procedure, although valid only for phase distortions in isotropic media, is useful in instances where it is not possible to retransmit the phase-conjugate signal back through the distorter in a double-pass configuration. We finally note that a single, circularly (or elliptically) polarized beam can also be used as the signal and reference beams in the present system instead of preparing the beams separately. In this case, however, the transparency as an input is limited to a binary one in order to maintain the original contrast.

References for Chapter 5

5.1. N.V. Kukhtarev, V.B. Markov, S.G. Odulov, M.S. Soskin, and V.L. Vinetskii, Ferroelect. **22**, 949, 961 (1979).

5.2. T. Tschudi, A. Herden, J. Goltz, H. Klumb, F. Laeri, and F. Albers, IEEE J. Quantum Electron. **QE-19**, 1493 (1986).

5.3. J.O. White, M. Cronin-Golomb, B. Fischer, and A. Yariv, Appl. Phys. Lett. **40**, 450 (1982).

5.4. M. Cronin-Golomb and A. Yariv, J. Appl. Phys. **57**, 4906 (1985).

5.5. A.E. Chiou and P. Yeh, Opt. Lett. **10**, 621 (1985); S.-K. Kwong and A. Yariv, Appl. Phys. Lett. **48**, 564 (1986).

5.6. D. Rak, I. Ledonx, and J.P. Huingnard, Opt. Commun. **49**, 302 (1984).

5.7. G.C. Valley and M.B. Klein, Opt. Eng. **22**, 704 (1983).

5.8. V.L. Vinetskii and N.V. Kukhtarev, Sov. Tech. Phys. Lett. **2**, 364 (1976).

5.9. V.L. Vinetskii, N.V. Kukhtarev, and M.S. Soskin, Sov. J. Quantum. Electron. **7**, 230 (1977).

5.10. N. Kukhtarev, V. Markov, and S. Odulov, Opt. Commun. **23**, 338 (1977).

5.11. L. Solymar and J.M. Heaton, Opt. Commun. **51**, 76 (1984).

5.12. M. Cronin-Golomb, in *Technical Digest, Topical Meeting on Photorefractive Materials, Effects, and Devices* (Optical Society of America, Washington DC, 1987), paper ThC5, p. 142.

5.13. J.M. Heaton and L. Solymar, Opt. Acta. **32**, 397 (1985).

5.14. N. S.-K. Kwong, Y. Tomita, and A. Yariv, J. Opt. Soc. Am. B **5**, 1788 (1988).

5.15. M. Peltier and F. Micheron, J. Appl. Phys. **48**, 3683 (1977).

5.16. J.P. Huignard and A. Marrakchi, Opt. Commun. **38**, 249 (1981).

5.17. D.Z. Anderson, D.M. Linger, and J. Feinberg, Opt. Lett. **12**, 123 (1987).

5.18. M. Cronin-Golomb, A.M. Biernacki, C. Lin, and H. Kong, Opt. Lett. **12**, 1029 (1987).

5.19. J.E. Ford, Y. Fainman, and S.H. Lee, Opt. Lett. **13**, 856 (1988).

5.20. R.S. Cudney, R.M. Pierce, and J. Feinberg, Nature **332**, 424 (1988).

5.21. A. Partovi, E.M. Garmire, and L.J. Cheng, Appl. Phys. Lett. **51**, 299 (1987).

5.22. J.F. Ebersole, Opt. Eng. **14**, 436(1975); H.K. Liu and T.H. Chao, Proc. Soc. Photo-Opt. Instrum. Eng. **638**, 55 (1986).

5.23. F.T.S. Yu, S. Jutamulia, and D.A. Gregory, Appl. Opt. **26**, 2738 (1987).

5.24. S-K. Kwong, G.A. Rakuljic, and A. Yariv, Appl. Phys. Lett. **48**, 201(1986); S-K. Kwong, G.A. Rakuljic, V. Leyva, and A. Yariv, Proc. Soc. Photo-Opt. Instrum. Eng. **613**, 36 (1986).

5.25. A.E. Chiou and P. Yeh, Opt. Lett. **11**, 306 (1986).

5.26. A.E. Chiou, P. Yeh, and M. Khoshnevisan, Opt. Eng. **27**, 385 (1988).

5.27. Y. Tomita, R. Yahalom, and A. Yariv, Appl. Phys. Lett. **52**, 425 (1988).

5.28. H.K. Liu, J.A. Davis, and R.A. Lilly, Opt. Lett. **10**, 635 (1985).

5.29. In the novelty tracking filter experiment described in Ref. [5.17], a tandem combination of a $\lambda/4$ plate and the LCTV was used to approximately modulate relative phases between two orthogonal polarized components of a linearly polarized beam, together with a polarization-preserving phase conjugator which cancels these relative phase modulations at a steady state(i.e., when the input object is at rest). In our case each orthogonally polarized beam is amplitude-modulated and phase conjugated for the operations.

5.30. S. Weiss, S. Sternklar, and B. Fischer, Opt. Lett. **12**, 114 (1987).

5.31. Y. Tomita, R. Yahalom, and A. Yariv, Opt. Lett. **12**, 1017 (1987).

5.32. Y. Tomita, R. Yahalom, K. Kyuma, A. Yariv, and N. S.-K. Kwong, IEEE J. Quantum Electron. **QE-25**, 315 (1989).

5.33. I. McMichael, M. Khoshnevisan, and P. Yeh, Opt. Lett. **11**, 525 (1986).

5.34. I. McMichael, P. Beckwidth, and P. Yeh, Opt. Lett. **12**, 1023 (1987).

5.35. D.M. Pepper and A. Yariv, Opt. Lett. **5**, 59 (1980).

5.36. S. Odoulov, M. Soskin, and M. Vasnetsov, Opt. Commun. **32**, 355 (1980).

5.37. J. Feinberg, Opt. Lett. **7**, 486 (1982).

5.38. J. Feinberg, Appl. Phys. Lett. **42**, 30 (1983).

5.39. V.V. Ivakhnik, V.M. Petnikova, V.S. Solomatin, M.A. Kharchenko, and V.V. Shuvalov, Sov. J. Quantum Electron. **10**, 514 (1980).

5.40. A. Yariv and T.L. Koch, Opt. Lett. **7**, 113 (1982).

5.41. B. Fischer, M. Cronin-Golomb, J.O. White, and A. Yariv, Appl. Phys. Lett. **41**, 141 (1982).

5.42. O. Ikeda, T. Suzuki, and T. Sato, Appl. Opt. **22**, 2192 (1983).

5.43. O. Ikeda, T. Sato, and M. Takehara, Appl. Opt. **22**, 3562 (1983).

5.44. K.R. MacDonald, W.R. Tompkin, and R.W. Boyd, Opt. Lett. **13**, 485 (1988).

5.45. K. Sayano, Y. Tomita, and A. Yariv, submitted for publication.

5.46. After the submission of Ref. [5.45], we learned that a similar experiment was reported by D.R. Martinez, T.G. Alley, and M.A. Kramer, in *Technical Digiest of Annual Meeting of Optical Society of America* (Optical Society of America, Washington DC, 1988), paper FY7, p. 180.

5.47. W.T. Welford, J. Opt. Soc. Am. **66**, 1172 (1976).

CHAPTER
SIX

Polarization and Spatial Information Recovery by Modal Dispersal and Phase Conjugation

6.1 Introduction

Optical phase conjugation has been investigated extensively in many areas of nonlinear optics [6.1]. In particular it is well known that it can be used to correct *phase* distortions because of the wave-front-reversal properties of an incoming optical wave. For this reason the main emphasis has been on the study of the properties of *ordinary* phase-conjugate mirrors (PCM's) that reflect waves of a particular polarization (usually a linear polarization). In spite of the usefulness of the ordinary PCM's, however, they cannot be applied to the cases where the distortions include optical anisotropies by which incident waves suffer from *polarization* scrambling as well as phase distortions. This is caused, for example, by the induced birefringence in high power (e.g., Nd-doped glass) optical amplifier stages, and by the strong intermodal coupling in multimode fibers. These call for phase conjugation of both polarization components of the beam.

In the late 1970's researchers in the Soviet Union theoretically and experimentally studied the possibilities of complete polarization and spatial wavefront reversal in stimulated Brillouin scattering (SBS) [6.2–5], degenerate four-wave mixing (DFWM) [6.6], and stimulated scattering of the Rayleigh line wing [6.7], for correcting wavefront and polarization distortions caused in high power optical amplifier stages. They found that the complete reversal of an *arbitrary* polarized wave can be achieved by means of the tensorial property of the phase

conjugation process via DFWM, whereas the usefulness of the above stimulated scattering processes is limited to the reversal of depolarized pump waves [6.8]. Subsequently the experimental demonstrations of complete reversal were conducted using DFWM in liquid CS_2 [6.9,10], Nd-doped glass [6.11], sodium vapor [6.12], and biochrome films [6.13]. Phase conjugation using self-pumped photorefractive PCM's [6.14,15] was also used for the complete reversal of an arbitrary polarized wave [6.16]. In this method, which is similar to Basov's scheme [6.5], an arbitrary polarized incident wave is decomposed into two orthogonally linear polarized components. The polarization of one of the two is rotated by 90° and the two components, now similarly polarized, are then reflected by a single self-pumped photorefractive PCM [6.17], and their phase-conjugated waves are coherently recombined into one wave. Consequently this method results in the vectorial wavefront reversal, provided that the phase-conjugate reflectivities of these two components are exactly equal both in amplitude and phase (i.e., the net reflectivity is scalar [6.18]).

A new and fundamentally different scheme for vector phase conjugation was reported by Kyuma *et al.* [6.19]. This scheme, which consists simply of a tandem combination of a multimode fiber and a self-pumped photorefractive PCM (see also Fig. 6.1), uses the inherent strong intermodal coupling (i.e., modal dispersal) in the fiber combined with phase conjugation of *one* polarization component of the depolarized field emitted from the fiber. It will be shown in this chapter that since the polarization and spatial information of an arbitrary polarized input wave is distributed via the strong intermodal coupling among all the fiber modes, this scheme permits vector phase conjugation in spite of the elimination of one polarization component upon phase conjugation. This is due to the fact that the surviving single polarization modes contain sufficient information about the missing modes so that the latter are reconstructed during the reverse propagation and the intermodal coupling in the fiber. The fact that modal scrambling plays a

role in phase conjugation of polarized beams was speculated several years earlier by Dunning and Lind [6.20]. Following the initial demonstration the properties of this phase conjugation process have been investigated both theoretically and experimentally [6.21–26]. Yariv *et al.* [6.21] explained the experimental observation of almost perfect polarization recovery by means of a model based on modal dispersal of input information and modal averaging upon phase conjugation. The first experiment [6.19] employed a spatial filter that limited the number of fiber modes excited at the inputs. The effect of increasing the number of input fiber modes on the fidelity of the phase conjugation was elucidated by several studies [6.22–26] where it was shown that nearly half the reflected power was not truly phase conjugated and was spread more or less among all the fiber modes (of both orthogonal polarizations), contributing a "white" spatial and polarization noise background. The detailed theoretical and experimental studies on these subjects will be discussed in this chapter. In parallel with these studies, a number of new applications have also been demonstrated [6.27–31]. Some of them will be described in the next chapter.

6.2 Theory

6.2.1 Basic physical processes

The theoretical models of polarization and spatial information recovery are based on modal dispersal of input information and modal averaging upon phase conjugation. In this section we describe a general theoretical treatment by means of a coherency matrix formalism [6.26]. The theory treats the analysis of the fidelity of polarization and spatial information recovery as a function of input-beam launching conditions.

The physical processes considered are twofold:(1) a (time-reversed) phase conjugation process, which is *deterministic* in nature and permits vector phase

conjugation, and (2) a scattering process in the fiber, which results from partial phase conjugation of the mode-scrambled field and is seemingly completely *random*(or *stochastic*) but is in fact constrained by the unitarity condition of the scattering matrix(i.e., the energy conservation condition). The latter becomes a noise source. In this case we take the coupling strength in the scattering process to be essentially the same between all the fiber guided modes, but its relative phases to be random under the constraint of the unitarity condition. In the analysis of the polarization properties of conjugate fields, modal averaging over phase mismatched fields after phase conjugation is used. (Unlike the treatment of the Jones calculus for random media [6.32], a statistical ensemble average over the coherency matrix elements is not applied because one fiber is involved in phase conjugation experiments.) This treatment may be analogous to the phase-matching condition in the coupled-mode theory [6.33]. In the SNR treatment, however, the analysis is simplified by using an *a priori* knowledge of the statistical properties of the (speckle) noise field instead of considering the statistical properties of the scattering matrix and its relation to the properties of the noise field. This is done by assuming a probability density function of the noise field in the free space, and the SNR can then be obtained from the root-mean-square (rms) value of (statistical) intensity fluctuations of the noise field.

With the above treatment the present analysis enables us to evaluate theoretically the properties of the fiber-coupled PCM and to give a criterion for the limitation of the use of the fiber-coupled PCM.

6.2.2 Basic formulation using scattering matrices

Figure 6.1 is a schematic diagram of the fiber-coupled PCM. An image-bearing incident field $\mathbf{E}^{(1)}$ of an arbitrary polarization is launched into a multimode modal-scrambling fiber which is assumed to be linear in response to optical fields with

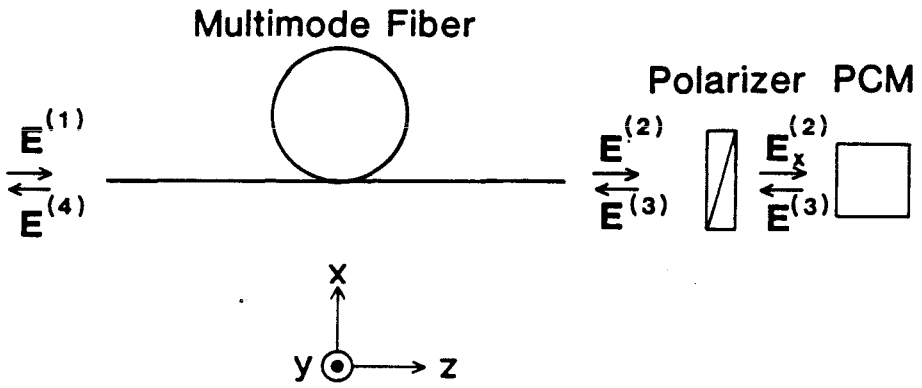

Figure 6.1 Schematic of the fiber-coupled PCM for polarization and spatial information recovery. The (polarization and modal-scrambling) multimode fiber is assumed to be linear with negligible loss.

negligible loss. Because of the strong intermodal coupling in the fiber, the input power initially coupled into any one fiber mode is distributed essentially uniformly among all the other spatial and polarization modes during propagation, and the outcoupled beam $\mathbf{E}^{(2)}$ from the fiber exhibits speckled spatial structures and nearly complete depolarization. The PCM, e.g., a self-pumped PCM [6.14,15], is placed after a polarizer (set to the x direction) and phase conjugates only the x component of the field $\mathbf{E}^{(2)}$. The phase-conjugate field $\mathbf{E}^{(3)}$ retraces the original path and is launched in reverse into the output side of the fiber. After the propagation and the strong intermodal coupling in the fiber, the left-traveling field forms the output field $\mathbf{E}^{(4)}$ at the input end of the fiber.

The input field $\mathbf{E}^{(1)}$ is expressed, in terms of the fiber guided modes, as

$$\begin{aligned}\mathbf{E}^{(1)} &= \sum_{n=1}^{N} \left(a_{xn}^{(1)} \mathbf{e}_{xn} + a_{yn}^{(1)} \mathbf{e}_{yn} \right) \\ &= \begin{pmatrix} a_{x1}^{(1)} \\ \vdots \\ a_{xN}^{(1)} \\ a_{y1}^{(1)} \\ \vdots \\ a_{yN}^{(1)} \end{pmatrix} \equiv \begin{pmatrix} A_x^{(1)} \\ A_y^{(1)} \end{pmatrix}, \end{aligned} \tag{6.1}$$

where N is the total number of the fiber guided modes in one polarization, $\mathbf{e}_{xn}$ is the n^{th} transverse fiber guided mode, which is predominantly x-polarized, $\mathbf{e}_{yn}$ is the n^{th} y-polarized mode, and $A_x^{(1)}$ and $A_y^{(1)}$ are column vectors of rank N whose elements are the complex amplitudes $a_{xn}^{(1)}$ and $a_{yn}^{(1)}$, respectively. Note that we neglect the coupling into the other possible fiber modes (e.g., leaky and radiation modes) for simplicity of the analysis. The propagation left to right through the fiber, including the intermodal coupling, can be expressed by the following matrix form:

$$\mathbf{E}^{(2)} = M\mathbf{E}^{(1)}, \tag{6.2}$$

where M is the scattering matrix of the fiber in the forward direction given by

$$M = \begin{pmatrix} M_{xx} & M_{xy} \\ M_{yx} & M_{yy} \end{pmatrix}, \tag{6.3}$$

in which $M_{ij}\,(i,j = x,y)$ are N × N submatrices. The field $\mathbf{E}^{(2)}$ is then passed through the polarizer and phase conjugated by the PCM, so the field $\mathbf{E}^{(3)}$ is given by

$$\mathbf{E}^{(3)} = rCM^*(\mathbf{E}^{(1)})^*, \tag{6.4}$$

where r is the PCM amplitude reflectivity and the matrix C, representing the removal of the y polarization by the polarizer, is given by

$$C = \begin{pmatrix} I & 0 \\ 0 & 0 \end{pmatrix}, \tag{6.5}$$

where I is an N × N unit matrix. A more general form of the matrix C will be considered in Chapter 7 where nonreciprocal and/or amplitude distortions prior to the PCM are taken into account.

The output field $\mathbf{E}^{(4)}$ is expressed as

$$\mathbf{E}^{(4)} = rM'CM^*(\mathbf{E}^{(1)})^*, \tag{6.6}$$

where M' is the scattering matrix in the backward direction. Note that a mode-independent (scalar) reflectivity r of the PCM is assumed in Eq. (6.6). If a mode-dependent reflectivity is taken into account, r should be replaced by a 2N × 2N diagonal matrix. This effect will be considered later in the next subsection.

In what follows we examine the properties of the scattering matrices and express the fields $\mathbf{E}^{(2)}$ and $\mathbf{E}^{(4)}$ in terms of the scattering matrix elements. Firstly because of the conservation of the energy in a lossless linear fiber, we require the following unitarity condition:

$$M^\dagger M = \begin{pmatrix} I & 0 \\ 0 & I \end{pmatrix}, \tag{6.7}$$

where † denotes the Hermite transpose operation. By using Eq. (6.3), Eq. (6.7) can be translated into the following sum rules:

$$(M_{xx})_{ik}(M_{xx})^*_{ik'} + (M_{yx})_{ik}(M_{yx})^*_{ik'} = \delta_{kk'}, \tag{6.8a}$$

$$(M_{yy})_{ik}(M_{yy})^*_{ik'} + (M_{xy})_{ik}(M_{xy})^*_{ik'} = \delta_{kk'}, \tag{6.8b}$$

$$(M_{xy})_{ik}(M_{xx})^*_{ik'} + (M_{yy})_{ik}(M_{yx})^*_{ik'} = 0, \tag{6.8c}$$

$$(M_{xx})_{ik}(M_{xy})^*_{ik'} + (M_{yx})_{ik}(M_{yy})^*_{ik'} = 0, \tag{6.8d}$$

and

$$(M_{xx})_{ki}(M_{xx})^*_{k'i} + (M_{xy})_{ki}(M_{xy})^*_{k'i} = \delta_{kk'}, \tag{6.9a}$$

$$(M_{yy})_{ki}(M_{yy})^*_{k'i} + (M_{yx})_{ki}(M_{yx})^*_{k'i} = \delta_{kk'}, \tag{6.9b}$$

$$(M_{yx})_{ki}(M_{xx})^*_{k'i} + (M_{yy})_{ki}(M_{xy})^*_{k'i} = 0, \tag{6.9c}$$

$$(M_{xx})_{ki}(M_{yx})^*_{k'i} + (M_{xy})_{ki}(M_{yy})^*_{k'i} = 0, \tag{6.9d}$$

where henceforth summation over repeated indices is understood.

Secondly consider the ideal case of vector phase conjugation by the PCM with the polarizer removed (i.e., the case where the field $\mathbf{E}^{(2)}$ is completely phase conjugated). In this case, viewing the fiber as some arbitrary lossless linear dielectric medium, the time-reversal symmetry of any field applies and we must recover the original field $\mathbf{E}^{(4)} = r(\mathbf{E}^{(1)})^*$. This happens when

$$M'M^* = \begin{pmatrix} I & 0 \\ 0 & I \end{pmatrix}. \tag{6.10}$$

From Eqs. (6.7) and (6.10) it is found that

$$M' = M^t, \tag{6.11}$$

where t denotes the transpose operation. Using the submatrices given in Eq. (6.3), Eq. (6.11) can be rewritten as

$$(M'_{xx})_{ij} = (M_{xx})_{ji}, \tag{6.12a}$$

$$(M'_{yy})_{ij} = (M_{yy})_{ji}, \tag{6.12b}$$

$$(M'_{xy})_{ij} = (M_{yx})_{ji}, \tag{6.12c}$$

$$(M'_{yx})_{ij} = (M_{xy})_{ji}. \tag{6.12d}$$

Here we note that the elements of the scattering matrices are interrelated by the constraint given by Eqs. (6.8), (6.9) and (6.12), which are used to find the results shown furtheron.

6.2.3 Polarization recovery

a) Spatial and Polarization Properties of the Field $\mathbf{E}^{(2)}$

With the relation $\mathbf{E}^{(2)} = M\mathbf{E}^{(1)}$ the correlations between the 2N modes of the field $\mathbf{E}^{(2)}$ can be expressed by means of the following 2N × 2N Hermitian coherency matrix:

$$\begin{aligned} L^{(2)} &\equiv < \mathbf{E}^{(2)}\mathbf{E}^{(2)\dagger} > \\ &= M < \mathbf{E}^{(1)}\mathbf{E}^{(1)\dagger} > M^{\dagger} = \begin{pmatrix} L^{(2)}_{xx} & L^{(2)}_{xy} \\ L^{(2)\dagger}_{xy} & L^{(2)}_{yy} \end{pmatrix}, \end{aligned} \tag{6.13}$$

where $< \cdots >$ denotes the time average and $L^{(2)}_{ij}$ (i,j=x,y) are N × N matrices given by

$$L^{(2)}_{xx} = M_{xx}L^{(1)}_{xx}M_{xx}^{\dagger} + M_{xx}L^{(1)}_{xy}M_{xy}^{\dagger} + M_{xy}L^{(1)\dagger}_{xy}M_{xx}^{\dagger} + M_{xy}L^{(1)}_{yy}M_{xy}^{\dagger}, \tag{6.14a}$$

$$L^{(2)}_{yy} = M_{yx}L^{(1)}_{xx}M_{yx}^{\dagger} + M_{yx}L^{(1)}_{xy}M_{yy}^{\dagger} + M_{yy}L^{(1)\dagger}_{xy}M_{yx}^{\dagger} + M_{yy}L^{(1)}_{yy}M_{yy}^{\dagger}, \tag{6.14b}$$

$$L^{(2)}_{xy} = M_{xx}L^{(1)}_{xx}M_{yx}^{\dagger} + M_{xx}L^{(1)}_{xy}M_{yy}^{\dagger} + M_{xy}L^{(1)\dagger}_{xy}M_{yx}^{\dagger} + M_{xy}L^{(1)}_{yy}M_{yy}^{\dagger}, \tag{6.14c}$$

in which $L^{(1)} \equiv < \mathbf{E}^{(1)}\mathbf{E}^{(1)\dagger} >$ denotes the correlations between the 2N modes of the input field $\mathbf{E}^{(1)}$. We note that the effect of possible decrease of the temporal coherence of the light source at the output, which is due to the modal dispersion in the fiber [6.34], is not taken into account in the present analysis. This implies the

assumption of a coherence time of the light source that is long enough to neglect the above effect.

We now introduce the following "modified" 2 × 2 coherency matrix:

$$J^{(2)} \equiv \begin{pmatrix} J_{xx}^{(2)} & J_{xy}^{(2)} \\ J_{xy}^{(2)*} & J_{yy}^{(2)} \end{pmatrix}. \tag{6.15}$$

Since the partition of the total power among the x and y polarization components in the field $\mathbf{E}^{(2)}$ is of interest, each element $J_{ij}^{(2)}$ $(i,j = x,y)$ in Eq. (6.15) is defined as

$$\begin{aligned} J_{ij}^{(2)} &= \sum_{k=1}^{N}\sum_{l=1}^{N} \iint_{\sigma} (L_{ij}^{(2)})_{kl} e_{ik} e_{jl}^{*}\, dx\, dy \\ &= (\text{const.}) \times \sum_{k=1}^{N} (L_{ij}^{(2)})_{kk} \\ &= (\text{const.}) \times \mathrm{Tr}(L_{ij}^{(2)}). \end{aligned} \tag{6.16}$$

In Eq. (6.16) Tr denotes a trace of a matrix, and the orthogonality of the fiber modes [6.35] is used, i.e., $\iint_{\sigma} e_{im} e_{jn}^{*} dx\, dy$ =(const.) × δ_{mn} (i, j = x, y; m, n = 1, ···, N), where σ denotes the whole fiber cross section and a circular fiber is assumed. It is seen from Eq. (6.16) that the off-diagonal elements of $L_{xx}^{(2)}$, $L_{xy}^{(2)}$ and $L_{yy}^{(2)}$ do no contribute to $J^{(2)}$ on the detection of the field $\mathbf{E}^{(2)}$ over σ. We note that, unlike the usual definition of the coherency matrix [6.36], the elements of $J^{(2)}$ have the dimensionality of power [hereafter, however, we omit the constant in Eq. (6.16) for brevity].

For the sake of simplicity we consider the x-polarized input here. Then, with $L_{xy}^{(1)} = L_{yy}^{(1)} = 0$, we can write the diagonal elements of the submatrices $L_{ij}^{(2)}$ in Eq. (6.13) as follows:

$$\begin{aligned} (L_{xx}^{(2)})_{ii} &= (M_{xx})_{ik} (M_{xx})_{ik'}^{*} (L_{xx}^{(1)})_{kk'} \\ &= |(M_{xx})_{ik}|^2 (L_{xx}^{(1)})_{kk} + (M_{xx})_{ik} (M_{xx})_{ik'}^{*} (L_{xx}^{(1)})_{\substack{kk' \\ (k \neq k')}}, \end{aligned} \tag{6.17a}$$

$$(L_{yy}^{(2)})_{ii} = |(M_{yx})_{ik}|^2 (L_{xx}^{(1)})_{kk} + (M_{yx})_{ik}(M_{yx})_{ik'}^{*} (L_{xx}^{(1)})_{\substack{kk' \\ (k \neq k')}}, \tag{6.17b}$$

$$(L_{xy}^{(2)})_{ii} = (M_{xx})_{ik}(M_{yx})_{ik'}^{*}(L_{xx}^{(1)})_{kk'}, \tag{6.17c}$$

where summation over repeated indices [but not over i in Eqs. (6.17a) – (6.17c)] is again understood. At this point, because of the strong intermodal coupling in the fiber, the amplitudes of the matrix elements M_{ij}, i.e., the coupling strength between modes, are assumed to be essentially the same (or symmetrically and widely distributed with respect to the diagonal elements M_{ii}), while their relative phases are distributed essentially uniformly over the $-\pi - +\pi$ interval (henceforth we refer this to as *the random-coupling approximation*; see Appendix B). Then we see from Eqs. (6.17a) – (6.17c) that the input power initially coupled into any one fiber guided mode is redistributed during propagation among all the other fiber guided modes, including those of the orthogonal y polarization. Consequently the out-coupled different spatial modes possessing random phases interfere with one another at any point, resulting in the speckled spatial structures in the free space.

The polarization state of the field $\mathbf{E}^{(2)}$ can be obtained using $J^{(2)}$. Introduce the following parameters:

$$a_{kk'} \equiv (M_{xx})_{ik}(M_{xx})_{ik'}^{*}, \tag{6.18a}$$

$$b_{kk'} \equiv (M_{xx})_{ik}(M_{yx})_{ik'}^{*}, \tag{6.18b}$$

$$d \equiv \sum_{k=1}^{N} (L_{xx}^{(1)})_{kk}, \tag{6.19}$$

$$q \equiv \frac{2a_{kk'}(L_{xx}^{(1)})_{\substack{kk' \\ (k \neq k')}}}{d}, \tag{6.20a}$$

and

$$u \equiv \frac{2b_{kk'}(L_{xx}^{(1)})_{kk'}}{d}. \tag{6.20b}$$

By substituting these parameters into Eqs. (6.15) - (6.17) together with the sum rules from Eqs. (6.8), (6.9), and (6.12), it is found that

$$J_{xx}^{(2)} = a_{kk}(L_{xx}^{(1)})_{kk} + \frac{1}{2}qd, \tag{6.21a}$$

$$J_{yy}^{(2)} = (1 - \frac{1}{2}q)d - a_{kk}(L_{xx}^{(1)})_{kk}, \tag{6.21b}$$

$$J_{xy}^{(2)} = \frac{1}{2}ud. \tag{6.21c}$$

Here we note that the terms $a_{\substack{kk' \\ (k \neq k')}}$ and $b_{kk'}$ in Eqs. (6.21a) - (6.21c) are much smaller than a_{kk} due to the modal averaging (see Appendix B), and that d is the total input power to the fiber. The Stokes parameters (s_0, s_1, s_2, s_3) and the degree of polarization ($P^{(2)}$) of the field $\mathbf{E}^{(2)}$ [6.36] are then given by

$$s_0 \equiv J_{xx}^{(2)} + J_{yy}^{(2)} = d, \tag{6.22a}$$

$$s_1 \equiv J_{xx}^{(2)} - J_{yy}^{(2)} = 2a_{kk}(L_{xx}^{(1)})_{kk} - (1-q)d, \tag{6.22b}$$

$$s_2 \equiv J_{xy}^{(2)} + J_{yx}^{(2)} = [Re(u)]d, \tag{6.22c}$$

$$s_3 \equiv i(J_{yx}^{(2)} - J_{xy}^{(2)}) = [Im(u)]d, \tag{6.22d}$$

and

$$P^{(2)} = \frac{\sqrt{s_1^2 + s_2^2 + s_3^2}}{s_0}. \tag{6.23}$$

By using the random-coupling approximation so that $a_{kk} \simeq 0.5$ for any k, $P^{(2)}$ is reduced to

$$P^{(2)} \simeq \sqrt{q^2 + |u|^2}, \tag{6.24}$$

and the power emitted from the fiber at each polarization is given by

$$J_{xx}^{(2)} = \frac{1}{2}(1+q)d \tag{6.25a}$$

and

$$J_{yy}^{(2)} = \frac{1}{2}(1-q)d. \tag{6.25b}$$

We see that the residual polarization of the field $\mathbf{E}^{(2)}$ is due to the parameters q and u, and is in general much smaller than unity in the strong intermodal coupling regime. For the complete modal scrambling (i.e., $q, u = 0$) the output power is equally divided between both orthogonal polarizations, i.e., $J_{xx}^{(2)} = J_{yy}^{(2)} = d/2$, so that the field $\mathbf{E}^{(2)}$ is completely depolarized, i.e.,$P^{(2)} = 0$. As will be seen from the experimental results in the next section, the field $\mathbf{E}^{(2)}$ exhibits spatial distortions and nearly complete depolarization due to the strong intermodal coupling in the fiber, thus verifying the random-coupling approximation and the modal averaging assumption. However we note that the parameters q and u will play a role in the fidelity of the reconstruction of the original information, as discussed below.

b) Spatial and Polarization Properties of the Field $\mathbf{E}^{(4)}$

Here we will show that the spatially distorted and depolarized field $\mathbf{E}^{(2)}$ can be corrected, under certain conditions, even when only one polarization component of the field $\mathbf{E}^{(2)}$ is phase conjugated.

First rewrite Eq. (6.6) as

$$\mathbf{E}^{(4)} = rS(\mathbf{E}^{(1)})^*, \tag{6.26}$$

where the scattering matrix S in the round-trip propagation is given by $S = M'CM^*$. Here we again use the random-coupling approximation, i.e., $\sum_{i=1}^{N}|(M_{xx})_{ik}|^2, \sum_{i=1}^{N}|(M_{xy})_{ik}|^2 \simeq 0.5$. Then $S = S_1 + S_2$, where

$$S_1 = \frac{1}{2}\begin{pmatrix} I & 0 \\ 0 & I \end{pmatrix}, \tag{6.27a}$$

and

$$S_2 = \begin{pmatrix} D & Q \\ Q^\dagger & D' \end{pmatrix}, \tag{6.27b}$$

in which D, D' and Q are N × N submatrices given by

$$D_{ij} = \begin{cases} 0, & (\text{i=j}) \\ (M_{xx})_{ki}(M_{xx})^*_{kj}, & (i \neq j) \end{cases} \tag{6.28a}$$

$$D'_{ij} = \begin{cases} 0, & (\text{i=j}) \\ -(M_{yy})_{ki}(M_{yy})^*_{kj}, & (i \neq j) \end{cases} \tag{6.28b}$$

$$Q_{ij} = (M_{xx})_{ki}(M_{xy})^*_{kj}. \tag{6.28c}$$

The field $\mathbf{E}^{(4)}$ given by Eq. (6.26) becomes

$$\mathbf{E}^{(4)} = \frac{1}{2} r(\mathbf{E}^{(1)})^* + \mathbf{V}, \tag{6.29}$$

where $\mathbf{V} = rS_2(\mathbf{E}^{(1)})^*$. We note that the decomposition of S given in Eq. (6.26) leads to the first term in Eq. (6.29), which corresponds to *the true phase-conjugate replica* of $\mathbf{E}^{(1)}$, and the second term in Eq. (6.29), which corresponds to *the noise* that possesses random phases in the field $\mathbf{E}^{(4)}$.

Figure 6.2 shows a diagramatic explanation of the formation of the field $\mathbf{E}^{(4)}$. The x-polarized i^{th} fiber guided mode excited initially at the input plane of the fiber is coupled into all the fiber guided modes at the output in the forward direction. After the elimination of the y-polarized component and phase conjugation of the x-polarized component, each mode at the output plane is, again, coupled into all the fiber guided modes at the input plane in the backward direction. In Fig. 6.2(a) the (time-reversed) paths in the backward direction are exactly the same as those in the forward direction, resulting in a constructive coherent superposition of the scattered fields at each mode at the input plane. This constructive interference is expressed by the scattering matrix S_1, and the resulting true phase-conjugate field, corresponding to the term $r(\mathbf{E}^{(1)})^*/2$ in Eq. (6.29), has almost one half of the total reflected power. On the other hand, in Fig. 6.2(b) the remainder of the paths in the backward direction are random and different from those in the forward direction. This random interference at each mode at the input plane is expressed by the scattering matrix S_2, and the resulting field forms the noise $\mathbf{V}$ given in Eq. (6.29). The total power of this noise is nearly the same as that of the true phase-conjugate field, but, as we will see later, it is distributed essentially uniformly

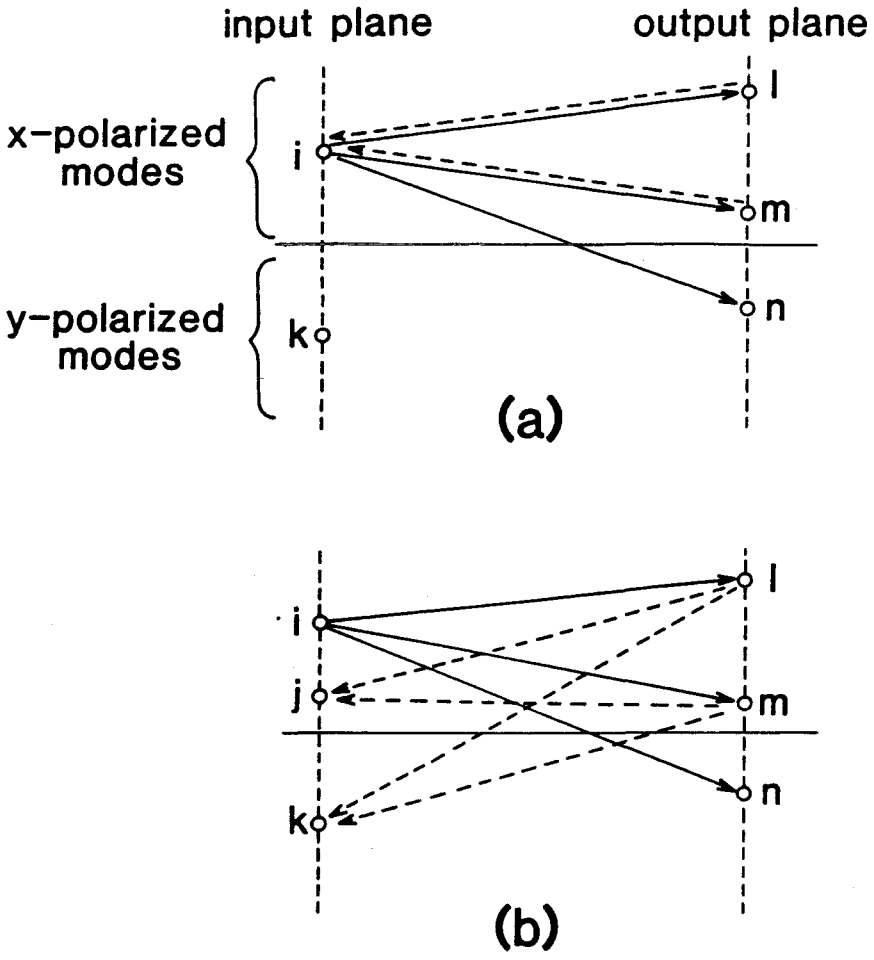

Figure 6.2 Diagramatic description of the formation of the field $\mathbf{E}^{(4)}$:(a) deterministic phase-conjugate paths that result in true phase conjugation of the input field $\mathbf{E}^{(1)}$, (b) randomly scattered phase-conjugate paths that result in the noise.

among all the fiber guided modes, independently of the input-beam numerical aperture (N.A.). For this reason the noise power per mode is much smaller than that of the true phase-conjugate field, provided that the input field initially excites only a small fraction, say f, of the fiber guided modes (i.e., that a small input-beam N.A. is used) and that the detection is made within such a small input N.A. In this case we can, to the order of f, neglect such noise contributions $\mathbf{V}$ in Eq. (6.29), and the detected part of the field $\mathbf{E}^{(4)}$ can be the true phase-conjugate replica of the input field $\mathbf{E}^{(1)}$. [Also see Appendix C for the qualitative proof of Eq. (6.29).] It is interesting to note that the above round-trip (time-reversed) scattering process is reminiscent of localization and coherent backscattering of photons in disordered media [6.37], which has recently attracted a great deal of attention mainly in connection with analogous phenomena on Anderson localization of electrons [6.38].

The correlations between the 2N modes of the field $\mathbf{E}^{(4)}$ can also be expressed by means of the following 2N × 2N Hermitian coherency matrix:

$$\begin{aligned} L^{(4)} &\equiv < \mathbf{E}^{(4)} \mathbf{E}^{(4)\dagger} > \\ &= |r|^2 S L^{(1)*} S^{\dagger} \\ &= |r|^2 [\frac{1}{4} L^{(1)*} + S_2 L^{(1)*} S_2{}^{\dagger} + \frac{1}{2}(S_2 L^{(1)*} + L^{(1)*} S_2{}^{\dagger})]. \end{aligned} \tag{6.30}$$

In the right-hand side of the last equation above, the first term corresponds to a time-reversed polarization state of the input field $\mathbf{E}^{(1)}$, while the rest of the terms correspond to the noise. It is again sufficient to consider the case of the x-polarized incidence. In this case the noise terms in Eq. (6.30) can be expressed in terms of the submatrices D and Q given in Eq. (6.27*b*) as

$$S_2 L^{(1)*} S_2{}^{\dagger} = \begin{pmatrix} D L_{xx}^{(1)*} D^{\dagger} & D L_{xx}^{(1)*} Q \\ Q^{\dagger} L_{xx}^{(1)*} D^{\dagger} & Q^{\dagger} L_{xx}^{(1)*} Q \end{pmatrix}, \tag{6.31a}$$

$$\frac{1}{2}(S_2 L^{(1)*} + L^{(1)*} S_2{}^{\dagger}) = \frac{1}{2} \begin{pmatrix} D L_{xx}^{(1)*} + L_{xx}^{(1)*} D^{\dagger} & L_{xx}^{(1)*} Q \\ Q^{\dagger} L_{xx}^{(1)*} & 0 \end{pmatrix}. \tag{6.31b}$$

Each diagonal element in Eq. (6.31a) can be rewritten as

$$(DL_{xx}^{(1)*}D^{\dagger})_{ii} = |D_{il}|^2(L_{xx}^{(1)})_{ll} + D_{il}D_{il'}{}^*(L_{xx}^{(1)})^*_{ll'_{(l\neq l')}}, \tag{6.32a}$$

$$(Q^{\dagger}L_{xx}^{(1)*}Q)_{ii} = |Q_{li}|^2(L_{xx}^{(1)})_{ll} + Q_{li}{}^*Q_{l'i}(L_{xx}^{(1)})^*_{ll'_{(l\neq l')}}, \tag{6.32b}$$

$$(DL_{xx}^{(1)*}Q)_{ii} = D_{il}Q_{l'i}(L_{xx}^{(1)})^*_{ll'}, \tag{6.32c}$$

where the summation over l and l' is understood. In the above expressions Eq. (6.32a) corresponds to the noise power of the x-polarized i^{th} fiber guided mode of the field $\mathbf{E}^{(4)}$. This consists of the interference between the other initial modes that are finally coupled into the x-polarized i^{th} fiber guided mode through different scattering paths after the round-trip propagation. Likewise Eq. (6.32b) corresponds to the y-polarized noise power of the i^{th} fiber guided mode. Each diagonal element in Eq. (6.31b) can also be rewritten as

$$(DL_{xx}^{(1)*} + L_{xx}^{(1)*}D^{\dagger})_{ii} = 2Re[D_{il}(L_{xx}^{(1)})^*_{li}], \tag{6.33a}$$

$$(L_{xx}^{(1)*}Q)_{ii} = Q_{li}(L_{xx}^{(1)})^*_{il}, \tag{6.33b}$$

where the summation over l is again understood. Equation (6.33a) corresponds to the interference between the true phase-conjugate field and the noise field at the i^{th} fiber guide mode of the x polarization. This term is related to the residual polarization of the field $\mathbf{E}^{(2)}$. [Note that $D_{il} = a_{il}$ for $i \neq l$ and therefore the total power of this noise contribution, $\sum_{i=1}^{N}[DL_{xx}^{(1)*} + L_{xx}^{(1)*}D^{\dagger}]_{ii}/2$, is equal to $qd/2$, see Eqs. (6.18a), (6.20a), and (6.28a).] We also note that this noise is distributed only inside the input-beam modal distribution $(L_{xx}^{(1)})_{ii}$, i.e., this noise is localized in space and polarization (in this example, x-polarized).

In order to estimate the ratio of this noise power to the true phase-conjugate beam power per mode, we consider the simple form of the scattering matrix elements, $M_{ij} = 1/\sqrt{2N}\exp i(\phi_{ij})$ [6.21]. Then, by inserting this form into Eqs.

(6.32a) –(6.32c), we immediately see that $(DL_{xx}^{(1)^*}D^\dagger)_{ii}$ and $(Q^\dagger L_{xx}^{(1)^*}Q)_{ii}$ are of the order of d/N independently of the mode number i, where the total input power d is given by Eq. (6.19a). It is therefore seen that the x- and y-polarized noise power given by Eqs. (6.32a) – (6.32c) do not differ from each other significantly at any i^{th} mode, so the noise power of the field $\mathbf{E}^{(4)}$ is almost essentially uniformly distributed among all the fiber guided modes, independently of the input-beam N.A., i.e., of the distribution of $(L_{xx}^{(1)})_{ii}$. We will see below that this noise is nearly completely depolarized. Therefore we refer this to as "the depolarized noise". The ratio of this noise power to the true phase-conjugate beam power per mode is of the order of M_0/N (M_0 is the number of the fiber guided modes that are excited initially). In addition, the noise given by Eq.(6.33a) is of the order of $|q|d/M_0$, where q is given by Eq.(6.20a). The ratio of this noise power to the true phase-conjugate beam power per mode is of the order of $|q|$. Although this noise is x-polarized and resides within the mode number M_0, its spatial structure is distorted because of the random phases. Therefore we refer this to as "the polarized noise". These two main noise contributions can be, however, negligibly small when $M_0/N \ll 1$ and $|q| \ll 1$, that is, when a small input N.A. is used and the field $\mathbf{E}^{(2)}$ is nearly completely depolarized (i.e., in the strong intermodal coupling regime).

We are now in a position to evaluate quantitatively the polarization recovery of the input field $\mathbf{E}^{(1)}$ as a function of input-beam N.A.'s. Suppose that the whole power of the field $\mathbf{E}^{(4)}$ is detected. Then the polarization state of the field $\mathbf{E}^{(4)}$ is expressed by means of the following 2 × 2 modified coherency matrix of the field $\mathbf{E}^{(4)}$:

$$J^{(4)} \equiv \begin{pmatrix} J_{xx}^{(4)} & J_{xy}^{(4)} \\ J_{xy}^{(4)^*} & J_{yy}^{(4)} \end{pmatrix} = \frac{1}{4}|r|^2 J^{(1)^*} + J_{noise}^{(4)}, \tag{6.34}$$

where

$$J^{(1)} = \begin{pmatrix} d & 0 \\ 0 & 0 \end{pmatrix}, \tag{6.35a}$$

and

$$J^{(4)}_{\text{noise}} = \begin{pmatrix} \text{Tr}(L^{(4)}_{xx}) - \frac{1}{4}|r|^2 d & \text{Tr}(L^{(4)}_{xy}) \\ \text{Tr}(L^{(4)}_{xy}{}^{\dagger}) & \text{Tr}(L^{(4)}_{yy}) \end{pmatrix}. \tag{6.35b}$$

After some calculations using Eqs. (6.30) – (6.32) together with the sum rules from Eqs. (6.7) and (6.11), each component of $J^{(4)}_{\text{noise}}$ can be written as

$$(J^{(4)}_{\text{noise}})_{xx} = (\alpha_1 + \frac{1}{2}qd)|r|^2, \tag{6.36a}$$

$$(J^{(4)}_{\text{noise}})_{yy} = (\frac{1}{4}d - \alpha_1)|r|^2, \tag{6.36b}$$

$$(J^{(4)}_{\text{noise}})_{xy} = (\alpha_2 + \frac{1}{4}vd)|r|^2, \tag{6.36c}$$

where

$$\alpha_1 = Tr(DL^{(1)*}_{xx}D^{\dagger}), \tag{6.37a}$$

$$\alpha_2 = Tr(DL^{(1)*}_{xx}Q), \tag{6.37b}$$

$$v = \frac{2(M_{xx})_{kl}(M_{xy})^*_{ki}(L^{(1)}_{xx})^*_{il}}{d}, \tag{6.37c}$$

and the total noise power P_{N} is found to be

$$P_{\text{N}} \equiv \text{Tr}(J^{(4)}_{\text{noise}}) = \frac{1}{4}|r|^2 d(1+2q), \tag{6.38}$$

where q ($|q| \ll 1$) is given by Eq. (6.20a). It is seen from Eqs. (6.34) – (6.38) that almost one half of the reflected power (i.e., $|r|^2(1+2q)d/4$) is from the noise and the rest is from the true phase-conjugate beam. Since the polarization noise terms (given by $\alpha_1|r|^2$ for the x polarization and by $(d/4-\alpha_1)|r|^2$ for the y polarization) can be regarded as the probabilities that the initial l^{th} mode of the x polarization is randomly coupled into all the other modes after the round-trip propagation, these

two terms may be almost equal, and then we have $\alpha_1 \approx d/8$. Consequently we can write the 2×2 coherency matrix of the noise as

$$J^{(4)}_{\text{noise}} \simeq \lambda \begin{pmatrix} 1+4q & 2v \\ 2v^* & 1 \end{pmatrix}, \tag{6.39}$$

where $\lambda \equiv |r|^2 d/8$ and we have neglected α_2 because it is much smaller than $vd/4$ due to the complete phase mismatching. Note that, since v is the same order of magnitude as that of q and u, most of the noise expressed by Eq. (6.39) is nearly completely depolarized, except for the excess x-polarized noise denoted by $4q\lambda$. From Eqs. (6.34) – (6.39) the degree of polarization of the total integrated intensity of the field $\mathbf{E}^{(4)}$ is then given by

$$P^{(4)} \simeq \frac{1+2q}{2(1+q)}, \tag{6.40a}$$

and the reflectivity R , defined as a ratio of the x-polarized reflected power to the input beam power for the x-polarized input, is given by

$$\begin{aligned} R &\equiv \frac{J^{(4)}_{xx}}{d} \\ &= \frac{1}{8}|r|^2(3+4q), \end{aligned} \tag{6.40b}$$

where the definition of the degree of polarization is given by Eq. (6.23) and the second order terms in q and v are neglected. It is seen from Eqs. (6.40a) and (6.40b) that $P^{(4)}$ and R depend on the residual polarization of the field $\mathbf{E}^{(2)}$, i.e., nonzero values of q. Furthermore the degree of polarization recovery p [6.19], which is defined as $p \equiv (J^{(4)}_{xx} - J^{(4)}_{yy})/(J^{(4)}_{xx} + J^{(4)}_{yy})$, i.e., the recovery of the linearly x-polarized component, is found to be equal to $P^{(4)}$ to the first order in q and v. Likewise if a lineary y-polarized light is used as an input, the same results with $q \equiv 2D'_{il}(L^{(1)}_{yy})^*_{il}/d$ can be obtained. Finally if the field $\mathbf{E}^{(2)}$ is completely depolarized (i.e., $q = v = 0$), it is found that

$$J^{(4)}_{noise} \simeq \begin{pmatrix} \lambda & 0 \\ 0 & \lambda \end{pmatrix}, \tag{6.41}$$

so that the noise field in the field $\mathbf{E}^{(4)}$ is also completely depolarized and one half of the reflected power is equally distributed among all the fiber guided modes of both polarizations. In this case the degree of polarization $P^{(4)}$ and the reflectivity R of the total integrated intensity of the field $\mathbf{E}^{(4)}$ become 0.5 and $3|r|^2/8$, respectively.

In practice, however, the input field $\mathbf{E}^{(1)}$ excites only a fraction of all the fiber guided modes (i.e., the input-beam N.A. is smaller than the fiber's N.A.), as was the case in the first experimental observation [6.19]. In this case the detection is usually made only within the same (input-beam) N.A., and therefore the total noise power within the detection area is smaller than the total noise power discussed above. To see the effect of the input-beam N.A. on the degree of polarization $P^{(4)}$, we introduce the following modal partition functions for the true phase-conjugate field and the noise field, respectively:

$$\Theta_i \equiv \frac{\text{true phase conjugate power in the } i^{th} \text{ mode}}{2\lambda} = \frac{(L_{xx}^{(1)})_{ii}}{d}, \tag{6.42a}$$

$$\Lambda_i \equiv \frac{\text{polarized noise power in the } i^{th} \text{ mode}}{4q\lambda} = \frac{Re(DL_{xx}^{(1)*})_{ii}}{(\frac{qd}{2})}, \tag{6.42b}$$

$$\Delta_i \equiv \frac{\text{depolarized noise power in the } i^{th} \text{ mode of each polarization}}{\lambda} = \frac{(DL_{xx}^{(1)*}D^{\dagger})_{ii}}{(\frac{d}{8})} \simeq \frac{(Q^{\dagger}L_{xx}^{(1)*}Q)_{ii}}{(\frac{d}{8})}. \tag{6.42c}$$

Using these partition functions and the maximum mode number M on the detection, and then by diagonalizing $J^{(4)}$, we can express the polarized power $P_{pol.}$ and the

depolarized noise power P_M as

$$P_{pol.} = 2\lambda(\sum_{i=1}^{M}\Theta_i + 2q\sum_{i=1}^{M}\Lambda_i), \tag{6.43a}$$

and

$$P_M = 2\lambda\sum_{i=1}^{M}\Delta_i, \tag{6.43b}$$

where we neglect the contributions of the off-diagonal elements in $L^{(4)}$ and also the second order terms in q and v. Then the degree of polarization $P^{(4)}$ and the reflectivity R on the detection are given by

$$\begin{aligned} P^{(4)} &\equiv \frac{P_{pol.}}{P_{pol.} + P_M} \\ &= \frac{1 + 2q\beta_1}{1 + 2q\beta_1 + \beta_2}, \end{aligned} \tag{6.44a}$$

and

$$R = \frac{1}{8}|r|^2\sum_{i=1}^{M}\Theta_i(2 + 4q\beta_1 + \beta_2), \tag{6.44b}$$

where

$$\beta_1 \equiv \frac{\sum_{i=1}^{M}\Lambda_i}{\sum_{i=1}^{M}\Theta_i}, \tag{6.45a}$$

and

$$\beta_2 \equiv \frac{\sum_{i=1}^{M}\Delta_i}{\sum_{i=1}^{M}\Theta_i}. \tag{6.45b}$$

It is seen that $P^{(4)}$ is again equal to the degree of polarization recovery p, and $P^{(4)}$ and R are reduced to Eqs. (6.40a) and (6.40b), respectively, as M $\rightarrow$ N.

So far we have treated r as a scalar value, i.e., r is independent of the spatial structure of the field $\mathbf{E}_x^{(2)}$. Since the field $\mathbf{E}^{(2)}$ emitted from the fiber has a large field of view, the fidelity of phase-conjugate field $\mathbf{E}^{(3)}$ reflected by the PCM may

be degraded because of the spatial frequency dependence of a phase-conjugate reflectivity of the PCM. To take this possible degradation into account, a scalar quantity r should be replaced by a 2N $\times$ 2N diagonal matrix. In what follows we consider the effect of this possible degradation on the polarization recovery.

We first decompose the field $\mathbf{E}^{(3)}$ into the true phase-conjugate field $\mathbf{E}_x^{(2)*}$ multiplied by a scalar reflectivity r_0 and the possible "wrong" phase-conjugate field $\mathbf{E}_w^{(3)}$:

$$\begin{aligned}\mathbf{E}^{(3)} &= r_0\mathbf{E}_x^{(2)*} + \mathbf{E}_w^{(3)} \\ &= r_0\mathbf{E}_x^{(2)*} + [r_1]\mathbf{E}_x^{(2)*},\end{aligned} \tag{6.46}$$

where $[r_1]$ is a mode-dependent reflectivity that is a 2N $\times$ 2N matrix. The explicit form of $[r_1]$ may depend on a type of the PCM. We then identify the scalar reflectivity r used so far as an effective scalar reflectivity such that

$$\begin{aligned}Tr(\mathbf{E}^{(3)}\mathbf{E}^{(3)\dagger}) &= |r_0|^2 Tr(\mathbf{E}_x^{(2)*}\mathbf{E}_x^{(2)*\dagger}) + Tr(\mathbf{E}_w^{(3)}\mathbf{E}_w^{(3)\dagger}) + 2Re[Tr(r_0\mathbf{E}_x^{(2)}\mathbf{E}_w^{(3)\dagger})] \\ &\equiv |r|^2 Tr(\mathbf{E}_x^{(2)*}\mathbf{E}_x^{(2)*\dagger}).\end{aligned} \tag{6.47}$$

We then define the efficiency η $(0 < \eta \leq 1)$ as

$$\eta \equiv \frac{|r_0|^2}{|r|^2}, \tag{6.48}$$

which denotes a fractional power of the true phase-conjugate field $\mathbf{E}_x^{(2)}$ in the total power of the field $\mathbf{E}^{(3)}$ reflected by the PCM. For the output field $\mathbf{E}^{(4)}$ we can write [see Eq. (6.26) for comparison]

$$\begin{aligned}\mathbf{E}^{(4)} &= r_0 S\mathbf{E}^{(1)*} + M'\mathbf{E}_w^{(3)} \\ &\equiv \mathbf{E}_t^{(4)} + \mathbf{E}_w^{(4)}.\end{aligned} \tag{6.49}$$

We further assume that each mode of the wrong phase-conjugate field $\mathbf{E}_w^{(4)}$ has no correlation to the other modes (i.e., the field $\mathbf{E}_w^{(4)}$ is completely depolarized), so that

we can neglect the interference between $\mathbf{E}_t^{(4)}$ and $\mathbf{E}_w^{(4)}$ and the residual polarization of $\mathbf{E}_w^{(4)}$ (and therefore $2Re\{Tr[r_0\mathbf{E}_x^{(2)*}\mathbf{E}_w^{(3)\dagger}]\}$). Under these assumptions we may express $J^{(4)}$ as

$$\begin{aligned} J^{(4)} &= J_t^{(4)} + J_w^{(4)} \\ &\simeq \eta\lambda \begin{pmatrix} 2+4q+1 & 2v \\ 2v & 1 \end{pmatrix} + 2(1-\eta)\lambda \begin{pmatrix} 1+q & 0 \\ 0 & 1+q \end{pmatrix}, \end{aligned} \tag{6.50}$$

where we have assumed that the detection of the whole power of the field $\mathbf{E}^{(4)}$ and λ is again given by $|r|^2 d/8$. From relation (6.50) we see that the true phase-conjugate beam power is decreased by the factor η but the depolarized noise power is increased because of the field $\mathbf{E}_w^{(4)}$. Consequently we can write the following general formulas for $P^{(4)}$ and R [see Eqs. (6.44a) and (6.44b) for comparison]:

$$P^{(4)} = \frac{1+2q\beta_1}{1+2q\beta_1+[1+2(\epsilon-1)(1+q)]\beta_2} \tag{6.51a}$$

and

$$R = \frac{1}{8\epsilon}|r|^2 \sum_{i=1}^{M} \Theta_i\{2+4q\beta_1+[1+2(\epsilon-1)(1+q)]\beta_2\}, \tag{6.51b}$$

where $\epsilon \equiv \eta^{-1}$, and we have assumed that the additional depolarized field $\mathbf{E}_w^{(4)}$ has the same partition function as Δ_i.

Consider now two specific forms of the modal partition functions. A uniform distribution of the depolarized noise field gives

$$\sum_{i=1}^{M} \Delta_i = \frac{M}{N}.$$

In the case of a gaussian distribution, a discrete modal intensity can be replaced by a continuous one for a large N, that is,

$$I_d = I_0 \exp(-\frac{8r^2}{\psi^2}), \tag{6.52}$$

where I_d is the average depolarized noise intensity in each polarization in the detection plane (which is usually a far-field plane of the fiber end), ψ is an effective

diameter of the depolarized noise intensity distribution in the detection plane, and $I_0 = |r|^2 d/\psi^2\pi$ so that $\iint_{-\infty}^{\infty} I_d dx\, dy = |r|^2 d/8$. We then find that

$$\sum_{i=1}^{M} \Delta_i \simeq 1 - \exp[-2(\phi/\phi_0)^2/(\psi/\phi_0)^2], \tag{6.53}$$

where

$$\phi_0 \equiv \text{ the input beam diameter corresponding to N}$$

and

$$\phi \equiv \text{ the input beam diameter corresponding to M,}$$

where the parameter $(\phi/\phi_0)^2$ is equal to M/N and to (input-beam N.A./fiber's N.A.)^2 [6.39].

Figure 6.3 shows the theoretical curves of (a) R/R_0 ($R_0 \equiv |r|^2 d(1+2q)/4\epsilon$) and (b) $P^{(4)}$ as a function of $(\phi/\phi_0)^2$(i.e., the input-beam N.A.) for uniform and gaussian($\psi/\phi_0 = 0.5$) distributions where, according to the experimental situation, M=M_0 is used so that $\sum_{i=1}^{M} \Theta_i = 1$ and $\beta_1 = 1$, i.e., the detection aperture is the same as the input-beam N.A. Three values of q's ($q = 0, \pm 0.035$) are used to see the effect of the residual polarization of the field $\mathbf{E}^{(2)}$. These values correspond to $P^{(2)} = 0$ and $P^{(2)} = 0.05$, respectively, when $|q| \simeq |u|$ is assumed [see Eq. (6.24)]. Here $\eta = 1(\epsilon = 1)$ is used, i.e., the PCM faithfully phase conjugates the field $\mathbf{E}_x^{(2)}$. It is seen that $P^{(4)}$ decreases as $(\phi/\phi_0)^2$ increases. Note, however, that when the input-beam N.A. is much smaller than the fiber's N.A. (i.e., $(\phi/\phi_0)^2 \ll 1$), then $P^{(4)}$ is close to unity independently of q, i.e., *almost complete polarization recovery* is possible. This is because the noise power is distributed among all the fiber guided modes so that for small input-beam N.A.'s, the noise power occupied within such a small fraction of all the fiber guided modes can be negligible compared to that of the true phase-conjugate beam. We see that the behavior of $P^{(4)}$ and R is sensitive to the forms of the noise distribution and the values of q's. When q is negative, the

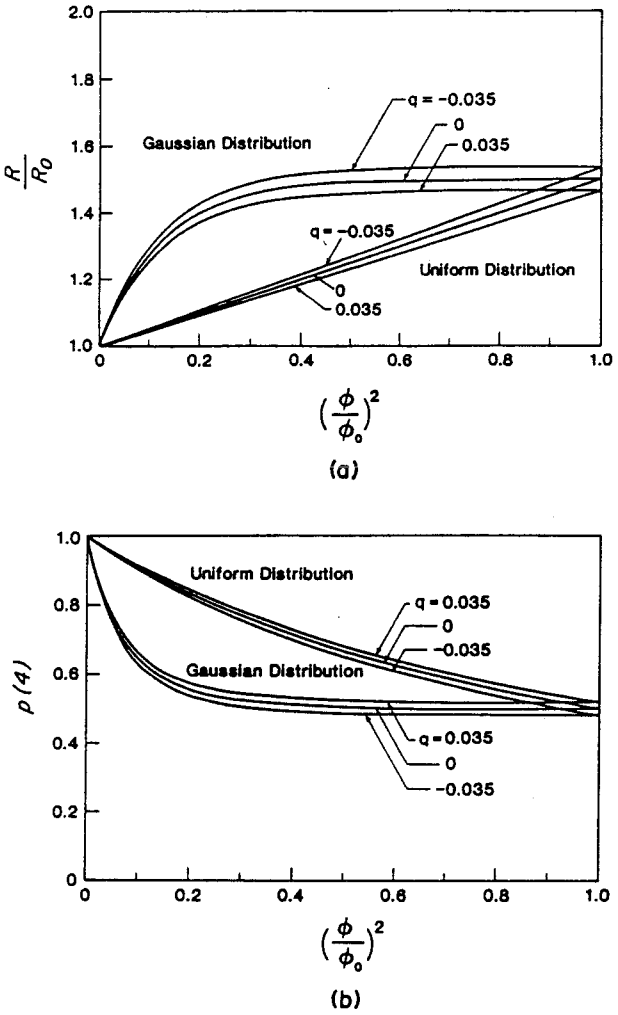

Figure 6.3 Theoretical curves of (a) the normalized reflectivity R/R_0 and (b) the degree of polarization $P^{(4)}$ as a function of $(\phi/\phi_0)^2$ for the uniform distribution and the gaussian noise distribution ($\psi/\phi_0 = 0.5$). The values $q = 0, \pm 0.035$ and $\eta = 1$ are used.

values of R and $P^{(4)}$ are higher than those for $q \geq 0$. This is because the residual x-polarized power is increased independently of q and $R_0|_{q>0} > R_0|_{q<0}$. We also see that as $(\phi/\phi_0)^2$ approaches unity, R/R_0 increases up to 1.5 while $P^{(4)}$ decreases down to 0.5 for $q = 0$.

6.2.4 Spatial information recovery

In this subsection we consider the SNR of the reconstructed spatial information in the present phase conjugation process. As was mentioned at the begining of this section, we employ the statistical treatment here. Goodman [6.40] analyzed the SNR, which is defined as the ratio of the deterministic image intensity I_s to the rms value σ_I of the total image intensity at the same point, in a reconstructed image by a hologram. In our case it is necessary to derive the expression for the rms value of speckle noise intensity that results from the depolarized noise field reflected from the fiber on phase conjugation. In addition, this speckle field, possessing both polarizations, is coherently added to the true phase-conjugate field, which acts as the x-polarized uniform coherent background signal.

The statistical properties of the sum of speckle patterns with coherent background intensities were studied theoretically by Ohtsubo *et al.* [6.41] for uncorrelated, partially developed speckles and by Steeger *et al.* [6.42] for partially polarized, partially developed speckles. For the case of speckles from a multimode fiber, Steeger *et al.* [6.43] found experimentally that the partially polarized speckle field of a multimode fiber follows a negative exponential distribution in each linearly polarized speckle intensity and the speckle field is spatially stationary in its intensity and polarization statistics when all the fiber modes are equally excited. From these results we may calculate the SNR in our case (for simplicity we put $q = 0$ and $\eta = 0$ in the following calculation). Before the calculation, the following features of the field $\mathbf{E}^{(4)}$ should be repeated:

(1) The true phase-conjugate field acts as a coherent background intensity I_s in the x-polarized intensity.

(2) The speckle noise field is completely depolarized so that there is no correlation between two orthogonal x- and y-polarized components, and that such speckle intensities in both polarizations are equal at one point in the detection plane.

(3) Each polarized component of the speckle noise field is fully developed and therefore its intensity statistics obey a negative exponential distribution.

First consider the x-polarized intensity that is the sum of fully developed speckle intensity and coherent background intensity. The probability-density function of such intensity is well known and is called a modified Rician density [6.44]. Its characteristic function [6.41] is given by

$$\Phi_{I_x}(iv) = \frac{1}{(1 - iv\bar{I}_{noise})} \exp[-\frac{I_s}{\bar{I}_{noise}} + \frac{I_s}{\bar{I}_{noise}(1 - iv\bar{I}_{noise})}], \tag{6.54}$$

where $\bar{I}_{noise}$ is the ensemble-averaged speckle noise intensity of one polarization at one point in the detection plane. For the y-polarized intensity, which is only fully developed speckle intensity, its characteristic function can be obtained from Eq. (6.54) with I_s=0:

$$\Phi_{I_y}(iv) = \frac{1}{(1 - iv\bar{I}_{noise})}. \tag{6.55}$$

Since there is no correlation between two orthogonal speckles, it follows immediately that the total characteristic function of interest is the product of Eqs. (6.54) and (6.55):

$$\Phi_I(iv) = \frac{1}{(1 - iv\bar{I}_{noise})^2} \exp[-\frac{I_s}{\bar{I}_{noise}} + \frac{I_s}{\bar{I}_{noise}(1 - iv\bar{I}_{noise})}]. \tag{6.56}$$

The rms noise intensity is then given by

$$\begin{aligned} \sigma_I &= [\bar{I^2} - (\bar{I})^2]^{\frac{1}{2}} \\ &= [\frac{1}{(i)^2}\frac{\partial^2}{\partial v^2}\Phi_I(iv)|_{v=0} - (I_s + 2\bar{I}_{noise})^2]^{\frac{1}{2}} \\ &= [2\bar{I}_{noise}(\bar{I}_{noise} + I_s)]^{\frac{1}{2}}. \end{aligned} \tag{6.57}$$

It is seen from Eq. (6.57) that the rms noise intensity is expressed by $\bar{I}_{noise}$ and the interference term between the true phase-conjugate field and the depolarized noise field. The SNR can be written as

$$(\mathrm{SNR})_{xy} \equiv \frac{I_s}{\sigma_I} = \gamma\sqrt{\frac{2}{1+2\gamma}}, \tag{6.58}$$

where $\gamma = I_s/2\bar{I}_{noise}$ is the beam ratio parameter [6.44]. If an analyzer (set to the x-polarization direction) is used to measure only the x-polarized component of the field $\mathbf{E}^{(4)}$, then the SNR can be found straightforwardly to be

$$(\mathrm{SNR})_x = \frac{2\gamma}{\sqrt{1+4\gamma}}. \tag{6.59}$$

To illustrate the dependence of these SNR's on the input-beam N.A., we identify $I_s = |r|^2 d/(\pi\phi^2)$ [i.e., the input is assumed to be a two-dimensionally uniform beam with the diameter ϕ so that the total power of the true phase-conjugate beam is $|r|^2 d/4$. See also Eq. (6.34)] and $\bar{I}_{noise}$ is given by $|r|^2 d/(2\pi\phi_0^2)$ for a uniform distribution and by I_d [see Eq. (6.52)] for a gaussian distribution. Then the beam ratio parameter γ at the center of the signal beam is given by

$$\gamma = \begin{cases} \frac{1}{(\frac{\phi}{\phi_0})^2}, & \text{for a uniform distribution;} \\ \frac{1}{2}\frac{(\frac{\psi}{\phi_0})^2}{(\frac{\phi}{\phi_0})^2}, & \text{for a gaussian distribution.} \end{cases}$$

We therefore see the parametric dependence of the SNR on $P^{(4)}$ given by Eq. (6.44*a*) through $(\phi/\phi_0)^2$ (i.e., an input-beam N.A.).

Figure 6.4 shows the dependence of the two SNR's, as given by Eqs. (6.58) and (6.59), on $(\phi/\phi_0)^2$ at the center of the true phase-conjugate beam for a uniform and a gaussian(ψ/ϕ_0=0.5) distributions. It is seen that for the gaussian distribution the

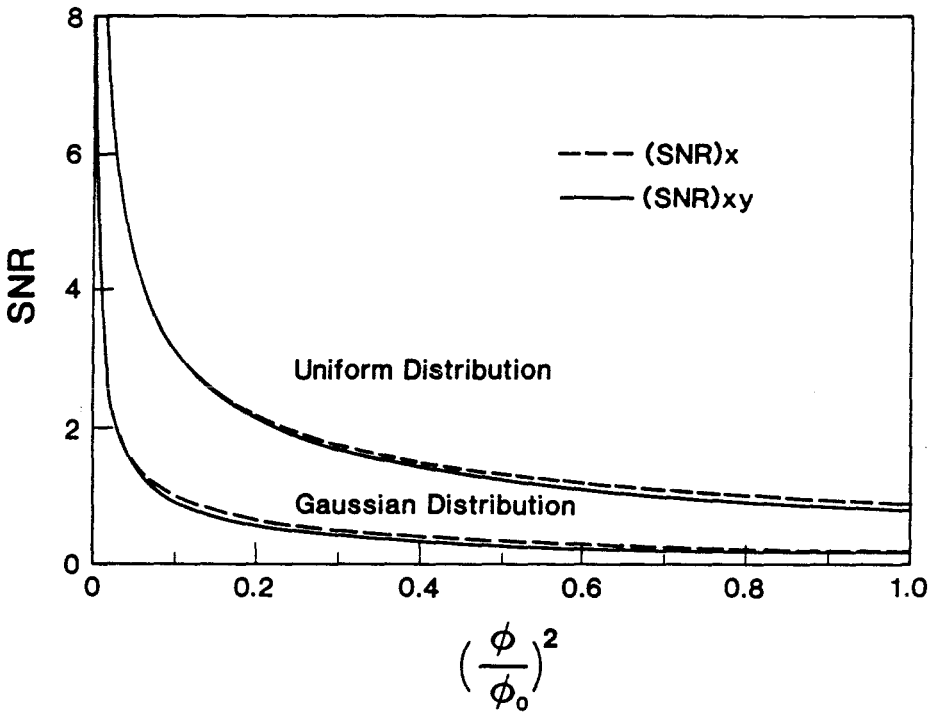

Figure 6.4 Theoretical curves of the two SNR's, $(\mathrm{SNR})_{xy}$, and $(\mathrm{SNR})_x$, at the center of the signal beam as a function of $(\phi/\phi_0)^2$ for the uniform distribution and the gaussian noise distribution $(\psi/\phi_0 = 0.5)$. The values q=0 and $\eta = 1$ are used.

two SNR's decrease rapidly when $(\phi/\phi_0)^2$ exceeds about 0.01, i.e., the input-beam N.A. exceeds about 10% of the fiber's N.A., while for the uniform distribution the changes of the SNR's are slower. This is because, given a deterministically constant value of the phase-conjugate reflective power (i.e., $|r|^2 d/4$), the intensity I_s at the center of the phase-conjugate beam decreases as the input-beam N.A. increases, while the noise intensity I_{noise} is almost constant independently of the input-beam N.A., resulting in decrease of γ (i.e., a decrease of the SNR). On the other hand, if the input-beam N.A. is much smaller than the fiber's N.A., then the intensity I_s is much larger than the noise intensity I_{noise}, resulting in a large value of γ and therefore in the increase of the SNR. It is also seen that the $(SNR)_{xy}$ and the $(SNR)_x$ are almost the same over an entire range of the input-beam N.A.'s. This indicates that, although an analyzer is inserted in order to eliminate unwanted speckle noise of the orthogonal polarization, the improvement of the SNR is very small [6.45]. Finally it should be noted that the qualitative dependence of the SNR on the input-beam N.A. is the same as that of the degree of polarization shown in Fig. 6.3(b), although the SNR in a linear scale seems to be more sensitive to the input-beam N.A.

6.3 Experiment

6.3.1 Polarization and spatial information recovery for small numerical aperture inputs

The experimental arrangement is shown in Fig. 6.5. The input-beam N.A. was about 0.01 which was much smaller than the fiber's N.A. If $\mathbf{E}^{(4)}$ is the true phase-conjugate replica of $\mathbf{E}^{(1)}$ (including the polarization state), then the output light $\mathbf{E}^{(5)}$ having retraversed the wave plate must return to the complex conjugate of the initial x-polarized state $\mathbf{E}^{(0)}$. Thus the degree of polarization recovery $p=(P_1 - P_2)/(P_1 + P_2)$ defined in the previous section can be a measure of the

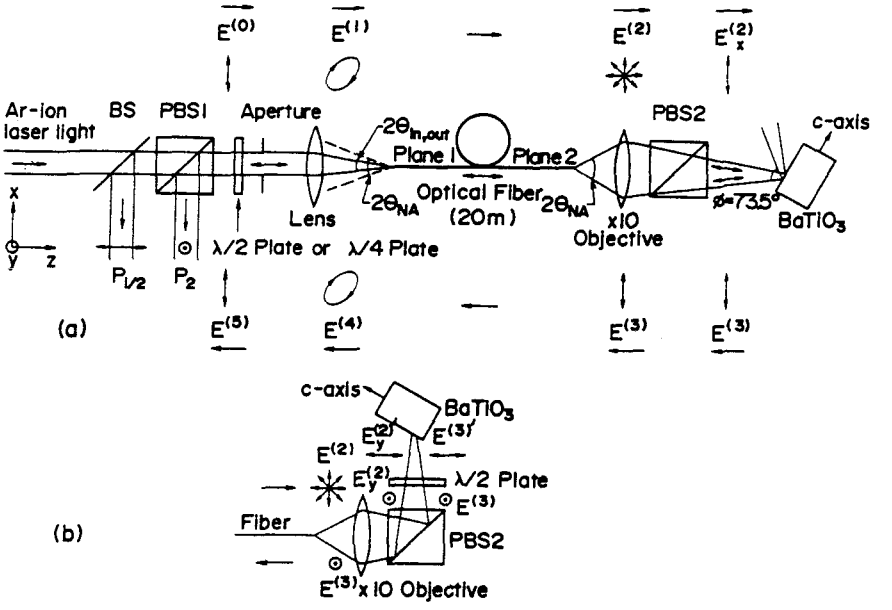

Figure 6.5 Experimental arrangement for polarization and spatial information recovery. In (a), the x-polarized component $\mathbf{E}_x^{(2)}$ in the depolarized light $\mathbf{E}^{(2)}$ is used to generate the phase conjugate light. In (b), the y-polarized component $\mathbf{E}_y^{(2)}$ is used.

polarization recovery, where P_1 and P_2 are, respectively, the power of the two orthogonal polarization components of $\mathbf{E}^{(5)}$. In Fig. 6.5(b), the y-polarized, rather than the x-polarized, component of $\mathbf{E}^{(2)}$ was used to generate the phase-conjugate field. Since the crystal reflects preferentially the x-polarized field, the polarization direction was rotated by 90° by the $\lambda/2$ plate prior to incidence of the crystal.

Figure 6.6(a) shows the experimentally observed dependence of p as a function of the direction of polarization(φ) of the linearly polarized light entering the fiber. This direction was controlled by the angular position of the $\lambda/2$ plate. The quantity p is seen to be very nearly unity over the whole range, indicating a very good (better than 96%) restoration of the original linear polarization. Also plotted in Fig. 6.6(a) is the reflectivity R_1 of the phase conjugator defined by $R_1 = P_1/P_0$ (P_0=input beam power at the crystal). When arbitrary elliptically-polarized light was used as the input $\mathbf{E}^{(1)}$, p was also close to unity. Figure 6.6(b) shows p and R_1 as a function of P_0 for the three different polarization states at the input: linearly-polarized, circularly-polarized and elliptically-polarized. The quantity p is seen to be also close to unity for the inputs of several polarization states, indicating the complete reversal of an arbitrary polarized input beam whose input-beam N.A. is much smaller than the fiber's N.A.: in this experiment $(\phi/\phi_0)^2 = 0.001$ [see the theoretical curves at this input-beam N.A. shown in Fig. 6.3(b)]. These results were obtained for both the experimental arrangements of Fig. 6.5(a) and 6.5(b). The spatial recovery of the input $\mathbf{E}^{(1)}$ (a uniform beam in the experiment) was also observed with high quality, as is predicted from the theory.

6.3.2 Fidelity of polarization and spatial information recovery

Here we show several experiments on the fidelity of the phase conjugation process as a function of the input-beam N.A. and compare them with the theory

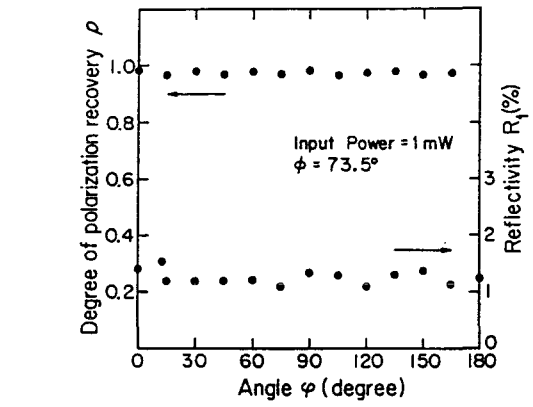

(a)

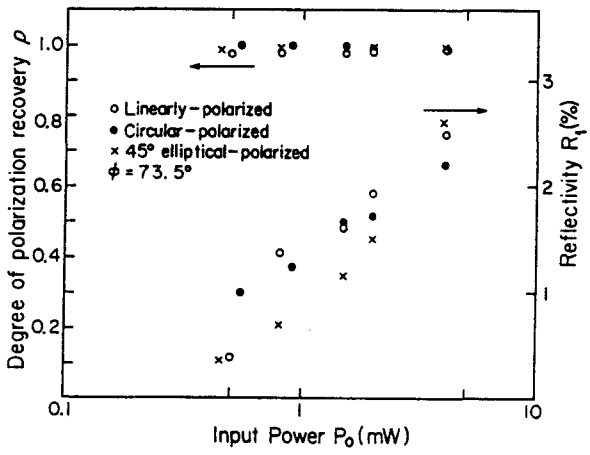

(b)

Figure 6.6 (a)Degree of polarization recovery p and reflectivity R of the fiber-coupled PCM are plotted as a function of the angle φ between the polarization direction of the input linearly polarized light and the x-axis; (b) Degree of polarization recovery p and reflectivity R_1 of the fiber-coupled PCM are plotted as a function of the input power P_0 for the three different input polarization states: linearly polarized(○), circular polarized(●) and 45° elliptical polarized(×).

given in the previous section. The experimental arrangement is shown in Fig. 6.7. The x-polarized input beam $\mathbf{E}^{(1)}$ from the multilongitudinal-mode argon-ion laser beam (λ = 514.5 nm) was focused into the multimode graded-index fiber (0.29 N.A., 5 m long) through a lens (L1). The input-beam diameter ϕ (and therefore the input-beam N.A. which we will also designate by ϕ) was controlled by an aperture (AP1). The microscope objective (L2) of 0.40 NA at the output end of the fiber was used to collect all the modes emitted from the fiber. A $BaTiO_3$ crystal (5 mm × 5 mm × 4 mm) was used as a self-pumped PCM [6.14] for an x-polarized incident beam of 1 mW. The detectors (D2 and D3) measure the power of the beam $\mathbf{E}_x^{(2)}$ and of the phase-conjugate beam $\mathbf{E}^{(3)}$, respectively. The transmissivity of the fiber ($\equiv \mid \mathbf{E}^{(2)}/\mathbf{E}^{(1)} \mid^2$) was about 60% (without Fresnel reflection correction), and the phase-conjugate reflectivity ($\equiv \mid \mathbf{E}^{(3)}/\mathbf{E}_x^{(2)} \mid^2$) at the crystal was 30%, independent of ϕ. The phase-conjugate beam $\mathbf{E}^{(4)}$ from the input end of the fiber is reflected by the nonpolarizing beam splitter (BS1). Its power and spatial structure were recorded by the detector (D4) and a TV camera, respectively. It was ascertained by means of the $\lambda/4$ plate and the analyzer (A) that BS1 has no effect on the ellipsometric measurement of the Stokes parameters (s_0, s_1, s_2, s_3) and the degree of polarization $P^{(4)}$ ($= \sqrt{s_1^2 + s_2^2 + s_3^2}/s_0$) given by Eq. (6.23) for $\mathbf{E}^{(4)}$. An aperture (AP2) with a diameter Φ was placed in front of the $\lambda/4$ plate to limit the detecting area for $\mathbf{E}^{(4)}$.

Figure 6.8 shows a typical photograph of the field $\mathbf{E}^{(2)}$. It is seen that the field has speckled structures because of the strong intermodal scattering in the fiber. Also, the measured polarization states of the field $\mathbf{E}^{(2)}$ for the different values of the input-beam N.A.'s are shown in Table 6.1. It is seen that s_1, s_2, and s_3 are much smaller than s_0, so the degree of polarization is much smaller than unity, i.e., the beam $\mathbf{E}^{(2)}$ is almost completely depolarized, independent of the input-beam N.A. This data clarifies the validity of the random-coupling approximation and the

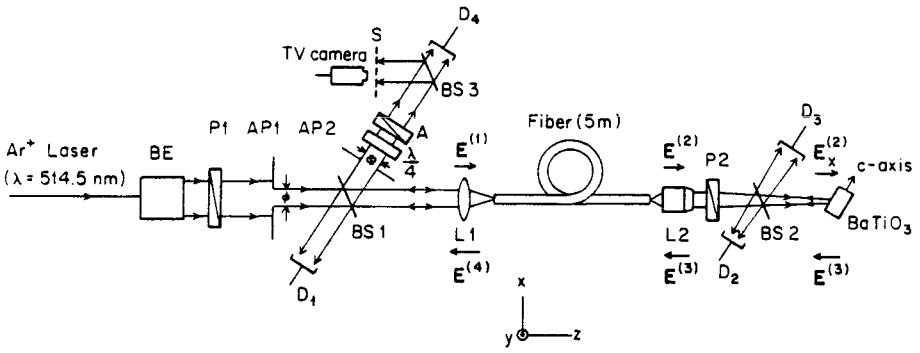

Figure 6.7 Experimental arrangement. BE:beam expander; P1,P2:polarizers to guarantee the x-polarized input to the fiber and the crystal, respectively; D1,D2,D3:detectors for measuring the power of the beams $\mathbf{E}^{(1)}$, $\mathbf{E}_x^{(2)}$, and $\mathbf{E}^{(3)}$, respectively.

Figure 6.8 Photograph of the field $\mathbf{E}^{(2)}$ emitted from a multimode fiber.

Table 6.1 Experimental data of the Stokes parameters and the degree of polarization of the field $\mathbf{E}^{(2)}$

Input-beam NA	s_1/s_0	s_2/s_0	s_3/s_0	$P^{(2)}$
0.02	0.003	0.008	−0.016	0.018
0.11	0.033	0.023	−0.028	0.049
0.25	0.004	0.041	−0.021	0.046

modal averaging assumption [i.e., the assumption that due to random phases of M_{ij}'s the cross terms $a_{\substack{kk' \\ (k\neq k')}}$ and $b_{kk'}$ given by Eqs. (6.18) and also q and u given by Eqs.(6.20) are much smaller than unity].

Figure 6.9 shows the experimental results of $R(\equiv |\mathbf{E}_x^{(4)}/\mathbf{E}^{(1)}|^2)$ [Fig.6.9(a)] and $P^{(4)}$ and p [Fig.6.9(b)], as a function of $(\phi/\phi_0)^2$ for the linearly x-polarized input($p, P > 0.99$). The theoretical plots of R and $P^{(4)}$ from Eqs. (6.51*a*) and (6.51*b*) are also shown using a gaussian distribution for the noise intensity(ψ/ϕ_0=0.5), and (q,η)=(0,1), (0.035,1), (0,0.8), and (0.035,0.8). According to the data shown in Table 6.1, a positive value of $q(= 0.035)$ was used in the theoretical calculation. [Note that $s_1 > 0$ corresponds to $q > 0$. See Eq. (6.22*b*) with $a_{kk} \simeq 0.5$.] Since the experimental data for R included unwanted losses due to reflection and absorption by optical components, the proportionality factors in the theoretical curves for R were determined by least square fits with the experimental data. The diameter Φ of AP2 was set to be $\Phi = \phi$ for all ϕ's. All the data was obtained within uncertainties of $\pm 10\%$. It is shown that for very small ϕ(i.e.,when the input-beam N.A. is very small compared to the fiber's N.A.), p is almost unity, i.e., true phase conjugation of the input beam $\mathbf{E}^{(1)}$ is possible, whereas R is low. On the other hand, p decreases appreciably with an increase of ϕ, accompanied by an increase in R. It is also seen that $p \approx P^{(4)}$ for all ϕ's, indicating that the polarized part of the phase-conjugate beam is almost x-polarized and that the rest of the phase-conjugate beam is completely depolarized. Thus the power in the depolarized component of the reflected beam increases with the increase of ϕ, making the total R increase but p and $P^{(4)}$ decrease. Note that the theoretical curves are in good agreement with the experimental data when the gaussian distribution of the noise intensity, the residual polarization of the field $\mathbf{E}^{(2)}$ and the fidelity of the PCM are taken into account [i.e., when $(q, \eta) = (0, 0.8)$ and (0.035,0.8).] The measurements of p and $P^{(4)}$ were also performed as a function of Φ/ϕ for $(\phi/\phi_0)^2 = 0.005$ and

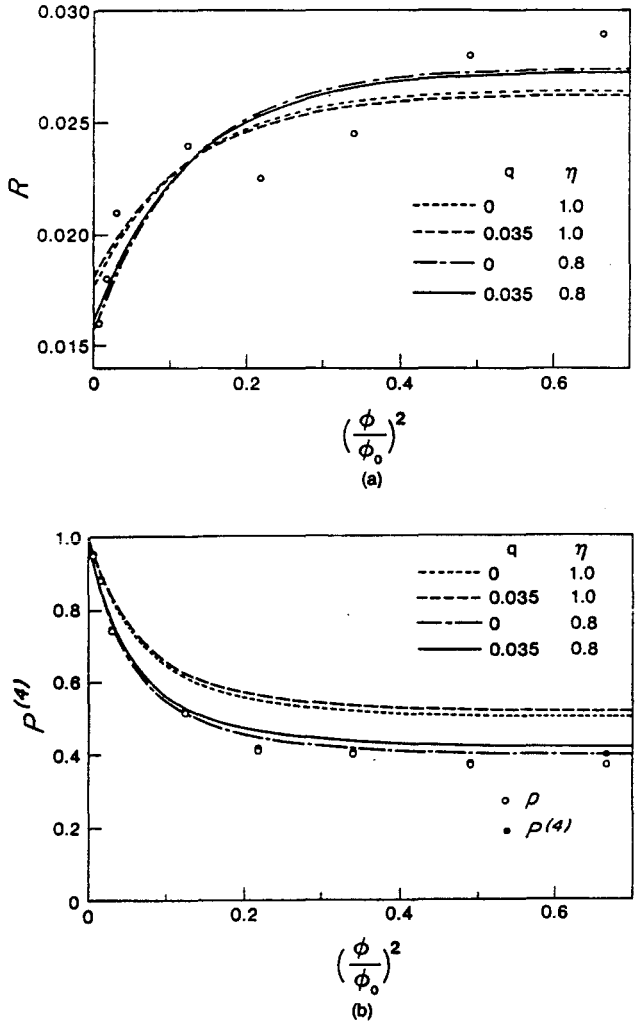

Figure 6.9 (a) Experimental data of the reflectivity R versus $(\phi/\phi_0)^2$. The solid lines are theoretical curves using a gaussian noise distribution ($\psi/\phi_0 = 0.5$) and (q, η) = (0,1), (0,0.8), (0.035,1), and (0.035,0.8). The proportional factor of R in the theoretical calculation is determined by least squre fits with the experimental data shown here. (b) Experimental data of the degree of polarization recovery $p(\circ)$ and the degree of polarization $P^{(4)}(\bullet)$. The solid lines are theoretical curves whose parameters are the same as those in (a).

$(\phi/\phi_0)^2 = 0.69$. It was found that for a small N.A. they start decreasing when Φ/ϕ exceeds unity, while for a large N.A. they are nearly constant regardless of Φ/ϕ. These results were also obtained with the single longitudinal-mode operation of an argon-ion laser, indicating that the phase conjugation process of interest was less sensitive to the source temporal coherence.

The results shown above support the theoretical model given in the previous section, according to which nearly 50% of the reflected power that is not the power of the true phase-conjugate component but is that of the depolarized noise component is distributed essentially uniformly over all the fiber modes, thus occupying ϕ_0 independently of ϕ. If the input beam occupies $\phi \ll \phi_0$, the full recovery of the true phase-conjugate signal is accomplished with an acceptance-beam diameter $\Phi = \phi$, resulting in a rejection of most of the noise power since only a small fraction $[(\phi/\phi_0)^2 \ll 1]$ of the noise power is contained within the N.A. (i.e., ϕ) occupied by the signal. This leads to high values (≥ 0.95) of p and $P^{(4)}$ with $\Phi/\phi \leq 1$. It also follows that under the above conditions as Φ/ϕ exceeds unity all the additional power reaching D_4 is due to the noise power, leading to decreases of p and $P^{(4)}$. If, on the other hand, the input-beam N.A. is increased untill $\phi \approx \phi_0$ so that the input signal excites almost all the fiber modes, the signal power per mode is reduced, while that of the noise remains the same, thus leading to a large R as well as to low constant values of p and $P^{(4)}$ that are almost independent of ϕ. This model is also confirmed by the data of Fig. 6.10. These were measured by means of one line scan of the TV camera at the center of the phase-conjugate beam, where the background noise was electronically eliminated with the aid of a digital oscilloscope. It is seen that for a small NA ($(\phi/\phi_0)^2 = 0.005$) the noise intensity [see Fig. 6.10(b)] is much smaller than that of the true phase-conjugate component [see Fig. 6.10(a)] and is distributed more or less uniformly over ϕ. In the case $(\phi/\phi_0)^2 = 0.69$ the noise is distributed over ϕ_0, but most of the noise power is occupied inside ϕ, resulting in

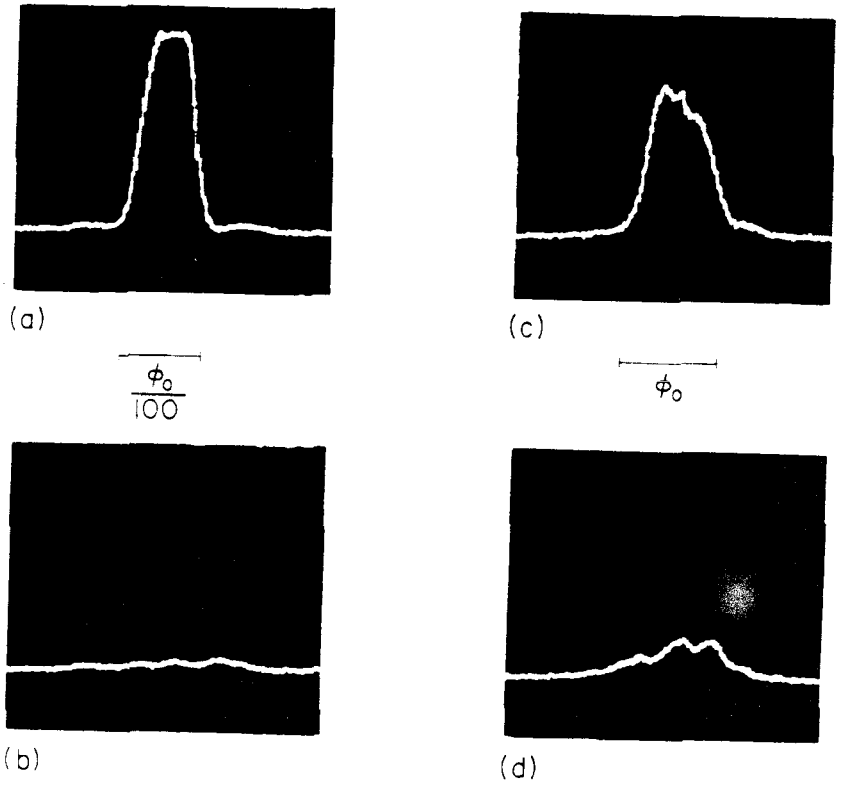

Figure 6.10 Intensity distributions of phase-conjugate output beams for the linearly x-polarized input: (a) x-polarized component (signal + noise) and (b) y-polarized component (noise) for $(\phi/\phi_0)^2 = 0.005$; (c) x-polarized component (signal + noise) and (b) y-polarized component (noise) for $(\phi/\phi_0)^2 = 0.69$.

the insensitivity of p and $P^{(4)}$ to Φ/ϕ.

Figure 6.11 shows the photographs of the x-polarized phase-conjugate images of the letter H when $(\phi/\phi_0)^2 = 0.015$ [Fig.6.11(a)] and $(\phi/\phi_0)^2 = 0.74$ [Fig.6.11(b)]. As was discussed in the previous section, the degradation of the SNR is apparent from these two distinct photographs.

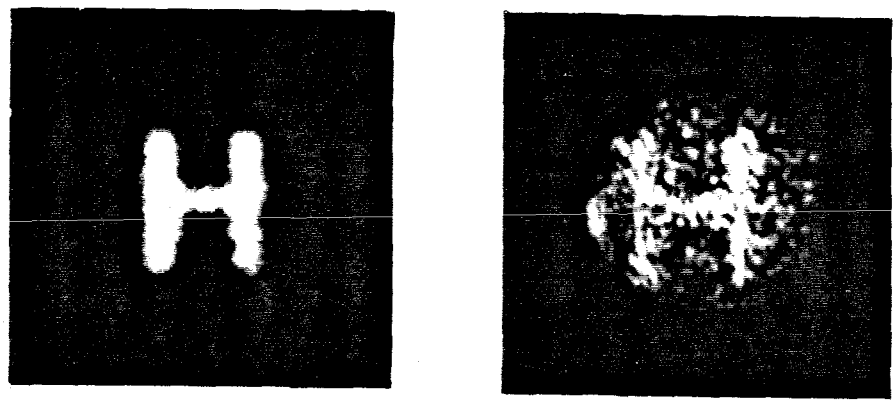

Figure 6.11 Photographs of the x-polarized phase-conjugate images of the letter H for (a) $(\phi/\phi_0)^2 = 0.015$ and (b) $(\phi/\phi_0)^2 = 0.74$.

APPENDIX B

Random Coupling Approximation

Each element of the scattering matrix M is expressed as

$$M_{ij} = m_{ij} \exp(i\phi_{ij}). \tag{B1}$$

These elements are interrelated by the unitarity condition given by Eqs. (6.8) and (6.9). For the case of strong intermodal coupling in the fiber, the initially excited fiber guided modes at the input are redistributed among all the fiber guided modes during propagation. Then it is appropriate to assume that the amplitudes m_{ij} are either nearly the same or symmetrically and widely distributed with respect to the diagonal elements m_{ii}, while the phases ϕ_{ij} are distributed essentially uniformly over the $-\pi - +\pi$ interval under the constraint of the unitarity condition. In this case the following *random-coupling approximation* may be adequate from Eqs. (6.8) and (6.9):

$$\sum_{i=1}^{N} |(M_{kl})_{ij}|^2 \simeq \frac{1}{2}, \tag{B2}$$

$$\sum_{j=1}^{N} |(M_{kl})_{ij}|^2 \simeq \frac{1}{2}, \tag{B3}$$

where $k, l = x, y$ and $i, j = 1, \cdots, \mathrm{N}$. In addition, because of the modal averaging over phase-mismatched terms, all the other cross terms are much smaller than unity for large N.

APPENDIX C

Qualitative Proof of Polarization and Spatial Information Recovery

In what follows, the qualitative proof of polarization and spatial information recovery is given by means of the random-coupling approximation. As the simplest form of the scattering matrix M it is written as

$$M_{ij} = \frac{1}{\sqrt{2N}} \exp(i\phi_{ij}). \tag{C1}$$

Then the scattering matrix S in the round-trip propagation given by Eq. (6.26) can be expressed as

$$S \equiv M'CM^* = \begin{pmatrix} M'_{xx}M^*_{xx} & M'_{xx}M^*_{xy} \\ M'_{yx}M^*_{xx} & M'_{yx}M^*_{xy} \end{pmatrix} \tag{C2}$$

and

$$\begin{aligned} (M'_{xx}M^*_{xx})_{ij} &= (M'_{xx})_{ik}(M_{xx})^*_{kj} \\ &= (M_{xx})_{ki}(M_{xx})^*_{kj} \\ &= \frac{1}{2N}\sum_{k=1}^{N} \exp\{i[(\phi_{xx})_{ki} - (\phi_{xx})_{kj}]\} \\ &= \begin{cases} \frac{1}{2} & \text{for } i = j, \\ O(1/\sqrt{N}) & \text{for } i \neq j, \end{cases} \end{aligned} \tag{C3}$$

where summation over repeated indices is made and Eqs. (6.12a) – (6.12d) are used. The $N^{-1/2}$ in Eq. ($C3$) is due to the random-walk nature represented by the summation of the phasors $\exp\{i[(\phi_{xx})_{ki} - (\phi_{xx})_{kj}]\}$, independently of the fiber guided modes that are excited initially.

In a similar fashion we find that

$$(M'_{yx}M^*_{xy})_{ij} = \begin{cases} \frac{1}{2} & \text{for } i = j, \\ O(1/\sqrt{N}) & \text{for } i \neq j, \end{cases}$$

$$(M'_{xx}M^*_{xy})_{ij} = O(1/\sqrt{N}),$$

$$(M'_{yx}M^*_{xx})_{ij} = O(1/\sqrt{N}). \qquad (C4)$$

Then it is found that

$$S = S_1 + S_2$$

and

$$\mathbf{E}^{(4)} = \frac{1}{2}r(\mathbf{E}^{(1)})^* + \mathbf{V}, \qquad (C5)$$

where S_1 and S_2 correspond to Eqs. (6.27*a*) and (6.27*b*), respectively, and $\mathbf{V}$ denotes the phase-mismatched noise field. We note that Eq. ($C5$) is equivalent to Eq. (6.29).

References for Chapter 6

6.1. For reviews see A. Yariv, IEEE J. Quantum Electron. **QE-14**, 650 (1978), also R.A. Fisher, ed., *Optical Phase Conjugation*, (Academic Press, New York, 1983) and references therein.

6.2. B.Ya. Zel'dovich and V.V. Shkunov, Sov. Phys. JETP **48**, 214 (1978).

6.3. V.N. Blashchuk, B.Ya. Zel'dovich, V.N. Krasheninnikov, N.A. Mel'nikov, N.F. Pilipetsky, V.V. Ragulsky, and V.V. Shkunov, Sov. Phys. Dokl. **23**, 588 (1978).

6.4. V.N. Blashchuk, V.N. Krasheninnikov, N.A. Mel'nikov, N.F. Pilipetsky, V.V. Ragulsky, V.V. Shkunov, and B.Ya. Zel'dovich, Opt. Commun. **27**, 137 (1978).

6.5. N.G. Basov, V.F. Efimkov, I.G. Zubarev, A.V. Kotov, S.I. Mikhailov, and M.G. Smirnov, Sov. Phys. JETP Lett. **28**, 197 (1978).

6.6. B.Ya. Zel'dovich and V.V. Shkunov, Sov. J. Quantum Electron. **9**, 379 (1979).

6.7. B.Ya. Zel'dovich and T.V. Yakovleva, Sov. J. Quantum Electron. **10**, 501 (1980).

6.8. In the past, spatial wavefront reversal of each of the two orthogonal polarizations having its own amplitude and phase (thereby incomplete spatial-polarization wavefront reversal) was found for depolarized pump waves in SBS [6.2]–[6.5]. An improved scheme which incorporates a two-plate tapered light guide prior to the SBS phase conjugator was recently reported for the complete reversal of depolarized pump waves. See I.D. Carr and D.C. Hanna, Opt. Commun. **52**, 396 (1987).

6.9. V.N. Blashchuk, B.Ya. Zel'dovich, A.V. Mamaev, N.T. Pilipetsky, and

6.28. Y. Tomita, K. Kyuma, R. Yahalom, and A. Yariv, Opt. Lett. **12**, 1020 (1987).

6.29. R. Yahalom, K. Kyuma, and A. Yariv, Appl. Phys. Lett. **50**, 792 (1987).

6.30. R. Yahalom and A. Yariv, Opt. Lett. **13**, 889 (1988).

6.31. I. McMichael, P.H. Beckwith, and P. Yeh, Opt. Lett. **12**, 1023 (1987).

6.32. K. Kim, L. Mandel, and E. Wolf, J. Opt. Soc. Am. A **4**, 433 (1987).

6.33. A. Yariv, *Quantum Electronics*, 2nd ed., (Wiley, New York, 1975), p. 357.

6.34. S. Solimeno, B. Crosignani and P. Di Porto, *Guiding, Diffraction, and Confinement of Optical Radiation*, (Academic Press, New York, 1986), pp. 569–573.

6.35. A.W. Snyder and J.D. Love, *Optical Waveguide Theory*, (Chapman and Hall, London, 1983), p. 292.

6.36. M. Born and E. Wolf, *Principles of Optics*, 5th ed., (Pargamon Press, New York, 1975), pp. 544–555.

6.37. See, for example, M.J. Stephen and G. Cwilich, Phys. Rev. B**34**, 7564 (1986); K.A. O'Donnell and E.R. Mendez, J. Opt. Soc. Am. A**4**, 1194 (1987); and M.B. Van der Mark, M.P. van Albada, and A. Lagendijk, Phys. Rev. B**37**, 3575 (1988).

6.38. For reviews see Y. Nagaoka, ed., *Anderson Localization*, Prog. Theor. Phys. Supp. **84** (1985); S. Chakravarty and A. Schmid, Phys. Rep. **140**, 193 (1986).

6.39. Since the input-beam N.A.$\approx\phi/2f$ (f is a focal length of a lens) and $M/N_{total}=(N.A./N.A._{fiber})^2/2$ (M is the number of modes corresponding to ϕ for one polarization; $N_{total}=2N$; $N.A._{fiber}$ is the fiber's N.A.), we obtain $M/N_{total}=(\phi/\phi_0)^2/2$. In addition, since ϕ^2 is proportional to the solid angle Ω subtended by the beam launched into the fiber, then it also gives $(\phi/\phi_0)^2 = \Omega/\Omega_0$.

6.40. J.W. Goodman, J. Opt. Soc. Am. **57**, 493 (1967).

6.41. J. Ohtsubo and T. Asakura, Opt. Lett. **1**, 98 (1977).

6.42. P.F. Steeger, T. Asakura, K. Zocha, and A.F. Fercher, J. Opt. Soc. Am. **A1**, 677 (1984).

6.43. P.F. Steeger, T. Asakura, and A.F. Fercher, IEEE J. Lightwave Technol. **LT-2**, 435 (1984).

6.44. J.W. Goodman, in *Laser Speckle and Related Phenomena*, J.C. Dainty ed., 2nd ed., (Springer-Verlag, Berlin, 1984), pp. 9–75.

6.45. In practice, however, the use of the analyzer may improve the SNR better than that in the calcualtion because of the rejection of unwanted noise that is due to the backreflection from optical components.

CHAPTER SEVEN

Applications of Modal Dispersal and Phase Conjugation to Information Retrieval and Sensing

7.1 Introduction

Image transmission and recovery in multimode fibers using phase conjugation, proposed by Yariv [7.1–3], may be the first application of a combination of multimode fibers and a PCM [7.4]. In this case multimode fibers act not only as thick modal distorters but also as polarization scramblers. The experimental demonstrations of image recovery based on a round-trip propagation via phase conjugation employed nonpolarization-preserving PCM's (NPPPCM's) which correspond to the present scheme [7.5–8]. We have discussed the quality of the image recovery in the previous chapter. This quality was also compared to the case of the polarization-preserving PCM (PPPCM) [7.9]. It was found that for large N.A. inputs the resolution of the restored image is limited by the finite number of the fiber guided modes independently of whether the PCM preserves polarization, and that the contrast is restored only when the PPPCM is used. The fiber-PCM combination that uses modal dispersal of information and phase conjugation [7.10], (which is described in the previous chapter), has also led to a number of new applications that include correction of nonreciprocal polarization distortions [7.11], correction of lossy amplitude distortions [7.12], temporal data channeling between beams [7.13], and all-optical beam thresholding [7.14]. Other applications using this combination include fiber-optic interferometers/sensors [7.8,10,15,16] and gyros [7.17–21]. Since these applications do not, in general, require large

N.A. inputs, high-quality returned signals can be obtained with the NPPPCM's. Also, photorefractive oscillation with multimode fibers [7.18, 22] and optical interconnection and communication [7.23, 24] have been reported so far. We note that the polarization-preserving property of the present scheme is also applicable to real-time image processing using wave polarization and phase conjugation [7.25].

In this chapter we describe three main applications using modal dispersal and phase conjugation: (a) correction of nonreciprocal polarization distortions [7.10,11]; (b) correction of lossy amplitude distortions [7.12]; and (c) phase-conjugate multimode fiber-optic sensors [7.10].

7.2 Correction of nonreciprocal polarization distortions

The basic property of time reversal and distortion correction by phase conjugation breaks down if the propagation path includes nonreciprocal media such as magnetic (or gyrotropic) components. This follows mathematically from the fact that the presence of imaginary elements in the expressions for the magnetic susceptibility tensor spoils the invariance of Maxwell equations under complex conjugation for the reflected wave. To illustrate the effect, consider the case shown in Fig. 7.1(a), where a plane wave initially with complex transverse components (E_{x1},E_{y1}) propagates through an element A, is phase conjugated, and returns to the initial plane after passing A in reverse. If the element A is a Faraday rotator with a Faraday angle θ, the round trip is described by

$$\begin{pmatrix} E_x \\ E_y \end{pmatrix}_4 = \begin{pmatrix} \cos 2\theta & -\sin 2\theta \\ \sin 2\theta & \cos 2\theta \end{pmatrix} \begin{pmatrix} E_x{}^* \\ E_y{}^* \end{pmatrix}_1 . \tag{7.1}$$

The vector $\mathbf{E}^{(4)}$ is thus *not* the complex conjugate of $\mathbf{E}^{(1)}$. [This can be compared to the case where the element A is dielectric (reciprocal), say, a retardation plate. Then the effect of the (reciprocal) retardation plate is canceled after a round trip (see Fig. 4.7).]

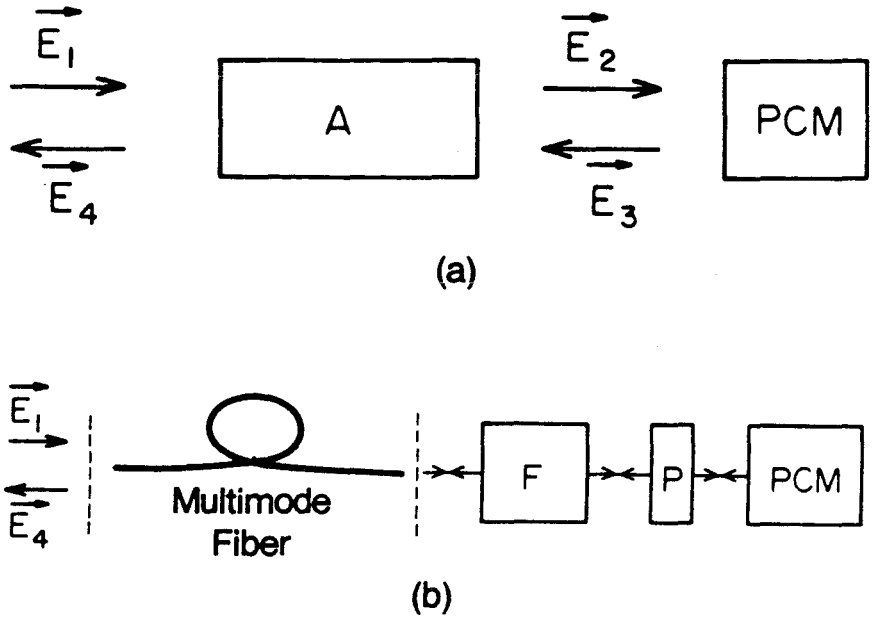

Figure 7.1 (a) Schematic diagram of a wave that propagates through an element A, is phase conjugated, and returns to the initial plane. (b) A method to undo the nonreciprocal effect. P, polarizer;F, Faraday rotator.

In this section we describe a method to undo the non-reciprocal effect on polarization by modal dispersal and phase conjugation [see Fig. 7.1(b)]. Assume a multimode fiber with a circular cross section. Adopting the same notations and procedure as those used in the previous Chapter but using a rotating coordinate (i.e., a circular polarization) representation, the phase-conjugate beam $\mathbf{E}^{(4)}$ can be written as

$$\mathbf{E}^{(4)} = rM'F'P'P^*F^*M^*(\mathbf{E}^{(1)})^*, \tag{7.2}$$

where

$$M = \begin{pmatrix} M_{RR} & M_{RL} \\ M_{LR} & M_{LL} \end{pmatrix}, \tag{7.3a}$$

and

$$M' = \begin{pmatrix} M'_{RR} & M'_{RL} \\ M'_{LR} & M'_{LL} \end{pmatrix}, \tag{7.3b}$$

are the 2N-rank scattering matrices of the fiber for the forward and the backward directions, respectively, and $R\,(L)$ denotes a right (left) circular polarization;

$$F = \begin{pmatrix} e^{i\theta}I & 0 \\ 0 & e^{-i\theta}I \end{pmatrix}, \tag{7.4a}$$

and

$$F' = \begin{pmatrix} e^{-i\theta}I & 0 \\ 0 & e^{i\theta}I \end{pmatrix}, \tag{7.4b}$$

are the 2N-rank Faraday rotation matrices for traveling along and opposite the magnetic field, respectively. In Eqs. (7.3a) and (7.3b) we assume that all the fiber guided modes suffer the same amount of Faraday rotation θ;

$$P = \frac{1}{2}\begin{pmatrix} I & I \\ I & I \end{pmatrix} = P', \tag{7.5}$$

is the matrix for the linear polarizer.

Substituting Eqs. (7.3) – (7.5) into Eq. (7.2), we obtain

$$\mathbf{E}^{(4)} = \frac{1}{2}\begin{pmatrix} M'_{RR}M_{RR}{}^*e^{-2i\theta} + M'_{RR}M_{LR}{}^* + M'_{RL}M_{RR}{}^* + M'_{RL}M_{LR}{}^*e^{2i\theta} \\ M'_{LR}M_{RR}{}^*e^{-2i\theta} + M'_{LR}M_{LR}{}^* + M'_{LL}M_{RR}{}^* + M'_{LL}M_{LR}{}^*e^{2i\theta} \end{pmatrix}$$

$$M'_{RR}M_{RL}{}^{*}e^{-2i\theta} + M'_{RR}M_{LL}{}^{*} + M'_{RL}M_{RL}{}^{*} + M'_{RL}M_{LL}{}^{*}e^{2i\theta}$$
$$M'_{LR}M_{RL}{}^{*}e^{-2i\theta} + M'_{LR}M_{LL}{}^{*} + M'_{LL}M_{RL}{}^{*} + M'_{LL}M_{LL}{}^{*}e^{2i\theta}\Big)(\mathbf{E}^{(1)})^{*}.$$

Using the random-coupling approximation used in Appendix C of Chapter 6, that is,

$$M'_{RR}M_{RR}{}^{*}, M'_{RL}M_{LR}{}^{*}, M'_{LR}M_{RR}{}^{*}, M'_{LL}M_{LR}{}^{*},$$

$$M'_{RR}M_{RL}{}^{*}, M'_{RL}M_{LL}{}^{*}, M'_{LR}M_{RL}{}^{*}, M'_{LL}M_{LL}{}^{*} \simeq \frac{1}{2}I,$$

and

$$M'_{RR}M_{LR}{}^{*}, M'_{RL}M_{RR}{}^{*}, M'_{LR}M_{LR}{}^{*}, M'_{LL}M_{RR}{}^{*},$$

$$M'_{RR}M_{LL}{}^{*}, M'_{RL}M_{RL}{}^{*}, M'_{LR}M_{LL}{}^{*}, M'_{LL}M_{RL}{}^{*} \simeq O(1/\sqrt{N}),$$

we find that

$$\mathbf{E}^{(4)} = \frac{1}{2}r\cos 2\theta(\mathbf{E}^{(1)})^{*} + \mathbf{U}, \tag{7.6}$$

where $\mathbf{U}$, like $\mathbf{V}$ in Eq. (6.29), denotes the depolarized noise field. We note that Eq. (7.6) has the same form as Eq. (6.29) except for the factor $\cos 2\theta$.

From the same arguments as those described in obtaining Eqs. (6.43*a*) and (6.43*b*) the polarized power $P_{\text{pol.}}$ and the depolarized noise power P_{M} can be expressed as

$$P_{\text{pol.}} = 2\lambda\cos^2 2\theta\sum_{i=1}^{\text{M}}\Theta_i, \tag{7.7a}$$

$$P_{\text{M}} = 2\lambda(2 - \cos^2 2\theta)\sum_{i=1}^{\text{M}}\Delta_i, \tag{7.7b}$$

where λ is again given by $|r|^2 d/8$ and the effects of the residual polarization and of the quality of phase conjugation by the PCM are neglected for simplicity (i.e., $q = 0$ and $\eta = 1$). From Eqs. (7.7*a*) and (7.7*b*) the degree of polarization $P^{(4)}$ and the reflectivity R for the field $\mathbf{E}^{(4)}$ can be written as

$$P^{(4)} = \frac{\cos^2 2\theta}{(1 - \beta_2)\cos^2 2\theta + 2\beta_2}$$
$$\simeq p, \tag{7.8a}$$

$$R(\theta) = \frac{1}{8}|r|^2 \sum_{i=1}^{M} \Theta_i [(2 - \beta_2)\cos^2 2\theta + 2\beta_2], \tag{7.8b}$$

where β_2 is defined by Eq. (6.45*b*). From Eqs. (7.6) and (7.8) we notice that the polarization and spatial information of the field $\mathbf{E}^{(1)}$ can be recovered, provided that the input-beam N.A. is small (i.e., $\beta_2 \ll 1$) and that the Faraday rotation θ gives non-negligible values of $\cos^2 2\theta$ compared to β_2 in Eqs. (7.8*a*) and (7.8*b*).

The experiment was performed using the x-polarized input beam with an N.A. of 0.01 (see Fig. 7.2). A variable Faraday rotator was used as the nonreciprocal media. The degree of the polarization recovery p (defined in Chapter 6) and the x-polarized phase-conjugate power at D_1 were measured. The experimental results are shown in Fig. 7.3, together with the theoretical curves of $P^{(4)}$ and $R(\theta)/R(0)$ calculated from Eqs. (7.8*a*) and (7.8*b*). In the theoretical curves $\sum_{i=1}^{M} \Theta_i = 1$ and the gaussian distribution of the noise intensity given by Eq. (6.52) with $(\phi/\phi_0)^2 = 0.001$ and $\psi/\phi = 0.5$ are used. It is seen that the normalized reflectivity $R(\theta)/R(0)$ varies almost as $\cos^2 2\theta$, while p is almost unity except in the vicinity of θ=45°. It is seen that these theoretical curves are in good agreement with the experiment.

7.3 Correction of lossy amplitude distortions

Most of the distortion correction schemes which are based on phase-conjugate optics involve phase distorting media (see, for example, Section 5.4 in Chapter 5). This is due to the fact that distortion corrections cannot be achieved in cases involving inhomogeneous losses since part of the spatial information is lost and is not available for a reconstruction.

In this section we describe a method of recovering an original image, including its polarization state, that has propagated through a lossy distorter by using modal dispersal in a multimode fiber and a photorefractive PCM. In this method, before its incidence upon the lossy distorting medium the image-bearing beam is intentionally

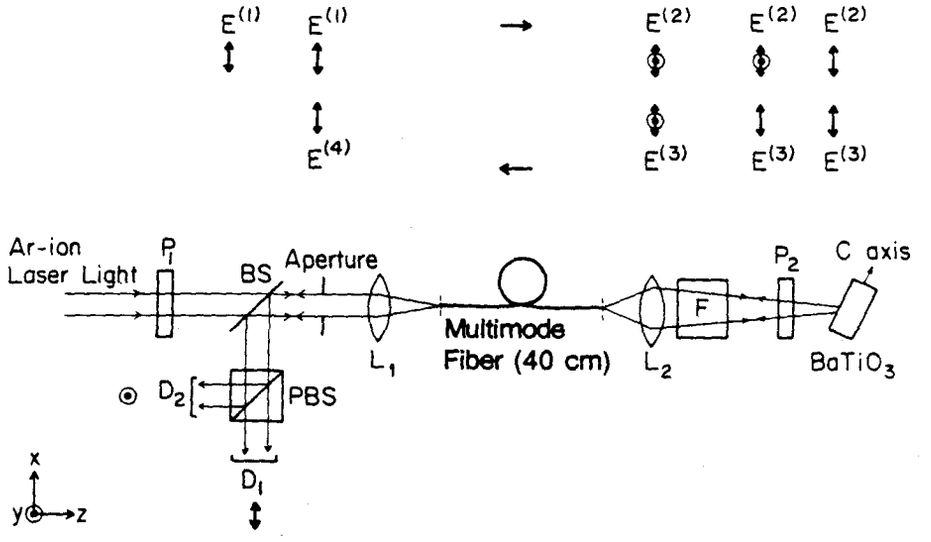

Figure 7.2 The experimental arrangement used to demonstrate polarization recovery with a nonreciprocal medium. P_1, P_2, are x polarizers; BS, beam splitter: PBS, polarizing beam splitter; L_1, L_2, lenses; D_1, D_2, photodetectors; F, variable Faraday rotator.

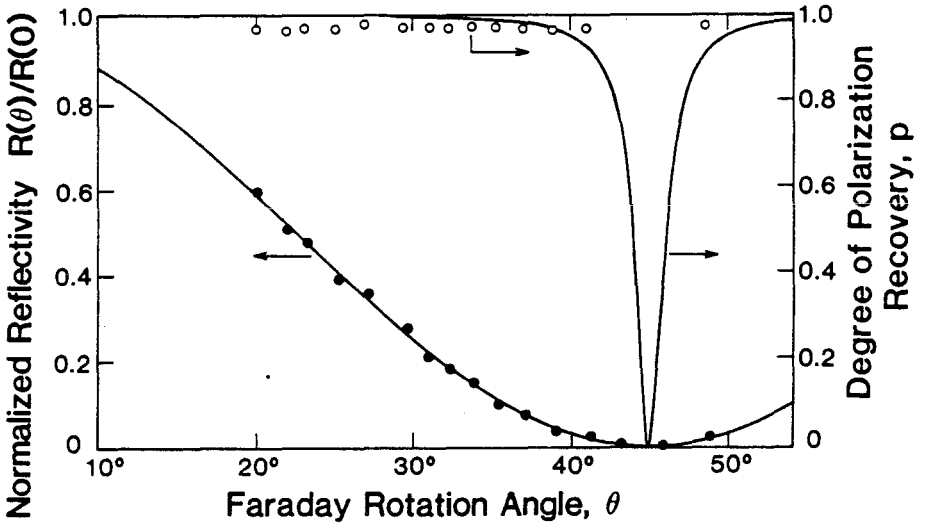

Figure 7.3 Experimental results of the degree of polarization recovery $p(\circ)$ and the normalized reflectivity $R(\theta)/R(0)$ $(\bullet)$. The solid lines are theoretical curves using the gaussian noise distribution$(\psi/\phi_0 = 0.5)$ and $(q, \eta) = (0, 1)$.

mode dispersed by propagating through a (multi)mode- and polarization-scrambling fiber so that the field exiting the fiber has the original pictorial and polarization information spread among a large number of modes; this robustness enables it, within certain limits, to reconstruct the original field including the polarization. We note that, unlike the past studies of image transmission through multimode fibers [7.1–9], the multimode fiber is used as a way to achieve mode and polarization scrambling of the input information.

The method is illlustrated in Fig. 7.4. In this case the lossy distortion occurs between the fiber and the PCM. Therefore the matrix C in Eq. (6.5), which accounts for the modal loss and mixing of the incoming field by the distortion, has the form of

$$C = \begin{pmatrix} C_{xx} & 0 \\ 0 & 0 \end{pmatrix}, \tag{7.9}$$

where C_{xx} is an $N \times N$ submatrix which accounts for the elimination of the y-polarized field and the modal loss and mixing of the x-polarized field in the distorting medium. The form of the matrix C also implies that the loss does not scramble the polarizations. In particular we have $(C_{xx})_{ij} = \delta_{ij}$ when only a polarizer (oriented to the x direction) acts as the distorting medium [see Eq. (6.5)]. From Eqs. (6.3) and (7.9) we find that

$$M'CM^* = \begin{pmatrix} M'_{xx}C_{xx}M^*_{xx} & M'_{xx}C_{xx}M^*_{xy} \\ M'_{yx}C_{xx}M^*_{xx} & M'_{yx}C_{xx}M^*_{xy} \end{pmatrix}. \tag{7.10}$$

In the case of a large number of nonvanishing elements $(C_{xx})_{ij}$ and using the random coupling approximation, each element in Eq. (7.10) can be approximated by

$$(M'CM^*)_{ij} \rightarrow \begin{cases} \dfrac{1}{2N}\displaystyle\sum_{k=1}^{N}(C_{xx})_{kk}, & for\ i = j \\ O(1/\sqrt{N}), & for\ i \neq j \end{cases}$$

where $M_{ij} = 1/\sqrt{2N}\exp(i\phi_{ij})$ is used (see Appendix C in Chapter 6). We therefore get

$$\mathbf{E}^{(6)} = \frac{1}{2}r\left[\frac{1}{N}\sum_{k=1}^{N}(C_{xx})_{kk}\right](\mathbf{E}^{(1)})^* + \mathbf{W}, \tag{7.11}$$

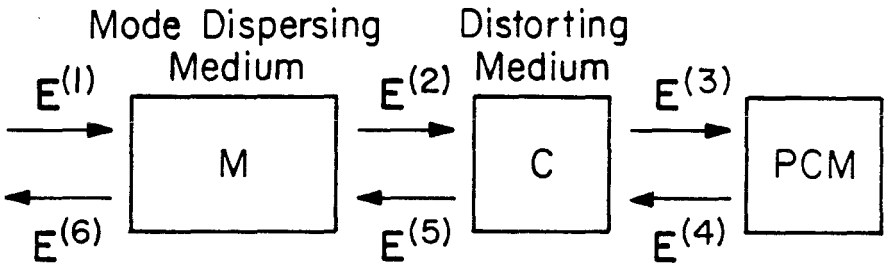

Figure 7.4 A method to undo the lossy distortion effect by means of the tandem combination of the mode-dispersing medium (M) and the PCM. The lossy distortion due to the distorting medium (C) occurs between the M and the PCM.

where $\mathbf{W}$ is a $2N$ rank vector whose elements depend on the elements of $\mathbf{E}^{(1)}$ and C_{xx} as well as N. We note that the first term on the right-hand side of Eq. (7.11) corresponds to the true phase-conjugate replica of the field $\mathbf{E}^{(1)}$ including its polarization state. The second term $\mathbf{W}$ corresponds to (depolarized) noise. And as shown in Chapter 6, in the absence of the lossy distorter [i.e., $(C_{xx})_{ij} = \delta_{ij}$] this noise contribution can be negligible in the limit where the input beam $\mathbf{E}^{(1)}$ excites, at the input, only a small fraction of the total number of modes $2N$, and the detection aperture is close to the input aperture so that only a small fraction of the noise power is included in the input aperture. In the present case it is seen from Eq. (7.11) that the true phase conjugation is possible, within the above limits, even when a large number of modes are lost by the distorting medium as long as the near equipartition of modal energy in the mode-dispersing medium is satisfied so that the input information is distributed equally among all the modes.

In the experiment shown in Fig. 7.5, a knife edge F was used as the simulated amplitude distorter (or medium) in order to eliminate some portions of the input information. In Fig. 7.5(a) a transparency T containing pictorial information was illuminated by the x-polarized beam from the multilongitudinal-mode argon-ion laser (λ=514.5 nm). The image-bearing beam $\mathbf{E}^{(1)}$ (5 mm in diameter) was launched into a multimode graded-index fiber (100 μm core diameter, 0.29 N.A. and 5 m long) with about 0.036 N.A. input by using an aperture AP and an f=70 mm lens L1. With this small N.A. of the input compared to the fiber's N.A., the (depolarized) noise contribution [corresponding to $\mathbf{W}$ in Eq. (7.11)] is negligible for the formation of the true phase conjugation. The knife edge F was placed in the image plane of the fiber end and eliminated some portions of the out-coupled beam $\mathbf{E}^{(2)}$. In this case the microscope objective L2 of 0.40 N.A. covering 0.29 N.A. of the fiber was used to image the fiber end through a polarizer P oriented to the x direction. A poled $BaTiO_3$ crystal was used as a self-pumped PCM, and its phase-

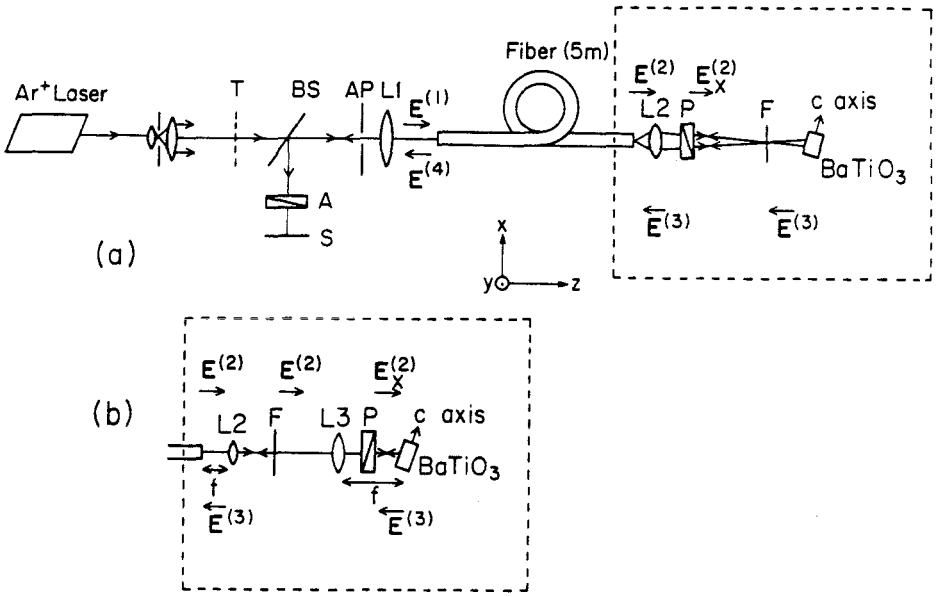

Figure 7.5 The experimental arrangement. In (a) the out-coupled beam $\mathbf{E}^{(2)}$ is imaged onto F. In (b) $\mathbf{E}^{(2)}$ is quasi-collimated onto F.

conjugate reflectivity was 35% for the incident power of 3 mW on the crystal. The reflected beam $\mathbf{E}^{(4)}$ from the input end of the fiber is picked off by a nonpolarizing beam splitter BS and forms the reconstructed image on the screen S. The analyzer A was used to partly eliminate the noise contribution.

In Fig. 7.5(b) F was placed in the far-field plane of the fiber end for a comparison of the results with those of the former configuration. In this case the out-coupled beam $\mathbf{E}^{(2)}$ was quasi-collimated (about 3 mm in diameter) by L2, and some portions of the quasi- collimated beam were eliminated by F.

First we measured the Stokes parameters (s_0, s_1, s_2, s_3) of the fields $\mathbf{E}^{(1)}, \mathbf{E}^{(2)}$, and $\mathbf{E}^{(4)}$ so that the degree of polarization $[P^{(i)}\ (i = 1, 2, 4)]$ and the degree of polarization recovery p could be calculated. The x-polarized uniform beam (5 mm in diameter and $P^{(1)}$, $p > 0.99$) was used as the input field $\mathbf{E}^{(1)}$ together with the configuration shown in Fig. 7.5(a). Because of the strong intermodal scattering in the fiber the field $\mathbf{E}^{(2)}$ exhibited speckled structures and nearly complete depolarization ($P^{(2)}$, $p < 0.09$). Figure 7.6 shows $P^{(4)}$ and p as a function of various transmission losses due to F. It is seen that p and $P^{(4)}$ are almost equal for all losses and both decrease as the loss increases. This shows that the original polarization recovery deteriorates gradually because of the relative increase of the depolarized noise as the loss increases. This may indicate, as noted before, that the equipartition of the input information among all the modes in the fiber used is incomplete. Nonetheless we see that the polarization recovery is still about 0.66, even in the case of the largest loss of 67%, i.e., 66% of the reflected beam power is in the true phase-conjugate beam and the remainder is in the depolarized noise.

Figures 7.7(a) – 7.7(f) show the results when the knife edge F was placed at the image plane of the out-coupled field $\mathbf{E}^{(2)}$. It is seen from Fig. 7.7(b) and 7.7(c) that the phase-conjugate image with F removed preserves its original polarization and spatial structure. It is also clear from Fig. 7.7(d) – 7.7(f) that, although the

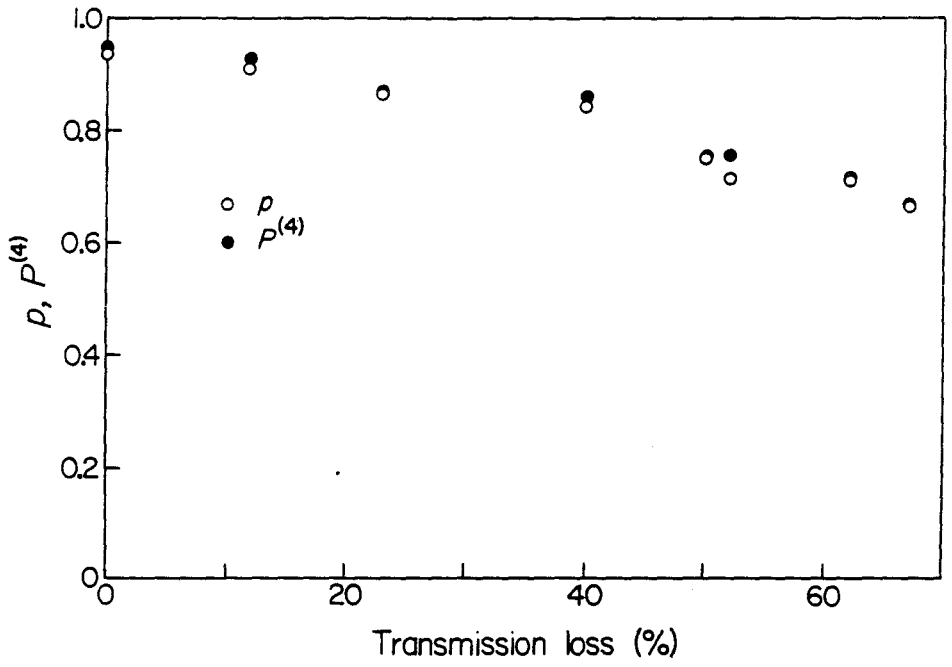

Figure 7.6 The degree of polarization recovery $p(\circ)$ and the degree of polarization $P^{(4)}$ $(\bullet)$ of the output field $\mathbf{E}^{(4)}$ as a function of the transmission loss due to F for the linearly x-polarized input beam.

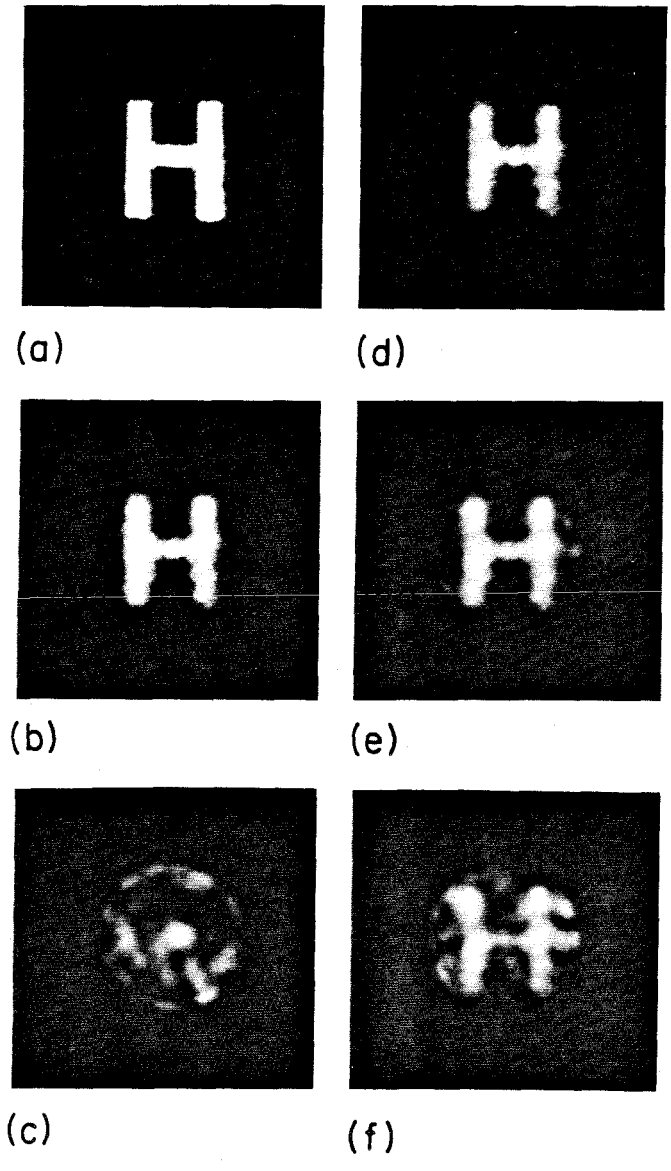

Figure 7.7 (a) The x-polarized input image. (b) Phase-conjugate image of the x polarization without F (12 times the intensity-attenuated image). (c) Phase-conjugate image of the y polarization without F. (d)–(f) Phase-conjugate images of the x polarization with various transmission losses due to F; (d) loss 23% (12 times the intensity-attenuated image), (e) loss 53% (2 times the intensity-attenuated image), (f) loss 68.5%.

intensities of the phase-conjugate images decrease as the transmission loss due to F increases, the phase-conjugate replica of the input image can be reconstructed. However, we see the apparent degradation of the spatial structure of the phase-conjugate image shown in Fig. 7.7(f). This may also be attributed, as mentioned above, to the incomplete equipartition of the input information among all the modes in the fiber. Therefore above a certain limit of the loss by F, [e.g., the case of Fig. 7.7(f)], the reconstructed image bears less information than the original image, resulting in the apparent degradation. This effect may be analogous to the case of image reconstruction in holography with a diffused signal [7.26], when the resolution in the reconstructed image decreases as the fragment of hologram becomes smaller. In the present scheme the degradation depends strongly on the modal-scrambling nature in the fiber. We could also obtain the same result with the configuration shown in Fig. 7.5(b). This fact indicates that, although the mode scrambling of the input information in the fiber used is not complete, the input information is redistributed among a sufficiently large number of modes (viz., spatial frequencies) of the out-coupled field from the fiber, and therefore the present method is almost insensitive to the position of the distorter between the fiber and the PCM [7.27].

7.4 Phase-conjugate multimode fiber-optic sensors

Fiber-optic sensors for detecting various physical perturbations (such as magnetic, acoustic, temperature, and rotation) offer orders of magnitude increased sensitivity over existing technologies with remote-sensing capabilities and flexible interconnections within instruments [7.28]. In order to obtain stable operations, single-mode fibers have been used, (particularly in the Mach-Zehnder-, Michelson-, and Fabry-Perot-type arrangements for interferometer configurations). On the other hand, multimode fibers have usually been employed as amplitude sensors, rather than as (interferometric) phase sensors, with less sensitivities [7.28]. This

is because coherent light suffers polarization scrambling and speckling during propagation in multimode fibers, as shown in Chapter 6. However, because of several advantages over single-mode fibers such as ease of use, cost, and multichannel carrying capability, multimode fiber-optic interferometers for sensor applications are still favored and suggested [7.29,30]. In this section we describe several possible applications as amplitude and/or phase sensors.

7.4.1 Amplitude sensors

The interesting property of correction of nonreciprocal polarization distortions described in Section 7.2 can be applied to several sensing schemes. One application is a magnetic field sensor. In such a case a tandem combination of the Faraday medium F and the PCM (or a part of the fiber) acts as the sensor part [7.31]. The magnetic field along the medium F (or along the sensor part of the fiber) induces Faraday rotations and can be detected by measuring the reflectivity R given by Eq.(7.8*b*). Because the detected signal is from the phase-conjugate wave of the input signal, self-aligned and stable operations can be expected.

Another application is a current sensor. In this case the current to be measured is enclosed by the multimode fiber coil (see Fig. 7.8). The current will be measured through the dependence of the reflectivity R on the magnetic field induced by the current. This proposed scheme is free from the problem of modal coupling that arises when a single-mode nonpolarization-preserving fiber is used for this purpose [7.32].

To simulate the above applications, i.e., distributed Faraday rotations in a fiber, the theory given in Section 7.2 was generalized to a sequence of N Faraday rotators separated by sections of fibers. The result, which was also proved experimentally with N=2, simply replaces $\cos^2 2\theta$ in Eqs.(7.8*a*) and (7.8*b*) by $\prod_{i=1}^{N}\cos^2(2\theta_i)$. An experiment in which the magnetic field was directly applied along a fraction of the

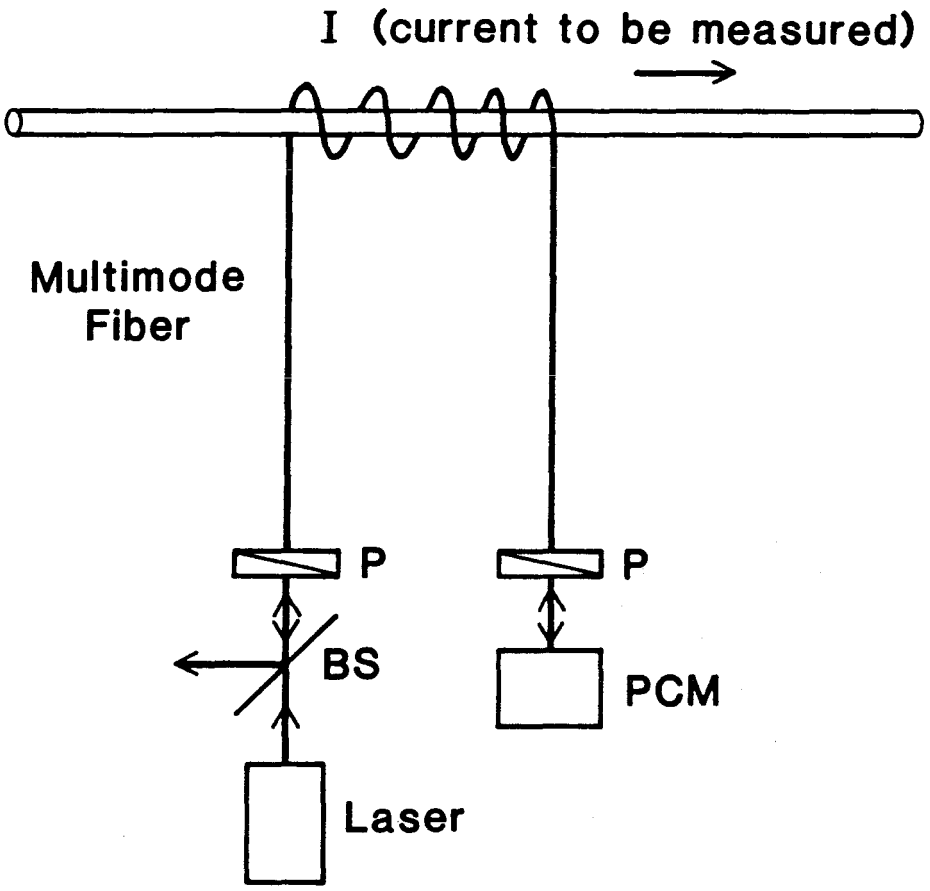

Figure 7.8 Schematic diagram of a proposed current sensor. A beam from the laser propagates through a linear polarizer P and a multimode fiber. It is then reflected by the PCM and retraces its path.

multimode fiber (about 3 m of the 20 m long fiber) was also conducted. It was observed that the degree of polarization recovery p is nearly unity in the range of 0 to 2 KG of the magnetic field, while the reflectivity R decreases monotonically with the increase of the magnetic field. It was found that Eq. (7.8*b*) replaced $\cos^2 2\theta$ by $\cos^{2N} 2\theta$ with θ=VHL/N (V is the Verdet constant of the fiber material, H the magnetic field, and L the fiber length under the magnetic field) fit well with the experimental data when N=100 was used. Although the reason for good agreement with N=100 has not been clear yet and should be the subject of future study, the insensitivity of the polarization recovery to the magnetic field in this situation is also an important factor for fiber-optic gyro applications [7.33].

7.4.2 (Interferometric) phase sensors

The use of PCM's for multimode fiber-optic interferometers can suppress polarization-scrambling and speckling noise problems. In particular the multimode fiber-optic Michelson interferometer using a self-pumped PCM has been proposed[7.8,15,16]. The reason why this scheme functions as an interferometer is, as described in Chapter 4, the fact that a self-pumped PCM preserves the same uniform phase change of the input probe beam upon reflection. Feinberg [7.34] qualitatively demonstrated this property, together with the correction capability of nonuniform phase distortions, in a Michelson interferometer with a self-pumped PCM using internal reflection in one arm. Tomita *et al.* [7.35] also showed the excellent linearity of the instantaneous response to the uniform phase change of the input by means of quantitative phase measurements.

The scheme, first proposed by Fischer and Sternklar [7.8], is shown in Fig. 7.9(a) where polarization scrambling and speckling of the field emitted from the fiber can be corrected in a double pass, yet the uniform phase change caused by some external perturbations to the fiber can be detected by the movement of the

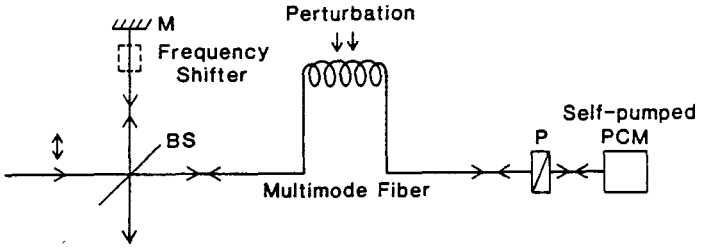

(a)

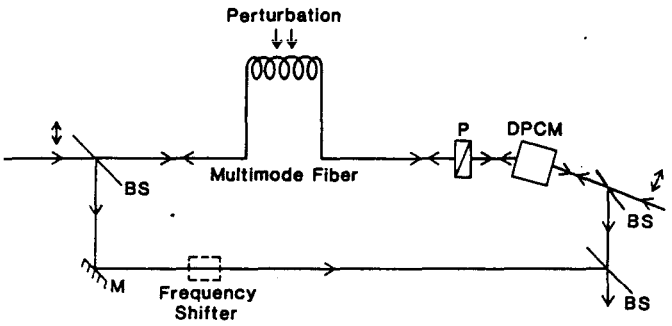

(b)

Figure 7.9 Two configurations of phase-conjugate multimode fiber-optic interferometers: (a) Michelson interferometer; (b) Mach-Zehnder interferometer. Input beams are linearly polarized for both (a) and (b). Uniform phase changes of the input beams propagating in the fibers are impressed by some external perturbations such as temperature changes. Note that the frequency shifters illustrated in (a) and (b) are not essential but are used for compensating the frequency shift of the conjugate beams relative to the input beams and/or for the heterodyne detection of the phase changes. P:polarizer; M:mirror; BS:beam splitter.

interference fringe. The problem of a frequency shift ($\leq$ a few Hz) of the conjugate beam relative to the input beam in a self-pumped PCM [7.36,37] may be eliminated by introducing a frequency shift in the reference beam. This intentional frequency shift also enables us to employ the heterodyne detection scheme used in usual fiber-optic interferometers [7.28]. Another scheme, proposed by Sternklar *et al.* [7.15], is also shown in Fig. 7.9(b). In this case a Mach-Zehnder interferometer with multimode fibers is used together with a double phase-conjugate mirror (DPCM) [7.38]. Because of the property of the DPCM a uniform phase change impressed on the beam propagating in the fiber is transfered to the other conjugate beam without any wavefront aberration, and the phase change can be detected by the fringe movement. In particular, these schemes can be applied to a temperature sensor since the temperature change at a small portion of the fiber causes the change of the refractive index of the fiber, thereby giving the fringe movement. We note that these interferometers using multimode fibers and the self-pumped PCM and/or the DPCM give not only many advantages of multimode fibers over single-mode fibers but also give high sensitivity and stability to the system.

Another possible application is a fiber-optic gyroscope [7.28,33] which is one of the most important applications in fiber-optic sensor systems. Because of the polarization-preserving property (even under a magnetic field) of the multimode fiber-PCM combination for small N.A. inputs, the combination can be applied to this purpose. A Sagnac interferometer has usually been employed for this purpose because it is inherently insensitive to reciprocal phase shifts but is sensitive to nonreciprocal phase shifts. In this case the phase difference ϕ between the recombining beams on the detection is given by

$$\phi = \frac{8\pi RL\Omega}{\lambda c}, \tag{7.12}$$

where R and L are the radius and length of the fiber coil, respectively, and Ω is the rotation rate, λ is the wavelength, and c is the speed of light. We note that,

because of the round-trip propagation nature of phase conjugation, for given R and L the phase difference ϕ is 2 times larger than that in a conventional fiber-optic loop interferometer [7.33]. This new type of gyro using the multimode fiber-PCM configuration also has advantages in that inexpensive and easy-to-use multimode fiber and couplers can be used, and that self-aligned coupling to the fiber can be obtained by phase conjugation.

The experimental proof-of-principle demonstrations of rotation sensing with phase-conjugate fiber-optic gyros were performed for the first time by using a Michelson interferometer with an externally pumped NPPPCM [7.19] and a Sagnac interferometer with a self-pumped PPPCM [7.20]. In both cases, however, single-mode polarization-preserving fibers were used. It should be noted that even for the latter case (i.e., the use of the self-pumped PCM) the nonreciprocal phase shift between two counter-propagating beams in the fiber can be detected since the relative phase change between the two input beams is truly reversed in a self-pumped PCM [7.35] (see Fig. 4.10). Later a multimode fiber and a self-pumped NPPPCM were employed for a Sagnac interferometer, and rotation sensing of 6°/sec (which corresponds to a phase shift of 0.09 rad in that experiment) was demonstrated [7.39]. A different type of multimode fiber-optic gyro [7.18], using a photorefractive ring passive PCM in which the ring consists of a multimode fiber, was previously reported.

In these phase-conjugate fiber-optic gyros the dynamic correction of reciprocal phase shifts is limited by the finite response time of phase conjugators, and changes in the phase-conjugate reflectivity of phase conjugators may be responsible for drift of output signals on a larger time scale [7.39]. The improvement of the system performance especially for the above problems may be done by using, for example, the double PCM configuration as shown in Fig. 5.9 with the phase modulation.

References for Chapter 7

7.1. A. Yariv, Appl. Phys. Lett. **28**, 88 (1976).

7.2. A. Yariv, J. Opt. Soc. Am. **66**, 301 (1976).

7.3. A. Gover, C.P. Lee, and A. Yariv, J. Opt. Soc. Am. **66**, 306 (1976).

7.4. The use of conjugate waves from a hologram was firstly reported by M.M. Ponte, C.R. Acad. Soc. Paris, t.**264**, 1015 (1967).

7.5. V.V. Ivakhnik, V.M. Petnikova, M.S. Solomatin, and V.V. Shuvalov, Sov. J. Quantum Electron. **10**, 373 (1980).

7.6. G.J. Dunning and R.C. Lind, Opt. Lett. **7**, 558 (1982).

7.7. B. Fischer and D. Peri, Opt. Lett. **10**, 182 (1985).

7.8. B. Fischer and S. Sternklar, Appl. Phys. Lett. **46**, 113 (1985).

7.9. P.H. Beckwith, I. McMichael, and P. Yeh, Opt. Lett. **12**, 510 (1987).

7.10. Y. Tomita, R. Yahalom, K. Kyuma, A. Yariv, and N. S.-K. Kwong, IEEE J. Quantum Electron. **QE-25**, 315 (1989).

7.11. S.-K. Kwong, R. Yahalom, K. Kyuma, and A. Yariv, Opt. Lett. **12**, 337 (1987).

7.12. Y. Tomita, K. Kyuma, R. Yahalom, and A. Yariv, Opt. Lett. **12**, 1020 (1987).

7.13. R. Yahalom, K. Kyuma, and A. Yariv, Appl. Phys. Lett. **50**, 792 (1987).

7.14. R. Yahalom and A. Yariv, Opt. Lett. **13**, 889 (1988).

7.15. S. Sternklar, S. Weiss, M. Segev, and B. Fischer, Appl. Opt. **25**, 4518 (1986).

7.16. N. S.-K. Kwong, in *Postdeadline Papers of Conference on Optical Fiber Sensors* (Optical Society of America, Washington, D.C., 1988).

7.17. C.J. Bode, in *Experimental Gravitation and Measurement Theory*, P. Mystre and M.O. Scully, eds., (Plenum, New York, 1983), pp. 269–291.

7.18. B. Fischer and S. Sternklar, Appl. Phys. Lett. **47**, 1 (1985).

7.19. P. Yeh, I. McMichael, and M. Khoshnevisan, Appl. Opt. **25**, 1029 (1986).

7.20. I. McMichael and P. Yeh, Opt. Lett. **11**, 686(1986).

7.21. I. McMichael, P.H. Beckwith, and P. Yeh, Opt. Lett. **12**, 1023 (1987).

7.22. B. Fischer, S. Sternklar, and S. Weiss, Appl. Phys. Lett. **48**, 1567 (1986).

7.23. H.J. Caulfield, J. Shamir, and Q. He, Appl. Opt. **26**, 2291 (1987).

7.24. S. Weiss, M. Segev, S. Sternklar, and B. Fischer, Appl. Opt. **27**, 3422 (1988).

7.25. Y. Tomita, R. Yahalom, and A. Yariv, Appl. Phys. Lett. **52**, 425 (1988).

7.26. R.J. Collier, C.B. Burckhardt, and L.H. Lin, *Optical Holography*, (Academic Press, New York, 1971), p. 197.

7.27. It should be noted that since the experiment is made for the distorter placed on both the image plane and the far-field plane of the fiber end, the phase-conjugate images obtained here *are not* a consequence of simple Fourier filtering of the input image.

7.28. T.G. Giallorenzi, J.A. Bucaro, A. Dandridge, G.H. Sigel, Jr., J.H. Cole, S.C. Rashleigh, and R.G. Priest, IEEE J. Quantum Electron. **QE-18**, 626 (1982).

7.29. M.R. Layton and J.A. Bucaro, Appl. Opt. **18**, 666 (1979).

7.30. M. Imai, T. Ohashi, and Y. Ohtsuka, J. Lightwave Technol. **LT-1**, 75 (1983).

7.31. A magnetic field sensor using a single-mode polarization-preserving fiber and a normal mirror has also been proposed by A. Enokihara, M. Izutsu, and T. Sueta, IEEE/OSA J. Lightwave Technol. **LT-5**, 1584 (1987).

7.32. A. Yariv, Appl. Opt. **26**, 4538 (1987).

7.33. R.A. Bergh, H.C. Lefevre, and H.J. Shaw, IEEE/OSA J. Lightwave Technol. **LT-2**, 91 (1984).

7.34. J. Feinberg, Opt. Lett. **8**, 569 (1983).

7.35. Y. Tomita, R. Yahalom, and A. Yariv, in *Technical Digest of Annual Meeting of Optical Society of America* (Optical Society of America, Washington D.C., 1988), paper FB8, p. 161.

7.36. W.B. Whitten and J.M. Ramsey, Opt. Lett. **9**, 44 (1984).

7.37. J. Feinberg and G.D. Bacher, Opt. Lett. **9**, 420 (1984).

7.38. S. Weiss, S. Sternklar, and B. Fischer, Opt. Lett. **12**, 114 (1987).

7.39. I. McMichael, P.H. Beckwith, and P. Yeh, Opt. Lett. **12**, 1023 (1987).